DEVELOPMENT OF NOVEL ACOUSTIC WAVE BIOSENSOR PLATFORMS

BASED ON MAGNETOSTRICTION AND FABRICATION OF

MAGNETOSTRICTIVE NANOWIRES

Except where reference is made to the work of others, the work described in this dissertation is my own or was done in collaboration with my advisory committee. This dissertation does not include proprietary or classified information.

_____
Suiqiong Li

Certificate of Approval:

_____
Bryan A. Chin
Professor
Materials Engineering

_____
Zhongyang Cheng, Chair
Associate Professor
Materials Engineering

_____
Barton C. Prorok
Associate Professor
Materials Engineering

_____
Curtis Shannon
Professor
Chemistry and Biochemistry

_____
Tung-shi Huang
Associate Professor
Nutrition and Food Science

_____
Joe F. Pittman
Interim Dean
Graduate School

DEVELOPMENT OF NOVEL ACOUSTIC WAVE BIOSENSOR PLATFORMS

BASED ON MAGNETOSTRICTION AND FABRICATION OF

MAGNETOSTRICTIVE NANOWIRES

Suiqiong Li

A Dissertation

Submitted to

the Graduate Faculty of

Auburn University

in Partial Fulfillment of the

Requirements for the

Degree of

Doctor of Philosophy

Auburn, Alabama
August 4, 2007

DEVELOPMENT OF NOVEL ACOUSTIC WAVE BIOSENSOR PLATFORMS

BASED ON MAGNETOSTRICTION AND FABRICATION OF

MAGNETOSTRICTIVE NANOWIRES

Suiqiong Li

_____
Signature of Author

_____
Date of Graduation

VITA

Suiqiong Li, daughter of Tiankai Li and Surong Xu, was born on June 2, 1973, in Beijing, P. R. China. She attended Beijing University of Technology (formerly known as Beijing Polytechnic University), Beijing, for five years and graduated with a Bachelor of Science degree in Material Science and Engineering in July, 1996. In August of 2001 she entered the Graduate School at Auburn University to pursue a doctoral degree in Material Science and Engineering. She has performed research for five years under the guidance of Dr. Zhongyang Cheng.

DISSERTATION ABSTRACT

DEVELOPMENT OF NOVEL ACOUSTIC WAVE BIOSENSOR PLATFORMS

BASED ON MAGNETOSTRICTION AND FABRICATION OF

MAGNETOSTRICTIVE NANOWIRES

Suiqiong Li

Doctor of Philosophy, August 4, 2007
(B.S., Beijing University of Technology, 1996)

269 Typed Pages

Directed by Zhongyang Cheng

There is an urgent need for biosensors that are able to detect and quantify the presence of a small amount of biological threat agents in a real-time manner. Acoustic wave (AW) devices, whose performance is defined by mass sensitivity (S_m) and merit quality factor (Q value), have been extensively studied as high performance biosensor platforms. However, current AW devices face some challenges in practical applications.

In this research, two types of AW devices – magnetostrictive microcantilever (MSMC) and completely free-standing magnetostrictive particle (MSP) – were developed. The research consists of two parts: 1) Design and the feasibility study of MSMC and MSP based sensor technology; 2) Fabrication and characterization of micro/nano MSPs

made of amorphous Fe-B alloy. Both MSMC and MSP based sensors are wireless/remote and work well in liquid, which makes the sensors good candidates for *in-situ* detection.

The performance of MSMC was simulated and compared with the state of art AW devices: microcantilevers. The MSMC exhibits the following advantages: 1) remote/wireless driving and sensing; 2) ease of fabrication; 3) works well in liquid; 4) exhibits a high Q value (> 500 in air); 5) well suited for sensor array development. MSMCs in milli/micro sizes were fabricated and their performance was characterized in air and liquid. The experimental results confirm the advantages of MSMC mentioned above. The *in situ* detection of the yeast cells and *Bacillus anthracis* spores in water were performed using MSMC biosensors.

MSPs in the shape of strip and bar were investigated. Strip-shape MSPs in milli/micro sizes were fabricated. The resonance behaviors of MSPs at the even and odd vibration modes were analyzed. MSP exhibits a S_m about 100 times greater, and a Q value about 10 times greater, than MCs. A multiple-sensor and a multiple-target approach were developed to further enhance the performance of MSP-based sensors. A unique methodology was created to detect the target species on the sensor surface at different locations by combining even and odd harmonic mode signals.

As with other AW devices, a smaller size results in a higher S_m. To create micro/nano sized MSMC & MSP sensors, amorphous Fe-B thin films and nanowires were fabricated using electrochemical deposition. The microstructure, morphology, composition and magnetic properties of the fabricated nanowires were determined. It is found that the films and the nanowires are excellent candidates for developing micro/nano MSPs and MSMCs.

ACKNOWLEDGMENTS

Style manual or journal used:

        <u>IEEE Transactions on Magnetics</u>

Computer software used:

        <u>Microsoft Word, Excel, OriginPro 7.5, Peakfitting</u>^{TM}

TABLE OF CONTENTS

CHAPTER 5

DESIGN AND FEASIBILITY STUDY OF MAGNETOSTRICTIVE PARTICLES AS
BIOSENSOR PLATFORM

LIST OF FIGURES

xvii

xix

LIST OF TABLES

CHAPTER 1

INTRODUCTION

Micro-organisms, such as bacteria and virus, are widely found in the nature and the environment, such as food, soil, water and the intestinal tracts of humans and animals. Although most of these micro-organisms have essential functions in nature and beneficial relations with humans, certain bacteria or viruses are harmful and can cause serious and infectious diseases. It is estimated that infectious diseases cause about 40% of the total annual deaths world-wide [1]. In the United States, approximate 76 million food borne illnesses occur each year, which accounts for 325,000 hospitalizations and 5,000 deaths [2]. The United States Department of Agriculture (USDA) reports that medical costs and productivity losses due to major food pathogens result in $2.9~$6.7 billion per year [3, 4]. The recent outbreak of *E. coli* O157 infections related to spinach was large and deadly, which shows that better control and prevention methods are needed in the food industry [5]. Since the 9-11 terrorist attack, the requirement of monitoring threat agents for biological weapons is growing. The spread of bio-threat microorganisms can cause high fatality rate diseases throughout a huge population. Prevention of microbial diseases depends on effective and rapid detection of various pathogenic micro-organisms in food, clinic medicine and the environment. Therefore, analytical technologies for detecting and quantifying the presence of a small amount of biological threat agents in a real-time manner are urgently needed in food safety, medical diagnostics, environmental

1

monitoring, and in public safety/security areas.

Effective biological-detection methods should meet a number of criteria, such as response time, sensitivity and specificity [1, 6, 7]. Rapid detection is critical for disease control. Meanwhile, extremely sensitive detection methods are required since for some pathogenic organisms, such as *E. coli* O157:H7, the presence of even several cells may be an infectious dose [1, 6, 8]. Additionally, since most of micro-organisms exist in liquid environments, detection methods that can be directly carried out in liquid are highly desired. At the same time, from the industry point of view, the microbiological detection methods should be inexpensive, robust and easy to operate [1, 9].

This research focuses on developing novel high performance biosensor platforms for effective biological detection. Two kinds of novel acoustic wave (AW) sensor platforms based on the magnetostrictive effect – magnetostrictive microcantilever (MSMC) and magnetostrictive particle (MSP) – are introduced as high performance biosensors. The results demonstrate the feasibility of developing high performance biosensors using MSP and MSMC. As the AW sensor platforms, the sensitivity of MSP and MSMC increases with reducing size. To develop an extremely sensitive platform, MSPs in micro/nano scale were fabricated. The MSMC and MSP have the potential to significantly advance the biological analysis technology and allow us to better protect the public.

1.1 Conventional Bacteria Detection Techniques

A. Visible Cell Counting Technique

Traditional method for enumerating bacteria is based on the ability of bacteria in a sample to grow into visible colonies on a defined nutrient medium [10-12]. As shown in Fig. 1-1, basically in this method, the pre- enriched cell sample is spread onto agar

2

plates that are subsequently incubated at a growth temperature. During incubation, bacteria cells grow into visible colonies. Theoretically, a colony is derived from a single bacteria cell. The count of cells in the original sample can be obtained by counting the colony number and multiplying it by dilution factor [12]. While this method can be very sensitive, it is time-consuming due to the long incubation period (typically 24-72 hours). Also, colony enumeration can not provide a definitive identification for unknown biological cells. Thus, complex tests are required for any confirmed identification, which requires well trained personnel [1, 12]. This method is not suitable for quick field testing.
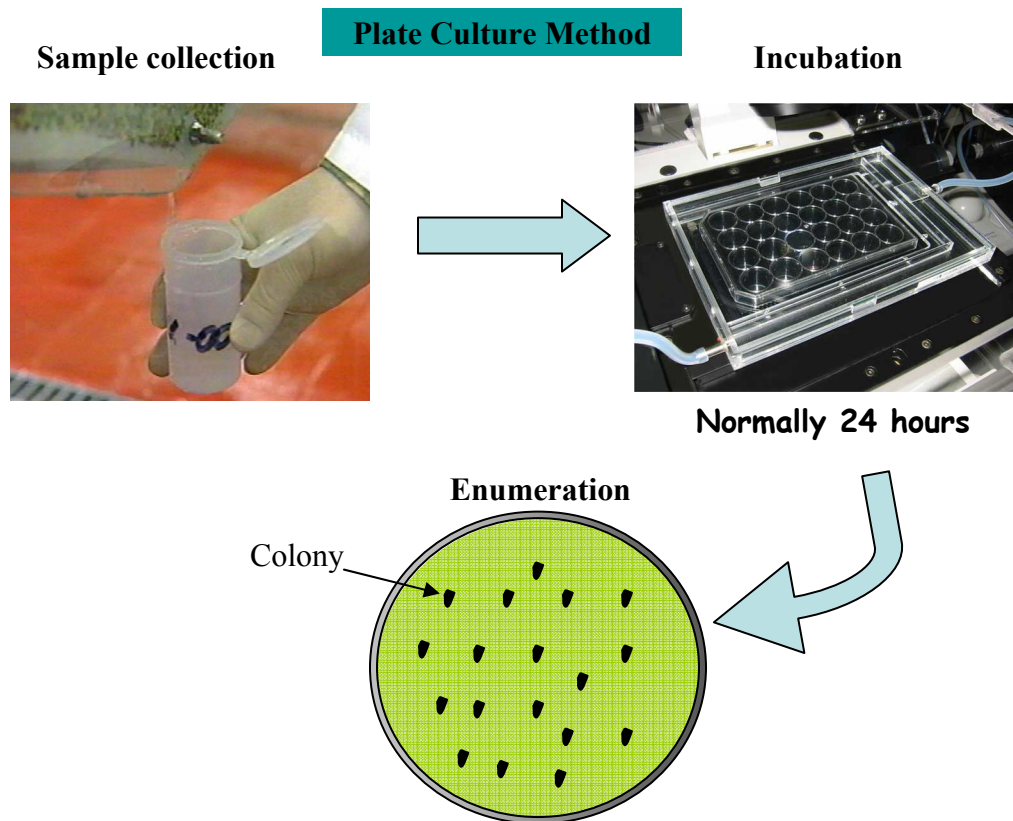
Fig. 1-1. Scheme of traditional visible cell counting method for microbial population detection [13].

B. Polymerase Chain Reaction (PCR)

The polymerase chain reaction (PCR) method has been extensively used in microbial detection since it was introduced in 1985 [6, 14-18]. By duplicating the DNA (deoxyribonucleic acid) of a small quantity of target pathogens over billions of times, PCR provides a sensitive method to determine the presence of small amounts of bacteria. Fig. 1-2 illustrates the principle of PCR. The DNA duplication involved three steps: denaturation, primer annealing and primer extension. In the first step, the DNA is heated and the double strand separates to two single stranded DNA; in the second step, at lower temperature, the primers, which are short DNA strands and uniquely match to portion of the DNA to be amplified, bind to the single stranded DNA; in the third step, the DNA-primers are incubated at higher temperature with DNA polymerase and a new copy of target DNA forms [15, 19]. By repeating PCR cycles, a large amount of identical copies of target DNA can be generated and detected. PCR is highly sensitive. However, the PCR method requires rigorous sample preparation, complex reactive components of limited shelf life, precise temperature regulation, sophisticated hardware, a complex detection process, and trained personnel [1, 6, 15].
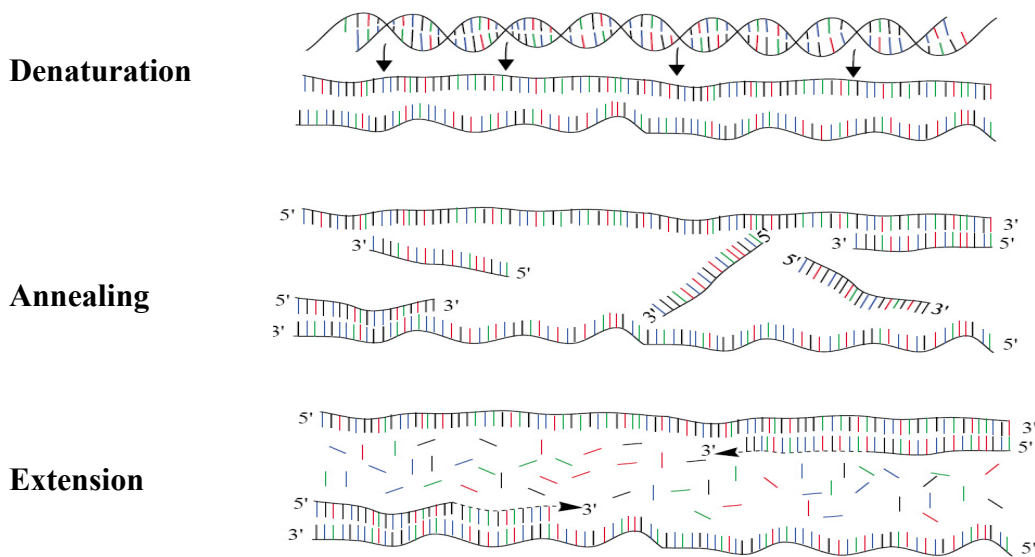
Fig. 1-2. DNA duplication by polymerase chain reaction (PCR) [20].

1.2 Review of Current Biosensor Techniques

Conventional microbiological tests must be undertaken in laboratories because of complicated testing procedures, expensive equipment and the requirement for qualified operators. Therefore, in the last decade, there has been intensive research focused on the development of portable, rapid, specific and sensitive techniques to suit the purpose of real-time and in-field detections. Biosensor techniques show particular promise to meet these requirements, and thus has been intensively studied [1].

A biosensor is an analytical device incorporating a biological sensing element (probe/receptor) to a transducer (platform) system. The specific biological reaction between the sensing element and the interested species agent causes a physical/chemical change at the bio-interface. The transducer/platform converts the observed change (physical or chemical) into a measurable signal, which is sent to an output system to

5

be amplified, processed and displayed [6]. A schematic diagram of a typical biosensor is shown in Fig. 1-3 [6]. The sensing elements can be DNA/RNA, proteins, enzymes, antibodies, or phages [6, 21]. According to their transducer/platform type, biosensors can be divided into electrochemical, optical, thermal, and mass sensors [1, 9, 22, 23].
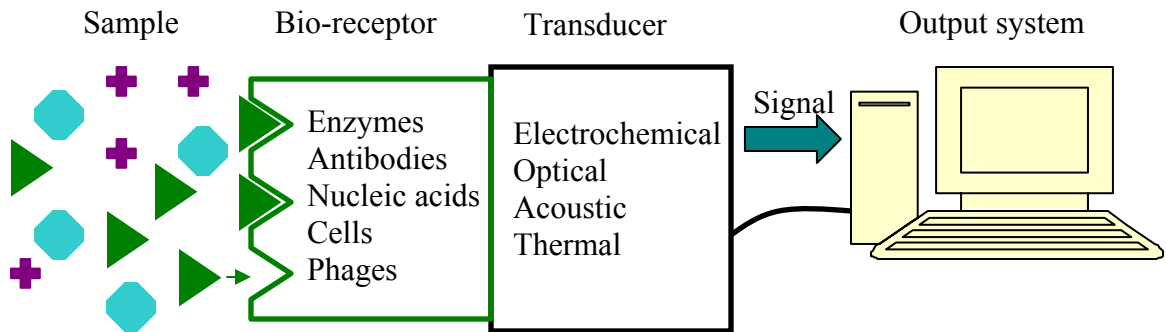
Fig. 1-3. Schematic diagram of a typical biosensor.

1.2.1 Electrochemical Biosensors

At present, electrochemical technology plays a very important role in clinical diagnosis, biochemical analysis and environmental monitoring. Electrochemical sensors obtain the analytical information from the electrical signal that results from the interaction of the target analyte and the recognition elements. Based on the electrical signals that the transducer detects, the electrochemical sensors can be classified into: conductimetric/impedimetric, potentiometric and amperometric [9].

When micro-organisms metabolize uncharged and weakly charged substances, such as carbohydrates, fats or proteins, into highly charged end products, such as organic acids, fatty acids, and amino acids, both conductance and capacitance of the medium change, causing the change of the impedance of the medium [1, 9]. The amount of the

6

charged   metabolites   is   proportional   to   the   metabolization   rate. Conductimetric/impedimetric biosensors detect the microbial concentration of the sample by measuring the change in electrical conductivity/impedance [1, 9, 24]. This method has been used to detect specific food pathogens [25, 26].

In potentiometric biosensors, the biological active materials, such as enzymes or antibodies, are immobilized on the surface of the electrode. When the target antigens in a sample react with the corresponding active materials, the potential between the enzyme/antibody immobilized electrode and a reference electrode will change [27]. The potential difference between the electrodes is proportional to the logarithms of the concentration of the analyte species [1, 27]. Based on this principle, potentiometric biosensors, such as Immuno-Field-Effect-Transistor (FET) sensor and light addressable potentiometric sensor (LAPS), are developed for detection of pathogenic bacteria [1, 28-31]. Fig. 1-4 shows a scheme of an Immuno-FET biosensor. A FET is a semiconductor device, in which the conductivity of the n-channel region in the p-type silicon is controlled by the potential at the oxide insulator (Gate) and is measured as a voltage (V_D) is applied between two n-type silicon (Source and Drain). The biological action between the interested species and the biological active materials immobilized on the Gate surface associates with the potential change at the Gate, which can be detected and used for bio-sensing [1, 9].
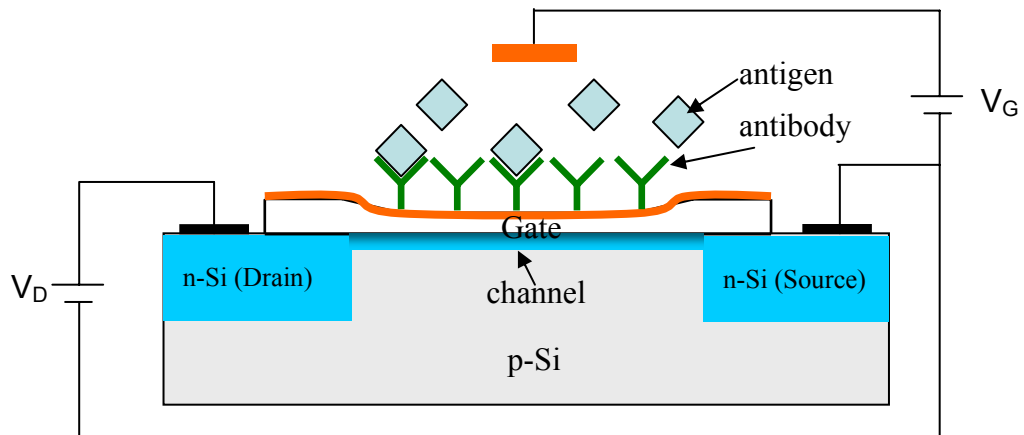
Fig. 1-4. Scheme of immuno-FET biosensor. V_G and V_D are Gate voltage and Drain voltage, respectively, for generating an initial current flow. The antigen-antibody interaction on the Gate surface associates with the potential change at the Gate, which can be detected and used for bio-sensing.

Instead of measuring the potential change, amperometric biosensors measure the current generated by the chemical/biological reaction of an electroactive species under an applied potential, which is proportional to the concentration of the electroactive species in the solution [9, 32]. Compared to the logarithmic concentration dependence in potentionmetric system, the amperometric system has a linear relationship. This makes amperometric biosensors more suitable for bacterial detection [1]. However, amperometric sensors suffer from poor selectivity, because their selectivity is governed by the redox potential of the electroactive species in the sample solution. Therefore, the current measured by the sensor can include the contributions of several chemical species [9].

To obtain adequate sensitivity and selectivity, electrochemical biosensors employ specific enzymes, which are only active in a narrow temperature or pH range, for the capture and catalytic generation of the product [9].

1.2.2 Optical Biosensors

Optical biosensors are very attractive for their direct (label-free) and quick detection of bacteria [6].

The direct fluoresce technique examines the fluorescent components of the bacteria. Under ultraviolet light, certain biospecies can emit light, usually with a lower wavelength. This phenomenon is known as fluorescence [1]. Fluorescence biosensors identify bacteria by measuring the characteristic fluorescent radiation of cells under an UV source [33, 34]. This approach is simple and rapid. However, their major limitation is that they only can detect the bacteria which contain or produce fluorescent components [1].

Some enzyme-catalyzed biochemical reactions result in emitting photons, a reaction which is known as bioluminescence [1]. Luminescence biosensors employ this phenomenon to detect a wide range of microorganisms [35-38]. The luminescence biosensors have very high specificity. However the main disadvantage is the relatively long response time which needs several hours, as well as the lack of sensitivity when very low numbers of bacterial cells are to be detected [1, 22].

Currently, the most attractive optical biosensor transducer is based on surface plasmon resonance (SPR). SPR is a quantum electro-optical phenomenon. When light hits the surface of a metal, energy carried by photons of the light can excite resonant oscillation of electrons on the surface of the metal. The "excited" free electron portion of the surface metal layer is called plasmon [6]. The SPR is sensitive to the environment

9

of the metal surface [9]. A SPR biosensor is made of two types of materials with different refractive indices; which normally are a metal (gold) and a glass. The incident light is reflected at the interface of these two materials. Utilizing total internal reflection, SPR is excited along the metal surface at a specific incident angle (θ_{SPR}), at which the intensity of the reflected light reduces to minimum. The change of the condition of the metal surface, such as antibody-antigen binding, affects the SPR in the metal layer and results in the changes of θ_{SPR} [9, 39]. Therefore, SPR biosensors are able to detect interested species binding to receptors immobilized on the transducer surface by measuring the shift of θ_{SPR}. Fig. 1-5 shows the operation principle of the SPR biosensor.
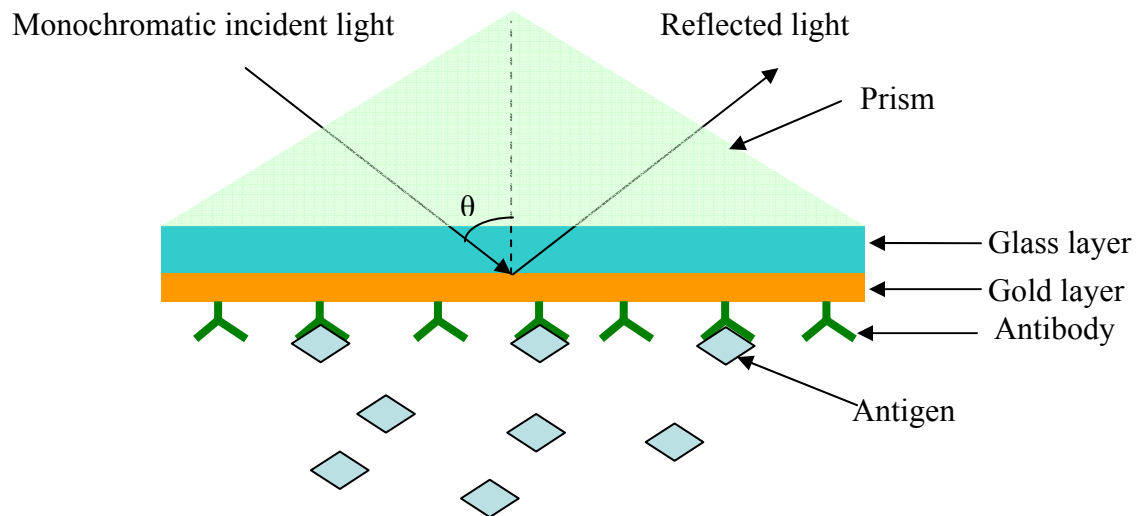
Fig. 1-5. Operation principle of the SPR biosensor.

SPR biosensors have been widely used in detecting food borne pathogens and chemical and biological agents [40-42]. SPR biosensors can provide easy to use, real-time, and label-free detection. However, at present, SPR sensors are mainly used in the

laboratory. Also, they are relatively expensive, and have difficulty measuring target species in very low concentration environments [1, 39].

1.3 Acoustic Devices

In the last decade, acoustic wave (AW) devices attracted a great deal of attention among the biosensor platforms, since, as a sensor platform, they can offer many advantages, such as a real-time detection, simplicity of use, and cost effectiveness [6, 43-45] .

1.3.1 Operating Principle

In AW devices, acoustic waves are generated causing oscillation of the device. The operating principle of all AW sensor platforms is the same. That is, when an AW device is operated as a resonator, its resonance frequency changes with the mechanical load on the device surface, as shown in Fig. 1-6. For developing a biosensor, the AW device is usually immobilized with a bio-molecular recognition layer, such as antibody and phage, on its surface to react with the target species [21, 45], which results in a change in the recognition layer, such as the mass and elastic property. Thus, the presence of target species can be detected by monitoring the shift in device's resonance frequency.
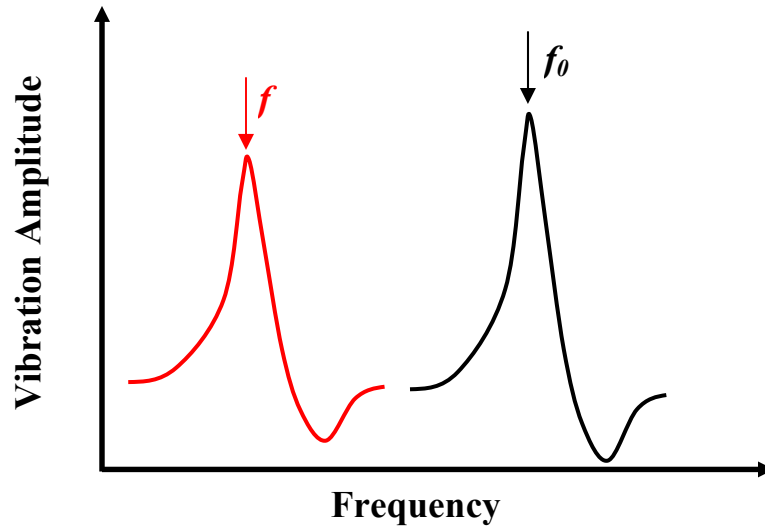
Fig. 1-6. Scheme of vibration amplitude vs. frequency of an AW sensor, where f_0 and f are the resonance frequency of the sensor at zero mass load and at certain mass load respectively.

The comparison of different AW devices can be found in several review articles [45-49]. The mass sensitivity of an AW sensor is the most important parameter to characterize its performance. Both normalized mass sensitivity (S'_m) and mass-detection sensitivity (S_m) have been introduced, as shown in Equation (1-1) and (1-2) respectively, to compare the sensitivities of these devices.

Normalized mass sensitivity (S'_m) [47]:

$$S'_m = -\frac{1}{f_0}\frac{df}{dm'} \tag{1-1}$$

where f_0 and f are the uninhibited resonance frequency and the resonance frequency under mass load (m'), respectively. The mass load, m', is the mass load per unit area rather than the absolute mass on the surface of the AW device.

Mass-detection sensitivity (S_m):

$$S_m = -\frac{df}{dm} \tag{1-2}$$

where m is the absolute mass of the load.

Although S'_m is widely used in bulk AW sensors, such as conventional TSM (thickness shear mode resonator) and SAW (surface acoustic wave resonance) for monitoring the thickness of the mass load, the S_m is more reasonable and is widely used to compare AW devices for detecting a small mass, such as single bacterium/spore cell [46, 48]. Therefore, in this dissertation, S_m is used to characterize the mass sensitivity of AW devices.

It should be noted that neither S'_m nor S_m completely describes the performance of an AW biosensor. The sensitivities defined above only show the shift in resonance frequency due to a mass load. Clearly, the ability to determine the resonance frequency accurately also affects overall device mass sensitivity. Therefore, besides mass sensitivity, the performance of an AW device is determined by another parameter: quality merit factor (Q value). The Q value is defined as the ratio of the energy stored in the resonant structure to the total energy losses per oscillation cycle. The Q value represents the sharpness of the resonance peak of an AW device. A higher Q value means a sharper resonance peak, which would result in a higher precision in determining resonance frequency and a smaller minimum detectable frequency change. Therefore, for

13

developing high performance sensors, the AW devices with a higher S_m and a higher Q value are desirable [50-52].

1.3.2 Common Acoustic Devices

At present, the majority of AW devices are based on piezoelectric materials, since by using the piezoelectric effect, the devices can be easily driven and sensed. The AW devices that have been widely investigated include the thickness shear mode (TSM) resonator, surface acoustic wave (SAW) device, flexural plate wave (FPW) device [43] and microcantilever (MC) [50].

Among the AW devices investigated, the thickness shear mode (TSM) resonator, also known as the quartz crystal microbalance (QCM), has met with the greatest commercial success in applications, such as plating thickness monitors [43]. TSM typically consists of a ZT-cut quartz disk with circular electrodes deposited on both sides. Application of an electric potential between the electrodes causes a shear deformation across the crystal due to piezoelectric effect. The shear mode oscillation is most sensitive to changes in mass at the crystal surface [6, 43]. By coating the TSM surface with biological active elements, TSM have been used to detect microbial contamination [53-55]. However, TSM sensors have the lowest sensitivity among AW devices [55].

The SAW sensor consists of a piezoelectric crystal with two patterned interdigitated electrodes on the same side of the crystal surface. When an alternating voltage is applied on one of the interdigitated electrodes, an acoustic wave, whose propagation is restricted to crystal surface, is excited and travels along the surface until it is received by the other interdigitated electrodes [6, 43]. This surface wave is very sensitive to the surface perturbation. Therefore, SAW sensors exhibit a much higher sensitivity than TSM,

as well as a lower cost and a better reliability [6, 56]. However, the surface acoustic wave becomes severely decreased in the liquid, thus SAW sensors can not work well in liquid media [6].

In a FPW device, an acoustic wave is excited in a thin plate, whose thickness is a fraction of the acoustic wavelength. Two interdigitated transducers are fabricated on the top of the plate acting as wave generator and wave receiver, respectively. During the wave propagating through the plate, the shape of the entire plate is like a flag waving in the wind [43, 57]. FPW have much higher S'_m [43]. Due to the fabrication difficulty, FPW device does not gain a great progress in terms of miniature.

1.3.3 Microcantilevers

In 1990's, researchers began to convert the micromachined cantilevers used in atomic force microscopy (AMF) into a new sensor platform [58, 59]. The microcantilevers (MCs) as a type of MEMS-based devices have many advantages over other AW devices, such as compact size and easy integration with analysis circuit [50, 60]. More importantly, the S_m of MCs is superior to that of traditional AW transducers. The MCs can detect a much smaller mass – as small as the mass of a single bacterium or spores even virus, due to their small size and mass [50-52]. For example, B. Ilic has demonstrated that silicon-based microcantilevers in length about 20 μm are capable to detect a single *E.coli* cell [61], and more recently, the detection of a single virus or even single NDA molecule has been demonstrated in vacuum using the nano-cantilevers with the length less than 5 μm [62-64]. These features are very attractive for current and future technologies. Therefore, a lot of efforts have been spent to develop MCs [45, 50, 60].

A typical microcantilever consists of a   long and thin micro-beam fixed at one end

15

with a support. There are two operation modes of microcantilevers working as sensor platforms [60]: static mode or dynamic mode. In static mode, MCs work as stress sensors by measuring the deflection/bending of the beam due to changes in the surface stress because of the adsorption of molecules. In dynamic mode, MCs are AW devices, whose resonance frequencies change due to the mass load attached on the beam [45, 60]. In the medium, MCs would undergo Brownian motion due to the mechanical thermal noise. Even though the amplitude of the Brownian motion is very small (0.01 ~ 0.1 nm), this slight vibration affects MCs' practice applications [52]. Operating MCs in dynamic mode can eliminate this effect since the MCs are excited at the resonance frequency. Therefore, most applications of MCs as sensor platforms employ dynamic mode.

Dynamic MCs investigated so far can be simply categorized into two types [50, 60]: the single beam MCs, such as silicon MCs [62, 64], and the composite-beam MCs, such as piezoelectric MCs [65, 66].

MCs made of non-piezoelectric materials, such as silicon, are driven by mechanical force. Usually, an external piezo-material is mounted near the cantilever, and the MC is actuated by mechanically shaking as an alternating electric field is applied on the driving piezo-material [60]. The vibration of the MC is detected by optical methods, such as optical level deflection detection [60] and interferometry [67]. Although the sensitivity of optical methods is very high, the required optical system is complicated, expensive, and occupies a significant amount of space, contrary to the development of compact and cost-effective detection devices. More importantly, optical sensing methods limit the application of the devices in liquid due to the dispersion of the laser beam in the medium [60]. Current high sensitive biological detection using silicon MCs is carried out by first

16

exposing the sensing surface to the target analyte, followed by drying the microcantilever before making the measurements in either air or vacuum [61, 67]. However, for most of devices to detect biological threat agents, a test conducted in liquid is required.

A great deal of effort has paid and a great progress has been made on piezoelectric-based MCs [65, 68-70]. Compared to silicon MCs, the piezoelectric-based MCs are much easier to actuate and sense since its resonance behavior can be simply characterized using the impedance spectrum (impedance versus frequency). Besides, driving and sensing by electric signal makes it possible to integrate the driving and characterizing circuits in a chip with the MC. Theoretically, two types of piezoelectric-based MCs can be used as sensor platform: unimorph and bimorph. The unimorph consists of a piezoelectric layer and a substrate layer, which can either conduct or insulation. The bimorph, which consists of two piezoelectric layers, has two types: parallel and series connections. Due to the complicate structure and the need for electrical connections for actuating and sensing, the fabrication of piezoelectric MCs is much difficult. Additionally, when the MCs have to be employed in liquid, especially conductive liquid, extra efforts are needed to insulate the electrodes.

The major drawback of MCs as sensor platforms is that the amplitude of the resonance peak and the Q value reduce significantly when the cantilever is operated in a viscous environment, such as air or liquid. This may limit their practical applications. Even though a MC has a high mass sensitivity, the shift in the resonance frequency caused by the mass load might not be identified due to the low Q value. For regular rectangular MCs, the Q value of silicon MCs in air is more than 100 [50, 60], while that of piezoelectric MCs in air is less than 100 [65, 66]. When MCs are operated in liquid,

17

most of MCs exhibit a Q value about 10 [50].

Many approaches have been investigated to increase the Q value of the MCs and to improve their performance in liquid [71, 72]. For example, for a piezoelectric MC, by employing a PZT layer with improved piezoelectric properties and the design with a nonpiezoelectric extension, a Q value higher than 300 in air has been achieved [72], while the performance in liquid can be improved by submerging only the nonpiezoelectric extension tip in liquid to reduce viscous damping effects [73]. However, high-resolution detection in liquid using MCs still remains a challenge. Recently, piezoelectric diaphragms with bending mode have been reported as a high performance AW sensor platform employed in liquid since the liquid viscosity has very little effect on the Q value of diaphragms [74, 75].

1.4 Fundamentals of Magnetostriction and Magnetostrictive Materials

1.4.1 Magnetoelastic Effects

James P. Joule first discovered that the dimensions of iron changed when it was exposed under a magnetic field in 1842. Since then, the magnetoelasticity has been intensively studied and enormous technical applications based on magnetoelasticity have been developed [76].

The magnetoelasticity is a science dealing with the coupling between the magnetic and elastic properties of a magnetic material. The size and shape of a magnetic material can vary with the magnitude and direction of its magnetization: this is the direct magnetoelastic effect, known as magnetostriction. Conversely, the magnetic properties of a material depend on the applied mechanical stress: this is the inverse magnetoelastic

18

effect. These effects can be observed in most of the ferromagnetic materials [76, 77].

The main magnetoelastic effects that are concerned for technical applications are summarized as follows [76]:

- Volume magnetostriction: The volume of a magnetostrictive materials changes due to the magnetic interaction between the materials and an external magnetic field. Its inverse effect is the pressure dependence of Curie temperature.

- Joule magnetostriction is a phenomenon that a magnetostrictive material stretches or compresses along the external magnetic field direction. Inversely, the magnetization of a magnetostrictive material varies with the mechanical stress and strains.

- Wiedemann effect is a variant of Joule magnetostriction: a helical magnetic field applied to a magnetostrictive wire causes a twisting in the wire. Its inverse effect is called Matteuci effect: the change of the magnetization in a magnetostrictive wire because of torsional deformation in the wire.

- ΔE effect describes the deviation of Young's modulus (E) of a magnetostrictive material from Hook's law. This is because that the stress applied on the material changes its magnetization, which will cause extra deformation in the material due to the magnetostriction.

In this research, we developed the novel AW biosensor platforms based on Joule magnetostriction.

Joule magnetostriction is an anisotropic deformation, as shown in Fig. 1-7 [78]. Under an external magnetic field, a magnetostrictive material elongates or contracts along the external magnetic field direction to minimize the sum of the magnetoelastic and

19

elastic energies. This strain is expressed as λ and is described as the relative change in length measured along the external field ($\boldsymbol{H}$) direction (Equation (1-3)).

$$\lambda = \Delta l \, / \, l \qquad\qquad (1\text{-}3)$$

When the magnetic saturation is achieved, λ reaches a limiting value, which is called saturation magnetostriction, λ_s. If the material elongates along the external field, λ_s is positive; while λ_s is negative if the strain is contraction. Below the saturation, the λ is very sensitive to the external magnetic field. λ is also very sensitive to the pre-stress condition in the material [76, 78].
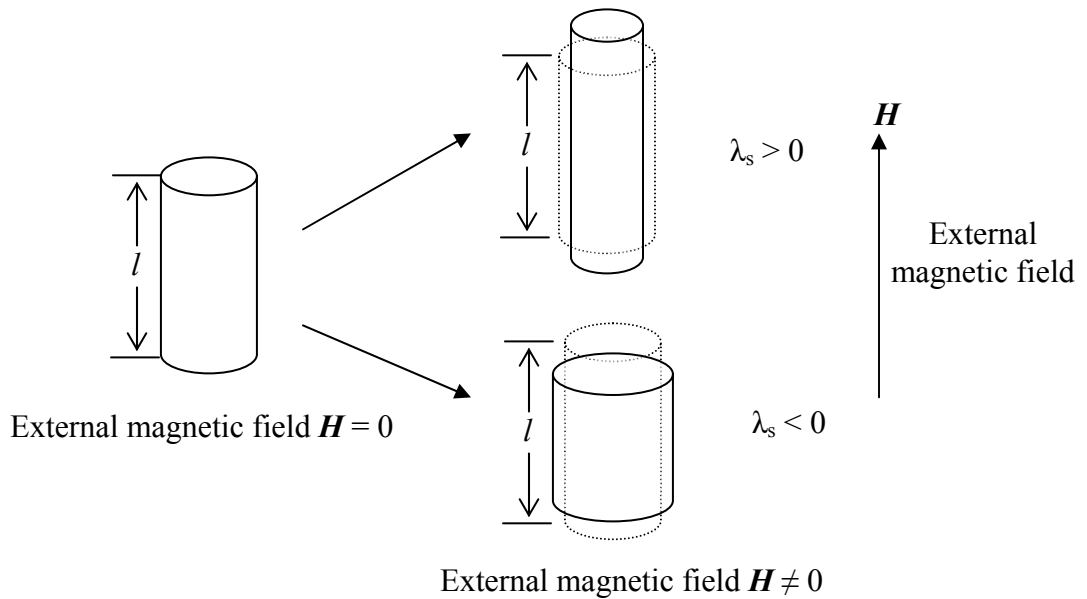
Fig. 1-7. Scheme of Joule magnetostriction.

20

1.4.2 Joule Magnetostriction in Ferromagnetic Materials

An external magnetic field (H) alerts the magnetic moments inside of a magnetic material, which results in magnetic induction (B) within the material, as well as magnetization (M) of the material. Their relations are described in Equations (1-4) [77]:

$$B = \mu\mu_0 H \qquad\qquad (1\text{-}4\ a)$$

$$B = \mu_0 H + \mu_0 M \qquad\qquad (1\text{-}4\ b)$$

$$M = (\mu - 1)H \qquad\qquad (1\text{-}4\ c)$$

where μ and μ_0 is the permeability of the material and the permeability of vacuum respectively.

In ferromagnetic materials, the magnetic moments align spontaneously to form small domains without the presence of an external magnetic field. This is the result of the compensation between magnetostatic energy and quantum mechanical exchange energy. The magnetostatic energy is reduced for antiparallel magnetic moments, while the quantum mechanical exchange energy is reduced when magnetic moments align to each other. To minimize the energy, individual domains spontaneously form in ferromagnetic materials with an energetically favorable domain size [77].

Due to the spontaneous magnetic domain within the ferromagnetic material, its magnetization under an external magnetic field exhibits a hysteresis loop. A typical *M-H* hysteresis loop of a ferromagnetic material is shown in Fig. 1-8 as solid black curve [77]. As all magnetic domains in the material aligned to the external field direction, the material reached technical saturation magnetization, M_s. When H is reduced to zero, some domains remain to align to the magnetization direction, which results a remanent magnetization, M_r. The remanent magnetization can be removed by applying

a reversed magnetic field with a magnitude of H_c, called coercive field [77]. Ferromagnetic materials with small M_r and H_c are called magnetically soft materials [77]. For magnetically soft materials, the area inside the **M-H** loop is very small and the slope $d\mathbf{M}/d\mathbf{H}$ is quite steep, which is favorable for minimizing the energy loss and amplifying the output. Therefore, for developing high performance AW sensor, magnetostrictive materials with soft magnetic properties are highly desired. The blue dotted line in Fig. 1-8 shows the **M-H** loop under the condition that there is no hysteresis ($M_r = 0$ and $H_c = 0$).

For magnetostrictive materials, an external magnetic field results in the magnetization and generates strain in the material. The strain (x_{ij}) caused by magnetostriction is related to the square of the magnetization ($M_k M_l$), which can be expressed as [79]:

$$x_{ij} = N_{ijkl} M_k M_l \qquad i, j, k,l = 1\text{-}3 \qquad (1\text{-}5)$$

where N_{ijkl} is the magnetostrictive coefficient. Therefore, only considering the strain along the external magnetic field and based on Equations (1-4) and (1-5), under saturation magnetic field, we can obtain:

$$\lambda \propto M^2 \qquad (1\text{-}6)$$

Thus, as shown in Fig. 1-9, although the magnetization of a ferromagnetic material is an odd function of the applied magnetic field **H**, the magnetostriction is an even function of **H** [78]. Due to the hysteresis loop for magnetization, the λ-**H** loop of a ferromagnetic material exhibits typical butterfly-shape, which is shown in Fig. 1-9 as solid black curve [78]. The magnetic softer the material, the narrower the λ-**H** loop. The blue dotted curve in Fig. 1-9 shows the λ-**H** relation if there is no hyteresis for magnetization (blue dotted line in Fig. 1-8).
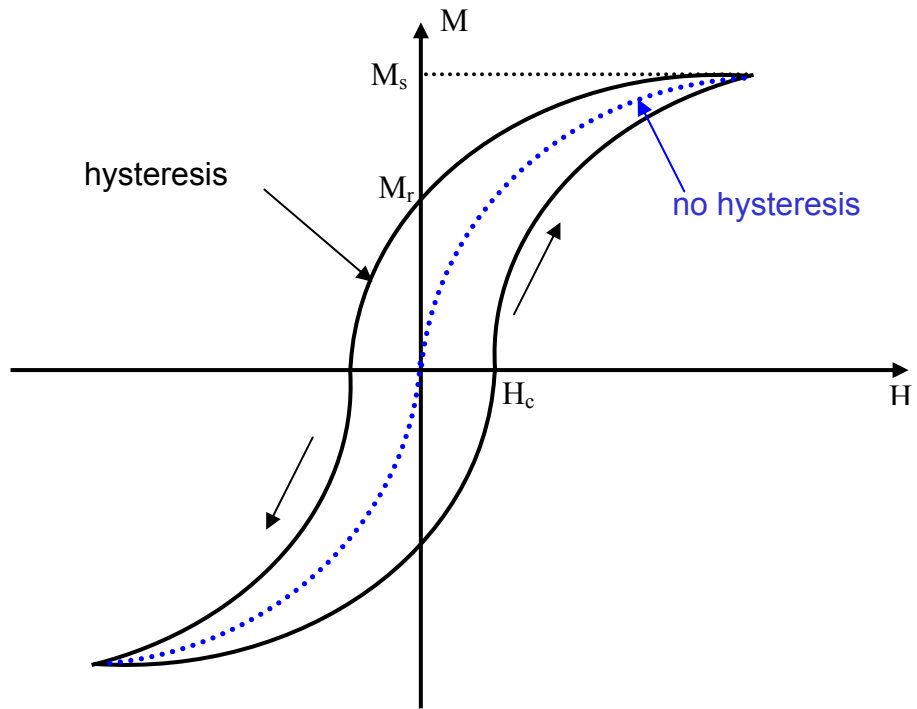
Fig. 1-8. Magnetization hysteresis loop of a ferromagnetic material.
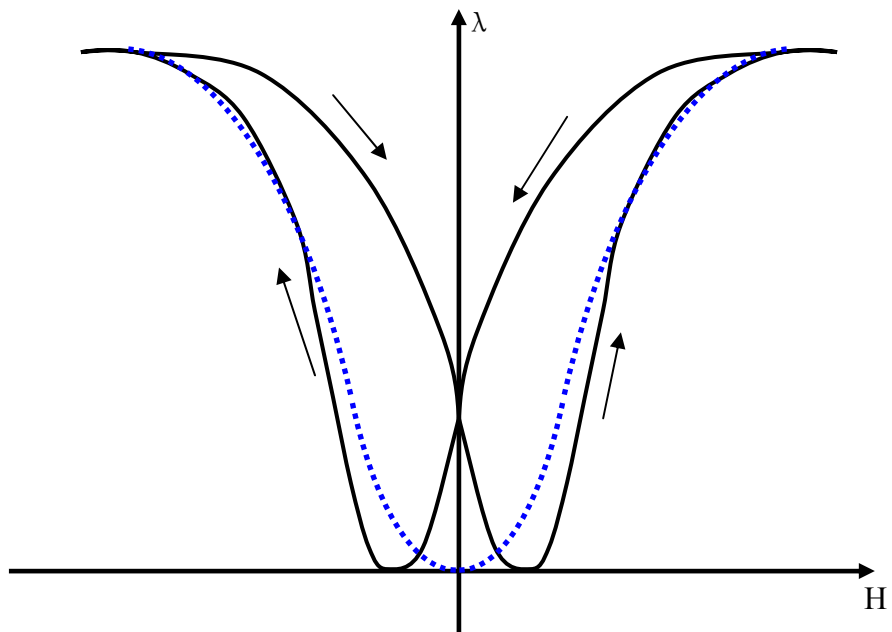
Fig. 1-9. Hysteresis loop for Joule magnetostriction.

1.4.3 Response of Magnetostrictive Material under Different DC Bias

As shown in Fig. 1-9, the behavior of magnetostrictive materials under external magnetic field H is non-linear. Assume, for a magnetically soft material, its λ-H curve is shown in Fig. 1-10. Based on Equation (1-6), near the origin (region I), the magnetostriction is a quadratic function of the external magnetic field [76]. When there is no DC bias ($H_{DC} = 0$), that is only an AC external magnetic field, $H_{AC} = H_0 \sin \omega t$, is applied on the material, the corresponding strain in region I would be:

$$\lambda(H) \propto H_0^2 \sin^2 \omega t$$

$$\propto \frac{H_0^2}{2}(1 - \sin 2\omega t)$$

$$\propto \frac{H_0^2}{2} - \frac{H_0^2}{2}\sin 2\omega t \tag{1-7}$$

Equation (1-7) indicates that the material oscillates at a double frequency of applied external field. Also, as shown in Fig. 1-10, the observed strain is very small [76].

On the other hand, if an AC magnetic field (H_{AC}) is applied on the material with a DC polarizing magnetic field ($H_{DC} = H_1 \neq 0$), and H_{DC} is much bigger than H_{AC}, as shown in Fig. 1-10 (region II), the resultant stain would be:

$$\lambda(H) = \lambda_{DC} + \lambda_{AC} \tag{1-8}$$

As shown in Fig. 1-10, when H_{AC} is small, λ_{AC} shows quasi-linear relationship with H_{AC} at region II. That is:

$$\lambda(H) \propto \lambda_{DC} + H_{AC}(\omega) \tag{1-9}$$

Equation (1-9) indicates that the obtained strain is almost proportional to the external AC driving magnetic field. Therefore, the material exhibit piezomagnetic behavior in

region II. Also, as shown in Fig. 1-10, the enhanced strain, and thus the enhanced output signal, can be obtained at this region. Therefore, generally, magnetostrictive devices are operated by super-imposing a small AC magnetic field on an applied DC bias field in order to avoid double frequency and obtain amplified quasi-linear output [76].

Based on Fig. 1-10, under different DC bias (H_1, H_2), similar linear outputs can be obtained from the magnetostrictive device, but the amplitudes of the outputs would be different. Thus, for a magnetostrictive device, high response can be obtained at optimized DC bias field.
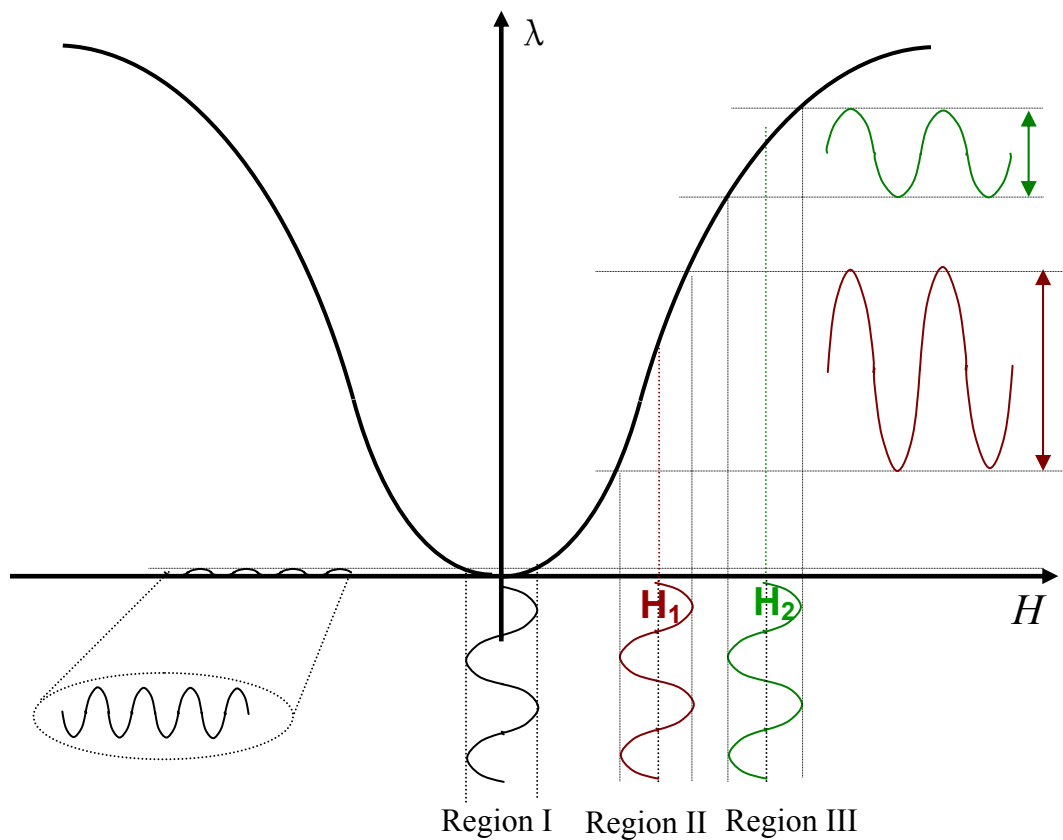
Fig. 1-10. Response of a magnetostrictive material under different DC bias.

1.4.4 Piezomagnetism in Polarized Magnetostrictive Materials

As discussed in above section, magnetostrictive materials behave in a quasi-linear manner if a bias magnetic field H_{DC} is applied on the material. That is, magnetostrictive materials behavior as piezomagnetic materials under the induced polarization, such as applying a bias magnetic field H_{DC} or a mechanical pre-stress T_0 on the material [80, 81]. The direction of H_{DC} or T_0 is the polarization direction. Based on IEEE standard, the polarization direction is conventionally defined as the 3-direction, while directions perpendicular to this axis can be chosen as the 1- or 2-direction, as shown in Fig. 1-11 [81].
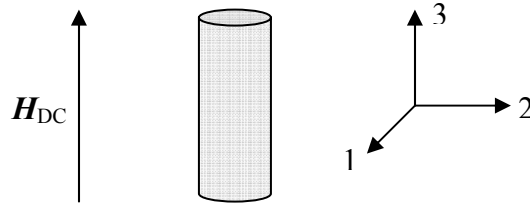
Fig. 1-11. Scheme of the conventional directions for a polarized magnetostrictive material.

In the polarization direction, the application of a mechanical stress, T, generates a mechanical strain, S, as well as a magnetic induction, B, in the material. Conversely, the application of a magnetic filed, H, produces not only a magnetic induction, B, but also a mechanical strain, S. Considering only the variations around the polarized state, the behaviors of the piezomagnetic material can be described as following [76, 78]:

$$S_{ij} = s^H_{ijkl}T_{kl} + d_{kij}H_k \qquad \text{i, j, k = 1-3} \qquad (1\text{-}10)$$

$$B_i = d_{ikl}T_{kl} + \mu^T_{ik}H_k \qquad \text{i, j, k = 1-3} \qquad (1\text{-}11)$$

where s^H is compliance at constant H, d is the piezomagnetic constant and μ^T is permeability at constant T, respectively. They are called the magneto-elastic coefficients. The value of piezomagnetic constant, d, is affected by the applied DC bias, which causes the different responses of the material under different DC bias, as discussed in previous section.

In order to write the magneto-elastic tensors in the form of a matrix array, Viogt rules are introduced. Based on Viogt's definition, *ij* and *kl* is replaced by p and q respectively according to [78]:

11 → 1, 22 → 2, 33 → 3, 23 or 32 → 4, 31 or 13 → 5, and 12 or 21 → 6

Therefore, elastomagnetic matrices can be defined by the following equations [78, 81]:

$$S_p = s^H_{pq}T_q + d_{kp}H_k \qquad (1\text{-}12)$$

$$B_i = d_{iq}T_q + \mu^T_{ik}H_k \qquad (1\text{-}13)$$

where *i, k* = 1-3 and *p, q* = 1-6.

1.4.5 Magnetomechanical Coupling Coefficient

The ability of a magnetostrictive material to convert magnetic energy to mechanical energy – or *vice versa* - is characterized by the magnetomechanical coupling coefficient, k, which is defined as [76]:

$$k^2 = \frac{E^2_{mel}}{E_{el}E_m} \qquad (1\text{-}14)$$

where E_{mel} is the magnetoelastic energy, E_{el} and E_m is the input elastic and magnetic energy, respectively.

Considering a magnetostrictive material as shown in Fig. 1-11, the actuating is normally applied along the polarization direction (3-direction). It is assumed that the transverse actuating fields are negligible ($H_1 = H_2 = 0$), also the radial stresses are zero ($T_1 = T_2 = 0$) and there is no shear effect ($T_4 = T_5 = T_6 = 0$) [80]. In this case, the longitudinal magnetomechanical coupling coefficient, k_{33}, is defined as [78, 80]:

$$k_{33}^2 = \frac{d_{33}^2}{s_{33}^H \mu_{33}^T} \tag{1-15}$$

This parameter is very crucial to the magnetostrictive sensors, actuators and transducers. Therefore, magnetostrictive materials with a large coupling factor are favorable for developing high performance magnetostrictive actuators.

1.4.6 Magnetostrictive Materials

Magnetostrictive materials have been intensively investigated and the magnetostrictive devices, such as magnetostrictive actuators and sensors, have been wildly used in current industry.

The magnetostrictive materials used for actuators are required to have a large magnetostriction, which means they should be able to generate a large deformation under a small magnetic field. Conventionally, magnetostrictive actuators were built based on Ni or Fe-based alloys that exhibits a saturation magnetostriction about 40 x 10^{-6} [76]. However, after World War II, most of magnetostrictive actuators were replaced by piezoelectric ceramics because of their much larger strains [76, 82].

Great attentions have been paid on magnetostrictive materials again due to the

28

discovery of giant magnetostriction in some rare-earth based alloys in 1970's [82]. It was discovered that R(rare-earth)Fe_2 compounds, have the magnetostriction 100 time higher than that of conventional magnetostrictive materials at room temperature [82]. But they are highly magnetocrystalline anisotropic, which causes it is very difficult to switch the magnetization away from its easy magnetic axis. Huge magnetic field is required to saturate the material. In 1975, A. E. Clark discovered $Tb_{0.3}Dy_{0.7}Fe_2$ alloy, which have giant magnetostriction and can be saturated at low magnetic field. This alloy was named as Terfenol-D (Ter for Terbium, Fe for iron, nol for Naval Ordnance Laboratory and D for Dysprosium). The remarkable prosperities of Terfenol-D make it comparable with piezoelectric ceramics due to its large strain response and high power density in the low-frequency range. Terfenol-D is commercial available [82]. However, Terfenol-D is brittle and exhibits poor mechanical properties. Recently, the $Fe_{1-x}Ga_x$ alloys (Galfenol) shows the promise to overcome the limitation of Terfenol-D due to their large magnetostriction at low-field as well as strong and ductile mechanical properties [83-85]. Galfenol in bulk form has been intensively studied by several groups, while, more recently, nanowires of Galfenol have been fabricated and studied [83-89].

The best material for AW magnetostrictive sensor is not a material with giant magnetostriction but a material that can exhibit high Q value during oscillation. Magnetostrictive materials with soft magnetic properties, high Young's modulus and high magnetomechanical coupling coefficient are favorable for AW sensor applications [82]. Excellent magnetoelastic and mechanical properties of magnetically soft metallic glasses make them good candidates for developing high performance magnetostrictive sensors. Metallic glasses are fabricated by quench the melting alloy at the cooling rate of

10^6 degree/s [82]. With amorphous structure, they exhibit soft and almost isotropic magnetic properties. The magnetomechanical coupling coefficient, as high as 0.97, has been achieved in an iron rich metallic glass, Metglas® 2605 SC, by annealing the material ribbon in a magnetic field perpendicular to the ribbon length [82].

Properties of some magnetostrictive materials are listed in Table 1-1.

TABLE 1-1

Properties of Some Magnetostrictive Materials [76, 82, 90, 91]

Material	T_C (K)	λ_s (10^{-6})	k_{33}^{max}	Young's modulus (GPa)
Nickel	631	-36	0.31	210
$Fe_{65}Ni_{35}$	773	40	0.32	~ 110
Magnetite (Fe_3O_4)	853	40	0.36	/
Terfenol ($TbFe_2$)	698	1750	0.35	94
Terfenol-D	653	1100	0.75	43
Metglas® 2605SC	643	30	0.97	100 - 110
Metglas® 2826MB	626	12	/	100 - 110

1.4.7 Applications of the Magnetostrictive Materials

The main industrial applications of giant magnetostrictive materials are actuators, such as sonars, fuel injectors, loudspeakers, vibration dampers, fast relays, rapid shutters, and magnetostrictive motors [82]. Due to the high magnetomechanical coupling factor and high energy density, underwater sonars based on Terfenol-D exhibit better performance than the ones built based on piezoelectric ceramics [80, 82].

Magnetostrictive metallic glasses are widely used to making high sensitive

magnetostrictive sensors. The conventional applications include strain gages, force sensors, pressure sensors, torque sensors, and position sensors [82, 92].

Since last decade, Fe-based amorphous alloys have been used to build magnetostrictive AW sensors [82]. For example, magneto-surface-acoustic-wave sensors are constructed by depositing magnetostrictive thin film on the conventional SAW substrate [93]. The velocity of the SAW propagating in the magnetostrictive film is controlled by an applied magnetic field. A change of external factors, such as magnetic field, force or pressure, affects this velocity, and thus can be sensed [93, 94].

Magnetostrictive AW sensors based on metallic glasses are also widely employed as surveillance devices by retailers to prevent theft [95]. In this system, a thin amorphous alloy strip is sealed in a small plastic box. The strip can move freely in the box and acts as a resonator. Also, a thin hard magnetic strip is placed at the bottom of the box to polarize the magnetostrictive strip. This sensor is attached on the item needed to be surveilled as a label. The alarm system, installed at the store exits, consists of a transmitter and an antenna. The transmitter generates a magnetic field pulse (~ 58 kHz), which has the same frequency as the resonance frequency of the magnetostrictive strip [95, 96]. If the item has not been paid for and brought within the alarm system, the magnetostrictive strip oscillates due to the magnetic pulse. This oscillation results in an emission of a magnetic pulse, which lasts longer than the actuating pulse, and then is picked up by the antenna [95]. When the item is paid, the sensor can be deactivated by demagnetizing the hard magnetic strip. This anti-theft system can provide a fast and wide-area detection without false alarm. Also, it is very inexpensive [95].

Recently, Crime et al. started to develop chemical and biological sensors based on the

magnetostrictive AW platform. The sensors are made from commercial amorphous metallic glass ribbon and are fixed at the middle for support. By measuring the resonance frequency shift of the magnetostrictive sensors, they have successfully detected temperature, pH value, pressure, viscosity, and bioagents, such as *E. coli* and rivin [97-106].

References

[1]   D. Ivnitski, I. Abdel-Hamid, P. Atanasov, and E. Wilkins, "Biosensors for detection of pathogenic bacteria," *Biosensors & Bioelectronics*, vol. 14, pp. 599-624, 1999.

[2]   P. S. Mead, L. Slutsker, V. Dietz, L. F. McCaig, J. S. Bresee, C. Shapiro, P. M. Griffin, and R. V. Tauxe, "Food-related illness and death in the United States," *Emerging Infectious Diseases*, vol. 5, pp. 607-625, 1999.

[3]   E. C. Alocilja and S. M. Radke, "Market analysis of biosensors for food safety," *Biosensors & Bioelectronics*, vol. 18, pp. 841-846, 2003.

[4]   J. C. Buzby, Roberts, T., Lin, C.T.J., MacDonald, J.M., "Bacterial Foodborne Disease: Medical Costs And Productivity Losses," Washington D.C., USDA Economic Research Service Agricultural Economics Report No. 741:100, 1996.

[5]   "http://www.hhs.gov/asl/testify/t061115.html."

[6]   P. Leonard, S. Hearty, J. Brennan, L. Dunne, J. Quinn, T. Chakraborty, and R. O'Kennedy, "Advances in biosensors for detection of pathogens in food and water," *Enzyme and Microbial Technology*, vol. 32, pp. 3-13, 2003.

[7]   M. N. Velasco-Garcia and T. Mottram, "Biosensor technology addressing agricultural problems," *Biosystems Engineering*, vol. 84, pp. 1-12, 2003.

[8]   A. E. Greenberg, Trussel, R.R., Clesceri, L.S., Franson, M.A.H. (Eds.), *Standard Methods for the Examination of Water and Wastewater*: American Public Health Association, Washington, D.C., 1992.

[9]   L. D. Mello and L. T. Kubota, "Review of the use of biosensors as analytical tools in the food and drink industries," *Food Chemistry*, vol. 77, pp. 237-256, 2002.

[10]   E. de Boer and R. R. Beumer, "Methodology for detection and typing of foodborne microorganisms," *International Journal of Food Microbiology*, vol. 50, pp. 119-130, 1999.

[11]   C. W. Kaspar and C. Tartera, "Methods for Detecting Microbial Pathogens in Food and Water," *Methods in Microbiology*, vol. 22, pp. 497-531, 1990.

[12]   N. S. Hobson, I. Tothill, and A. P. F. Turner, "Microbial detection," *Biosensors & Bioelectronics*, vol. 11, pp. 455-477, 1996.

[13]   L. J. Harris, "http://ucce.ucdavis.edu/freeform/UC_GAPs/documents/ Extension_Presentations3035.pdf."

[14]   R. K. Saiki, S. Scharf, F. Faloona, K. B. Mullis, G. T. Horn, H. A. Erlich, and N. Arnheim, "Enzymatic Amplification of Beta-Globin Genomic Sequences and Restriction Site Analysis for Diagnosis of Sickle-Cell Anemia," *Science*, vol. 230, pp. 1350-1354, 1985.

[15]   Y. Kim, T. R. Flynn, R. B. Donoff, D. W. Wong, and R. Todd, "The gene: The polymerase chain reaction and its clinical application," *Journal of Oral and Maxillofacial Surgery*, vol. 60, pp. 808-815, 2002.

[16]   O. Traore, C. Arnal, B. Mignotte, A. Maul, H. Laveran, S. Billaudel, and L. Schwartzbrod, "Reverse transcriptase PCR detection of astrovirus, hepatitis A virus, and poliovirus in experimentally contaminated mussels: Comparison of several extraction and concentration methods," *Applied and Environmental Microbiology*, vol. 64, pp. 3118-3122, 1998.

[17]   E. Giakoumaki, M. Minunni, S. Tombelli, I. E. Tothill, M. Mascini, P. Bogani, and M. Buiatti, "Combination of amplification and post-amplification strategies to improve optical DNA sensing," *Biosensors & Bioelectronics*, vol. 19, pp. 337-344, 2003.

[18]   S. Riyaz-Ul-Hassan, V. Verma, and G. N. Qazi, "Rapid detection of Salmonella by polymerase chain reaction," *Molecular and Cellular Probes*, vol. 18, pp. 333-339, 2004.

[19]   A. van Belkum, "Molecular diagnostics in medical microbiology: yesterday, today and tomorrow," *Current Opinion in Pharmacology*, vol. 3, pp. 497-501, 2003.

[20]   "http://users.ugent.be/~avierstr/principles/pcr.html."

[21]   V. A. Petrenko, Vodyanoy, V.J., "Phage Display for Detection of Biological Threat Agents," *Journal of Microbiological Methods*, vol. 53 (20), pp. 243-252, 2003.

[22]   R. A. Walsh, *Electromechanical design handbook*: McGraw-Hill : New York, 2000.

[23]   R. S. Sethi, "Transducer Aspects of Biosensors," *Biosensors & Bioelectronics*, vol. 9, pp. 243-264, 1994.

[24]   P. Feng, "Commercial Assay Systems for Detecting Foodborne Salmonella - a Review," *Journal of Food Protection*, vol. 55, pp. 927-934, 1992.

[25]   B. Swaminathan and P. Feng, "Rapid Detection of Food-Borne Pathogenic Bacteria," *Annual Review of Microbiology*, vol. 48, pp. 401-426, 1994.

[26] P. Silley and S. Forsythe, "Impedance microbiology - A rapid change for microbiologists," *Journal of Applied Bacteriology*, vol. 80, pp. 233-243, 1996.

[27] P. D. Patel, "(Bio)sensors for measurement of analytes implicated in food safety: a review," *Trac-Trends in Analytical Chemistry*, vol. 21, pp. 96-115, 2002.

[28] S. S. Deshpande and R. M. Rocco, "Biosensors and Their Potential Use in Food Quality-Control," *Food Technology*, vol. 48, pp. 146-150, 1994.

[29] A. G. Gehring, D. L. Patterson, and S. I. Tu, "Use of a light-addressable potentiometric sensor for the detection of Escherichia coli O157 : H7," *Analytical Biochemistry*, vol. 258, pp. 293-298, 1998.

[30] C. Ercole, M. Del Gallo, L. Mosiello, S. Baccella, and A. Lepidi, "Escherichia coli detection in vegetable food by a potentiometric biosensor," *Sensors and Actuators B-Chemical*, vol. 91, pp. 163-168, 2003.

[31] F. Patolsky, G. F. Zheng, and C. M. Lieber, "Nanowire-based biosensors," *Analytical Chemistry*, vol. 78, pp. 4260-4269, 2006.

[32] D. Ivnitski, T. Wolf, B. Solomon, G. Fleminger, and J. Rishpon, "An amperometric biosensor for real-time analysis of molecular recognition," *Bioelectrochemistry and Bioenergetics*, vol. 45, pp. 27-32, 1998.

[33] T. M. Rossi, Warner, M., *Bacterial identification using fluorescence spectroscopy*: VCH Pulisher, 1985.

[34] S. A. Glazier and H. H. Weetall, "Autofluorescence Detection of Escherichia-Coli on Silver Membrane Filters," *Journal of Microbiological Methods*, vol. 20, pp. 23-27, 1994.

[35] J. I. Prosser, "Molecular Marker Systems for Detection of Genetically-Engineered Microorganisms in the Environment," *Microbiology-UK* vol. 140, pp. 5-17, 1994.

[36] J. I. Prosser, K. Killham, L. A. Glover, and E. A. S. Rattray, "Luminescence-based systems for detection of bacteria in the environment," *Critical Reviews in Biotechnology*, vol. 16, pp. 157-183, 1996.

[37] S. Ramanathan, W. P. Shi, B. P. Rosen, and S. Daunert, "Bacteria-based chemiluminescence sensing system using beta-galactosidase under the control of the ArsR regulatory protein of the ars operon," *Analytica Chimica Acta*, vol. 369, pp. 189-195, 1998.

[38] R. Blasco, M. J. Murphy, M. F. Sanders, and D. J. Squirrell, "Specific assays for bacteria using phage mediated release of adenylate kinase," *Journal of Applied Microbiology*, vol. 84, pp. 661-666, 1998.

[39]   J. Homola, S. S. Yee, and G. Gauglitz, "Surface plasmon resonance sensors: review," *Sensors and Actuators B-Chemical*, vol. 54, pp. 3-15, 1999.

[40]   A. N. Naimushin, C. B. Spinelli, S. D. Soelberg, T. Mann, R. C. Stevens, T. Chinowsky, P. Kauffman, S. Yee, and C. E. Furlong, "Airborne analyte detection with an aircraft-adapted surface plasmon resonance sensor system," *Sensors and Actuators B-Chemical*, vol. 104, pp. 237-248, 2005.

[41]   V. Koubova, E. Brynda, L. Karasova, J. Skvor, J. Homola, J. Dostalek, P. Tobiska, and J. Rosicky, "Detection of foodborne pathogens using surface plasmon resonance biosensors," *Sensors and Actuators B-Chemical*, vol. 74, pp. 100-105, 2001.

[42]   A. V. Samoylov, V. M. Mirsky, Q. Hao, C. Swart, Y. M. Shirshov, and O. S. Wolfbeis, "Nanometer-thick SPR sensor for gaseous HCl," *Sensors and Actuators B-Chemical*, vol. 106, pp. 369-372, 2005.

[43]   D. S. Ballantine, White, R.M., Martin, S.J., Ricco, A.J., Frye, G.C., Zellers, E.T., Wohltjen, H., *Acoustic wave sensors: theory, design and physico-chemical applications*: Academic Press, 1997.

[44]   O. Tamarin, C. Dejous, D. Rebiere, J. Pistre, S. Comeau, D. Moynet, and J. Bezian, "Study of acoustic Love wave devices for real time bacteriophage detection," *Sensors and Actuators B-Chemical*, vol. 91, pp. 275-284, 2003.

[45]   R. Raiteri, M. Grattarola, H. J. Butt, and P. Skladal, "Micromechanical cantilever-based biosensors," *Sensors and Actuators B-Chemical*, vol. 79, pp. 115-126, 2001.

[46]   T. Thundat, P. I. Oden, and R. J. Warmack, "Microcantilever sensors," *Microscale Thermophysical Engineering*, vol. 1, pp. 185-199, 1997.

[47]   M. D. Ward and D. A. Buttry, "Insitu Interfacial Mass Detection with Piezoelectric Transducers," *Science*, vol. 249, pp. 1000-1007, 1990.

[48]   J. W. Grate, S. J. Martin, and R. M. White, "Acoustic-Wave Microsensors .2," *Analytical Chemistry*, vol. 65, pp. A987-A996, 1993.

[49]   J. W. Grate, S. J. Martin, and R. M. White, "Acoustic-Wave Microsensors .1," *Analytical Chemistry*, vol. 65, pp. A940-A948, 1993.

[50]   N. V. Lavrik, M. J. Sepaniak, and P. G. Datskos, "Cantilever transducers as a platform for chemical and biological sensors," *Review of Scientific Instruments*, vol. 75, pp. 2229-2253, 2004.

[51]   J. Mertz, O. Marti, and J. Mlynek, "Regulation of a Microcantilever Response by Force Feedback," *Applied Physics Letters*, vol. 62, pp. 2344-2346, 1993.

[52]   A. Mehta, S. Cherian, D. Hedden, and T. Thundat, "Manipulation and controlled amplification of Brownian motion of microcantilever sensors," *Applied Physics Letters*, vol. 78, pp. 1637-1639, 2001.

[53]   S. T. Pathirana, J. Barbaree, B. A. Chin, M. G. Hartell, W. C. Neely, and V. Vodyanoy, "Rapid and sensitive biosensor for Salmonella," *Biosensors & Bioelectronics*, vol. 15, pp. 135-141, 2000.

[54]   X. D. Su, S. Low, J. Kwang, V. H. T. Chew, and S. F. Y. Li, "Piezoelectric quartz crystal based veterinary diagnosis for Salmonella enteritidis infection in chicken and egg," *Sensors and Actuators B-Chemical*, vol. 75, pp. 29-35, 2001.

[55]   B. Drafts, "Acoustic wave technology sensors," *IEEE Transactions on Microwave Theory and Techniques*, vol. 49, pp. 795-802, 2001.

[56]   D. W. Galipeau, P. R. Story, K. A. Vetelino, and R. D. Mileham, "Surface acoustic wave microsensors and applications," *Smart Materials & Structures*, vol. 6, pp. 658-667, 1997.

[57]   A. Hierlemann and H. Baltes, "CMOS-based chemical microsensors," *Analyst*, vol. 128, pp. 15-28, 2003.

[58]   T. Thundat, R. J. Warmack, G. Y. Chen, and D. P. Allison, "Thermal and Ambient-Induced Deflections of Scanning Force Microscope Cantilevers," *Applied Physics Letters*, vol. 64, pp. 2894-2896, 1994.

[59]   J. R. Barnes, R. J. Stephenson, M. E. Welland, C. Gerber, and J. K. Gimzewski, "Photothermal Spectroscopy with Femtojoule Sensitivity Using a Micromechanical Device," *Nature*, vol. 372, pp. 79-81, 1994.

[60]   C. Ziegler, "Cantilever-based biosensors," *Analytical and Bioanalytical Chemistry*, vol. 379, pp. 946-959, 2004.

[61]   B. Ilic, D. Czaplewski, H. G. Craighead, P. Neuzil, C. Campagnolo, and C. Batt, "Mechanical resonant immunospecific biological detector," *Applied Physics Letters*, vol. 77, pp. 450-452, 2000.

[62]   B. Ilic, Y. Yang, and H. G. Craighead, "Virus detection using nanoelectromechanical devices," *Applied Physics Letters*, vol. 85, pp. 2604-2606, 2004.

[63]   A. Gupta, D. Akin, and R. Bashir, "Single virus particle mass detection using microresonators with nanoscale thickness," *Applied Physics Letters*, vol. 84, pp. 1976-1978, 2004.

[64]   B. Ilic, Y. Yang, K. Aubin, R. Reichenbach, S. Krylov, and H. G. Craighead, "Enumeration of DNA molecules bound to a nanomechanical oscillator," *Nano Letters*, vol. 5, pp. 925-929, 2005.

[65]   J. W. Yi, W. Y. Shih, and W. H. Shih, "Effect of length, width, and mode on the mass detection sensitivity of piezoelectric unimorph cantilevers," *Journal of Applied Physics*, vol. 91, pp. 1680-1686, 2002.

[66]   G. A. Campbell and R. Mutharasan, "Sensing of liquid level at micron resolution using self-excited millimeter-sized PZT-cantilever," *Sensors and Actuators a-Physical*, vol. 122, pp. 326-334, 2005.

[67]   B. Ilic, D. Czaplewski, M. Zalalutdinov, H. G. Craighead, P. Neuzil, C. Campagnolo, and C. Batt, "Single cell detection with micromechanical oscillators," *Journal of Vacuum Science & Technology B*, vol. 19, pp. 2825-2828, 2001.

[68]   J. W. Yi, W. Y. Shih, R. Mutharasan, and W. H. Shih, "In situ cell detection using piezoelectric lead zirconate titanate-stainless steel cantilevers," *Journal of Applied Physics*, vol. 93, pp. 619-625, 2003.

[69]   W. Y. Shih, X. P. Li, H. M. Gu, W. H. Shih, and I. A. Aksay, "Simultaneous liquid viscosity and density determination with piezoelectric unimorph cantilevers," *Journal of Applied Physics*, vol. 89, pp. 1497-1505, 2001.

[70]   H. Y. Luo, W. Y. Shih, and W. H. Shih, "Miniaturized cantilever sensor from highly piezoelectric PMN-PT thick films," *Abstracts of Papers of the American Chemical Society*, vol. 228, pp. U888-U888, 2004.

[71]   C. Lee, T. Itoh, and T. Suga, "Self-excited piezoelectric PZT microcantilevers for dynamic SFM - with inherent sensing and actuating capabilities," *Sensors and Actuators A-Physical,* vol. 72, pp. 179-188, 1999.

[72]   Z. Y. Shen, W. Y. Shih, and W. H. Shih, "Self-exciting, self-sensing PbZr0.53Ti0.47O3/SiO2 piezoelectric microcantilevers with femtogram/Hertz sensitivity," *Applied Physics Letters*, vol. 89, Art. No. 023506, 2006.

[73]   Z. Y. Shen, W. Y. Shih, and W. H. Shih, "Mass detection sensitivity of piezoelectric cantilevers with a nonpiezoelectric extension," *Review of Scientific Instruments*, vol. 77, Art. No. 065101, 2006.

[74]   Y. Xin, Z. M. Li, L. Odum, Z. Y. Cheng, and Z. Xu, "Piezoelectric diaphragm as a high performance biosensor platform," *Applied Physics Letters*, vol. 89, Art. No. 223508, 2006.

[75]   C. Ayela, L. Nicu, C. Soyer, E. Cattan, and C. Bergaud, "Determination of the d(31) piezoelectric coefficient of PbZrxTi1-xO3 thin films using multilayer buckled micromembranes," *Journal of Applied Physics*, vol. 100, Art. No. 054908, 2006.

[76]   E. Lacheisserie, *Magnetostriction - Theory and Applications of Magnetoelasticity*: CRC Press, Inc., 1993.

[77]   R. E. Hummel, *Electronic Properties of Materials*, Third ed: Springer-Verlag New York, Inc., 2001.

[78]   E. T. Lacheisserie, D. Gignoux, and M. Schlenker, *Magnetism - Fundamentals*: First Springer Science + Business Media, Inc., 2005.

[79]   R. E. Newnham, *Properties of Materials*: Oxford University Press, 2005.

[80]   F. Claeyssen, N. Lhermet, R. LeLetty, and P. Bouchilloux, "Actuators, transducers and motors based on giant magnetostrictive materials," *Journal of Alloys and Compounds*, vol. 258, pp. 61-73, 1997.

[81]   IEEE, "IEEE Standard on Magnetostrictive Materials: Piezomagnetic Namenclature," *IEEE Std. 319-1990*, 1990.

[82]   E. T. Lacheisserie, D. Gignoux, and M. Schlenker, *Magnetism - Materials and Applications*: First Spring Science + Business Media, Inc, 2005.

[83]   A. E. Clark, J. B. Restorff, M. Wun-Fogle, T. A. Lograsso, and D. L. Schlagel, "Magnetostrictive properties of body-centered cubic Fe-Ga and Fe-Ga-Al alloys," *IEEE Transactions on Magnetics*, vol. 36, pp. 3238-3240, 2000.

[84]   S. Guruswamy, N. Srisukhumbowornchai, A. E. Clark, J. B. Restorff, and M. Wun-Fogle, "Strong, ductile, and low-field-magnetostrictive alloys based on Fe-Ga," *Scripta Materialia*, vol. 43, pp. 239-244, 2000.

[85]   J. R. Cullen, A. E. Clark, M. Wun-Fogle, J. B. Restorff, and T. A. Lograsso, "Magnetoelasticity of Fe-Ga and Fe-Al alloys," *Journal of Magnetism and Magnetic Materials*, vol. 226, pp. 948-949, 2001.

[86]   R. A. Kellogg, A. B. Flatau, A. E. Clark, M. Wun-Fogle, and T. A. Lograsso, "Temperature and stress dependencies of the magnetic and magnetostrictive properties of Fe0.81Ga0.19," *Journal of Applied Physics*, vol. 91, pp. 7821-7823, 2002.

[87]   A. E. Clark, K. B. Hathaway, M. Wun-Fogle, J. B. Restorff, T. A. Lograsso, V. M. Keppens, G. Petculescu, and R. A. Taylor, "Extraordinary magnetoelasticity and lattice softening in bcc Fe-Ga alloys," *Journal of Applied Physics*, vol. 93, pp. 8621-8623, 2003.

[88]   M. Wun-Fogle, J. B. Restorff, and A. E. Clark, "Magnetomechanical coupling in stress-annealed Fe-Ga (Galfenol) alloys," *IEEE Transactions on Magnetics*, vol. 42, pp. 3120-3122, 2006.

[89]   P. D. McGary and B. J. H. Stadler, "Electrochemical deposition of Fe1-xGax nanowire arrays," *Journal of Applied Physics*, vol. 97, Art. No. 10R503, 2005.

[90]   S. Harada, "Thermal-Expansion Coefficient and Youngs Modulus of Hydrogenated Fcc Fe-Ni Invar-Alloys," *Journal of the Physical Society of Japan*, vol. 52, pp. 1306-1310, 1983.

[91]   Metglas, "http://www.metglas.com/PRODUCTS/page5_1_2_7_1.htm."

[92]   M. Pasquale, "Mechanical sensors and actuators," *Sensors and Actuators a-Physical*, vol. 106, pp. 142-148, 2003.

[93]   H. Chiriac, M. Pletea, and E. Hristoforou, "Magneto-surface-acoustic-waves microdevice using thin film technology: design and fabrication process," *Sensors and Actuators a-Physical*, vol. 91, pp. 107-111, 2001.

[94]   E. M. Simpson and W. P. Robbins, "Magnetostrictive Fe-Si Thin-Films for Tunable Saw Devices," *Ieee Transactions on Magnetics*, vol. 16, pp. 919-921, 1980.

[95]   U. Zechbauer, "To Catch a Thief," *Research and Innovation: Features, Interviews, and Reports in Siemens' Science and Technology Magazine*, 1999.

[96]   G. Herzer and G. Rauscher, "Elongated Member Serving as a Pulse Generator in an Electromagnetic Anti-Theft or Article Identification System and Method for Manufacturing Same and Method for Producing a Pronounced Pulse in The System," *US Patent 5,757,272,* 1998.

[97]   Q. Y. Cai and C. A. Grimes, "A remote query magnetoelastic pH sensor," *Sensors and Actuators B-Chemical*, vol. 71, pp. 112-117, 2000.

[98]   C. A. Grimes, K. G. Ong, K. Loiselle, P. G. Stoyanov, D. Kouzoudis, Y. Liu, C. Tong, and F. Tefiku, "Magnetoelastic sensors for remote query environmental monitoring," *Smart Materials & Structures*, vol. 8, pp. 639-646, 1999.

[99]   C. A. Grimes and D. Kouzoudis, "Remote query measurement of pressure, fluid-flow velocity, and humidity using magnetoelastic thick-film sensors," *Sensors and Actuators a-Physical*, vol. 84, pp. 205-212, 2000.

[100]   C. A. Grimes, P. G. Stoyanov, D. Kouzoudis, and K. G. Ong, "Remote query pressure measurement using magnetoelastic sensors," *Review of Scientific Instruments*, vol. 70, pp. 4711-4714, 1999.

[101]   K. G. Ong, K. F. Zeng, X. P. Yang, K. Shankar, C. M. Ruan, and C. A. Grimes, "Quantification of multiple bioagents with wireless, remote-query magnetoelastic microsensors," *IEEE Sensors Journal*, vol. 6, pp. 514-523, 2006.

[102]   S. H. Wu, Y. Zhu, Q. Y. Cai, K. F. Zeng, and C. A. Grimes, "A wireless magnetoelastic alpha-amylase sensor," *Sensors and Actuators B-Chemical*, vol. 121, pp. 476-481, 2007.

[103] K. G. Ong, X. P. Yang, N. Mukherjee, H. D. Wang, S. Surender, and C. A. Grimes, "A wireless sensor network for long-term monitoring of aquatic environments: Design and implementation," *Sensor Letters*, vol. 2, pp. 48-57, 2004.

[104] Q. Y. Cai, K. F. Zeng, C. M. Ruan, T. A. Desai, and C. A. Grimes, "A wireless, remote query glucose biosensor based on a pH-sensitive polymer," *Analytical Chemistry*, vol. 76, pp. 4038-4043, 2004.

[105] M. Zourob, K. G. Ong, K. F. Zeng, F. Mouffouk, and C. A. Grimes, "A wireless magnetoelastic biosensor for the direct detection of organophosphorus pesticides," *Analyst*, vol. 132, pp. 338-343, 2007.

[106] L. G. Puckett, G. Barrett, D. Kouzoudis, C. Grimes, and L. G. Bachas, "Monitoring blood coagulation with magnetoelastic sensors," *Biosensors & Bioelectronics*, vol. 18, pp. 675-681, 2003.

CHAPTER 2

RESEARCH OBJECTIVES

2.1 Design and Feasibility Study of Magnetostrictive Microcantilever (MSMC) as a Biosensor Platform

Acoustic wave (AW) devices as high performance sensor platforms have been widely investigated in order to develop highly sensitive biosensors capable of rapid detection of a small amount of target species in a small volume of sample, mostly in liquid. Among these AW sensor platforms, microcantilevers (MCs) demonstrate the highest sensitivity in the terms of minimum detectable mass. So far, investigations of MCs as biosensor platforms mainly focus on two kinds of MCs: one is the single beam MCs, such as silicon-based MCs; another one is the composite-beam MCs, such as the piezoelectric unimorph/bimorph MCs. The advantage of silicon-based MCs is that the microfabrication process of silicon is well established, but it is difficult to actuate and sense. On the other hand, piezoelectric-based MCs are easy to be actuated and sensed, but have a complicated configuration and low Q value.

In this research, we introduce a novel type of MC – magnetostrictive microcantilever (MSMC) based on magnetostriction – as a biosensor platform. The MSMC is compared with Si-based and piezoelectric-based MCs. The advantages of the MSMC over other MCs are presented and discussed. The MSMC can be wirelessly actuated and sensed, and has a simple structure. The MSMCs are fabricated and their performance as sensor

platforms is characterized. To demonstrate the performance of the MSMC as a biosensor platform, yeast and *Salmonella* cells are detected using MSMC biosensors in a real-time manner.

2.2 Design and Feasibility Study of Magnetostrictive Particle (MSP) as a High Performance Biosensor Platform

The goal of this research is to develop a novel AW sensor platform – magnetostrictive particle (MSP) in the shape of strip or bar – as a high performance biosensor platform. The MSP not only inherits the advantages of other AW devices, but has its own unique advantages. Based on magnetostriction rather than piezoelectriction, the MSP is a wireless and completely free-standing sensor platform. This is its principle advantage over other AW devices. In this research, the feasibility of the MSP as a biosensor platform is studied. Some important parameters of the MSP, such as the resonance behavior, mass sensitivity and Q value, are characterized. Based on the unique features of the MSP, new detection methods (multiple-sensor approach and multiple-target approach) are designed, and their feasibilities are investigated. Multiple target approach allows simultaneous detection of different types of bioagents. Multiple sensor approach will provide a solution to the challenge of detecting biological cells in a very low concentration condition.

2.3 Synthesis of Amorphous Fe-B Alloy and Fe-B Nanowires for Magnetostrictive Biosensor Platform Application

The sensitivity of AW devices depends on the size of the device: the smaller the size, the higher the mass sensitivity. To obtain a high sensitivity, magnetostrictive sensors in

the size of micrometers or nanometers are required. In order to develop MSMC & MSP with extremely high mass sensitivity, the synthesis of magnetostrictive thin films and fabrication of micro-MSPs and magnetostrictive nanowires are investigated.

This research includes two parts. The first part is to synthesize and characterize the magnetostrictive material for magnetostrictive AW device fabrication. Amorphous Fe-B alloy is synthesized and studied as the magnetostrictive material since it exhibits favorable magnetic and mechanical properties. The Fe-B thin films are synthesized by electrochemical deposition. The deposition conditions are studied and optimized. The properties and resonance behaviors of the deposited Fe-B thin films are characterized. Combining microelectronic fabrication methods and electrochemical deposition of Fe-B films, the processes of fabricating micro-size MSPs are explored.

The second part of this research is to synthesize amorphous Fe-B nanowires as biosensor platforms based on the results obtained from first part of the research. The Fe-B nanowires are fabricated by template-based electrochemical deposition. The fabrication process is optimized and the fabricated nanowires are characterized.

CHAPTER 3

CHARACTERIZATION OF RESONANCE BEHAVIOR OF

MAGNETOSTRICTIVE AW DEVICES

As a sensor platform, the resonance frequency of the AW device is used as the output signal. To characterize the resonance frequency of a magnetostrictive device, two set-ups have been built/used in this research.

3.1 Set-up (A) Based on Helmholtz Coil and Lock-in Amplifier

3.1.1 Configuration of the Setup

The schematic of set-up (A) is shown in Fig. 3-1. As discussed in Chapter 1, a magnetostrictive AW device is driven by a small AC magnetic field superimposing on a relatively larger DC magnetic field (bias).

$$H_{driving} = H_{AC} + H_{DCbias} \tag{3-1}$$

In this setup, the driving magnetic field is generated by a custom designed Helmholtz coil, which consists of two pairs of coils: one pair is used to generate a DC magnetic field to polarize the magnetostrictive material, while another pair is used to generate an AC magnetic field for exciting the device. The DC Helmholtz coil is connected to a DC power supply, which applies a constant DC current on the coil. The AC Helmholtz coil is connected to a lock-in amplifier (SRS830, Standford research system, Sunnyvale, CA),

which provides a sine wave signal with constant RMS (root-mean-square) amplitude of voltage to the coil.
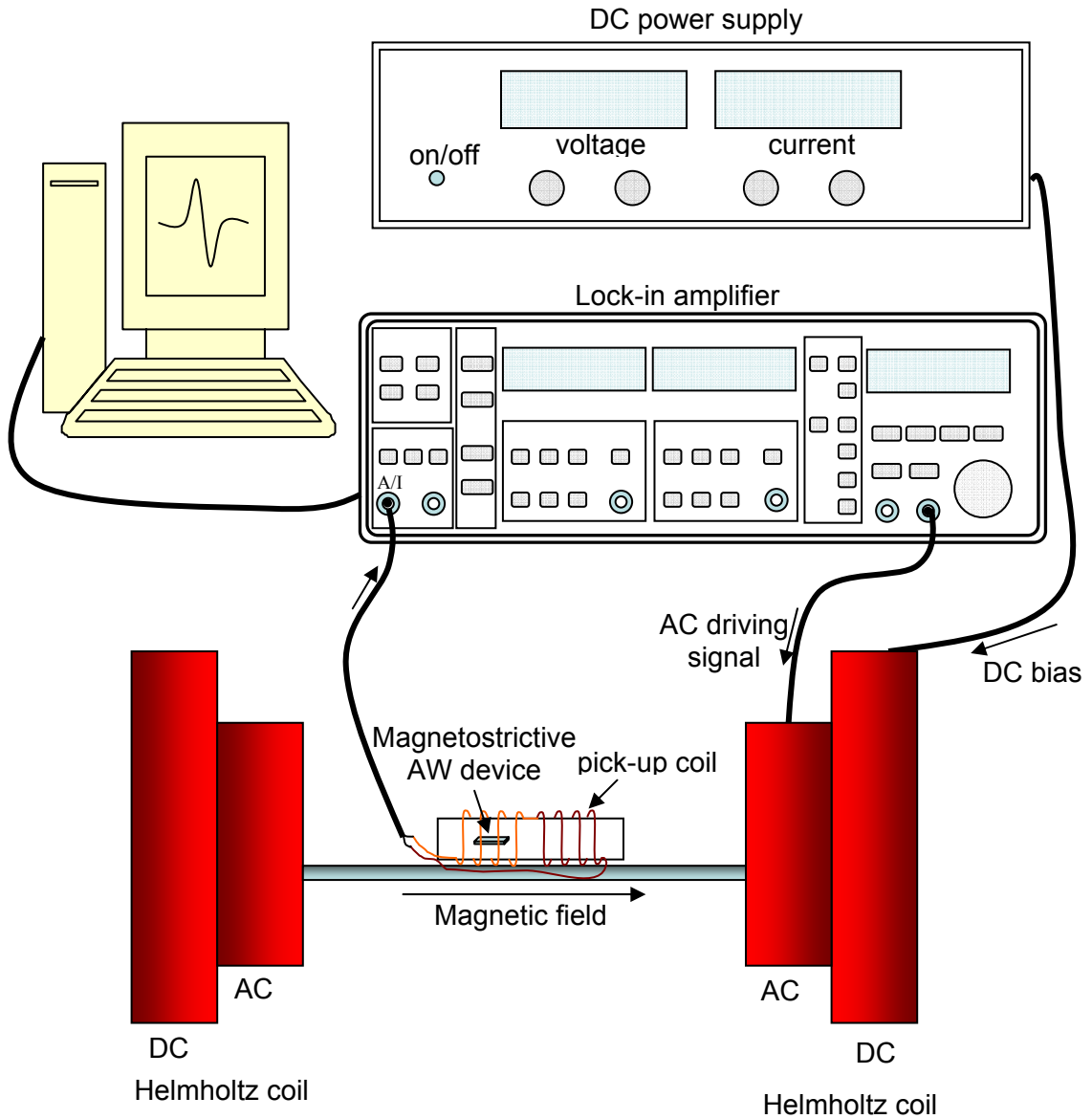
Fig. 3-1. Schematic of set-up (A) based on a Helmholtz coil and a lock-in amplifier.

A uniform driving magnetic field is generated in the middle of the Helmholtz coil. The AC magnetic field sweeps over a broad frequency range to drive the magnetostrictive device, which is placed in the middle of the Helmholtz coil. The shape of the magnetostrictive material changes in response to the driving field, thus the magnetostrictive AW device works as a resonator. Due to the magnetic nature of the magnetostrictive material, the oscillation of the device will result in the emission of a magnetic signal. In this setup, a pair of home made pickup coils is used to measure the magnetic signal emitted from the magnetostrictive device. The reason of employing a pair of pickup coils is to eliminate the background. Since the pickup coil is also placed in the middle of Helmholtz coils, it can pickup the driving magnetic field, which causes strong background and might even surpass the signal from the device. To eliminate this background, the pair of pickup coils consists of two same coils. However, they were wound in opposite directions and connected in series so that the output signal is zero if there is no device inside. The magnetostrictive AW device is placed in one of the pickup coils. Therefore, the outputs of the pickup coils only reflects the magnetic signal from the device due to its oscillation and are sent back to the lock-in amplifier. The lock-in amplifier has two output signals: amplitude and phase. The amplitude represents the oscillating amplitude of the magnetostrictive device; while the phase represents the phase different between the AC driving magnetic field and the magnetic signal from the device. Both the amplitude and the phase versus frequency were recorded by a computer using a data acquisition program to obtain the resonance spectrum.
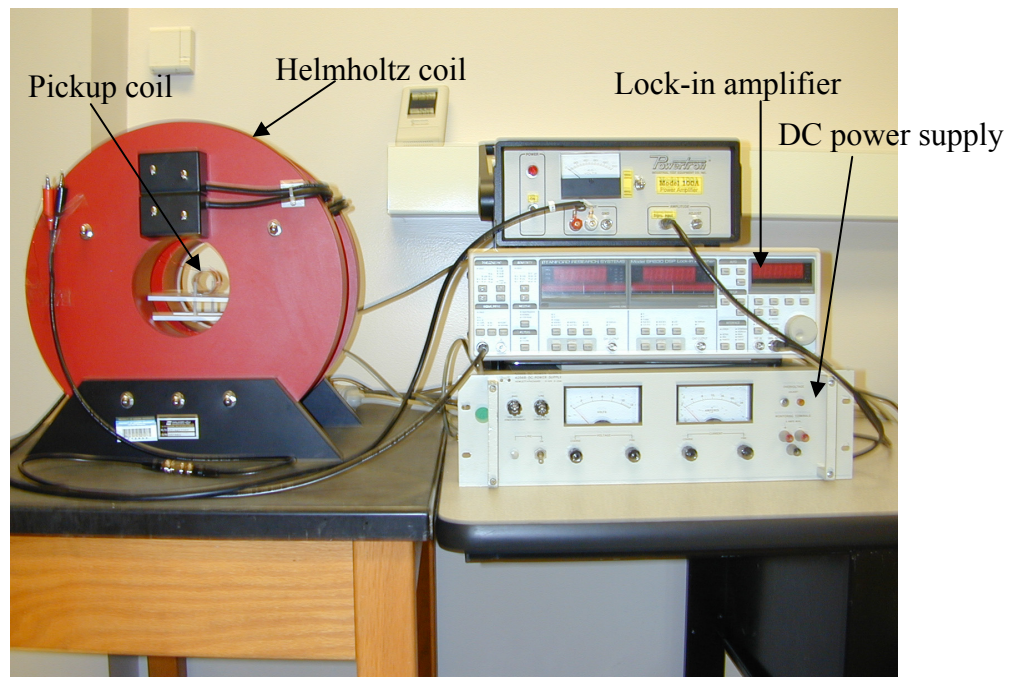
Fig. 3-2. Picture of set-up (A) based on a Helmholtz coil and a lock-in amplifier.

For the ideal case, the background signal detected by the pair of pickup coils should be zero. However, it is very difficult to make the two coils exactly identical in practice. Therefore, the background signals generated in two coils does not totally cancel each other and, in this study, a non-zero signal is observed when the magnetostrictive device is not inside the pickup coils. Fig. 3-3 shows the background signal collected by a pair of pickup coils. The results shown in Fig. 3-3 reflect the amplitude & phase change with frequency.
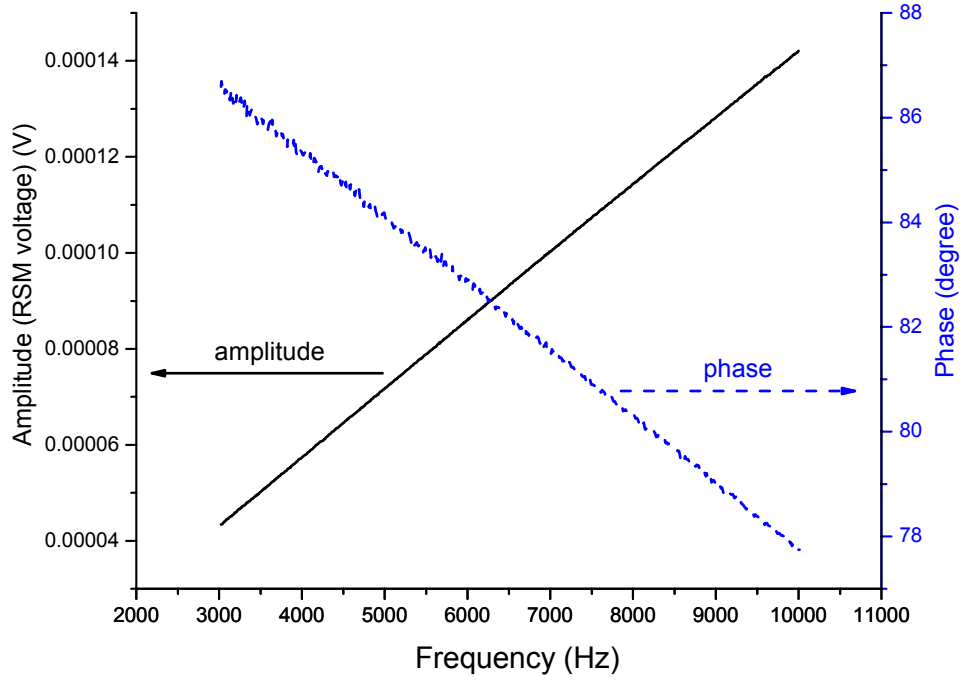
Fig. 3-3. Background signal detected by a pair of pickup coils.

Therefore, in this research, the measured resonance spectrum of the magnetostrictive AW device includes two signals: the background signal and the signal from the device. The effect of the background can be minimized by correcting the experimental output using collected background signal. The correction principle is shown as below.

Let, I_m = Measured signal; I_s = Magnetostrictive device signal; I_b = Background signal.

Therefore,

$$I_m = I_m \sin(\omega t + \theta_m) = I_s \sin(\omega t + \theta_s) + I_b \sin(\omega t + \theta_b)$$

$$
\begin{aligned}
I_s \sin(\omega t + \theta_s) &= I_m \sin(\omega t + \theta_m) - I_b \sin(\omega t + \theta_b) \\
&= I_m \sin \omega t \cos \theta_m + I_m \cos \omega t \sin \theta_m - I_b \sin \omega t \cos \theta_b - I_b \cos \omega t \sin \theta_b \\
&= \sin \omega t (I_m \cos \theta_m - I_b \cos \theta_b) + \cos \omega t (I_m \sin \theta_m - I_b \sin \theta_b)
\end{aligned}
$$

Let, $A = I_m \cos \theta_m - I_b \cos \theta_b$; $B = I_m \sin \theta_m - I_b \sin \theta_b$.

49

$$I_s \sin(\omega t + \theta_s) = A \sin \omega t + B \cos \omega t$$

$$= \sqrt{A^2 + B^2} \left(\frac{A}{\sqrt{A^2 + B^2}} \sin \omega t + \frac{B}{\sqrt{A^2 + B^2}} \cos \omega t \right)$$

Let, $\cos \theta = \dfrac{A}{\sqrt{A^2 + B^2}}$; $\sin \theta = \dfrac{B}{\sqrt{A^2 + B^2}}$.

$$I_s \sin(\omega t + \theta_s) = \sqrt{A^2 + B^2} \left(\cos \theta \sin \omega t + \sin \theta \cos \omega t \right)$$

$$= \sqrt{A^2 + B^2} \sin(\omega t + \theta)$$

So, $I_s = \sqrt{A^2 + B^2}$; $\theta_s = \theta$

Thus, we can get:

$$I_s = \sqrt{A^2 + B^2}$$

$$= \sqrt{(I_m \cos \theta_m - I_b \cos \theta_b)^2 + (I_m \sin \theta_m - I_b \sin \theta_b)^2}$$

$$= \sqrt{I_m^2 \cos^2 \theta_m - 2 I_m I_b \cos \theta_m \cos \theta_b + I_b^2 \cos^2 \theta_b + I_m^2 \sin^2 \theta_m - 2 I_m I_b \sin \theta_m \sin \theta_b + I_b^2 \sin^2 \theta_b}$$

$$= \sqrt{I_m^2 + I_b^2 - 2 I_m I_b \cos(\theta_m - \theta_b)}$$

$$(3\text{-}2)$$

$$\theta_s = \arctan(\tan \theta)$$

$$= \arctan\left(\frac{\sin \theta}{\cos \theta} \right) = \arctan\left(\frac{B}{A} \right) = \arctan\left(\frac{I_m \sin \theta_m - I_b \sin \theta_b}{I_m \cos \theta_m - I_b \cos \theta_b} \right) \qquad (3\text{-}3)$$

Fig. 3-4 shows the measured output signal and the corrected output signal of a magnetostrictive cantilever in the size of 2.8 mm x 1 mm x 35 μm. In Fig. 3-4, the solid black curves are the measured data, and the wine curves are the corrected data. The amplitude and phase signal are corrected based on Equation (3-2) and (3-3), respectively. The corrected signal shows a stronger and sharper peak. Clearly, the correction results in a better output signal.
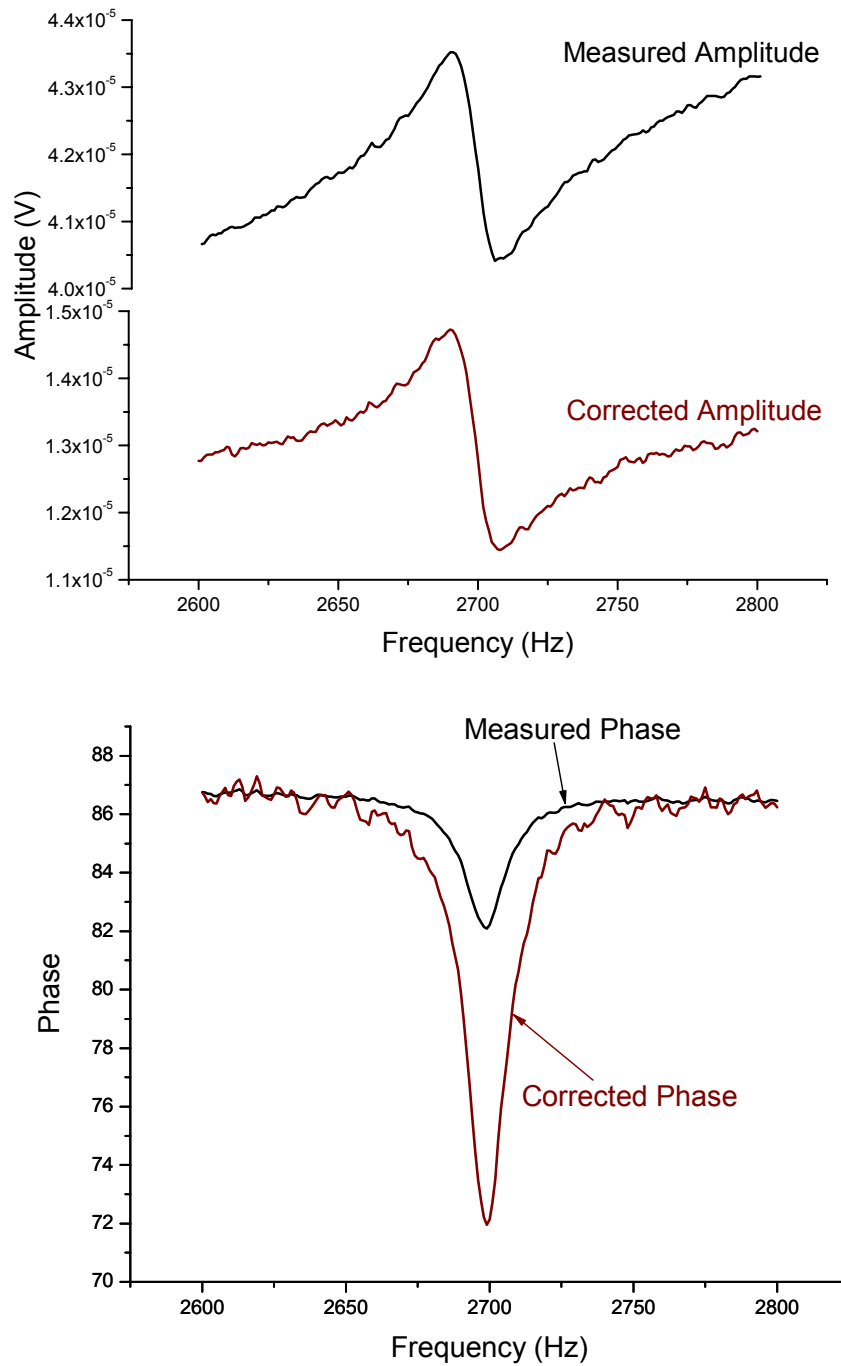
Fig. 3-4. Experimental output (black curve) of a magnetostrictive cantilever measured using setup A, and its corresponding corrected results (wine curve) based on Equation (3-2) and (3-3). The size of the cantilever is 2.8 mm x 1 mm x 35 μm.

For the results reported in this research, the characterization of the device was based on the measured output signals without background correction, since the background is small enough to obtain a clear resonance frequency peak. Thus, it is expected that the real performance of the device can be better than the data reported in this dissertation.

3.1.2 Resonance Frequency and Q Value Determination

As discussed above, the output signals of the lock-in amplifier are used to obtain the resonance spectrum of the device. Fig. 3-5 shows a typical resonance spectrum of a magnetostrictive AW device, where (a) is the typical output for a magnetostrictive particle, and (b) is the typical output for a magnetostrictive microcantilever. Both amplitude and phase signals are shown in Fig. 3-5.

As shown in Fig. 3-5, when the frequency of driving magnetic field is the same as the natural resonance frequency of the magnetostrictive AW device, the device undergoes the resonance oscillation. At this frequency, the device has the biggest vibration, thus the emitted magnetic flux and the measured amplitude reach the maximum. This frequency is the resonance frequency (f_r). Continuously increasing the frequency of driving field, the vibration and the magnetic flux emission reach the minimum. The frequency at this point is the anti-resonance frequency ($f_r^{'}$). The correspondent phase signals around the resonance frequency are also shown in Fig. 3-5. In practice, the experimental resonance frequency (f_0) of the device can be determined from either the amplitude or phase signal.
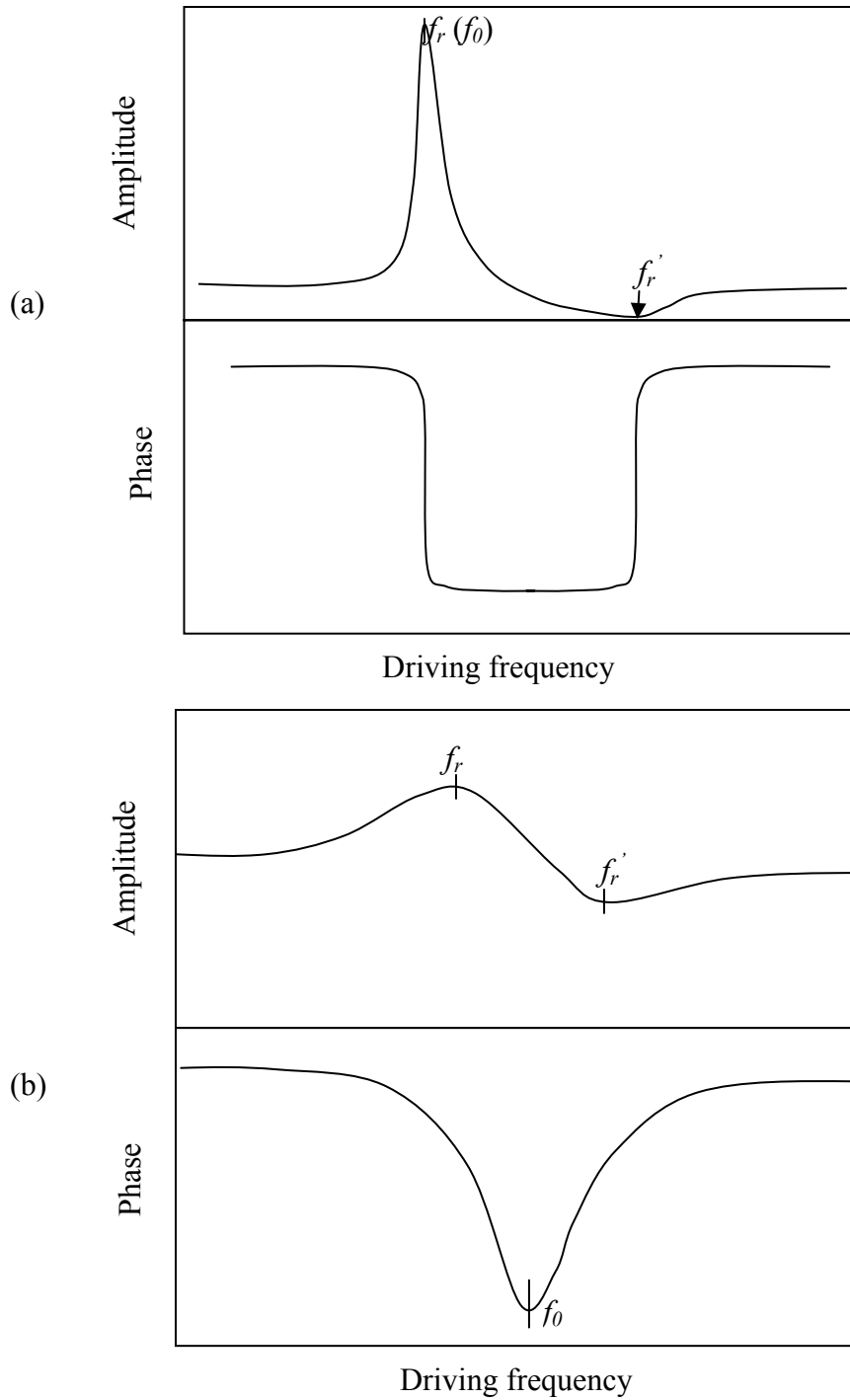
Fig. 3-5. Typical resonance spectrum of a magnetostrictive AW device: (a) the typical output of a magnetostrictive particle; (b) the typical output of a magnetostrictive microcantilever.

It should be pointed out here that the above discussion is for the ideal case: that is the device is loss free during the vibration. Practically, due to the loss, the frequencies corresponding to the maximum and minimum magnetic signals are smaller than the real natural resonance frequency and anti-resonance frequency of the device, respectively. However, since the loss for the devices studied here is very small, the difference can be neglected. The frequency f_0 determined from the amplitude or phase signal can be assumed as the resonance frequency of the device.

For a magnetostrictive particle, whose typical resonance spectrum is shown as Fig. 3-5 (a), its amplitude signal exhibits a sharp resonance frequency peak. Therefore, the frequency corresponding to this peak is used to determine the resonance frequency of the device. In order to determine the f_0 and the Q value, the amplitude signal of the device is fitted at frequencies around the resonance frequency. Based on the experimental results, it is found that, if we choose the baseline as shown in Fig. 3-6, the Lorentz function (Equation (3-4)) can be used to fit the resonance peak.
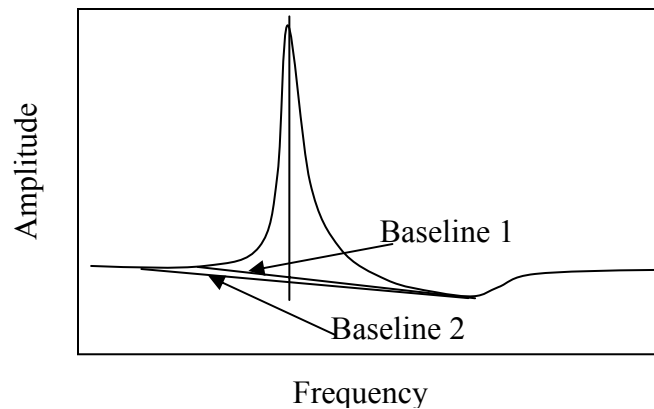
Fig. 3-6. Baselines for fitting the resonance frequency peak from the amplitude signal. The baseline is chosen through two points; one of the points is where the amplitude reaches minimum.

The Lorentz function is expressed as:

$$D(f) = D_0 + \frac{2A}{\pi} \frac{w}{4(f - f_0)^2 + w^2}$$

(3-4)

where $D(f)$ is the amplitude as the function of driving frequency, f. D_0 is the baseline, which is determined using a two-point linear function. The A, w, f_0 are constants obtained from the fitting. The f_0 is resonance frequency of the device, the w is the width of the peak at its half height, and the ratio of the A to the w is the strength of the peak, and the ratio of the f_0 to w is the Q value. Fig. 3-7 shows the Lorentz fitting curve for the amplitude signal of a magnetostrictive particle in strip shape. The results indicate that the Lorentz function can reasonably fit the resonance peak.
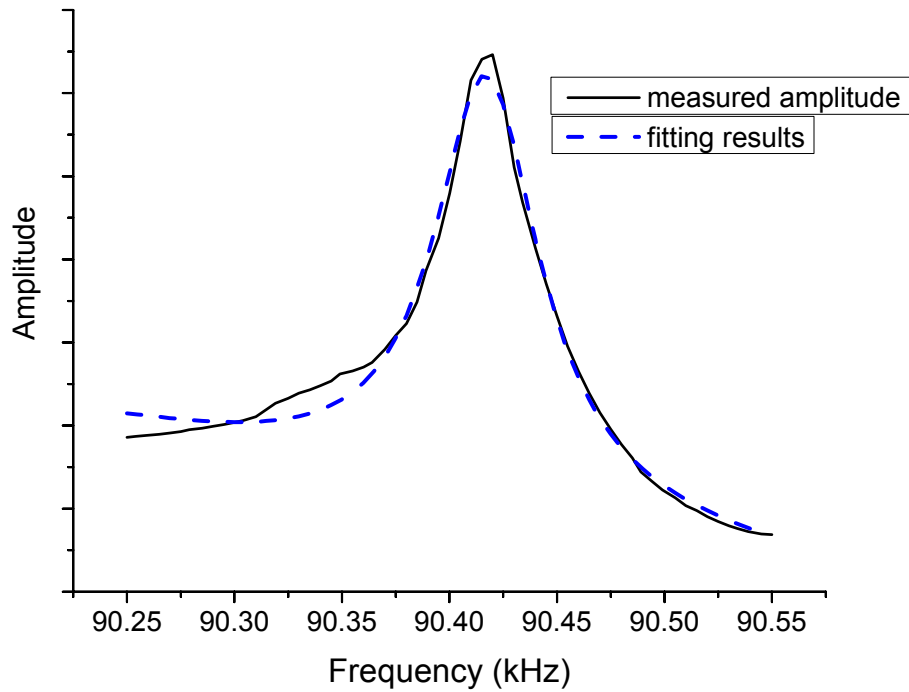
Fig. 3-7. Lorentz fitting curve for the measured amplitude resonance peak of a magnetostrictive particle. Solid black curve is the measured signal, while dashed blue curve is the fitting curve.

When fitting the amplitude peak using Lorentz function, we need to choose the baseline (parameter D_0), and the frequency range. In order to determine how these factors affect the fitting results, we chose four different baselines to fit the data. The baselines are chosen as shown in Fig. 3-6, and they all pass the minimum point of the amplitude but with different ranges. The fitting results are shown in Table 3-1. The baseline and the frequency ranges have little effect on f_0. With the frequency range increasing, the calculated Q value increases a little, with a variation of about 5%, which is a tolerable error. This gives us confidence to determine Q and f_0 by using the Lorentz function.

TABLE 3-1

Fitting Results of Amplitude Data Based on Lorentz Function Using Different Baselines

Baseline frequency range (kHz)	f_0 (kHz)	w	$Q(=f_0/w)$
90.15 – 90.55	90.416	0.064	1413
90.2 – 90.55	90.417	0.063	1435
90.25 – 90.55	90.417	0.06	1507
90.3 – 90.55	90.418	0.056	1614
Average	90.417 ± 0.0007	0.061 ± 0.003	1492 ± 78

For a magnetostrictive microcantilever, whose typical resonance spectrum is shown as Fig. 3-5 (b), the phase signal is used to determine the resonance frequency (f_0) and the Q value of the device, since, in this case, the resonance phase is a better indicator to show how strong the resonance is. The resonance frequency (f_0) is determined by the corresponding frequency of the phase peak. For simplicity, the Q value of the device is determined as Shih did to determine the Q value for piezoelectric-based microcantilevers [1]. That is, the Q value is defined as $\Delta f/f_0$, where f_0 is the resonance frequency of the

device determined by the phase peak, and Δf is the width of the phase peak at its half height.

To precisely determinate the resonance frequency, the phase data was fitted at frequencies around the resonance. As shown in Fig. 3-8, Lorentz function (Equation (3-4)) can fit the phase peak very well. In this fitting, $D(f)$ is the phase angle as the function of driving frequency, f. D_0 is the baseline, which can be a constant or a linear function dependent on the frequency range. The A, w, f_0 are constants obtained from the fitting. The f_0 is resonance frequency of the device; the w is the width of the phase peak at its half height. Therefore, the Q value is calculated as w/f_0.
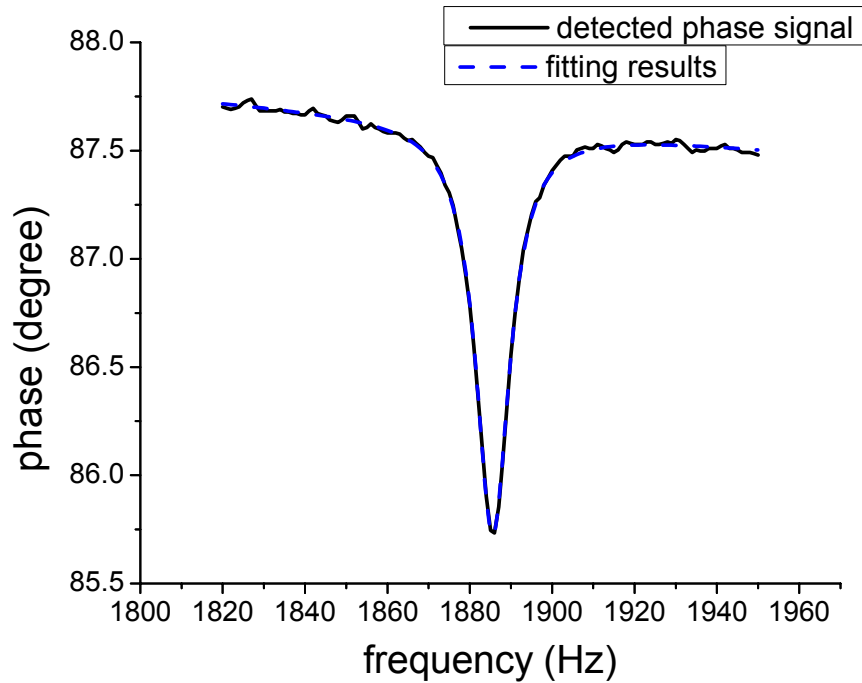
Fig. 3-8. Lorentz fitting results for the detected phase signal of a magnetostrictive cantilever measured in air. The black solid line is the detected signal, while the dashed blue line is the fitting curve.

To determine the effects of fitting parameters, D_0 and frequency range, on the fitting results, we chose three different frequency ranges to fit the measured data shown in Fig. 3-8. For each range, both a constant baseline and a linear baseline were used. The fitting results are shown in Table 3-2. The baseline and the frequency ranges have very little effects on the determination of f_0 and Q value. This indicates Lorentz function works very well to fitting the measured phase signal.

TABLE 3-2

Fitting Results of Phase Data Based on Lorentz Function with Different Fitting

Parameters

Frequency range (Hz)	Baseline	f_0 (Hz)	w	$Q(=f_0/w)$
1865 - 1907	Linear, D2	1885.58	10.08	187
	Constant, D2	1885.63	10.02	188
1855 -1915	Linear, D2	1885.58	9.95	189
	Constant, D2	1885.64	9.96	189
1845 - 1925	Linear, D2	1885.58	9.92	190
	Constant, D2	1885.64	9.95	189
Average	Linear, D2	1885.58 ± 0	9.98 ± 0.07	189 ± 1
	Constant, D2	1885.637 ±0.003	9.98 ± 0.03	189 ± 0.6

It should be pointed out that the Q value determined here is not the intrinsic Q value of the AW device. The output we analyzed is the magnetic signal measured by the pickup coil, not the real deformation of the device. The couplings between the driving coil, device and pickup coil, as well as the measurement circuit, all contribute to the final output. The Q value calculated here reflects the Q value of the whole system,

also includes the fitting error. The improvement of the driving/sensing system might be able to increase the measured Q value.

3.2 Set-up (B) Based on Network Analyzer

3.2.1 Configuration of the Setup

This characterization system was built based on a network analyzer (HP 8751A) with an S-Parameter adapter (HP 87511). A network analyzer is an electric analysis instrument, which provides a known stimulus to a device and measures its response [2]. As shown in Fig. 3-9, the response can be the reflected response or the transmitted response.
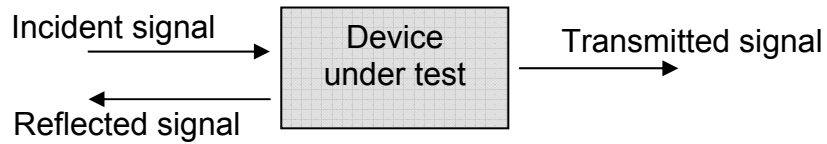
Fig. 3-9. A stimulus/response test system.

A network analyzer characterizes the device by determining the ratios of incident signal to the response signal over a certain frequency range. The output of a network analyzer is S-parameter. The definition of an S-parameter is dependent on the testing configuration. A network analyzer provides two output ports for device characterization. Therefore, four S-parameters can be defined, which is shown in Fig. 3-10 [2].
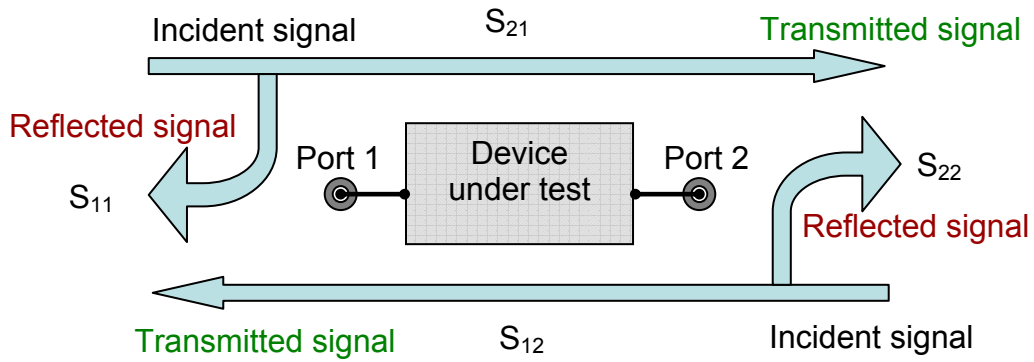
Fig. 3-10. Definitions of S-parameters.

S-parameters are expressed as the letter S with two subscripts. The first subscript represents the port number, at which the response signal is measured; while the second subscript is the port number, at which the incident signal is applied. In this set-up, we use one-port configuration to characterize the device using reflected signal, that is, the test parameter is the S_{11} parameter, which is defined as follow [2]:

$$S_{11} = \frac{Power_{reflected}}{Power_{incident}} = \left(\frac{Voltage_{reflected}}{Voltage_{incident}}\right)^2 \qquad (3\text{-}5)$$

S_{11} parameter is a complex number including a Real and Imaginary component pair. The magnitude of S_{11} parameter (normally logarithm format is used), which represents the power ratio of reflected signal to the incident signal, is calculated as follow [2]:

$$\text{Log magnitude} = 20\log_{10}\sqrt{Real^2 + Imaginary^2} \qquad (3\text{-}6)$$

The phase of S_{11} parameter, which represents the phase difference between reflected signal and incident signal is obtained through Equation (3-7) [2].

$$phase = \tan^{-1}\frac{Imaginary}{Real} \qquad (3\text{-}7)$$

60

coil

magnetic field

test chamber

magnetostrictive AW device

magnet

On/off

Port 1

Port 2
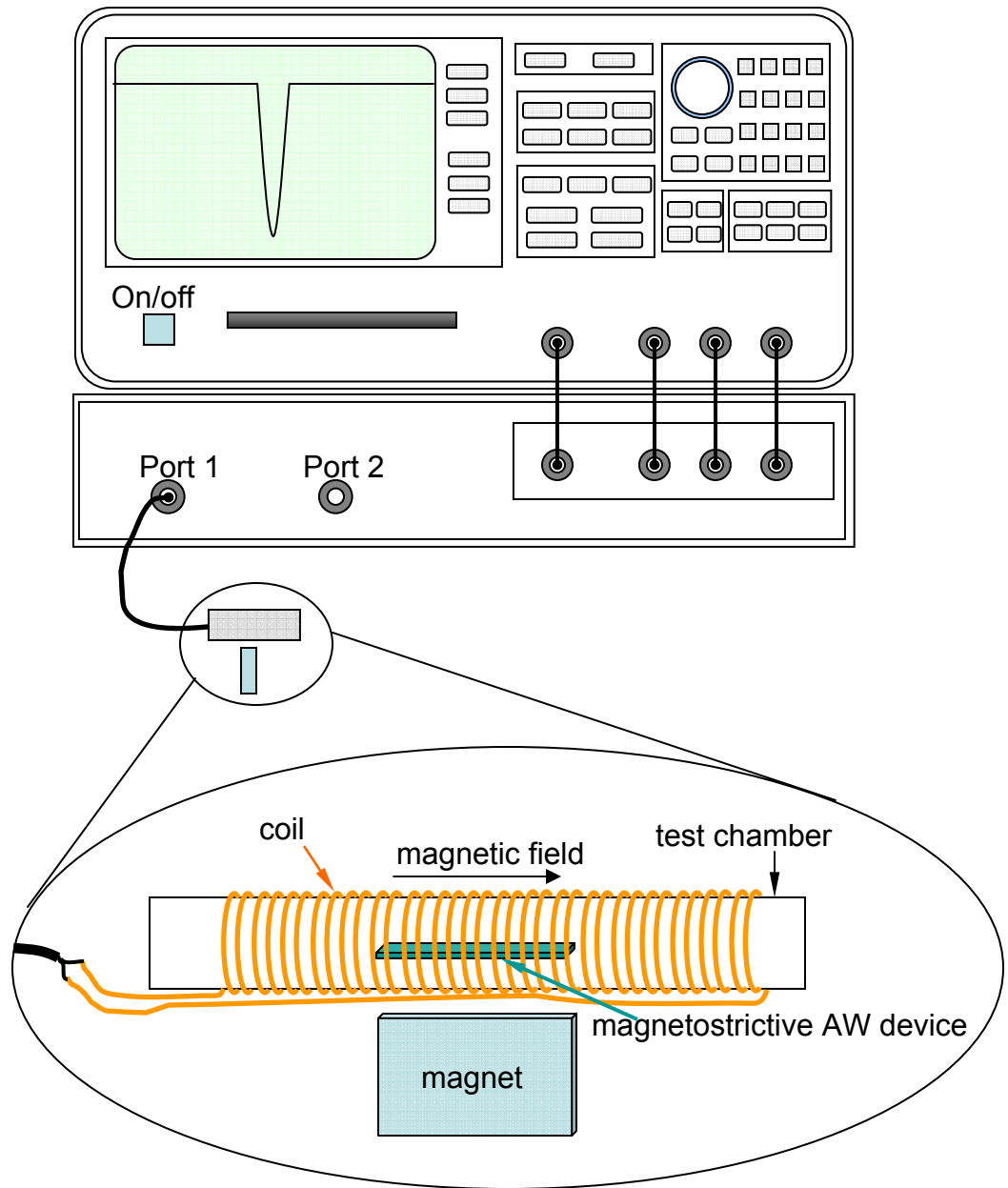
Fig. 3-11. Set-up (B) based on a network analyzer.

The schematic of this set-up is shown in Fig. 3-11. A homemade coil was wound around the test chamber, and connected to the port 1 of the network analyzer. The magnetostrictive device is placed in the middle of the coil. The network analyzer applies a RF signal sweeping over a certain frequency range to the coil and generates an AC magnetic field in the coil to drive the device. To obtain a relatively uniform magnetic field, the length of the coil is at least twice of the length of the device. S_{11} parameter is measured at port 1, and its magnitude and phase are calculated based on Equation (3-6) and (3-7). A permanent magnet is placed close to the chamber as the DC magnetic bias. The applied DC magnetic field can be tuned by slightly adjusting the distance between the test chamber and the magnet. Before putting the magnetostrictive device into the test chamber, the analyzer was calibrated to zero base-line to set the intrinsic reflection signal of the coil as zero. Therefore, the recording signal would only reflect the signal from the magnetostrictive device, which represents its oscillating amplitude.

The resonance spectrum of the magnetostrictive device is obtained by recording the magnitude and phase of S_{11} parameter changing with the frequency.

3.2.2 Resonance Frequency and Q Value Determination

Fig. 3-12 shows the S_{11} parameter changing with the frequency of a magnetostrictive strip, whose size is 10 mm x 1 mm x 30 μm. Both the magnitude in logarithm format and the phase are shown in Fig. 3-12.

When the frequency of the incident signal equates to the natural resonance frequency of the device, the device undergoes resonance oscillation, and the amount of incident power converted into the elastic energy reaches maximum. At this point, the reflected power reaches minimum, and thus the magnitude of S_{11} reaches minimum.

The measured S_{11} data can be converted to the equivalent complex impedance (Z) of the device using Equation (3-8).

$$Z = 50\frac{1+S_{11}}{1-S_{11}}$$

(3-8)

Based on Equation (3-8), the correspondent impedance based on the S_{11} data shown in Fig. 3-12 was calculated and shown in Fig. 3-13. The magnetostrictive AW device vibrates under the driving field, and then emits a magnetic signal, which generates an electric field in the coil. At resonance frequency (f_r), the magnetostrictive device has the biggest vibration and causes the biggest magnetic flux change. Therefore, at f_r, the current through the coil reaches the maximum and the impedance reaches the minimum, as shown in Fig. 3-13. Continuously increasing the driving frequency, the vibration and the magnetic flux change reach the minimum, thus the magnitude of impedance reaches the maximum. The frequency at this point is the anti-resonance frequency ($f_r^{'}$).
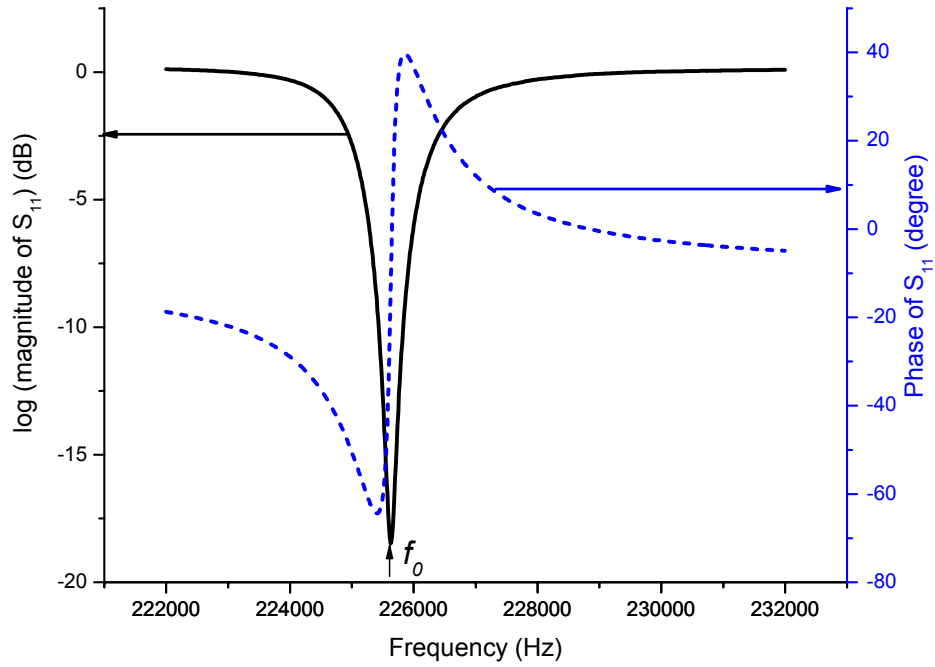
Fig. 3-12. Magnitude and phase curve of S_{11} parameter changing with the frequency of a magnetostrictive strip, whose size is 10 mm x 1 mm x 30 μm.
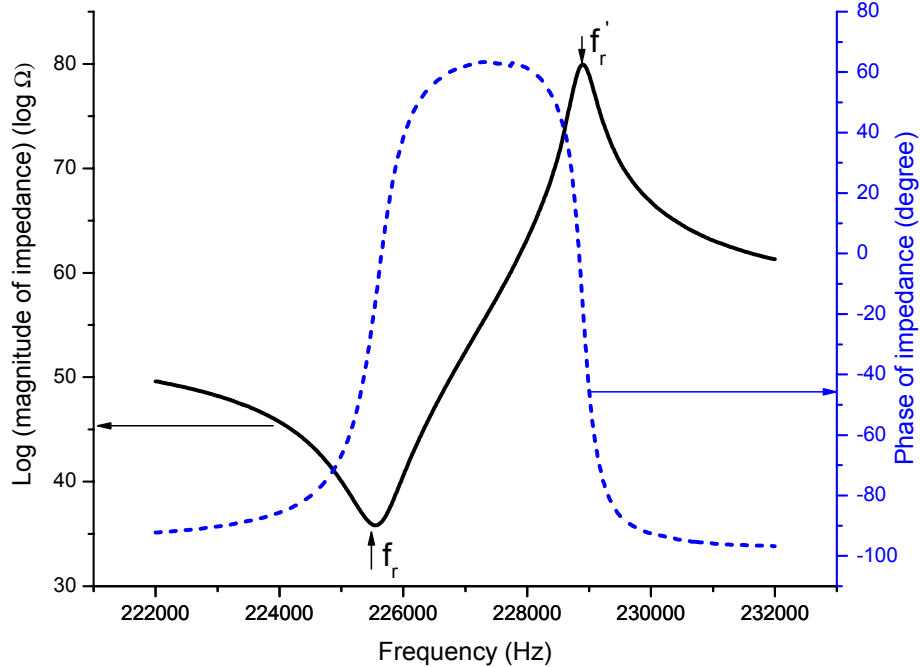
Fig. 3-13. The equivalent impedance based on S_{11} data shown in Fig. 3-12. The conversion is based on Equation (3-8).

The method for characterizing the magnetostrictive device is similar to that used for setup A. In this research, for simplicity, the magnitude of the S_{11} signal is used to determine the resonance frequency (f_0) and the Q value of the device. The f_0 is the frequency at which the S_{11} magnitude reaches the minimum. The Q value is defined as $\Delta f/f_0$, where Δf is the width of the peak at its half height. The measured data are fitted to obtain precise f_0 and Q value. Also, it is found that Lorentz function (Equation (3-4)) is a good candidate to fit S_{11} magnitude peak. Fig. 3-14 shows the fitting curve for the S_{11} magnitude signal of a magnetostrictive strip in the size of 6.4 mm x 1 mm x 30 μm.
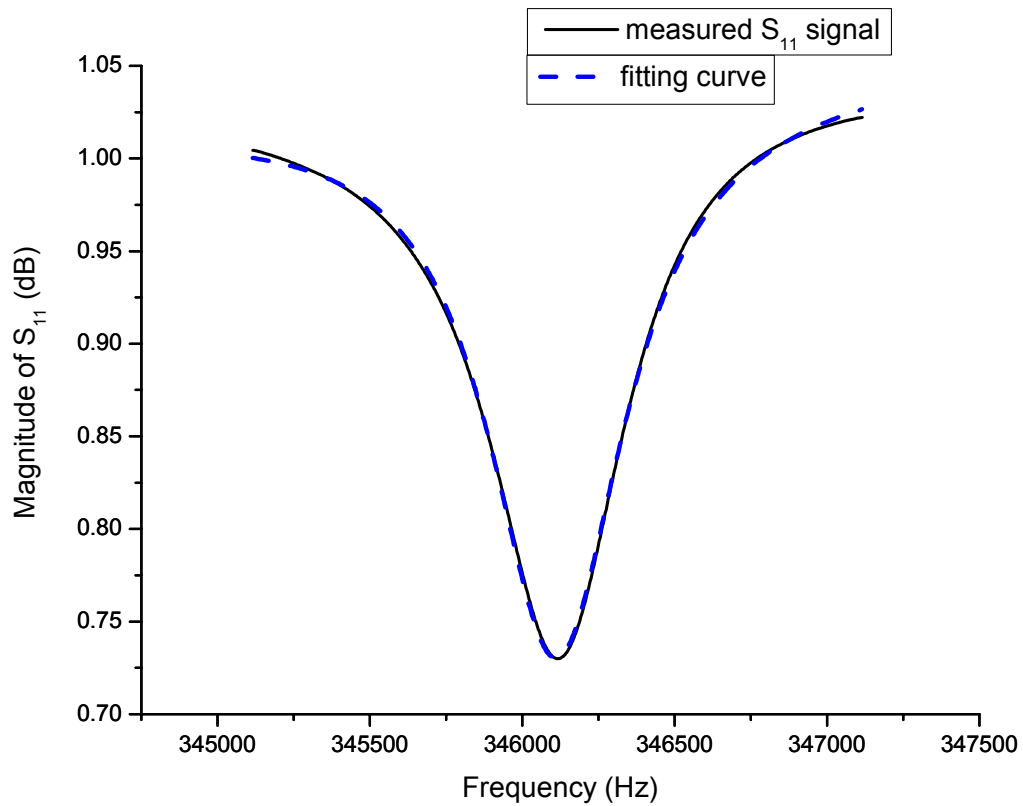
Fig. 3-14 Lorentz fitting results for the measured S_{11} magnitude peak of a magnetostrictive strip in the size of 6.4 mm x 1 mm x 30 μm. The black solid line is the detected signal, while the dashed blue line is the fitting curve.

Different frequency ranges and baselines were chosen to fit the data shown in Fig. 3-14 to determine the effects of the fitting parameters. The fitting results are shown in Table 3-3. The baselines and the frequency ranges do not have much effect on the determination of f_0 and the Q value, which gave us confidence of using the Lorentz function to fit the data.

TABLE 3-3

S_{11} Magnitude Peak Fitting Results Based on Lorentz Function using Different Fitting

Parameters

Frequency range (Hz)	Baseline	f_0 (kHz)	w	$Q(=f_0/w)$
345000 - 347200	Linear, D2	346.11	0.544	636
	Constant, D2	346.10	0.548	631
345300 - 347000	Linear, D2	346.11	0.544	636
	Constant, D2	346.10	0.549	630
345000 - 346800	Linear, D2	346.12	0.539	642
	Constant, D2	346.10	0.560	618
Average	Linear, D2	346.11 ± 0.007	0.542 ± 0.003	638 ± 5
	Constant, D2	346.10 ± 0	0.552 ± 0.007	626 ± 7

References

[1]   J. W. Yi, W. Y. Shih, and W. H. Shih, "Effect of length, width, and mode on the mass detection sensitivity of piezoelectric unimorph cantilevers," *Journal of Applied Physics*, vol. 91, pp. 1680-1686, 2002.

[2]   "Agilent 4395A Network/Spectrum/Impedance Analyzer Operation Manual," Agilent Technologies.

CHAPTER 4

DESIGN AND FEASIBILITY STUDY OF BIOSENSOR BASED ON MAGNETOSTRICITVE MICROCANTILEVER

4.1 Introduction

Based on the comparison of different AW devices, it is found that MEMS-based MCs provide a much better sensitivity in terms of the minimum detectable mass [1-7]. In other words, the MCs have the capability to detect a much smaller mass attachment. Additionally, MCs have many advantages over bulk AW devices, such as compact size and easy integration with analysis circuits. Therefore, it is interesting to employ MCs as a sensor platform for developing high performance biosensors [6-8].

As discussed in Chapter 1, much research has been conducted on MC-based biosensors. However, even though these MCs exhibit good performance and many advantages, they are facing some challenges in practical biological detection. Detection using silicon-based MCs requires complicated and expensive optical equipment. Compared to silicon-based MCs, the piezoelectric MCs are easy to actuate and sense. However, the piezoelectric MCs have much more complicated structure and exhibit a smaller Q value than silicon-based MCs. More importantly, both silicon-based and piezoelectric MCs face difficulties when they are operated in liquid [4, 5]. However, most of biological analyses are carried out in liquid medium.

In this chapter, a design of a novel type of MC, which is made of magnetostrictive

materials and referred to as magnetostrictive microcantilever (MSMC), is presented. The MSMC can be employed as a high performance biosensor platform, which is operated based on magnetostriction rather than piezoelectricity. The MSMCs inherit all the advantages of other MCs. For example, MSMC has the similar sensitivity as other MCs. Additionally, due to the magnetostrictive effect and the magnetic nature, the MSMC can be driven and sensed wirelessly. There is no physical connection between the MSMC sensor and the interrogation system. In our preliminary research, the MSMCs were fabricated and their resonance behaviors were characterized. It is experimentally found that the MSMCs exhibit high Q value and work well in either air or liquid. For MSMCs operated in air, a Q value of more than 500 was obtained. For MSMCs operated in water, the Q value reaches more than 30. The application of the MSMC as a high performance biosensor platform is demonstrated by detecting yeast and *Salmonella* cells in water.

4.2 Design and Operation Principle of MSMC as Biosensor Platform

4.2.1 Configuration and Operation Principle of MSMC

The configuration of the MSMC is shown in Fig. 4-1 (a). Similar to piezoelectric unimorph, the MSMC consists of two layers: one is active (magnetostrictive), and the other is inactive. The length of the magnetostrictive layer changes under an external magnetic field. This dimension change is restricted by the inactive layer, which causes the bending of the cantilever beam, as illustrated in Fig. 4-1 (b). Therefore, the bending oscillation of the cantilever can be actuated by an alternating magnetic field. Because of the magnetic nature of the magnetostrictive material, the oscillation of the cantilever beam results in an emission of a magnetic signal, which can be sensed/measured

wirelessly using a pick-up coil. That is, MSMC can be actuated and sensed without direct physical connections between the sensor and the interrogation device. Therefore, it allows developing a sensor for *in-situ* biological analysis. This is the principle advantage the MSMC offered over other MCs. Additionally, compared with piezoelectric MCs, MSMC has a simple structure and does not need to have electronic circuit on board, which greatly simplifies the fabrication process.
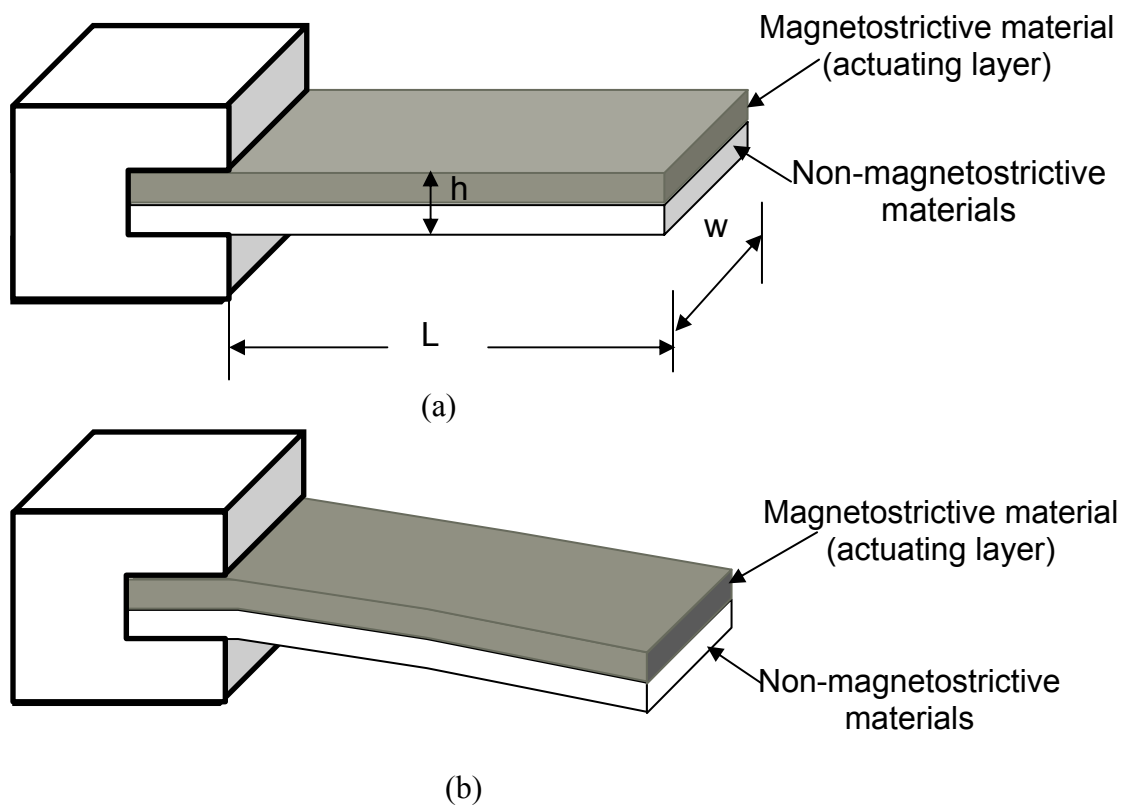
Fig. 4-1. Structure of the magnetostrictive microcantilever (MSMC), where L and W are the length and width of the cantilever respectively, while h is the thickness of the MSMC beam, including the magnetostrictive layer and the inactive layer. (a) MSMC under zero magnetic field; (b) MSMC under an external magnetic field.

The operating principle of a MSMC as a biosensor is similar to other MC sensor platforms. To form a biosensor, the surface of the MSMC is immobilized with the bio-receptor or bio-molecular recognition element. When the MSMC sensor is placed in the environment to be tested, the target species will be captured by the bio-receptor/recognition element. The captured species is a mass load for the MSMC, which results in a change in the resonance frequency. As described above, the oscillation of the MSMC can be actuated by a magnetic field and its resonance frequency can be detected by a pick-up coil. Therefore, as shown in Fig. 4-2, the presence of target species can be wirelessly determined by monitoring the shift in the MSMC sensor's resonance frequency.
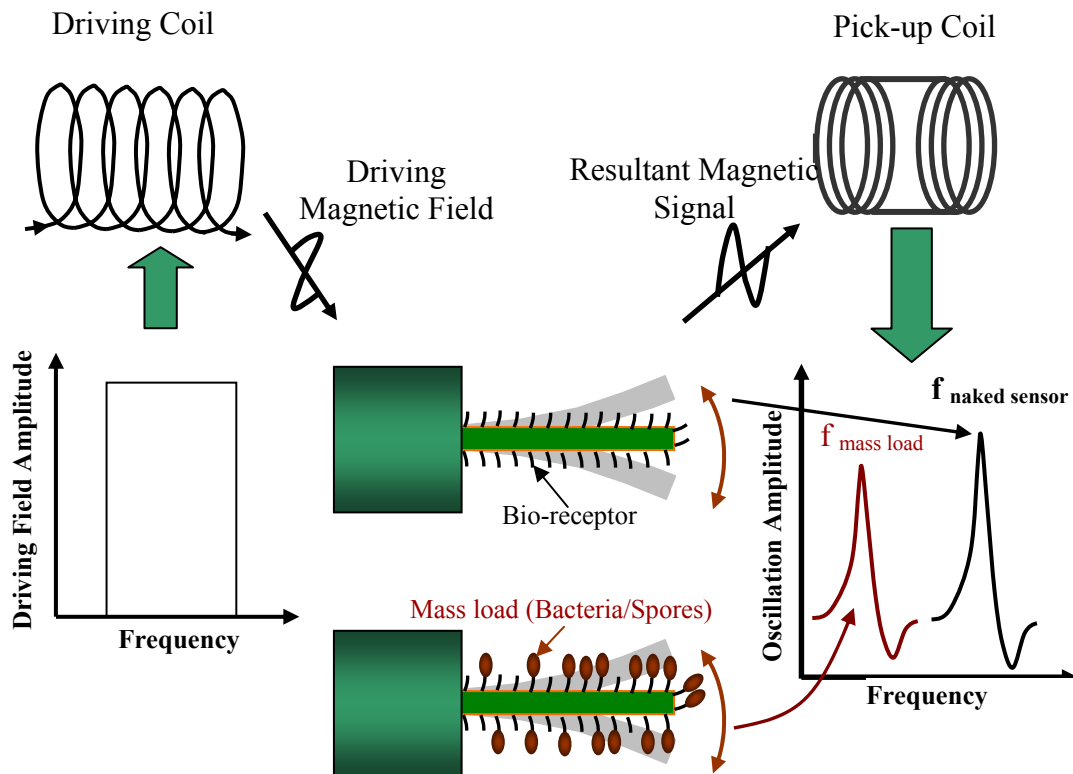
Fig. 4-2. Operating/detecting principle of the MSMC as a biosensor platform.

4.2.2 Natural Resonance Behavior of Magnetostrictive Microcantilever

4.2.2.1 Flexural (Bending) Resonance Frequency of Cantilever with One End Fixed

For a uniform cantilever beam (in the length of L, width of w and thickness of h) shown in Fig. 4-3, the wave equation of its flexural oscillation can be expressed as [9]:

$$\frac{\partial^2 \eta}{\partial t^2} + \frac{\hat{E}I}{\rho A} \frac{\partial^4 \eta}{\partial x^4} = 0 \tag{4-1}$$

where η is the flexural deformation of the beam at the point x, $\hat{E}$ and ρ are the apparent Young's modulus and equivalent mass density of the beam materials, respectively; A is the cross sectional area of the beam, and I is the moment inertia. For a rectangular beam of width w and height h, the A and I are given by [9]:

$$A = wh \tag{4-2}$$

$$I = \frac{1}{12} wh^3 \tag{4-3}$$

Under the assumption of a beam structure with $w >> h$, the apparent Young's modulus is given by [5]:

$$\hat{E} = \frac{E}{1 - \sigma^2} \tag{4-4}$$

where σ is the Poisson's ration and E is the Young's modulus of the beam material.
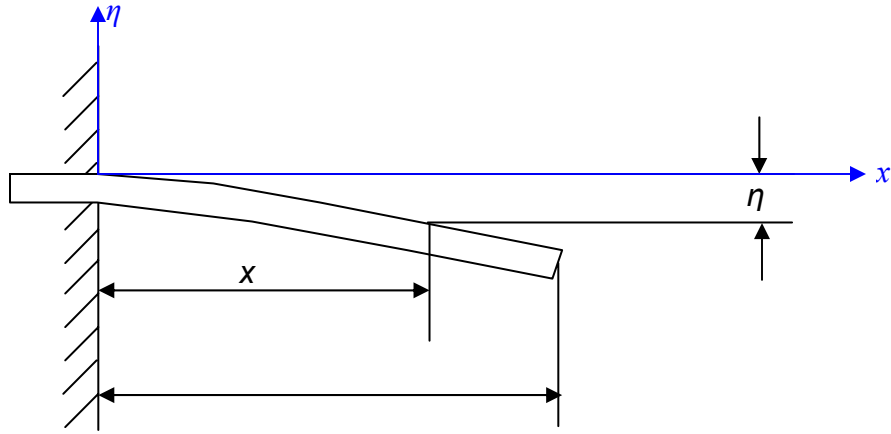
Fig. 4-3. Rectangular cantilever beam with a length of L, width of w and thickness of h, rigidly fixed at one end and free at the other.

For harmonic oscillations in Equation (4-1), the flexural deformation of the beam can be written as [9]:

$$\frac{\hat{E}I}{\rho A}\frac{\partial^4 \eta}{\partial x^4} - \omega_0^2 \eta = 0 \tag{4-5}$$

where ω_0 is the resonance frequency.

The general solution of the wave Equation (4-5) is [5]:

$$\eta(x) = c_1 \cos(\frac{\lambda}{L}x) + c_2 \sin(\frac{\lambda}{L}x) + c_3 \sinh(\frac{\lambda}{L}x) + c_4 \cosh(\frac{\lambda}{L}x) \tag{4-6}$$

where, c_1, c_2, c_3 and c_4 are the constants, and λ is the non-dimensional parameter; while [5]:

$$\left(\frac{\lambda}{L}\right)^4 = \frac{\rho A \omega_0^2}{\hat{E}I} \tag{4-7}$$

By considering the boundary conditions, we can obtain the resonance frequencies for

73

the flexural oscillations. For the cantilever beam rigidly fixed at one end and free at the other end, the boundary conditions are [5, 9]:

$$\eta(0) = 0, \ \left.\frac{d\eta(x)}{dx}\right|_{x=0} = 0, \ \left.\frac{d^2\eta(x)}{dx^2}\right|_{x=L} = 0, \text{ and } \left.\frac{d^3\eta(x)}{dx^3}\right|_{x=L} = 0 \qquad (4\text{-}8)$$

The first two boundary conditions are due to the fact that one end of the beam (at $x = 0$) is rigidly fixed. Since there is no shear force and moment acting at the free end of the beam (at $x = L$), the third and forth boundary conditions exclude any bending moment and torsion [5]. Based on Equation (4-6) and the boundary conditions, the characteristic equations for which the flexural oscillation of the beam is at resonance frequencies, is given by [5, 9]:

$$\coth\frac{\lambda}{2} = \tan\frac{\lambda}{2} \qquad (4\text{-}9)$$

$$\coth\frac{\lambda}{2} = -\tan\frac{\lambda}{2} \qquad (4\text{-}10)$$

The characteristic Eigenvalues of resonance oscillation can be obtained from Equation (4-9) and (4-10). Therefore, the resonance frequencies of natural oscillation can be determined by inserting Eigenvalues into Equation (4-7):

$$\omega_n = 2\pi f_n = \frac{\lambda_n^2}{L^2}\sqrt{\frac{\hat{E}I}{\rho A}} \qquad (4\text{-}11)$$

Combining Equation (4-2), (4-3), (4-4) and (4-11), the nth-mode flexural resonance frequency of a cantilever with one end clamped can be expressed as Equation (4-12):

$$f_n = \frac{\lambda_n^2}{2\pi\sqrt{12}}\frac{h}{L^2}\sqrt{\frac{E}{\rho(1-\sigma^2)}} \qquad (n=0, 1, 2, \ldots.) \qquad (4\text{-}12)$$

where the λ_n is the dimensionless n^{th}-mode Eigenvalue dependent on the vibration mode,

74

h and L are the thickness and length of the cantilever, while E, ρ and σ are the effective

Young's modulus, density and the Poisson's ratio of the beam material.

4.2.2.2 Determination of Eigenvalues for Flexural Resonance Oscillation

The characteristic Eigenvalues for bending resonance oscillation of a cantilever beam

with one end fixed can be obtained from Equation (4-9) and (4-10), which can be solved

graphically.
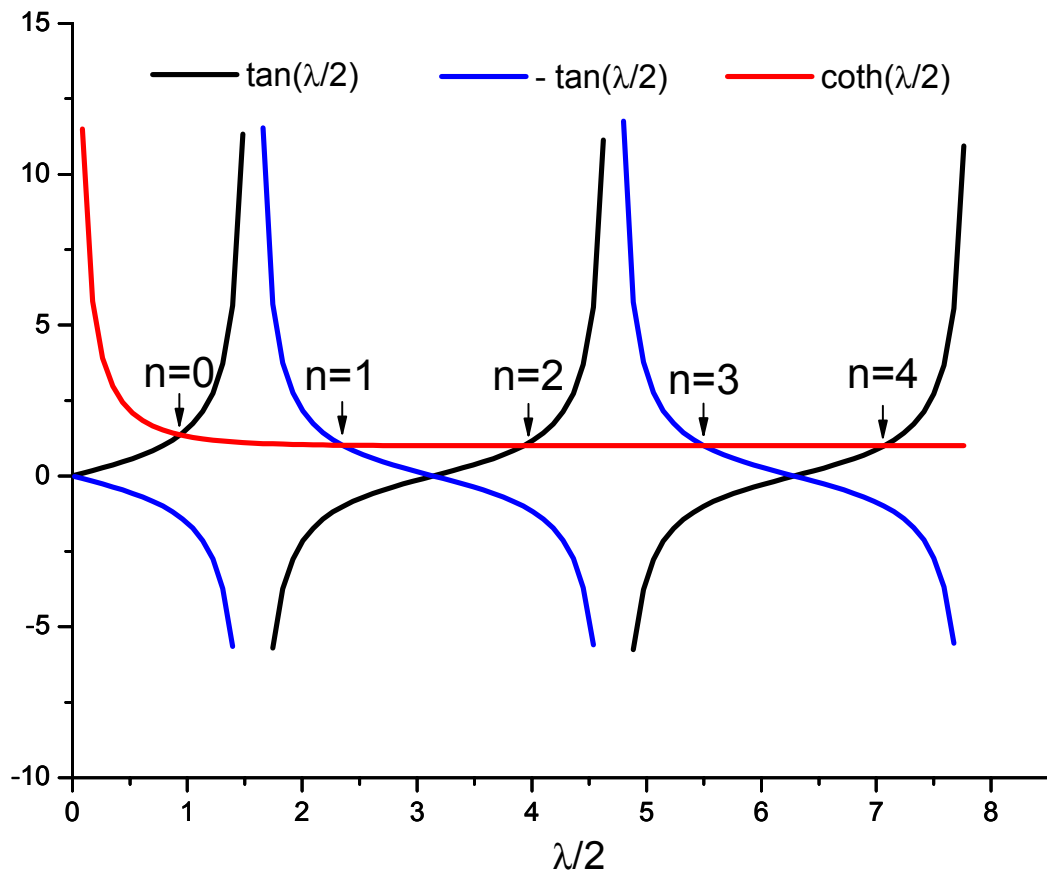
Fig. 4-4. Curves of function $\tan(\lambda/2)$, $-\tan(\lambda/2)$ and $\coth(\lambda/2)$. The Eigenvalues for

bending resonance oscillation of a cantilever beam with one end fixed can be graphically

obtained from the intersections of the functions.

Fig. 4-4 shows the curves of function $\tan(\lambda/2)$, $-\tan(\lambda/2)$ and $\coth(\lambda/2)$. The solutions of Equation (4-9) and (4-10) are the intersection points of function $\coth(\lambda/2)$ with function $\tan(\lambda/2)$ and $-\tan(\lambda/2)$. Therefore, Equation (4-9) and (4-10) can be graphically solved from Fig. 4-4. Table 4-1 lists the graphically obtained solutions of Equation (4-9) and (4-10), as well as the Eigenvalues for the first ten flexural resonance modes. Thus, the first ten resonance frequencies can be calculated based on these Eigenvalues.

TABLE 4-1

Graphically Obtained Eigenvalues for the First Ten Flexural Resonance Modes

Resonance mode	$\lambda_n/2$	λ_n	λ_n^2
n = 0	0.93755	1.87510	3.5160
n = 1	2.34705	4.69410	22.03457
n = 2	3.92738	7.85476	61.69725
n = 3	5.49777	10.99554	120.90190
n = 4	7.06858	14.13716	199.85929
n = 5	8.63938	17.27876	298.55555
n = 6	10.21018	20.42036	416.99110
n = 7	11.78097	23.56194	555.16502
n = 8	13.35177	26.70354	713.07905
n = 9	14.92257	29.84514	890.732382

4.2.3 Mass Sensitivity of MC & MSMC

A) Uniform Mass Load

If a mass load (Δm) is uniformly distributed on the surface of the microcantilever beam, as shown in Fig. 4-5 (a), the mass sensitivity of the cantilever can be expressed as [5, 10]:

$$S_{m,uni} = -\frac{\Delta f_n}{\Delta m} \cong \frac{f_n}{2M_e} \qquad (\Delta m << M_e) \qquad\qquad (4\text{-}13)$$

where M_e is the effective mass of the cantilever beam, f_n is nature resonance frequency

of the cantilever, and Δf is the shift in the resonant frequency due to the mass load (Δm).

Therefore, for a uniform mass load, the mass sensitivity of a MC can be written as:

$$\begin{aligned}
S_{m,uni} &= \frac{\lambda_n^2}{2\pi\sqrt{12}} \frac{1}{2wL^3} \sqrt{\frac{E}{\rho^3(1-\sigma^2)}} \\
&= \frac{\lambda_n^2}{4\pi\sqrt{12}} \frac{1}{wL^3} K
\end{aligned} \qquad\qquad (4\text{-}14)$$

where $K = \sqrt{\dfrac{E}{\rho^3(1-\sigma^2)}}$ is the material index, which is only related to the properties of

the cantilever beam material. The mass load Δm added here is assumed an ideal mass

load, which does not form a solid film rigidly bonded to the cantilever surface and change

the bending modulus of the cantilever [10]. Otherwise, it tends to increase the bending

modulus of the cantilever and thus its resonance frequency.
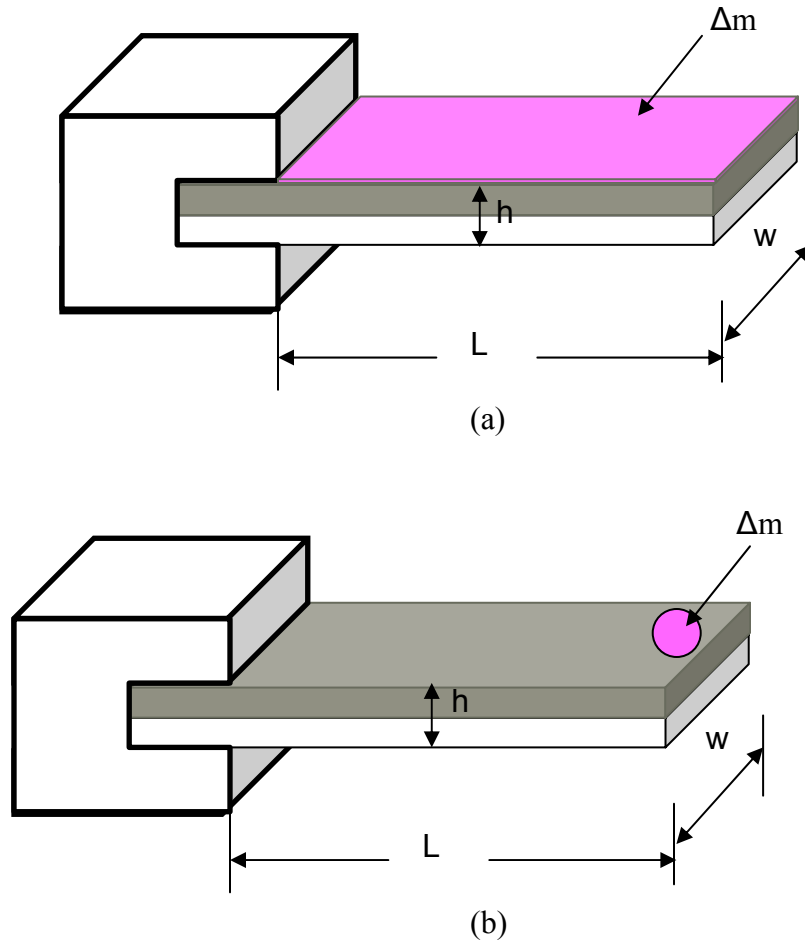
Fig. 4-5. MSMC (a) with a uniform mass load on the surface; and (b) with a point mass load at the cantilever tip.

B) Point Mass at the Tip

To calculate the shift in the resonance frequency due to a point mass (Δm) loaded at the free end of the cantilever (as shown in Fig. 4-5 (b)), we need to consider the mass (M_e) of the cantilever beam as the equivalent effective mass ($M_e^{'}$) at the tip of the

cantilever. For a rectangular beam, with w (width) $<< L$ (length), the effective mass at the cantilever tip is [10]:

$$M_e^{'} = 0.236 M_e = 0.236 \rho h w L \qquad (4\text{-}15)$$

Therefore, the shift (Δf_n) in the resonance frequency due to per unit loaded mass is:

$$S_{m,tip} = -\frac{\Delta f_n}{\Delta m} = \frac{f_n}{2M_e^{'}} = \frac{f_n}{0.472 M_e} \qquad (4\text{-}16)$$

Combing Equation (4-12) and (4-16), for a point mass loaded at the cantilever tip, the mass sensitivity can be written as:

$$\begin{aligned} S_{m,tip} &= \frac{\lambda_n^2}{2\pi\sqrt{12}} \frac{1}{0.472 w L^3} \sqrt{\frac{E}{\rho^3 (1-\sigma^2)}} \\ &= \frac{\lambda_n^2}{0.944\pi\sqrt{12}} \frac{1}{w L^3} K \end{aligned} \qquad (4\text{-}17)$$

Comparing Equation (4-14) and (4-17), for a given MC and mass load Δm, one can find that the S_m of a cantilever for Δm evenly distributed over the entire cantilever surface is only 23.6% of that for Δm at the tip. In other words, for the same mass load Δm, the location of Δm affects the Δf. The closer the Δm to the tip, the larger the change in Δf, thus the higher the S_m.

4.2.4 Comparison of Mass Sensitivity of MSMC and Other MCs

Equation (4-14) and (4-17) indicate that, given the material properties of the MC beam (constant K), the mass sensitivity of a MC increases with decreasing L & w, but is independent of h. Keeping the ratio of length (L) to width (w) as constant ($L = \alpha w$), the S_m of the MSMC only depends on its length. Therefore, Equations (4-14) and (4-17) become:

$$S_{m,uni} = \frac{\alpha \lambda_n^2}{43.508} \frac{1}{L^4} K \propto \frac{\alpha}{L^4}$$ (4-18)

$$S_{m,tip} = \frac{\alpha \lambda_n^2}{10.268} \frac{1}{L^4} K \propto \frac{\alpha}{L^4}$$ (4-19)

Therefore, if the size of the MC is reduced by a factor of ξ proportionally in all dimensions ($L_{reduce} = \xi L$, $w_{reduce} = \xi w$), the mass sensitivity of the MC will enhanced by a factor of ξ^{-4}. Therefore, the smaller the size of the MC, the higher the mass sensitivity.

The mass sensitivities shown in Equation (4-18) and (4-19) indicate that, given the dimensions of a MC, its mass sensitivity depends on the material index K of the cantilever beam. K is directly related to the combination of Young's modulus, density and Poisson ratio of the material. The MC which is made of a higher Young's modulus and a lower density material gives a higher value for K, and thus has a higher mass sensitivity.

Table 4-2 lists the mechanical properties of a commercially available magnetostrictive material [8] (Metglas[TM] 2826 MB, Honeywell, Morristown, NJ), piezoelectric materials [11], and silicon [12]. By using the material properties shown in Table 4-2 as effective Young's modulus, density and Poisson ratio, the mass sensitivities of MCs made of different materials can be compared. For silicon, the K value of 3.34 can be obtained. If two widely used piezoelectric ceramics (lead zirconate titanate (PZT)), PZT4 and PZT5A, are employed to make the MC, the K values of 0.41 and 0.36 are obtained, respectively. However, if the MC is made of Metglas[TM] 2826 MB, an amorphous alloy widely employed in magnetostrictive sensors, a K value of 0.55 is obtained. This means that for MC with the same dimensions, a MC made of Metglas[TM] 2826 MB exhibit higher mass sensitivity than a MC made of PZT.

80

TABLE 4-2

Mechanical Properties of a Commercially Available Magnetostrictive Alloy,

Piezoelectric Ceramics and Silicon [8, 11, 12].

	Metglas$^{\text{TM}}$ 2826 MB	PZT4	PZT5A	Si
Young's Modulus (GPa)	110	66	53	130
Density (Kg/m^3)	7.9×10^3	7.6×10^3	7.7×10^3	2.33×10^3
Poisson Ratio	0.5	0.31	0.31	0.28
K	0.55	0.41	0.36	3.34

Fig. 4-6 (a) shows the theoretical mass sensitivity calculated based on Equation (4-18) for MCs made of Metglas$^{\text{TM}}$ 2826 MB, PZT4, PZT5A and silicon. In Fig. 4-6 (a), the ratio of MCs' length to width is chosen as 5 ($\alpha = 5$). The mass sensitivities increase with the reducing lengths of MCs. The results in Fig. 4-6 (a) indicate that MSMC has a similar mass sensitivity as other MCs. For MCs with the same dimensions, the MCs made of Si exhibit the highest S_m due to the high K value of Si, while the mass sensitivity of the MSMC made from Metglas$^{\text{TM}}$ 2826 MB is higher than that of PZT MCs.

Equation (4-18) and (4-19) indicate that the location of the mass load affects the S_m of MCs. The theoretical S_m of MSMC made of Metglas$^{\text{TM}}$ 2826 MB was calculated based on Equation (4-18) and (4-19), and is shown in Fig. 6-4 (b), where the black line is the S_m for uniform mass load (Equation (4-18)), and the red line is the S_m for mass load at the tip of the cantilever (Equation (4-19)). The results revealed that, for the same mass load, larger change in resonance frequency can be obtained if the mass load is closer to the tip of the cantilever beam.
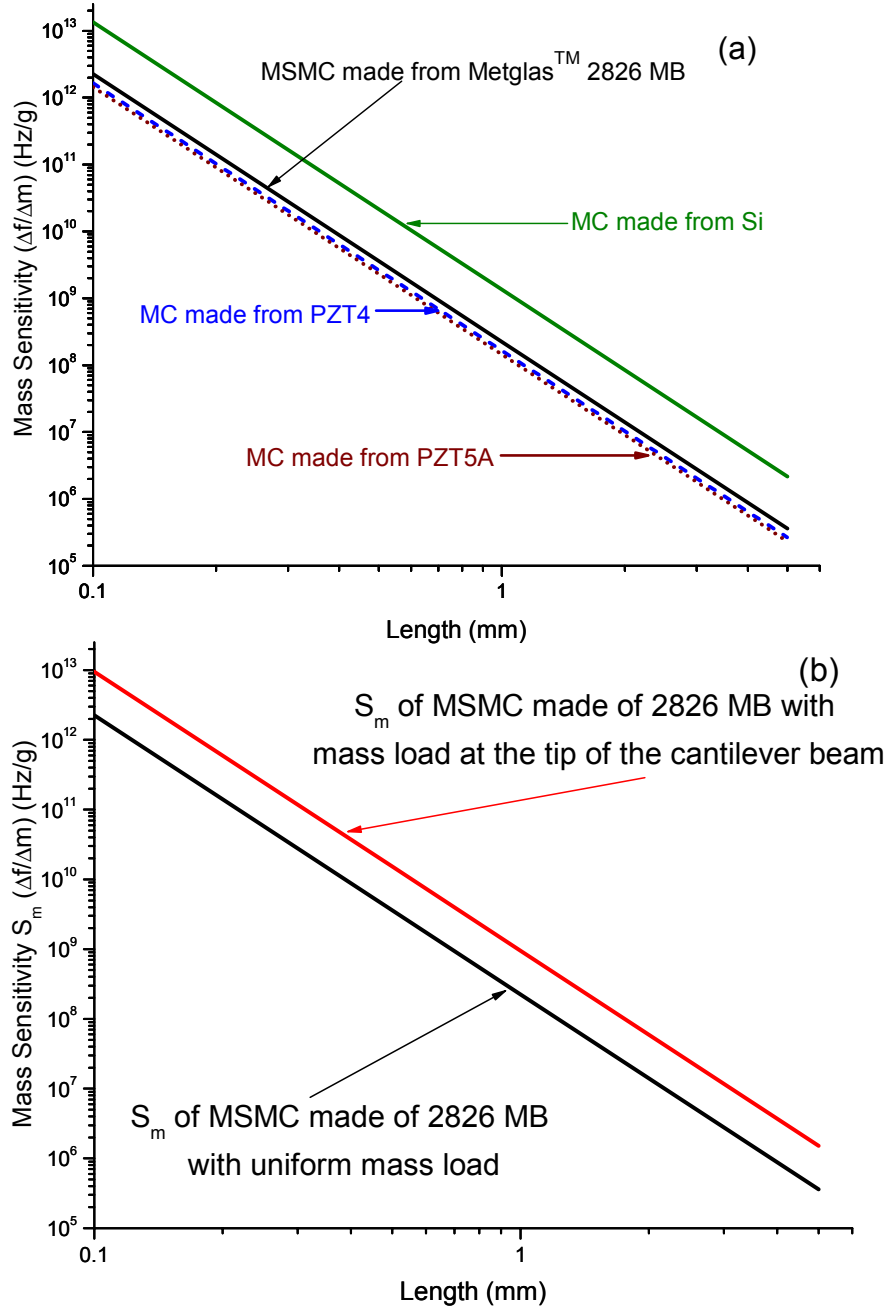
Fig. 4-6 (a) Theoretical mass sensitivity calculated based on Equation (4-18) for MCs made of Metglas^TM 2826 MB, PZT4, PZT5A, and Si. The material properties used in the calculation are listed in Table 4-2, while the ratio of MCs' length to width is chosen as 5. (b) Theoretical mass sensitivity calculated based on Equation (4-18) and (4-19) for MCs made of Metglas^TM 2826 MB.

82

4.2.5 Comparison of MSMC with Current MCs

The MSMC exhibits many advantages compared with Si-based and piezoelectric-based MCs. Interrogated through magnetic field, MSMC is a wireless sensor platform. Therefore it can be used to develop sensors for *in situ* and *in vivo* detections. Additionally, since there is no physical connection required between the MSMC sensor and the interrogation system, the MSMC has a much simpler structure than piezoelectric-based MCs. More importantly, it is experimentally found that MSMCs exhibit a higher Q value and works well in liquid. This is a crucial feature for biosensor platforms since most of real-time biological analyses take place in liquid environments. The summary of the comparison of MSMC with current MCs is listed in Table 4-3.

TABLE 4-3

Comparison of Different Microcantilever-based Sensor Platforms

Characteristics	Silicon-based	Piezoelectric-based	MSMC
Actuation	Mechanical (separated bulk system)	Electrical (on-broad, wire connected)	Magnetically (wireless, no connection)
Transduction	Optical (separated bulk system)	Electrical (on-broad circuit)	Magnetically (wireless, no connection)
Operate in air	Yes	Yes	Yes
Operate in insulate liquid	Difficult	Difficult (low performance)	Works well (high performance)
Operate in conductive liquid	Difficult	Very difficult	Works well (high performance)
Q value	High (> 100 in air) (~ 10 in liquid)	Low (≤100 in air) (<10 in liquid)	Very high (~ 500 in air) (~ 30 in liquid)
Structure	Simplest	Complicated	Simpler
Fabrication	Easy	Difficult	Easy
Overall sensitivity	High	Low	High
Array-Actuation	Very difficult (individually)	Difficult (each cantilever needs a driving circuit)	Easy (one driving system can drive all cantilevers at the same time)
Array-Transduction	Very difficult (individually)	Difficult (each cantilever needs analyzing circuit)	Easy (one circuit can collect the signal from all cantilevers at the same time)

4.3 Experimental

4.3.1 Fabrication of MSMCs

In this research, the unimorph type MSMCs were fabricated. The active layer is a commercial magnetostrictive material, Metglas^{TM} 2826 MB ribbon from Honeywell (Morristown, NJ), while the inactive layer is a copper layer. The material properties of the Metglas^{TM} ribbon are listed in Table 4-2. The Metglas^{TM} ribbon was polished down to a 20 μm thickness using 2000# polish paper, and then a copper (Cu) layer, 10 um in thickness, was deposited by magnetron DC sputtering. To increase the adhesion between Metglas^{TM} and copper, prior to sputtering the copper layer, a chromium (Cr) thin film of 100 nm in thickness was deposited on the polished ribbon by magnetron RF sputtering. Strips with different lengths and widths were cut from the Metglas^{TM}/copper film. The MSMCs, in lengths from 2 mm to 5 mm, were obtained by clamping the strip at one end using a plastic holder made of poly(methyl methacrylate).

4.3.2 Characterization of Resonance Behavior of MSMC

In this research, the resonance behaviors of MSMCs were characterized using the setup A described in Chapter 3. The MSMC was put into a sample chamber that was placed inside of the Helmholtz coil. In this study, a DC magnetic field of 20 Oe was employed. The AC field, which is swept over a broad frequency range, has amplitude less than 3.2 Oe. The magnetic signal emitted from the MSMC was detected by the pair of home-made pick-up coils. The output potential signal of the pick-up coil was measured using a lock-in amplifier (SRS830, Standford research systems, Sunnyvale, CA). The lock-in amplifier has two output signals: amplitude and phase. In this research, the

phase signal, as used to determine the resonance frequency of piezoelectric MCs [13], was used to characterize the resonance behavior of MSMCs. To determine the resonance frequency and Q value of MSMCs, the measured phase data were fitted using the Lorentz function as described in Chapter 3.

The resonance behaviors of the MSMCs with different dimensions were characterized. The performance of MSMC in liquid was studied by characterizing and comparing the resonance behaviors of the MSMCs in air, water and ethanol.

4.3.3 Characterization of Mass Sensitivity of MSMCs

The mass sensitivity of MSMC was characterized by measuring the resonance spectra of the cantilever with different mass loads. In this research, a small piece of tape, in the size about 0.5 mm x 1 mm, was stuck on the free tip of the MSMC as the mass load. The shifts in the resonance frequency of the MSMC with different the mass loads were used to determine the mass sensitivity.

4.3.4 Demonstration of In-situ Yeast Cells Detection Using the MSMC Sensors

In-water yeast cell detection was employed to demonstrate the feasibility of MSMCs as biosensor platforms. In the experiment, the surface of the MSMC was coated with a thin layer of poly-L-lysine. The poly-L-lysine offers a positively charged environment to which negatively charged yeast cells are attracted. Yeast cells suspensions were prepared by suspending bakers yeast (*Saccharomyces cerevisae*, Fleischmann's Yeast, obtained from a local store) in de-ionized water at room temperature. Two MSMCs were employed in this study. The MSMC in size of 2.8 mm x 1.2 mm x 30 μm was used to detect yeast cells in suspension with the concentration of 1 mg/ml, while an MSMC in

size of 2.6 mm x 1.1 mm x 30 μm was employed to do the test in yeast suspension with a concentration of 2 mg/ml. To do the real-time test, the whole MSMC was immersed into the yeast suspension, and then its resonance frequency was monitored and recorded as a function of time. After the test, the MSMCs were observed under an optical microscope in a Probe station (Signatone probing division, Gilroy, CA) for viewing the cells bonded on the surface of the MSMCs.

4.3.5 Detection of Bacillus Anthracis Spores Using MSMC Biosensor

MSMC biosensors were employed to detect *Bacillus anthracis* spores in water. In the study, the phage agent for *Bacillus anthracis* spores was immobilized on the MSMC surface as the biological receptor. The phage displaying the peptide EPRLSPHS on the surface was selected from the f8/8 landscape phage library and provided by the Department of Pathobiology of Auburn University. To immobilize the phage, a thin Au layer ($\sim$ 400 nm) was sputtered on both sides of the MSMC to protect against corrosion and provide a favorable binding site for phage, while a chromium layer in thickness of 100 nm was deposited between the Au layer and the MSMC for adhesion purposes. The MSMC with a freshly sputtered Au layer was immersed into 1.5 mL of phage culture with the concentration of 2.6 x 10^{12} viruses/mL for 80 minutes. And then the MSMC was rinsed three times using sterile distilled water. The MSMC was now immobilized with phage on all surfaces to form a phage based biosensor and ready for spore detection.

The detected agent used in this study was the spores with nonpathogenic Sterne strain of *B. anthracis* provided by the Department of Pathobiology of Auburn University. The MSMC/phage biosensor was put into the test chamber containing increasing concentrations (5 x 10^4 to 5 x 10^8 spores/mL) of *B. anthracis* suspensions.

And then the shifts in the MSMC's resonance frequency were monitored and recorded as a function of time. The data was recorded at 5-minute intervals. For each concentration of spore suspension, the data were recorded for 2 hours.

4.4 Results and Discussions

4.4.1 Resonance Behavior of MSMC in air

A typical resonance behavior of an MSMC in air at room temperature is shown in Fig. 4-7, where an MSMC in size of 4 mm x 1.5 mm x 30 μm was utilized. For this MSMC, the first six resonance modes were presented. Based on the data shown in Fig. 4-7, the resonance frequencies are 1.129, 7.877, 22.178, 41.168, 50.157 and 69.466 kHz, for fundamental (n = 0) to 5th harmonic modes, respectively. The Q values for fundamental to 5th harmonic modes are 216, 334, 463, 516, 422 and 419 respectively. The Q values of the MSMC obtained here is much higher than that (30~100) of most currently existing regular rectangular microcantilevers [5, 14].
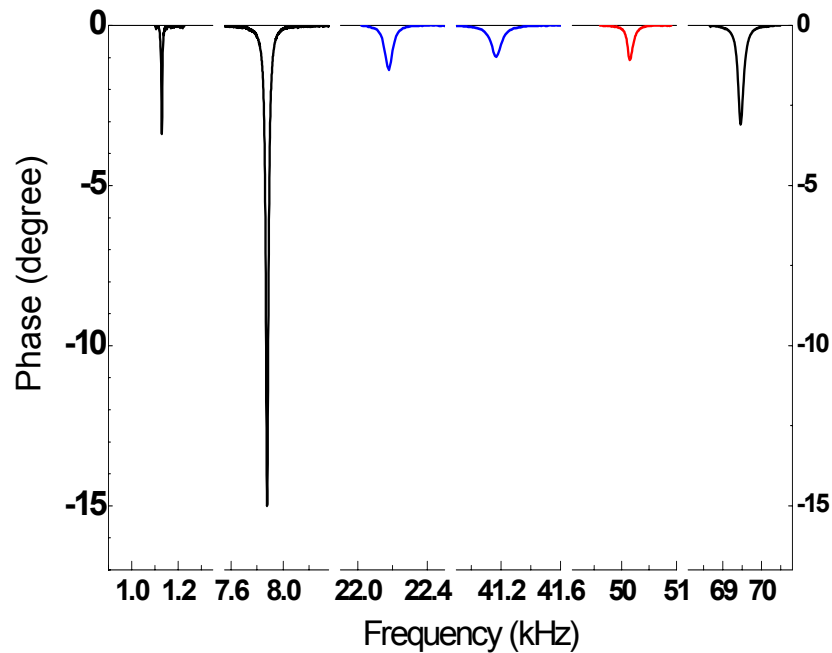
Fig. 4-7. The phase difference between the driving magnetic field and the magnetic signal from a MSMC. The size of the MSMC is 4 mm x 1.5 mm x 30 μm. For this MSMC, the first six harmonic vibration modes were observed.

It is interesting to find that the Q value of fundamental harmonic mode (n = 0) for the MSMC studied here is lower than that of its higher harmonic modes. This is consistent with the results obtained from the ZnO nanocantilever, where the ZnO nanowire is attached to an electrochemically sharpened tungsten (W) wire using epoxy [15]. However, the results obtained from piezoelectric cantilevers, which were rigidly bonded onto a metal holder, showed that the fundamental harmonic peak has the highest Q value [10, 16]. A theoretical simulation for cantilevers with rigid clamping indicates that the Q value is lower for higher modes [17]. Therefore, considering the bonding condition, the fact that a higher Q value observed for higher modes in the MSMCs studied here and the

ZnO nanocantilevers is due to the fact that the clamping condition is not strong, which is known as anchor loss [18]. The experimental data indicate that the anchor loss has a stronger influence on fundamental mode than higher modes. One can conclude that if the MSMC is rigidly clamped onto a stiff holder, the Q value of more than 500 would be expected, since the Q value of higher harmonic peaks reaches more than 500.

Based on Equation (4-12) and the Eigenvalues of different flexural vibration modes listed in Table 4-1, the ratios of the nth-mode resonance frequency to the fundamental resonance (n = 0) frequency for the first to third mode, and the ratios of the nth-mode resonance frequency to the first resonance (n = 1) frequency for the second and third mode were calculated. The results were listed in Table 4-4. From the experimental data shown in Fig. 4-7, the corresponding resonance frequency ratios were also calculated, and listed in Table 4-4. Comparing the theoretical and experimental results, it is found that the ratios of the first, second and third-mode resonance frequency to fundamental resonance frequency is 6.977, 19.644, and 36.464, respectively, which are slightly higher than that obtained from Equation (4-12). The difference between the theoretical and experimental results is about 10 %. On the other hand, the ratios of the second-mode resonance frequency to the first-mode resonance frequency (which is 2.82), as well as the ratio of the third-mode resonance frequency to the first-mode resonance frequency (which is 5.23) are very close (the difference is less than 5%) to the theoretical results. These results indicate that the anchor loss has a stronger influence on the resonance frequency of the fundamental mode, which is consistent with the conclusion based on the Q value.

90

TABLE 4-4

Theoretical/experimental Resonance Frequency Ratios of the nth-mode Resonance

Frequency to the Fundamental Resonance (n = 0) Frequency for the First to Third Mode,

and the Ratios of the nth-mode Resonance Frequency to the First Resonance (n = 1)

Frequency for the Second and Third Mode.

	Theoretical value	Experimental value	Difference
f_1/f_0	6.267	6.977	11%
f_2/f_0	17.548	19.644	12%
f_3/f_0	34.386	36.464	6%
f_2/f_1	2.80	2.816	0.6%
f_3/f_1	5.487	5.226	5%

4.4.2 Resonance Frequency Changing with the MSMC Dimensions

Based on Equation (4-12), given material properties and the thickness of the MSMC, the flexural resonance frequency is expected to linearly increase with $1/L^2$. The experimentally obtained resonance frequencies of the MSMCs with different lengths and the same thickness (30 μm) are plotted versus $1/L^2$ in Fig. 4-8, where the frequencies of fundamental (n = 0) and the first (n = 1) resonance mode are presented as solid triangles and solid squares, respectively. As expected from Equation (4-12), the experimental frequencies of MSMCs are linearly dependent on the $1/L^2$.

The theoretical resonance frequencies of the MSMCs were calculated based on Equation (4-12). For the MSMCs investigated here, the E, ρ, and σ should be the effective modulus, effective density and effective Poisson's ratio of the Metglas™/copper film. The density and the mechanical properties of the Metglas™ were listed in Table 4-2.

Considering the thickness of Metglas™ (20 μm) and the copper (10 μm) as well as the density of Metglas™ (7.9 g/cm^3) and copper (8.9 g/cm^3), the effective density of 8.23 g/cm^3 could be used for the MSMC. Regarding the Young's modulus: although the bulk copper has a Young's modulus of 130 GPa, it was reported that the Young's modulus of sputtered copper thin film with a thickness about 1 μm is about 110 GPa [19]. Therefore, we assume the effective E of 110 GPa for the MSMCs. The Poison ratio of bulk copper and Metglas™ is 0.34 and 0.5, respectively. Based on the thickness of copper and Metglas™ film, the effective Poison's ratio of 0.45 is employed. The resonance frequencies of the MSMCs with different lengths were simulated using Equation (4-12) with the effective properties and $h = 30$ μm, and are shown in Fig. 4-8 as solid lines. The results indicate that the consistency between the experimental data and the theoretical calculation.
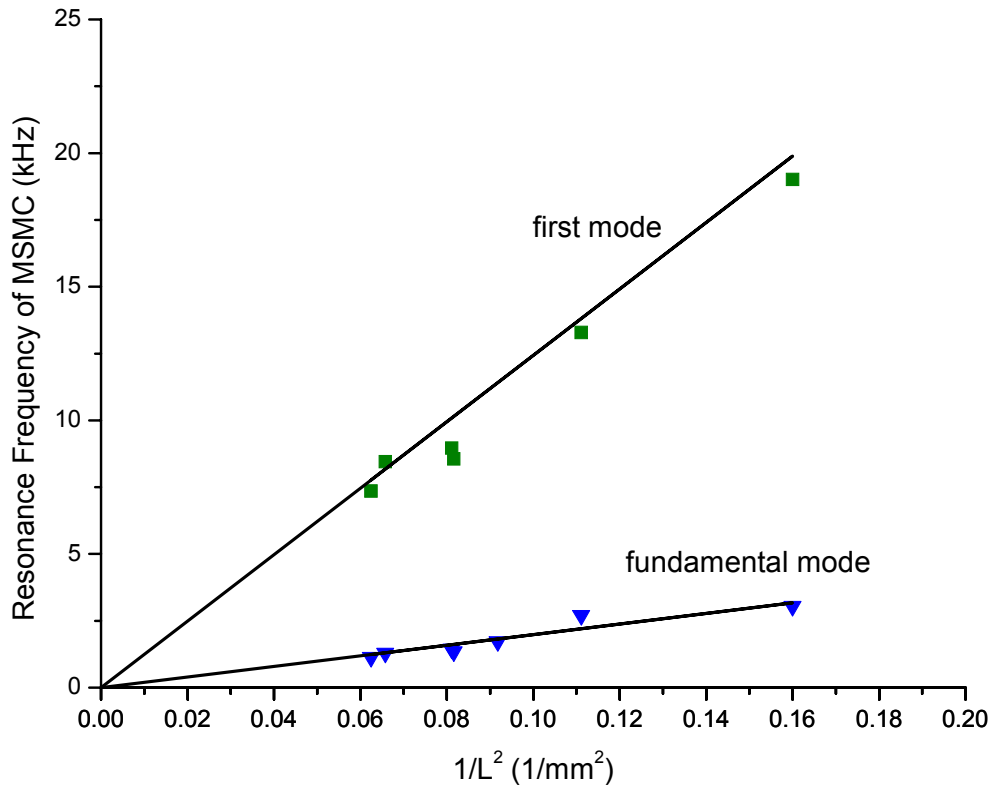
Fig. 4-8. Resonance frequency of the fundamental and the first flexural mode vs $1/L^2$ for the MSMCs with a thickness about 30 μm, where L is the length of the MSMCs. The solid triangles and solid squares are the experimental results for the fundamental and the first flexural mode, while the solid lines are results of theoretical calculation.

4.4.3 Stability of the MSMC

In the biosensor application, the resonance frequency shift due to the mass load is the output of the MSMC-based device. Therefore, a big concern of the sensor performance is how stable the resonance frequency is. That is, whether or not the resonance frequency would drift with time. The stability for the MSMC was studied by monitoring its fundamental and first harmonic resonance frequency in air over 24 hours. An MSMC, in

size of 3.05 mm x 1 mm x 30 μm, was employed in the experiment. The driving frequency was set close to its fundamental resonance frequency to keep the MSMC vibrating, while its resonance frequencies of the fundamental and first mode were recorded at different duration times. During the experiment, the temperature was controlled at 25 ± 0.2 $^{\circ}$C, while the humidity changed from 13% to 21%. A set of the results are shown in Fig. 4-9, where the solid squares are the experimental results, and the average of the resonance frequency is given by the solid straight line. Based on the results shown in Fig. 4-9, the average of the resonance frequencies for the fundamental and first harmonic mode are 2258.41 Hz and 14206.75 Hz, respectively. Over 24 hours, the standard deviation of the resonance frequency is 0.288 Hz for the fundamental harmonic resonance and 2.51 Hz for the first harmonic resonance mode. The drift percentage is about 0.01% and 0.017% for the fundamental and first mode, respectively. To estimate the error caused by peak fitting, Table 4-5 and 4-6 shows the resonance frequencies of this MSMC obtained from fitting results using Lorentz function over different frequency ranges for the fundamental and first mode, respectively. The results indicate that about 0.15 Hz and 0.05 Hz variation in the measured fundamental and first resonance frequencies, respectively, are caused by fitting error. Also, considering the variation of the environment condition, the MSMC exhibits good stability. In real applications, any experimental error caused by a frequency drift can be minimized by resonance frequency calibration before use, while the effect of the change in environment can be compromised by employing a sensor array with a reference sensor.
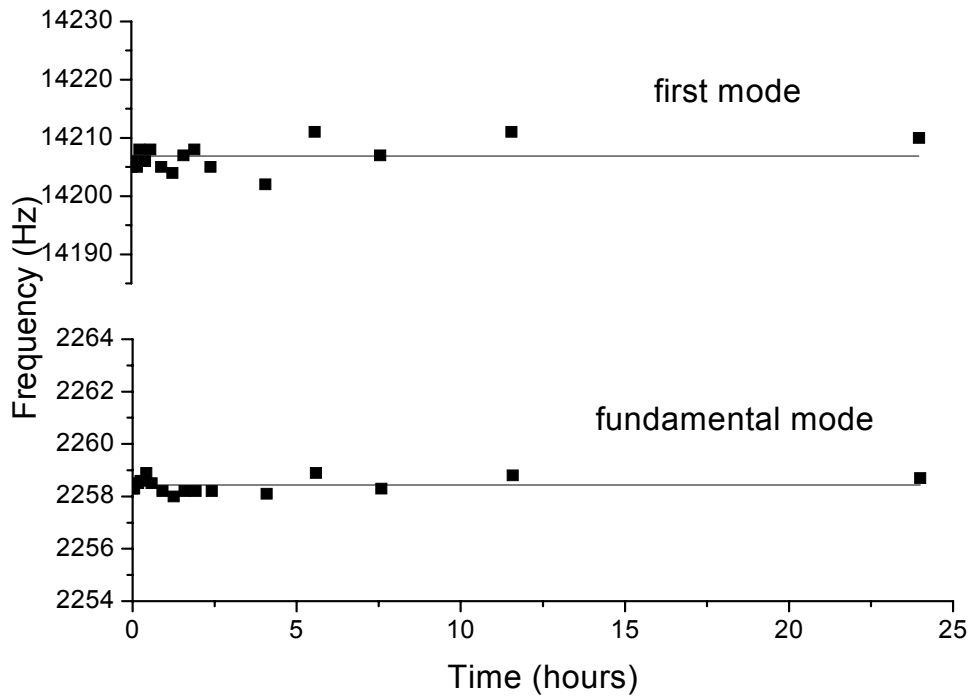
Fig. 4-9. Resonance frequency of a MSMC with size of 3.05 mm x 1 mm x 30 μm measured in air over 24 hours.

TABLE 4-5

Fitting Results of the Fundamental Mode Resonance Frequency Based on Lorentz Function over Different Frequency Ranges for the MSMC Used in Stability Study

Frequency range (Hz)	Baseline	f_0 (Hz)
2200 ~ 2350	Linear, D2	2258.5
2225 ~ 2300	Linear, D2	2258.4
2240 ~ 2280	Linear, D2	2258.2
Average	Linear, D2	2258.4 ± 0.15

TABLE 4-6

Fitting Results of the First Mode Resonance Frequency Based on Lorentz Function over

Different Frequency Ranges for the MSMC Used in Stability Study

Frequency range (Hz)	Baseline	f_0 (Hz)
14100 ~ 14300	Linear, D2	14205.2
14125 ~ 14275	Linear, D2	14205.1
14160 ~ 14260	Linear, D2	14205.0
Average	Linear, D2	14205.1 ± 0.05

4.4.4 MSMC Performance in Liquid

Since most of the biological analyses are carried out in the liquid environments, the performance of biosensors in liquid is very important for real-time or *in-vivo* detection. To study the performance of the MSMC in liquid, the resonance behavior of an MSMC, in size of 3.3 mm x 1 mm x 30 μm, was characterized in air, distilled water and ethanol. When measuring the resonance frequencies of the MSMC in liquid, the whole device was immersed into the distilled water or ethanol. The resonance spectra of the fundamental and first mode of this MSMC in different media are shown in Fig. 4-10 (a) and (b), respectively. In the liquid media, the oscillating cantilever beam has to push the surrounding liquid, which acts as induced mass. Also, the viscous drag of the liquid adds additional force on the cantilever beam. Therefore, the resonance frequency, signal amplitude and the Q value of the MSMC decrease due to the dampling effect caused by the surrounding liquid. Based the results shown in Fig. 4-10, the performance of this

MSMC is summarized in Table 4-7. For this MSMC, whose Q value is 191 and 265 for the fundamental mode and the first mode, respectively, when operated in air, it is experimentally found that the Q value is 19 and 38 for the fundamental and the first mode respectively when it is operated in water, and 9 and 27 for the fundamental and the first mode respectively when it is operated in ethanol. Considering that other cantilevers in aqueous solution rarely have a Q value above 10, the Q value of the MSMC in water is clearly higher than that of the other microcantilevers [5].
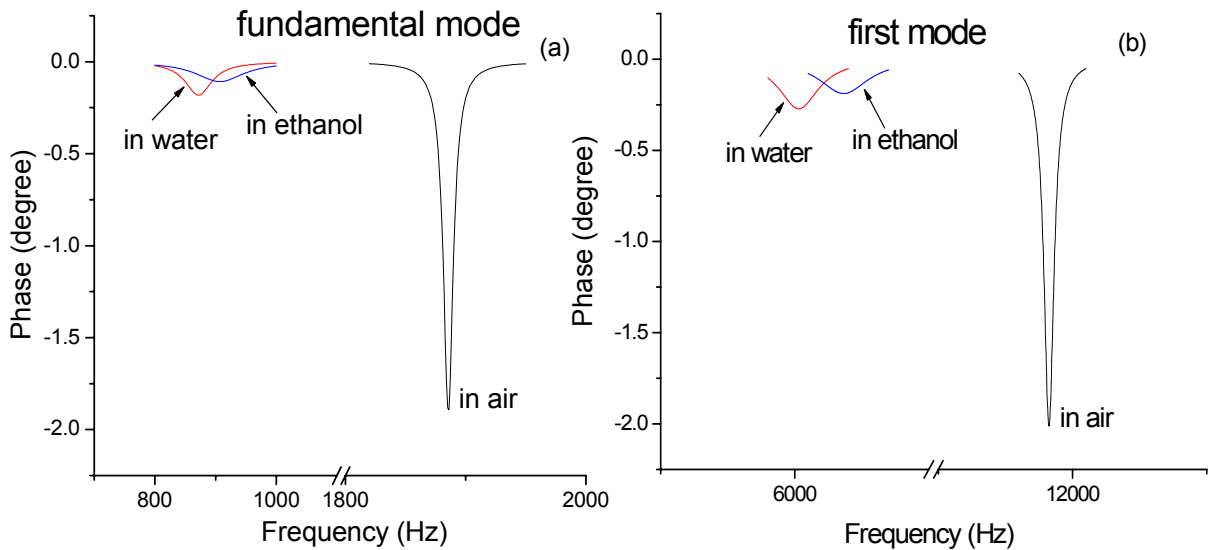
Fig. 4-10. MSMC performance in liquid. (a) Fundamental mode resonance spectra for a MSMC in different media. (b) First flexural mode resonance spectra for a MSMC in different media.

TABLE 4-7

MSMC Performance in Liquid

	fundamental harmonic			first harmonic		
	air	water	ethanol	air	water	ethanol
Resonance frequency (Hz)	1885	871	907	11912	6915	6182
Q value	191	16	9	265	38	27

According to the literature, the viscosity of water and ethanol is 0.89×10^{-3} kg/m•s and 1.08×10^{-3} kg/m•s at room temperature, respectively [20]. The densities of water and ethanol are 1×10^{3} kg/m^3 and 0.806×10^{3} kg/m^3, respectively [21]. Clearly, the Q value of MSMC reduces with the increasing viscosity of the liquid. One may notice that although the Q value of the MSMC in water is higher than that in ethanol, the resonance frequency of this MSMC is lower in water. The reason behind this phenomenon may be that the density of water is higher than that of ethanol, which causes higher induced mass and bigger decrease in the resonance frequency of the MSMC. This indicates that although both the viscosity and density of the liquid affect the resonance frequency and Q value of the MSMC, the density has a stronger influence on the resonance frequency and the viscosity has a stronger effect on the Q value.

4.4.5 MSMC Array

In sensor applications, an array of sensors is highly desired, since a sensor array has many advantages over individual sensors. The change in the environment, such as temperature, varies the properties of the material, and thus affects the output resonance frequency of the device. This effect can be   compromised by employing a sensor array

that includes reference sensors. Additionally, by coating sensors with different recognition elements, a sensor array can detect multiple targets simultaneously. For current MCs, a sensor array is difficult to operate. To form a Si-based MC array, each MC requires an optical system for sensing; while for piezoelectric MC array, individual electric circuit for operating each MC is needed.

As wireless sensors, arrays of MSMCs can be easily formed, and actuated/sensed by a single scan. Fig. 4-11 shows a MSMC array consisting of three MSMCs: MSMC1 (3.5 mm x1.3 mm x 30 μm), MSMC2 (3.3 mm x 1.3 mm x 30 μm), and MSMC3 (2.5 mm x 1.2 mm x 30 μm). As shown in Fig. 4-11, using the same setup for measuring single MSMC, the MSMC array can be driven and sensed by a single scan.
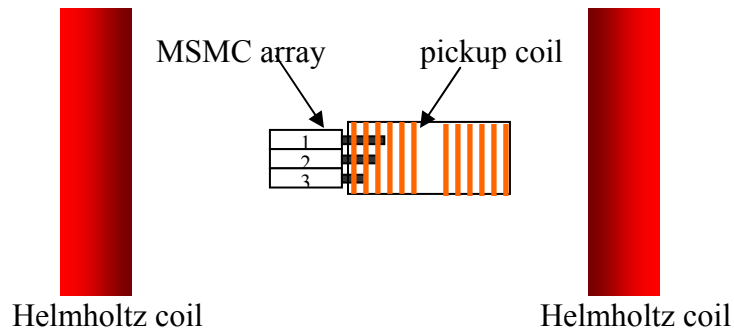
Fig. 4-11. Scheme of a MSMC array characterized using setup A.

Fig. 4-12 shows the spectrum of this MSMC array measured by a single scan. Three resonance peaks were observed in the spectrum. The resonance frequencies of the three peaks are 1.35, 1.73, and 3.02 kHz, which are corresponding to the fundamental resonance frequencies of MSMC1, MSMC2 and MSMC3, respectively. The results indicate that MSMC array can be easily formed and characterized.

99
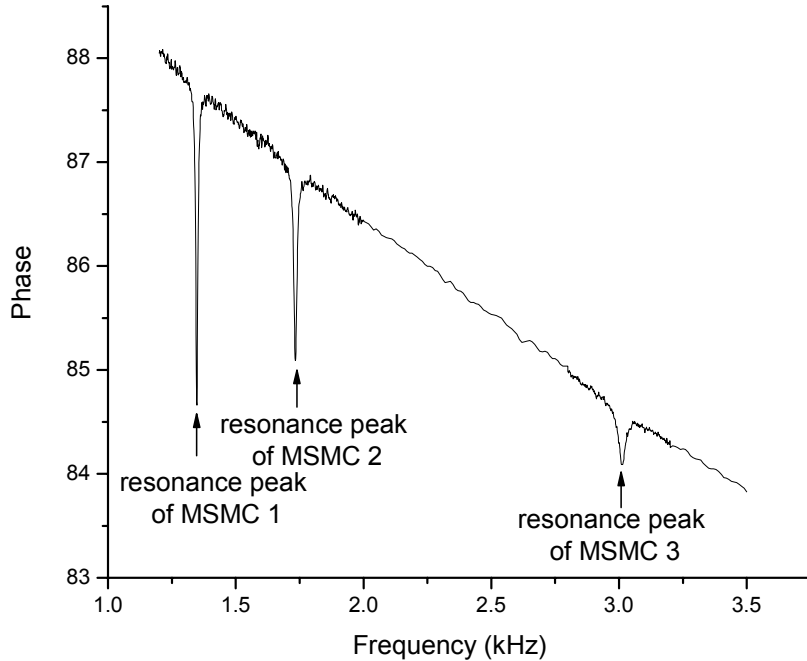
Fig. 4-12. Spectrum of a MSMC array consisting of three MSMCs.

4.4.6 Characterization of the Mass Sensitivity of MSMC

The mass sensitivity of the MSMC was characterized by measuring the resonance spectrum with different mass loads, where the mass load is a small piece of tape, in the size about 0.5 mm x 1 mm, attached at the tip of the MSMC. The resonance frequency shifts to a lower frequency with a mass load. One set of experimental results for determining the mass sensitivity of the MSMC is shown in Fig. 4-13, where an MSMC with a size of 4 mm x 1.2 mm x 30 μm was used. The fundamental and first harmonic resonance spectra of this MSMC with different mass loads are shown in Fig. 4-13 (a) and (b), respectively. With the mass load increased up to 0.306 mg, a 295 Hz shift for fundamental harmonic resonance and an 869 Hz shift for first harmonic resonance were observed. The shift in the resonance frequency versus mass load is plotted in Fig. 4-13 (c).

100

Based on the data shown in Fig. 4-13 (c), a mass sensitivity of 1003 Hz/mg and 2577 Hz/mg was obtained for fundamental and first harmonic modes respectively.
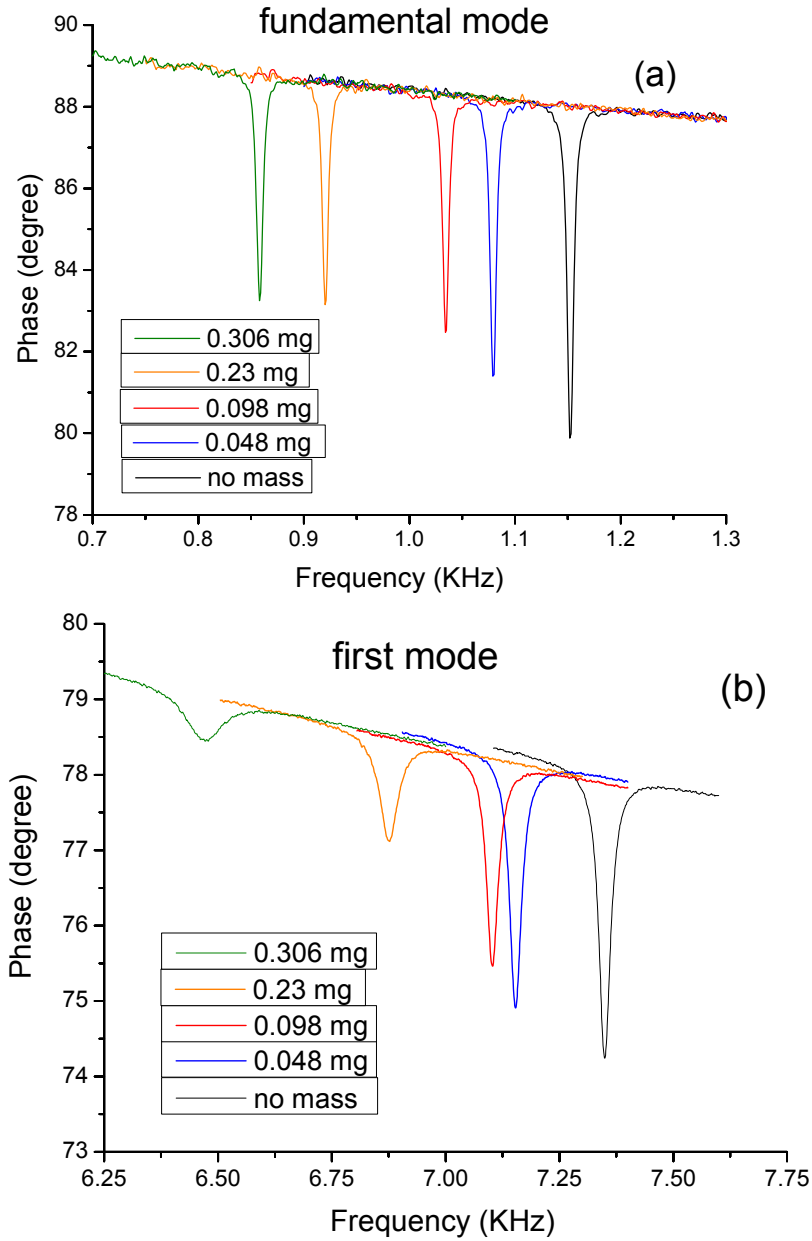
Fig. 4-13. S_m characterization of an MSMC (4 mm x 1.2 mm x 30μm): (a) The fundamental harmonic mode resonance spectra for the MSMC with different mass loads; (b) The first harmonic mode resonance spectra for the MSMC with different mass loads.
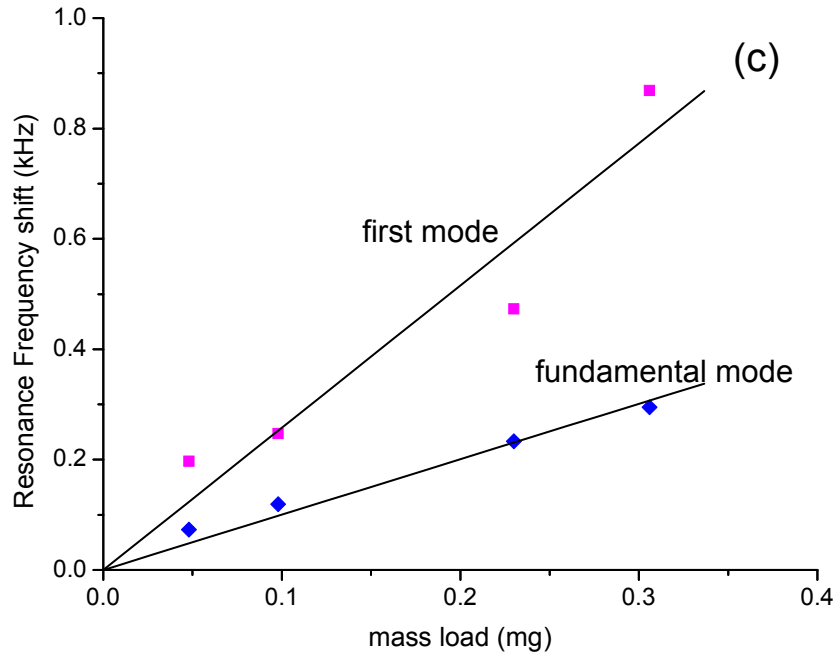
Fig. 4-13. Mass sensitivity characterization of an MSMC (4 mm x 1.2 mm x 30 μm): (c) *Δf* versus *Δm* of the MSMC for the fundamental and first harmonic resonance.

Since mass loads were added on the tip of the MSMC in this research, we may use Equation (4-17) to simulate the mass sensitivity of the MSMC. Based on Equation (4-17), the theoretical mass sensitivity of a MSMC in size of 4 mm x 1.2 mm x 30 μm is 2029 Hz/mg and 12717 Hz/mg for the fundamental and first harmonic modes, respectively. It is found that the experimental result is lower than the calculated mass sensitivity. The reason behind this is that Equation (4-17) assumed that the mass load is a point mass at the tip of the cantilever, while, in this experiment, the size of the mass load (0.5 mm x 1 mm) for sensitivity characterization is comparable to the size (4 mm x 1.2 mm) of the MSMC.

4.4.7 Yeast Detection in Water

To demonstrate the feasibility of using the MSMC as a sensor platform, the MSMC was used to detect the yeast cells in real-time manner. A set of data is shown in Fig. 4-14. The solid triangles are the results of testing yeast cells in yeast cell suspension with 1 mg/ml concentration, where an MSMC (MSMC-A) in size of 2.8 mm x 1.2 mm x 30 μm was utilized; and the solid squares are the results of testing yeast cells in 2 mg/ml yeast suspension, where an MSMC in size of 2.6 mm x 1.1 mm x 30 μm (MSMC-B) was utilized. The results were obtained by monitoring the change in the resonance frequency of fundamental harmonic mode with time after the whole MSMC was immersed into the yeast cell suspension. The exponential trend lines were drawn as solid lines based on experimental results. The results show that the MSMC sensor works well in liquid and can provide real-time detection.

To determine the resolution of the MSMC operating in liquid, the phase signals of MASMC-A and MSMC-B in pure water were fitted based on Lorentz function over different frequency ranges, and the obtained resonance frequencies were listed in Table 4-8 and Table 4-9, respectively. The results indicate the fitting error is ± 0.7 Hz. Therefore, the shift of 1.5 Hz in the resonance frequency can be identified.
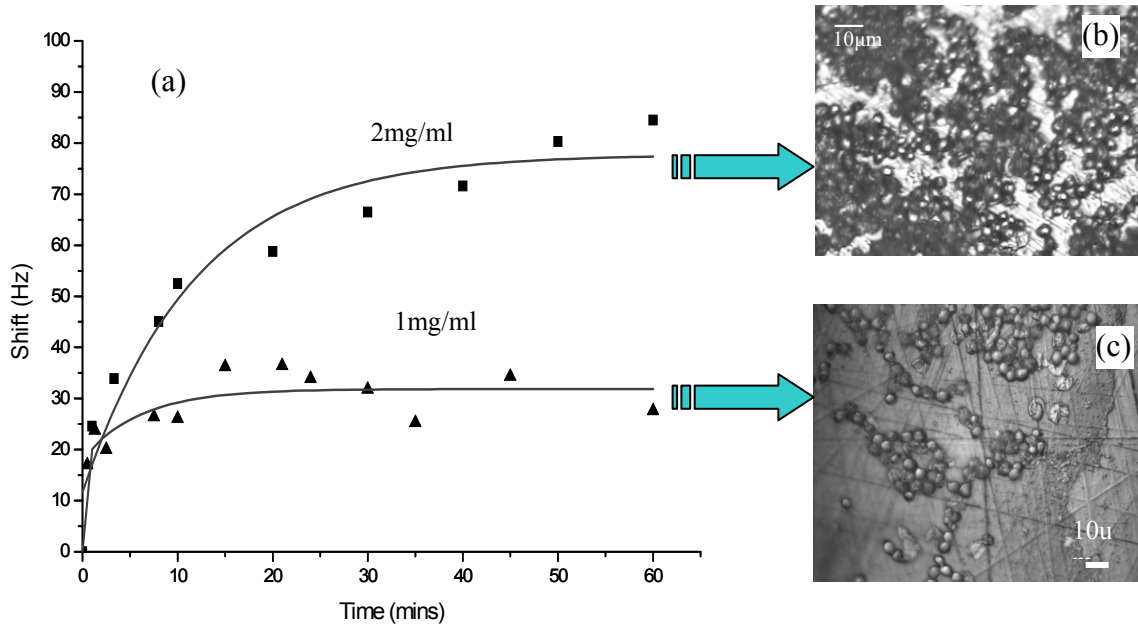
Fig. 4-14. Response of fundamental harmonic mode for real-time yeast cells detection using MSMCs: (a) frequency shift with time after MSMC-A and MSMC-B immersed in yeast suspension with concentration of 1 mg/ml and 2 mg/ml, respectively; (b) the picture of yeast cells on the MSMC-B surface after the sensor was tested in 2 mg/ml yeast cell suspension. (c) the picture of yeast cells on the MSMC-A surface after the sensor was tested in 1 mg/ml yeast cell suspension.

TABLE 4-8

Fitting Results of Resonance Frequencies of MSMC-A in Pure Water Based on Lorentz Function over Different Frequency Ranges

Frequency range (Hz)	Baseline	f_0 (Hz)
1300 ~ 1600	Linear, D2	1437.1
1325 ~1550	Linear, D2	1436.3
1300 ~ 1550	Linear, D2	1435.7
Average	Linear, D2	1436.37 ± 0.7

TABLE 4-9

Fitting Results of Resonance Frequencies of MSMC-B in Pure Water Based on Lorentz

Function over Different Frequency Ranges

Frequency range (Hz)	Baseline	f_0 (Hz)
1450 ~ 1800	Linear, D2	1612.5
1500 ~ 1750	Linear, D2	1611.4
1550 ~ 1700	Linear, D2	1612.8
Average	Linear, D2	1612.23 ± 0.7

It is found that the Q values of the MSMC-A and MSMC-B in the yeast cell suspension are 21 (the Q value of MSMC-A is 130 in air) and 15 (the Q value of MSMC-B is 120 in air), respectively. As discussed above, the MSMC-A and MSMC-B can easily detect a shift in resonance frequency at least 1.5 Hz. Based on the data shown in Fig. 4-12, an almost saturated shift in resonance frequency is obtained after the MSMCs were immersed in yeast suspension for 1 hour. The saturated shifts are about 35 Hz and 85 Hz for the detection in 1 mg/ml and 2 mg/ml yeast cell suspension, respectively. The optical micrograph of immobilized yeast cells on MSMC surface were taken and shown in Fig. 4-14 (b) and (c) after the MSMCs were immersed in yeast cell suspension for 1 hour. The images indicate the obtained shift in resonance frequency is due to the yeast cells attachment.

4.4.8 Detection of Bacillus Anthracis Spore Using MSMC-based Biosensor

Bacillus anthracis spore is a fatal bio-threat agent. Prevention of diseases caused by *B. anthracis* spores depends on immediate detection and control of the pathogenic spores in

the environment. Although the conventional method is sensitive, it requires incubation and takes several days to complete. Combining landscape phase probes with MSMC platform provides a rapid bio-analysis tool to monitor the *B. anthracis* spores. MSMC/Phage biosensors, in the size of 2.7 mm x 1 mm x 35 μm, were employed to demonstrate real-time detection of *B. anthracis* spores in water. Fig. 4-15 shows the real time resonance frequency shifts of a MSMC biosensor, when it was exposed to spore suspensions with increasing concentrations. The black squares, red dots and green triangles represent the resonance frequency shifts as the MSMC was exposed to 5×10^4, 5×10^6, and 5×10^8 spores/mL of spore suspensions, respectively. As the MSMC was exposed to 5×10^4 spores/mL of spore suspension, no obvious shift can be observed. When the MSMC was exposed to spore suspensions with the concentration of 5×10^6 and 5×10^8 spores/mL, the resonance frequency shifts quickly at first due to the binding of the spores, and then reaches the saturation after about 1 hour exposure. The higher the spore concentration, the bigger the total resonance frequency shifts. For the concentration of 5×10^6 spores/mL, a total frequency shift about 15 Hz was observed, while a total frequency shift about 50 Hz was observed for the concentration of 5×10^8 spores/mL.
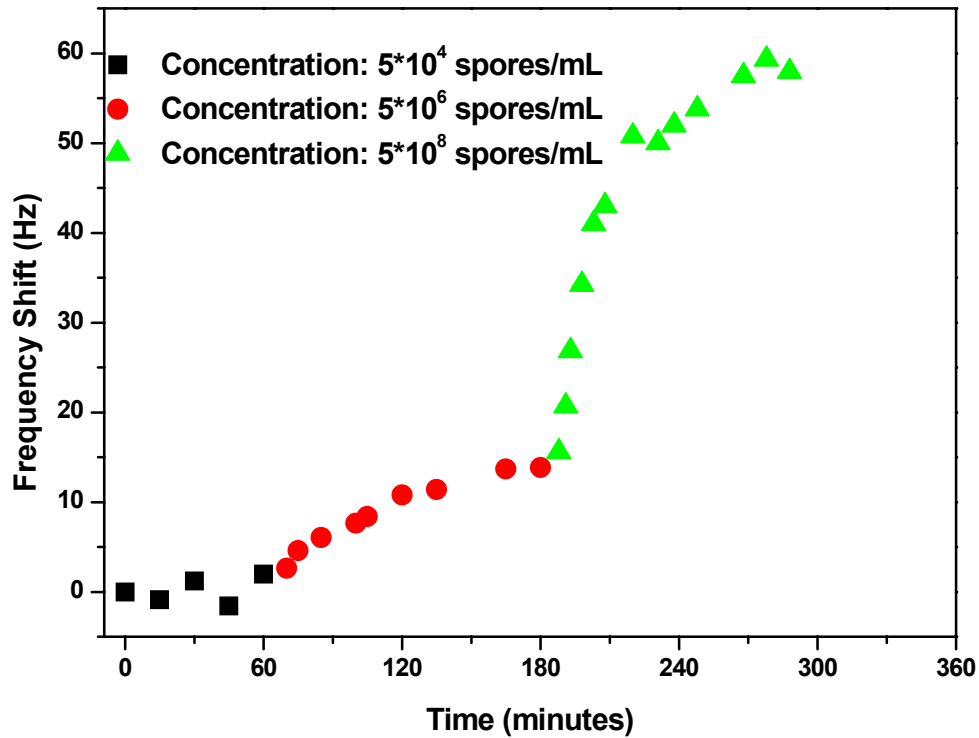
Fig. 4-15. Real-time resonance frequency shifts as the MSMC/Phage biosensor exposed to *B. anthracis* suspension with increasing concentration. The MSMC biosensor is in the size of 2.7 mm x 1.0 mm x 35 μm.

After the sensor was exposed to spore suspensions, the MSMC was rinsed using distilled water and dried, and then the surface of the MSMC was observed using a SEM. The SEM images shown in Fig. 4-16 confirm the binding of the spores on the surface, and indicate that obtained shifts in resonance frequency were due to the spores' attachment. The images clearly show that the phage clone used in this study exhibits good binding capability. It also revealed that the spores' binding was not uniform: more

spores attached at end of the MSMC, while much less spores attached at the middle of the cantilever beam. According to Equation (4-14) and (4-17), mass load at free end of the beam results in a higher sensitivity and is favorable for the detection.
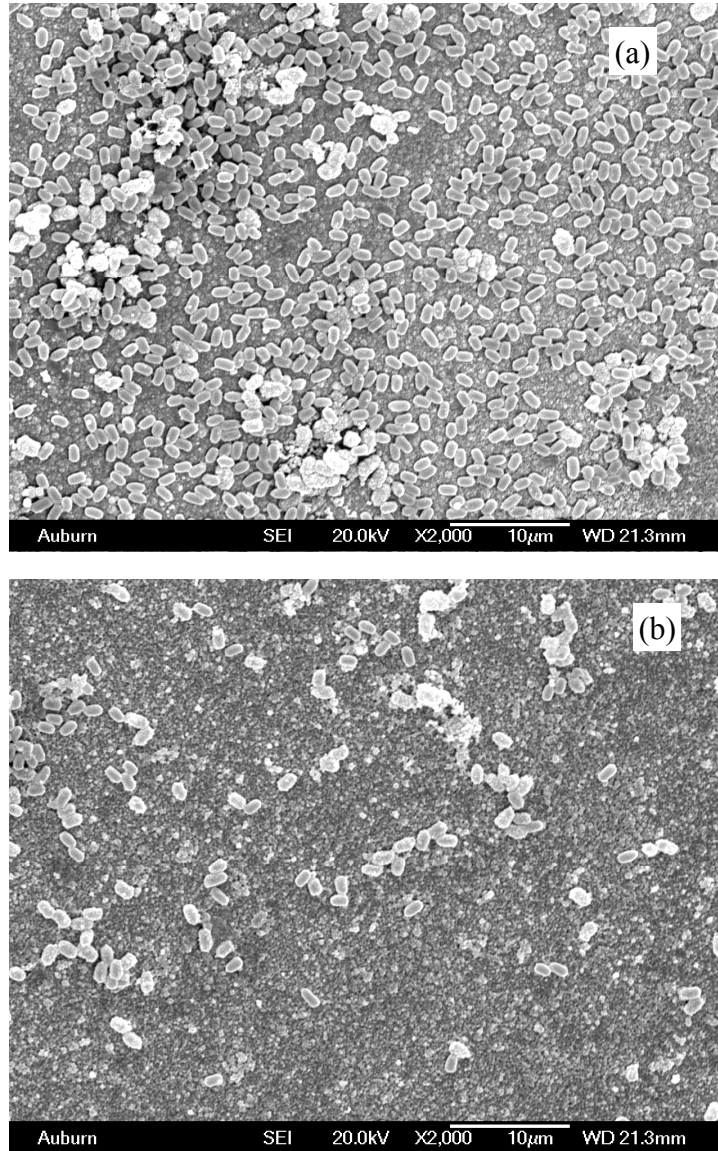
Fig. 4-16. SEM images of the MSMC surface after the biosensor was exposed to the spore suspension with increasing concentration. (a) at the tip of the cantilever beam; (b) at the middle of the cantilever beam.

When the MSMC/phage biosensor was exposed to spore suspension, the shift in its resonance frequency eventually reached saturation if the concentration of the suspension was not changed. Fig. 4-17 shows the saturated resonance frequency shift as a function of the spore concentration, which was measured by the phage-coated MSMC biosensors in the size of 2.7 mm x 1 mm x 35 μm. A good dose-response relationship was observed between 10^6 spores/mL to 10^8 spores/mL. From the results shown in Fig. 4-17, a detection limit of 10^5 spores/mL is obtained for the MSMCs used in this research.
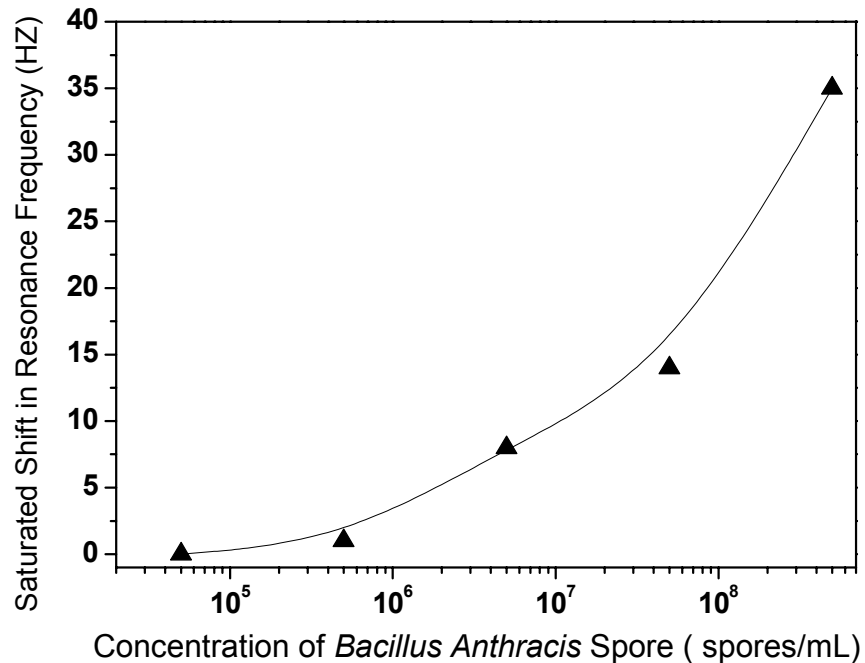
Fig. 4-17. The saturated resonance frequency shifts as the MSMC/phage biosensors, in the size of 2.7 mm x 1 mm x 35 μm, were exposed to spore suspensions with different concentrations.

The detection limit is affected by the binding of spore cells on the MSMC, as well as the mass sensitivity of the MSMC. The study of spore/phage bound density on the gold-coated Metglas[TM] 2826MB particles revealed that, for small size particles (size comparable to the MSMC beam used in this research), the chance of spore binding was pretty low for low spore concentration ($< 10^4$ spores/mL) [22]. At a concentration of 5 x 10^6 spores/mL, good spore binding can be observed, and dense spore binding was observed as the particle was exposed to a 5 x 10^8 spores/mL spore suspension [22]. This is consistent with the results shown in Fig. 4-15.

It is found that, for the MSMCs used in this experiment, whose resonance frequency (f_0) and Q value are about 2600 Hz and 200 in air, respectively, its f_0 and Q value are about 1400 and 20 when it is operated in water. Based on the discussion in previous, the resolution of MSMCs used in this experiment is about 1.5 Hz when operated in water. Based on Equation (4-14), assuming the spores uniformly binding on the surface of the MSMC, the theoretical mass sensitivity of the MSMC used in this study is about 0.6 µg/Hz. Thus, it is difficult to obtain observable frequency shift if the attached mass is less than 1 µg. If we assume the spores bind at the free end of the MSMC, based on Equation (4-17), theoretically, a mass load of about 0.2 µg is needed for a detectable frequency shift. Considering that a spore cell weights about 2 pg, for the MSMC used in this research, a dense spore binding is required, thus a good dose-response relationship was observed only as the spore concentration higher than 5 x 10^6 spores/mL. Based on Equation (4-14) and (4-17), the mass sensitivity of the MSMC exponentially increases with the decreasing size of the MSMCs. The size of the MSMC used in this experiment is still relatively large. As demonstrated by other MCs, it is expected that the sensitivity and

110

the detection limit can be great improved if the MSMC with a smaller size is employed.

4.5 Conclusion

The magnetostrictive microcantilever (MSMC) is introduced as a new type of MC as sensor platform for developing a high performance biosensor. The performance of the MSMCs was experimentally determined using the MSMCs made of a commercial magnetostrictive alloy—Metglas™. Compared to the piezoelectric MCs, the MSMC has a simple configuration. Based on material properties, it is expected that the MSMC sensors would exhibit a higher sensitivity than the piezoelectric MCs. More importantly, it is experimentally found that the MSMC works well in air or liquid and exhibits a much higher Q value than the other MCs. For example, the Q value of those MSMCs in air reaches more than 500 and that in water reaches 38. The experimental results also indicate that the anchor loss in MC has a stronger influence on the fundamental mode than on the higher modes. As wireless sensors, an array of MSMCs can be easily formed and characterized by a single scan. The application of the MSMC as a high performance biosensor platform is demonstrated by detecting yeast cells and *B. anthracis* spores in water. The MSMCs exhibit advantages over other microcantilevers in high performance biosensor development.

References

[1] P. Leonard, S. Hearty, J. Brennan, L. Dunne, J. Quinn, T. Chakraborty, and R. O'Kennedy, "Advances in biosensors for detection of pathogens in food and water," *Enzyme and Microbial Technology*, vol. 32, pp. 3-13, 2003.

[2] D. S. Ballantine, White, R.M., Martin, S.J., Ricco, A.J., Frye, G.C., Zellers, E.T., Wohltjen, H., *Acoustic wave sensors: theory, design and physico-chemical applications*: Academic Press, 1997.

[3] O. Tamarin, C. Dejous, D. Rebiere, J. Pistre, S. Comeau, D. Moynet, and J. Bezian, "Study of acoustic Love wave devices for real time bacteriophage detection," *Sensors and Actuators B-Chemical*, vol. 91, pp. 275-284, 2003.

[4] R. Raiteri, M. Grattarola, H. J. Butt, and P. Skladal, "Micromechanical cantilever-based biosensors," *Sensors and Actuators B-Chemical*, vol. 79, pp. 115-126, 2001.

[5] C. Ziegler, "Cantilever-based biosensors," *Analytical and Bioanalytical Chemistry*, vol. 379, pp. 946-959, 2004.

[6] B. Ilic, Y. Yang, K. Aubin, R. Reichenbach, S. Krylov, and H. G. Craighead, "Enumeration of DNA molecules bound to a nanomechanical oscillator," *Nano Letters*, vol. 5, pp. 925-929, 2005.

[7] Z. Y. Shen, W. Y. Shih, and W. H. Shih, "Mass detection sensitivity of piezoelectric cantilevers with a nonpiezoelectric extension," *Review of Scientific Instruments*, vol. 77, 2006.

[8] B. Ilic, Y. Yang, and H. G. Craighead, "Virus detection using nanoelectromechanical devices," *Applied Physics Letters*, vol. 85, pp. 2604-2606, 2004.

[9] J. Merhaut, *Theory of electroacoustics*: New York ; London : McGraw-Hill International Book Co., 1981.

[10] J. W. Yi, W. Y. Shih, and W. H. Shih, "Effect of length, width, and mode on the mass detection sensitivity of piezoelectric unimorph cantilevers," *Journal of Applied Physics*, vol. 91, pp. 1680-1686, 2002.

[11] *Guide to modern piezoelectric ceramics*: Morgan Matroc, Inc.

[12] S. M. Sze, *Semiconductor Sensors*: John Wiley & Sons, Inc., 1994.

[13] W. Y. Shih, X. P. Li, H. M. Gu, W. H. Shih, and I. A. Aksay, "Simultaneous liquid viscosity and density determination with piezoelectric unimorph cantilevers," *Journal of Applied Physics*, vol. 89, pp. 1497-1505, 2001.

[14] B. Ilic, D. Czaplewski, M. Zalalutdinov, H. G. Craighead, P. Neuzil, C. Campagnolo, and C. Batt, "Single cell detection with micromechanical oscillators," *Journal of Vacuum Science & Technology B*, vol. 19, pp. 2825-2828, 2001.

[15] K. Yum, Z. Y. Wang, A. P. Suryavanshi, and M. F. Yu, "Experimental measurement and model analysis of damping effect in nanoscale mechanical beam resonators in air," *Journal of Applied Physics*, vol. 96, pp. 3933-3938, 2004.

[16] J. W. Yi, W. Y. Shih, R. Mutharasan, and W. H. Shih, "In situ cell detection using piezoelectric lead zirconate titanate-stainless steel cantilevers," *Journal of Applied Physics*, vol. 93, pp. 619-625, 2003.

[17] S. Rast, C. Wattinger, U. Gysin, and E. Meyer, "Dynamics of damped cantilevers," *Review of Scientific Instruments*, vol. 71, pp. 2772-2775, 2000.

[18] Y. H. Park and K. C. Park, "High-fidelity Modeling of MEMS resonators - Part 1: Anchor loss mechanisms through substrate," *Journal of Microelectromechanical Systems*, vol. 13, pp. 238-247, 2004.

[19] D. T. Read, "Young's modulus of thin films by speckle interferometry," *Measurement Science & Technology*, vol. 9, pp. 676-685, 1998.

[20] P. H. Rieger, *Electrochemistry*: Prentice-Hall, Inc., 1987.

[21] R. A. Serway, *Physics for scientists and engineers*, second ed: CBS College Publishing, 1986.

[22] J. Wan, H. Shu, S. Huang, B. Fiebor, I.-H. BChen, V. A. Petrenko, and B. A. Chin, "Phage-Based Magnetoelastic Wireless Biosensors for Detecting Bacillus Anthracis Spores," *IEEE Sensors Journal*, vol. 7, pp. 470 - 477, 2007.

113

CHAPTER 5

DESIGN AND FEASIBILITY STUDY OF MAGNETOSTRICTIVE PARTICLES

AS BIOSENSOR PLATFORM

5.1 Introduction

Development of biosensors based on AW devices has attracted a great deal of attention due to the fact that AW devices can provide high sensitivity and real-time detection [1-3]. However, as mentioned in Chapter 1, current AW devices face challenges in practical applications. Some AW devices, such as TSM, can work well in liquid, but have a small S_m; while some AW devices, such as MCs, exhibit a very high S_m, but with a small Q value. There is an urgent need to develop high performance portable biosensors that can be used to rapidly quantify the presence of various pathogens. Also, the biosensors that are able to perform *in vivo* detection are highly desirable for applications such as in-body medical diagnosis, urine and excrement tests, and quality monitoring of food during processing, storage and transportation. Another challenge facing biosensors is how to bring target species onto sensors, especially when detecting pathogen cells in very low concentration environment. For example, MCs in nano-scale have achieved the capability to detect a single cell. However, based on the study in bio-reaction dynamics, the chance of the target pathogen cells binding on the sensor platform is very low, and a very long response time is required to generate measurable signals, when the sensors are

114

in very small size or when they are used to detect pathogens in very low concentration cultures [4].

Magnetic beads have been widely used in bio-detection techniques, such as biological separation, labeling and targeting, since they provide an efficient way to capture and isolate biological targets such as DNA, cell, and protein [5]. Magnetic bead consists of an inorganic core of iron oxide, such as magnetite Fe_2O_3, magnetite or other insoluble ferrites, coated with polymer such as dextran. Their size is from nanometers to micrometers in diameters. Bounded to a suitable antibody, they can selectively attach to the biomaterial of interest. For manipulation or purification of biological cells/molecules, magnetic beads are mixed and stirred in the solution. And then suspended beads tagged to the biomaterial of interest can be removed from the surrounding environment using a magnetic field [5]. By this way, magnetic beads can be used to separate and enrich the target cells to make low number cell detection easier.

Magnetic beads have been combined with biosensor techniques to improve the biosensors' performance in very low concentration environments. For example, Brewster et al. combined antibody-coated superparamagnetic beads with the electrochemical biosensor to detect *S. typhimurium* [6]. Target bacteria cells were captured by antibody-coated magnetic beads, then separated and purified from the sample solution. With the aid of the magnet, the beads were localized on the surface of the disposable graphite ink electrodes. By adding an enzyme solution, the bacteria can be detected using a voltammetric system. Using this technique, a minimum of $8\text{x}10^3$ cell/ml of *S. typhimurium* can be detected [6]. More recently, Nam et al. also reported a nanoparticle-based bio-bar-code approach to detect a protein target at low attomolar concentrations [7].

With the use of the magnetic bead as separator, antibody functionalized magnetic particles can readily remove the aggregate from the assay solution to leave only the barcode DNA, which can be quickly identified by standard DNA detection methodologies, such as gel electrophoresis, fluorophore-labeling, and scanometric approaches. This approach can improve the detection limitation about six orders compared to conventional methods [7]. However, these approaches are both labor intensive and time-consuming due to the separation and many washing steps. Also, complex instrumentation is required for the detection.

In this chapter, a novel AW device – magnetostrictive particle (MSP) in the shape of strip or bar – is introduced as a high performance biosensor platform. A MSP is a free standing magnetostrictive sensor platform operated based on magnetostriction. A single MSP can work as an individual sensor, while a number of MSPs can also work together as multiple sensors. Interrogated through magnetic field, there are no physical connections between the sensor and interrogation system required for driving and sensing MSPs. Therefore, MSPs are wireless sensors, which enable remote *in vivo* detection. Furthermore, the theoretical simulation indicates that the MSPs have much better sensitivity than MCs in the term of minimum detectable mass; and the feasibility study demonstrates that the MSPs exhibit a high Q-value and work well in liquid media. The presented MSP biosensors are cost effective and disposable, since the magnetostrictive alloys are very inexpensive and environmental friendly.

The MSP also exhibits unique features as a sensor platform. MSPs have the advantages to overcome the limitations of currently existing sensors in detecting target species with low concentration. Since MSPs are magnetic, similar to magnetic beads,

they can be stirred using a magnetic field in the sample solution, which greatly increases the chance of target species binding on the MSP sensor. Meanwhile, since the individual MSP itself is a biosensor platform, it can directly output the signal without combining to some other sensor platforms. Based on this feature, a simple and efficient approach is presented to detect target species with very low concentration. MSPs also can overcome the effect of non-uniform mass load on the sensor surface. AW mass sensors exhibit maximum sensitivity when the mass is loaded at the place where the device undergoes maximum displacement during the resonance vibration, but can not detect the mass loaded at the place where zero displacement occurs during the vibration. Since the MSP is totally free standing, multiple harmonic resonance modes can be easily actuated and sensed by a single scan. Even with non-uniform mass load, the sensitivity of MSPs can be fully used by monitoring multiple harmonic resonance frequencies.

5.2 Design and Operation Principle of Magnetostrictive Particles (MSPs)

5.2.1 Configuration of MSPs and Their Resonance Behavior

The MSP sensor platform has very simple configuration: it is a free-standing particle made from a magnetostrictive alloy. In the design, the MSP can be in the shape of strip with the length of L, width of w and thickness of t, or in the shape of bar with the length of L and diameter of d. For the MSP in strip shape, its length is bigger than its width and much bigger than its thickness ($L > w > t$). For the MSP in bar shape, its length is much bigger than its diameter ($L \gg d$). The configuration is shown in Fig. 5-1.

117

(a)

(b)
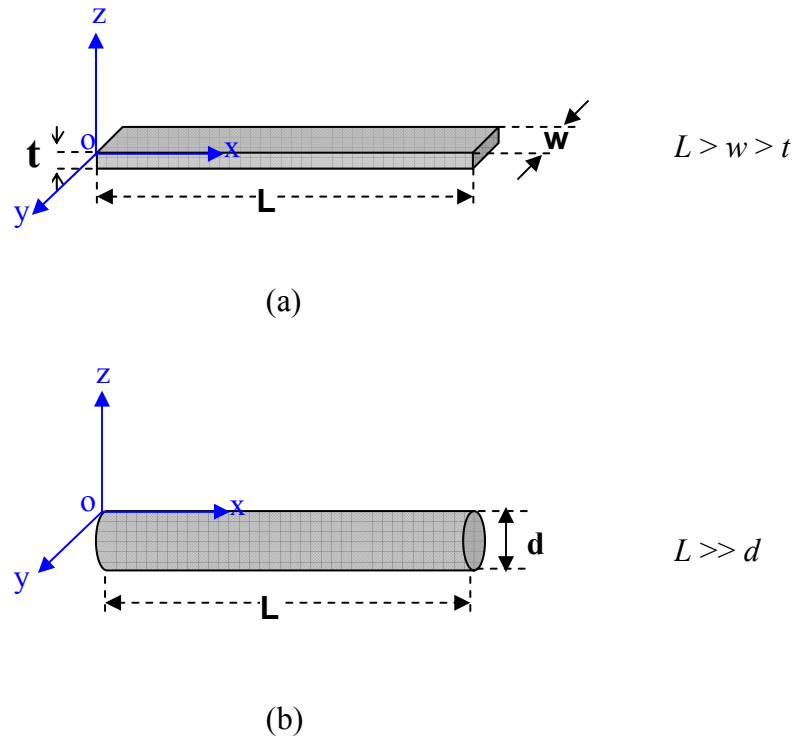
Fig. 5-1. Magnetostrictive particle (MSP) configuration. (a) MSP in strip-shape and (b) MSP in bar-shape.

Based on the magnetostrictive effect, the MSP will be deformed under an external magnetic field. Thus, if an alternating magnetic field is applied, extensions or compressions along all directions would be generated. In the design, the resonance along the length direction, that is the longitudinal vibration mode, is used. Assuming the MSP is oriented in its basal XY plane, with the length of the MSP along the x-axis as shown in Fig. 5-1, the vibration of the MSP along its length direction (x-direction) can be described using the theoretical model that describes the longitudinal oscillation of a thin elastic

plate, as follows [8]:

$$\frac{\partial^2 u(x,t)}{\partial t^2} - \frac{E}{\rho(1-\sigma^2)} \frac{\partial^2 u(x,t)}{\partial x^2} = 0 \qquad (5\text{-}1)$$

where E, ρ, and σ are the Young's modulus, density, and Poisson ratio of the material respectively, while the $u(x, t)$ is the displacement vector along x-axis. For harmonic oscillations, the displacement can be expressed as [9]:

$$u(x,t) = u(x)e^{i\omega t} \qquad (5\text{-}2)$$

where ω is the resonance frequency. Therefore, Equation (5-1) can be written as [9]:

$$\frac{E}{\rho(1-\sigma^2)} \frac{\partial^2 u(x)}{\partial x^2} + \omega^2 u(x) = 0 \qquad (5\text{-}3)$$

The general solution of the wave Equation (5-3) is [9]:

$$u(x) = A\sin kx + B\cos kx = u_0 \sin(kx + \varphi) \qquad (5\text{-}4)$$

where $k = \omega\sqrt{\dfrac{\rho(1-\sigma^2)}{E}}$ is the wave number [9], and $u_0 = \sqrt{A^2 + B^2}$ is the displacement amplitude.

When a free-standing particle shown in Fig. 5-1 is operated, the two ends of the MSP experience no restoring force and are stress free, which means that $\partial u(x)/\partial x = 0$ at both ends of the MSP ($x = 0$ and $x = L$). Applying these boundary conditions to Equation (5-4), we can obtain:

$$u_0 k \cos(\varphi) = 0 \qquad (5\text{-}5)$$

$$u_0 k \cos(kL + \varphi) = 0 \qquad (5\text{-}6)$$

Equation (5-5) and (5-6) yields:

$$\varphi = \frac{\pi}{2} \tag{5-7}$$

$$kL = n\pi \qquad (n = 1, 2, 3\ldots) \tag{5-8}$$

From the condition of Equation (5-8), it yields:

$$\omega_n = 2\pi f_n = k\sqrt{\frac{E}{\rho(1-\sigma^2)}} = \frac{n\pi}{L}\sqrt{\frac{E}{\rho(1-\sigma^2)}} \tag{5-9}$$

Therefore, for the magnetostrictive strip or bar shown in Fig. 5-1, its characteristic frequency of the longitudinal oscillation is given by [8]:

$$f_n = \frac{n}{2L}\sqrt{\frac{E}{\rho(1-\sigma^2)}} \qquad (n = 1, 2, 3\ldots) \tag{5-10}$$

Equation (5-10) indicates that the characteristic frequency of the MSPs with the designed structure is only dependent on their length and material properties.

Considering the boundary conditions of the MSP oscillation allows the amplitude profile of the displacement at resonance to be calculated. Inserting Equation (5-7) and (5-8) into Equation (5-4), we can obtain the displacement along the MSP length at longitudinal resonance, which is [10].

$$u(x,t) = u_0 \cos(\frac{n\pi}{L}x)e^{j\omega t} \tag{5-11}$$

where u_0 is the displacement amplitude and ω is the angular excitation frequency ($\omega = 2\pi f$). In Equation (5-11), $e^{j\omega t}$ represents the oscillation of each point of the MSP, while $u_0 \cos(\frac{n\pi}{L}x)$ represents the amplitude profile of displacement for the MSP along the length direction at resonance frequency.

5.2.2 The Mass Sensitivity (S$_m$) of MSPs

5.2.2.1 Mass Sensitivity (S$_m$) of MSPs with Uniform Mass Load

If an ideal pure mass Δm is uniformly added on the surface of a MSP shown in Fig. 5-1, the additional mass corresponds to an increase in the MSP density. Assuming the original mass of the MSP is M, with the mass load Δm, the density of the MSP increases by a factor of "$1 + \Delta m/M$". Thus Equation (5-1) becomes:

$$\frac{\partial^2 u_x}{\partial t^2} - \frac{E}{(1+\frac{\Delta m}{M})\rho(1-\sigma^2)}\frac{\partial^2 u_x}{\partial x^2} = 0 \tag{5-12}$$

Based on Equation (5-10), the characteristic frequency of a MSP with uniform mass load Δm is:

$$f_{mass} = \frac{n}{2L}\sqrt{\frac{E}{\left(1+\frac{\Delta m}{M}\right)\rho(1-\sigma^2)}} = f_n\sqrt{\frac{M}{M+\Delta m}} \quad (n = 1, 2, 3...) \tag{5-13}$$

Therefore, the change in the resonance frequency (Δf) caused by the mass load (Δm) can be expressed as:

$$\frac{\Delta f}{\Delta m} = \frac{f_n - f_{mass}}{\Delta m} = f_n\frac{1-\sqrt{\frac{1}{1+\frac{\Delta m}{M}}}}{\Delta m} \tag{5-14}$$

When the mass load (Δm) is much smaller than the mass (M) of the MSP ($\Delta m/M << 1$), Equation (5-14) can be expressed as:

$$\frac{\Delta f}{\Delta m} = \frac{f_n - f_{mass}}{\Delta m} \cong f_n\frac{1-\sqrt{1-\frac{\Delta m}{M}}}{\Delta m} \cong f_n\frac{1-(1+\frac{1}{2}\frac{\Delta m}{M})}{\Delta m} \tag{5-15}$$

121

Therefore, for a small mass load, we can obtain:

$$\frac{\Delta f}{\Delta m} = -\frac{f_n}{2M} \qquad (\Delta m << M) \tag{5-16}$$

The negative sign means the resonance frequency of the MSP decreases with the increase of the mass load. Thus, the mass load on the MSP can be very easily obtained by simply measuring the shift in the natural frequency.

Based on the definition of the mass sensitivity of the AW device (Equation (1-2)) and Equation (5-16), we can calculate the mass sensitivity for a MSP with the uniform mass load as:

$$S_m = -\frac{\Delta f}{\Delta m} = \frac{f_n}{2M} \qquad (m << M) \tag{5-17}$$

Combining Equation (5-10) and Equation (5-17), the mass sensitivity of the magnetostrictive strips and bars can be obtained as Equation (5-18 a) and (5-18 b), respectively:

$$S_{m,strip} = \frac{1}{2}\left(\frac{n}{2L}\sqrt{\frac{E}{\rho(1-\sigma^2)}}\right)\frac{1}{Lwt\rho}$$

$$= \frac{1}{4}\sqrt{\frac{E}{\rho^3(1-\sigma^2)}}\frac{n}{L^2wt}$$

$$= \frac{1}{4}K\frac{n}{L^2wt} \tag{5-18 a}$$

$$S_{m,bar} = \frac{1}{2}\left(\frac{n}{2L}\sqrt{\frac{E}{\rho(1-\sigma^2)}}\right)\frac{4}{\pi d^2 L\rho}$$

$$= \sqrt{\frac{E}{\rho^3(1-\sigma^2)}}\frac{n}{\pi d^2 L^2}$$

$$= K\frac{n}{\pi d^2 L^2} \qquad\qquad\qquad (5\text{-}18\ b)$$

where $K = \sqrt{\dfrac{E}{\rho^3(1-\sigma^2)}}$ is the material index only related to the properties of the

magnetostrictive materials of which the MSP is made. Equation (5-18 a) and (5-18 b) show that, given the material index K, the S_m increases with decreasing dimensions. To conveniently compare the sensitivities, the ratio of the MSP dimensions are kept constant (for strip-shape MSP, $L:w = \alpha$ and $L:t = \beta$; for bar-shape MSP, $L:d = \gamma$) for calculations. Therefore, the Equation (5-18) can be written as:

$$S_{m,strip} = \frac{\alpha\beta Kn}{4}\frac{1}{L^4} \qquad\qquad\qquad (5\text{-}19\ a)$$

$$S_{m,bar} = \frac{\gamma^2 Kn}{\pi}\frac{1}{L^4} \qquad\qquad\qquad (5\text{-}19\ b)$$

Equation (5-19 a) and (5-19 b) indicate that, given the size of MSP, the MSP with a higher value of material index K has a higher mass sensitivity. The K value is directly affected by the combination of the material's Young's modulus, density and the Poisson ratio. MSPs made of higher Young's modulus and lower density materials would have a higher value of K, thus a higher S_m.

Also, based on Equation (5-19 a) and (5-19 b), given the material used to make

123

MSP, the S_m of the MSP greatly increases with the decreasing size. Assuming commercially available magnetostrictive alloy - 2826MB^{TM} – is used to make MSPs, based on materials properties shown in Table 4-2 and Equation (5-19), the S_m of MSP can be calculated theoretically. Fig. 5-2 shows the theoretical S_m of MSPs for the first harmonic resonance mode ($n = 1$) changing with the length of the MSPs. In Fig. 5-2, for strip-shape MSPs, $\alpha = 5$ and $\beta = 10$ were used; for bar-shape MSPs, $\gamma = 10$ was used. For the MSP with same length, if we increase the value of α, β and γ, that is to reduce the size of other dimensions, the S_m would increase further.

Recall the S_m of MC with uniform mass load (Equation (4-18)):

$$S_{m,uni} = \frac{\alpha \lambda_n^2}{43.508} \frac{1}{L^4} K \propto \frac{\alpha}{L^4} \tag{4-18}$$

Comparing Equation (4-18) with Equation (5-14), one can find that, if the same material is employed to make the MC and MSP, with the same geometry, the MSPs exhibit a higher mass sensitivity than that of MCs. If the strip-like MSPs have the same geometry shown in Fig. 5-2 ($\alpha = 5$ and $\beta = 10$), and α is 5 for the MCs, for the fundamental resonance mode, strip-shape MSPs exhibit a S_m about 31 times better than the MCs. For the MCs ($\alpha = 5$) made from 2826MB^{TM}, their theoretical S_m for the fundamental resonance were calculated using Equation (4-18), and shown in Fig. 5-2 as the wine dashed line. The result clearly shows that MSPs exhibit a much better mass sensitivity than that of MCs.
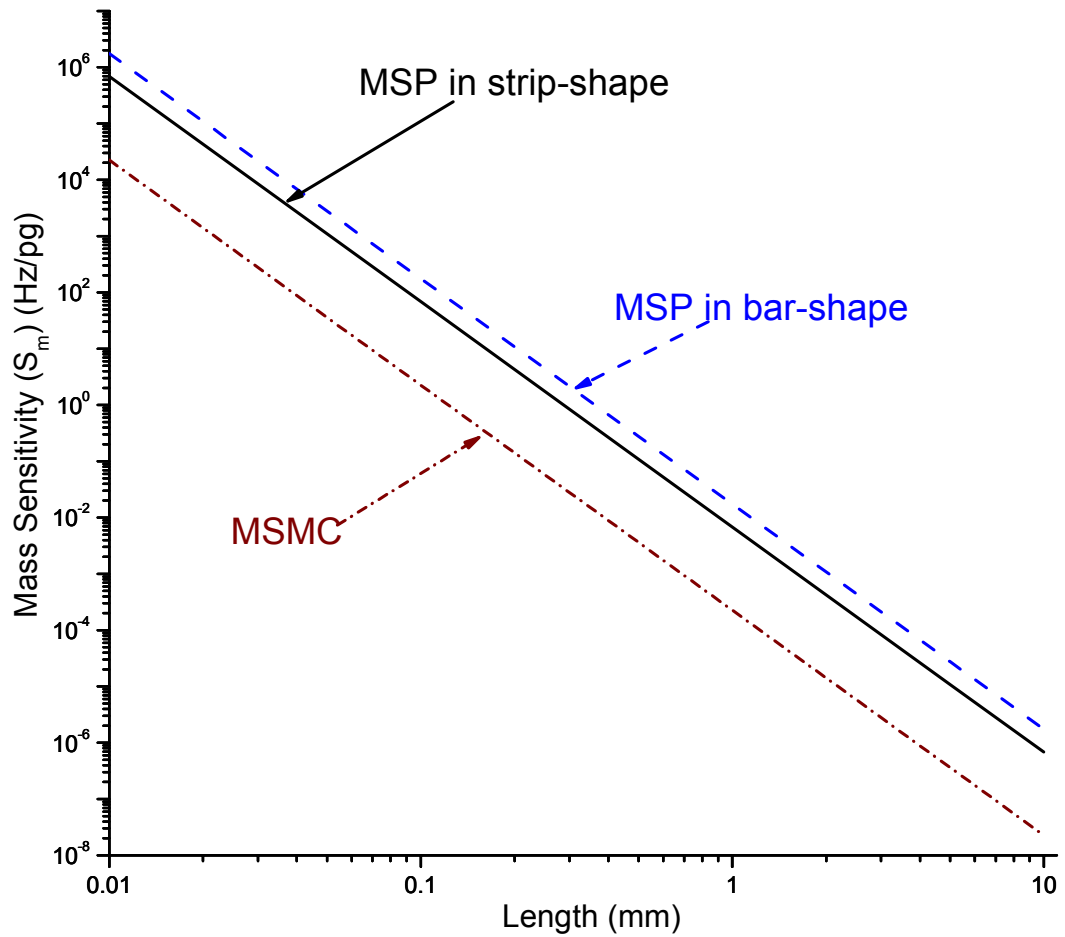
Fig. 5-2. Theoretical S_m of MSPs and MSMCs made of a commercially available magnetostrictive alloy 2826MB^{TM}. For strip-shape MSPs, the ratio of the length to width is set 5 ($\alpha = 5$), and the ratio of the width to thickness is set 10 ($\beta = 10$); for bar-shape MSPs, the ratio of the length to diameter is set 10 ($\gamma = 10$). For MCs, the ratio α of the length to width is set 5.

5.2.2.2 Mass Sensitivity (S_m) of MSP with Non-uniform Mass Load

The performance of all AW devices as sensor platforms is strongly affected by the uniformity of the mass load. An AW sensor is most sensitive to the mass attached at where the vibration amplitude is the maximum, but can not sense the mass attached at the node point of the vibration, at which the vibration amplitude is zero. For example, even though theoretically MC exhibits very high sensitivity with uniform mass load, it can not detect the mass loaded close to the fixed end of the cantilever beam, since this part of the beam has almost zero vibration amplitude. On the other hand, maximum S_m is achieved as the mass attached at the free end of the cantilever for fundamental mode oscillation. Therefore, controlling the binding position is important for AW devices to obtain reasonable response, especially for highly sensitive detection, such as detecting individual cells. Currently, to maximize the mass sensitivity, efforts have been given to localize the binding position on the favorable area of the AW sensor. For instant, nanoscale golden dots were located at the free end of nano-cantilevers to act as binding sites for DNA detection [11].

Since MSP is a completely free-standing sensor, it provides a simple way to overcome the influence of binding location of the mass load on the sensor. As discussed above, Equation (5-11) describes the amplitude profiles of displacement of MSP at longitudinal resonance. Fig. 5-3 (a), 5-4 (a) and 5-5 (a) illustrate the amplitude profiles of displacement of MSP for the first ($n = 1$), second ($n = 2$) and third ($n = 3$) longitudinal harmonic modes, respectively; while Fig. 5-3 (b), 5-4 (b) and 5-5 (b) are the schematic illustration for the deformation of the MSP at different times for the first ($n = 1$), second ($n = 2$) and third ($n = 3$) harmonic mode resonances, respectively.
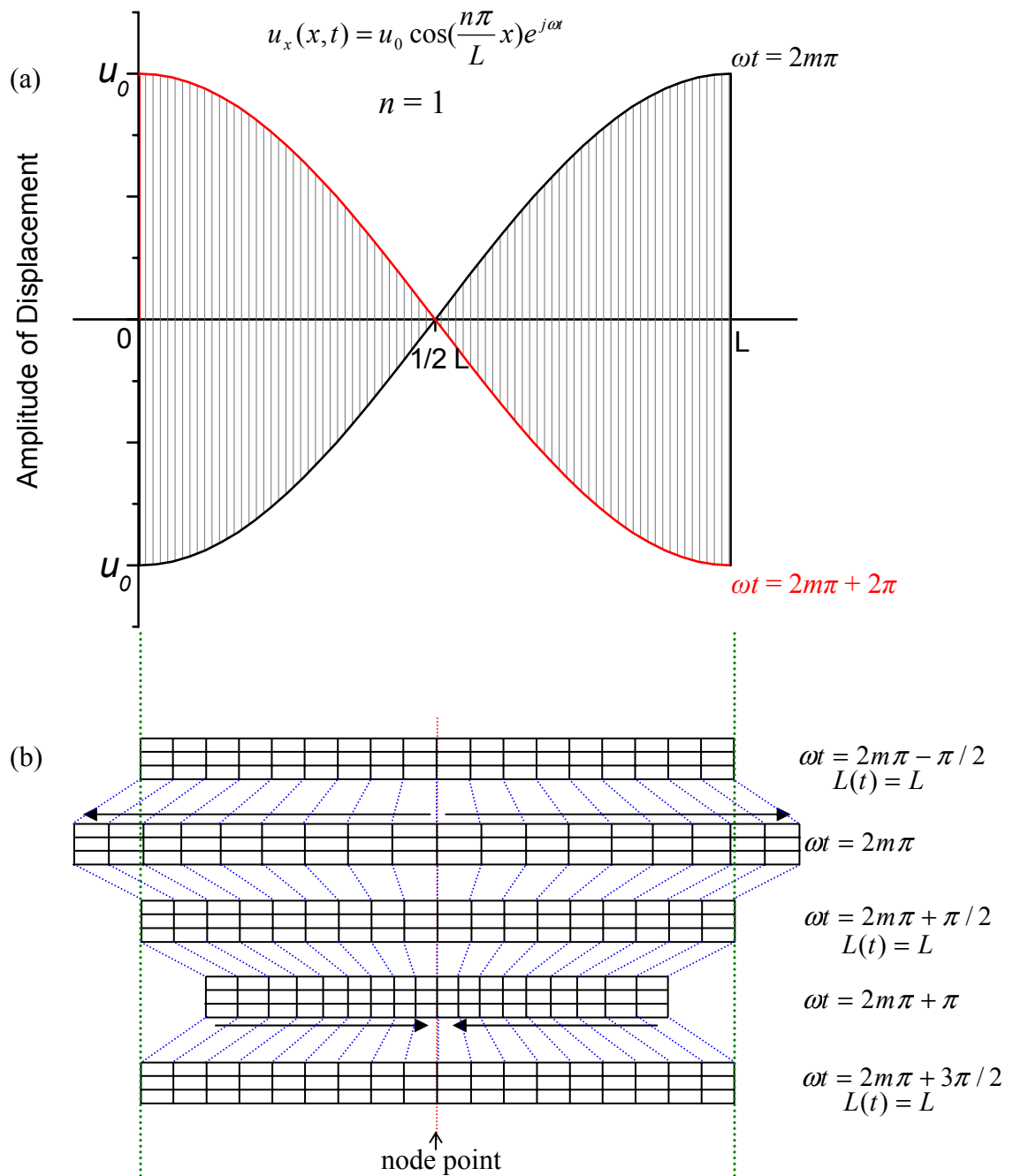
Fig. 5-3. (a) Amplitude profile of displacement of MSP for the first ($n = 1$) harmonic mode; (b) schematic illustration for the deformation of the MSP at different times for the first ($n = 1$) harmonic mode resonance.

(a)

$$u_x(x,t) = u_0 \cos(\frac{n\pi}{L}x)e^{j\omega t}$$

$$n = 2$$

u_0

$\omega t = 2m\pi$

Amplitude of Displacment

0

1/2 L

L

u_0

$\omega t = 2m\pi + 2\pi$

(b)

$\omega t = 2m\pi - \pi/2$
$L(t) \equiv L$

$\omega t = 2m\pi$
$L(t) \equiv L$

$\omega t = 2m\pi + \pi/2$
$L(t) \equiv L$

$\omega t = 2m\pi + \pi$
$L(t) \equiv L$

$\omega t = 2m\pi + 3\pi/2$
$L(t) \equiv L$

node point

node point
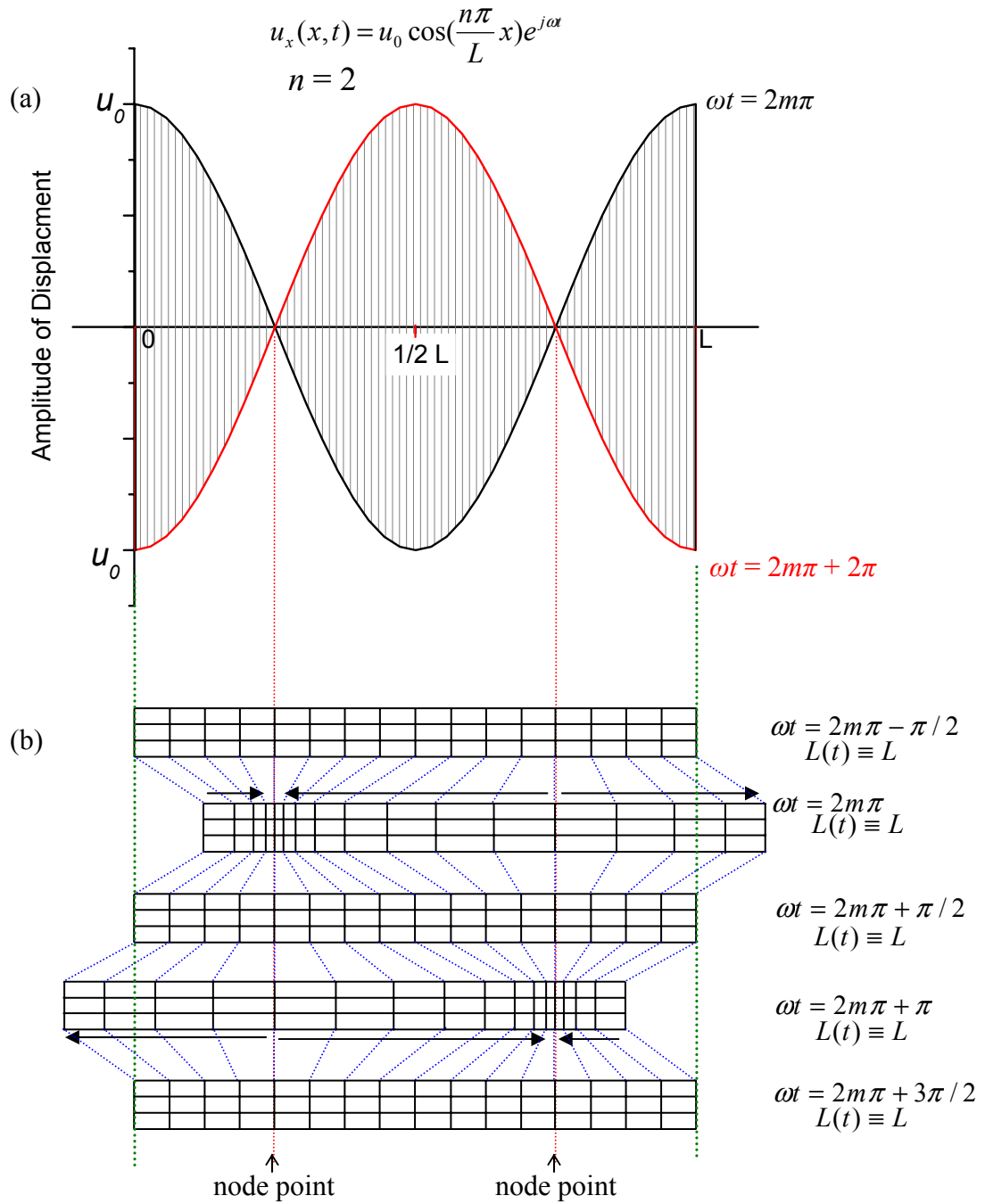
Fig. 5-4. (a) Amplitude profile of displacement of MSP for the second ($n = 2$) harmonic mode; (b) schematic illustration for the deformation of the MSP at different times for the second ($n = 2$) harmonic mode resonance.

128

(a)

$$u_x(x,t) = u_0 \cos(\frac{n\pi}{L}x)e^{j\omega t}$$

$\omega t = 2m\pi$

u_0 $n = 3$

Amplitude of Displacement

1/2 L

L

u_0 $\omega t = 2m\pi + 2\pi$

(b)

$\omega t = 2m\pi - \pi/2$
$L(t) = L$

$\omega t = 2m\pi$

$\omega t = 2m\pi + \pi/2$
$L(t) = L$

$\omega t = 2m\pi + \pi$

$\omega t = 2m\pi + 3\pi/2$
$L(t) = L$

node point   node point   node point
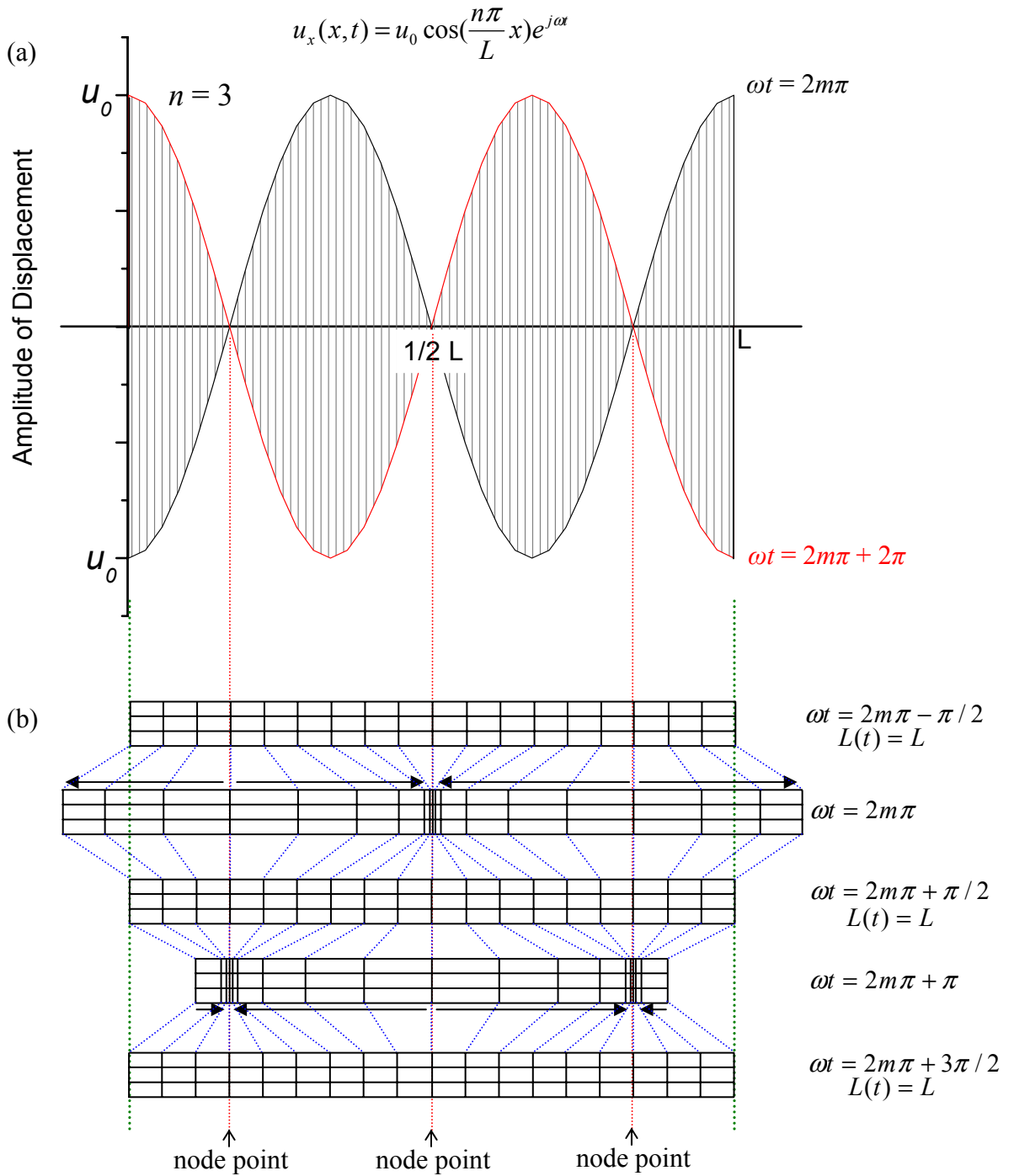
Fig. 5-5. (a) Amplitude profile of displacement of MSP for the third ($n = 3$) harmonic mode; (b) schematic illustration for the deformation of the MSP at different times for the third ($n = 3$) harmonic mode resonance.

129

odd harmonic modes

n = 1

½ L   ½ L

n = 3

1/6 L   1/6 L

n = 5

1/10 L   1/10 L

even harmonic modes

n = 2

¼ L   ¼ L

n = 4

1/8 L   1/8 L

n = 6

1/12 L   1/12 L
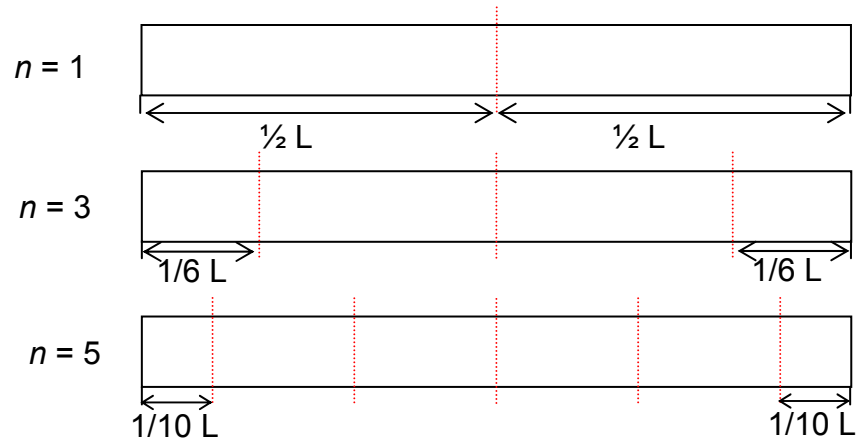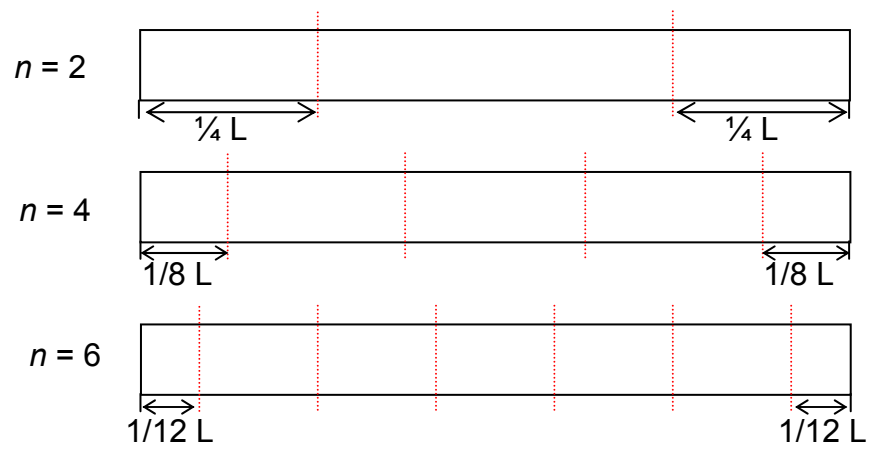
Fig. 5-6. Node points of free-standing longitudinal resonance for different harmonic modes. The red dot lines represent the location of the node points on the MSP.

According to the amplitude profiles, the number of node points for n^{th} harmonic mode equals to n. Fig. 5-6 shows the node points of longitudinal resonance for different harmonic modes, where the red dot lines represent the location of the node points on the MSP. The node point for the first ($n = 1$) harmonic mode is always a node point for all odd modes. For the odd resonance modes ($n = 1, 3, 5…$), the two free ends of the MSP have the biggest displacement in opposite direction, while the middle point of the MSP is the node point. Under these resonances, the MSP undergoes the maximum shape change. The amplitude profiles indicate that MSP is not sensitive to the mass attached at the middle point of the sensor under odd modes. On the other hand, the amplitude profiles of even harmonic modes ($n = 2, 4, 6…$) show that the two free ends of the MSP have the biggest displacement along in same direction. Therefore, under these resonances, the length of the MSP keeps original length, that is $L(t) \equiv L$, but the correspondent position changes. At the same time, the middle point of the MSP also undergoes the maximum displacement the same as the free ends. Therefore, the middle point has the highest S_m, while the node points (at ¼ lengths from the end for second harmonic mode) have a zero sensitivity. Therefore, when the AW sensor is operated at second harmonic resonance, the mass load at middle point (node point for first harmonic resonance) can be sensed with a high S_m. However, the even modes have not been used in any AW devices so far for the following reasons. For piezoelectric-based AW sensors, whose resonance behavior is usually determined by impedance spectrum (impedance versus frequency), the even harmonic resonance can not be determined, since the size (i.e. length) does not change at resonance frequency. For mechanical AW devices, whose resonance behavior is determined by the size/dimension change of the device, the even harmonic resonance

131

cannot be sensed.

However, since MSP is a totally free standing platform, it can be operated at even harmonic modes. For MSP, although the length (L) does not change at even harmonic resonance, the location of two ends changes with time as shown in Fig. 5-4 (b). Therefore, at even harmonic resonance, there would be a magnetic signal generated by the motion of two ends. That is, a resonance behavior of even harmonic modes should be observed by the interrogating system. This is another advantage of MSP over other AW devices.

In a short summary, MSP sensors can measure the mass loaded at any location on the sensor surface, simply by operating the MSP using different harmonic resonances including both odd and even modes.

5.2.3 Operation Principle of MSPs as Biosensor Platform

Due to magnetostrictive effect, the size (dimensions) of MSP changes with an external magnetic field. Under the driving magnetic field, a small AC magnetic field superimposed on a relatively stronger DC magnetic field, the MSP vibrates at the frequency of the AC driving field. Due to the magnetic nature, the oscillation of the MSP results in an emission of a magnetic flux. This magnetic flux can be remotely detected by a sensing/pick-up coil. Therefore, the signal from the pick-up coil would reflect the oscillation behavior, such as amplitude and phase, of the MSP. By sweeping the AC magnetic field over a frequency range, the frequency spectrum of the MSP sensor can be obtained using the sensing/pick-up coil. There is no physical connection between the MSP and interrogating system. MSP is a wireless and totally free standing sensor platform.

To form a MSP biosensor, a biological   recognition element, such as phage or

antibody, is immobilized on the MSP surface. The biological recognition element would capture the interested species when the MSP sensor touches the target species, which would result in an additional mass load on the MSP. As discussed above, this mass will result in a shift in the resonance frequency of the MSP. Therefore, the presence of the target species, such as bacteria/viruses/spores, can be identified by monitoring the shift of the MSP resonance frequency. The scheme of MSP operation principle is shown in Fig. 5-7.
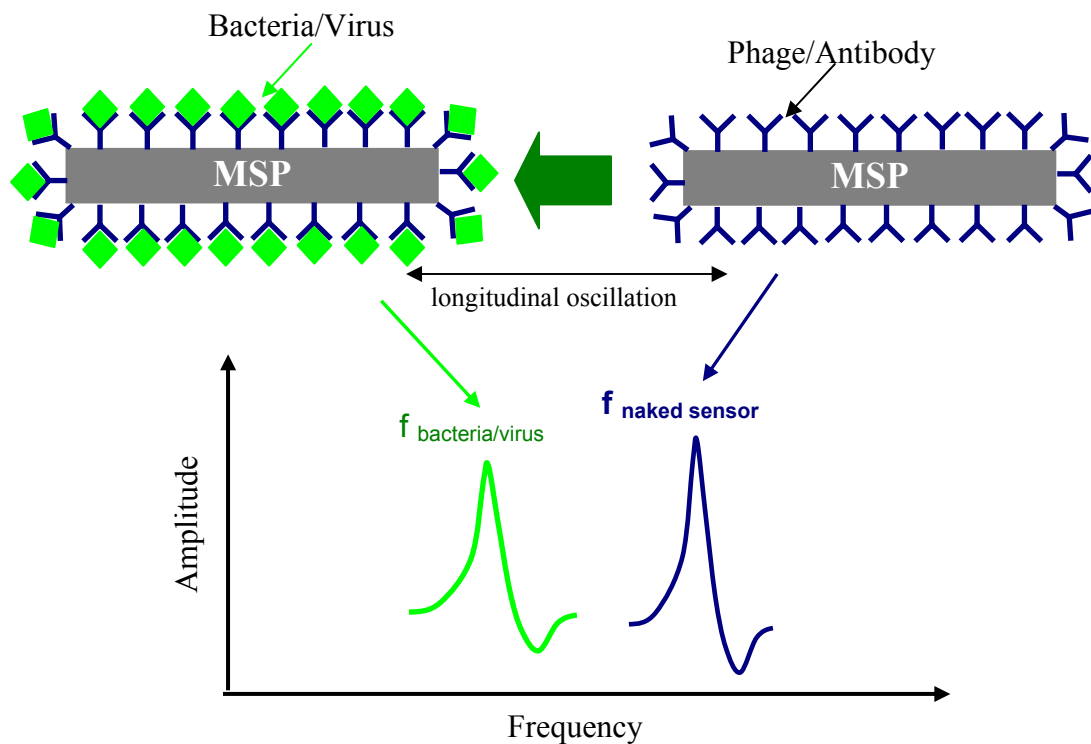
Fig. 5-7. Operating/detecting principle of a MSP sensor.

When the MSP biosensor is used to detect target species, the mass load on the MSP includes the mass (m_0) due to the biological recognition elements immobilization, and the mass (Δm) of the captured bacteria. The m_0 includes the immobilization layer, such as Au coating layer, and the immobilized antibodies/phages. For biosensor application, the shift in MSP resonance frequency caused by mass Δm is the output signal. Assuming the resonance frequency for naked MSP with mass M is f_0, the resonance frequency (f_{m_0}) of the MSP biosensor with biological recognition elements is:

$$f_{m_0} = f_0\sqrt{\frac{M}{M+m_0}} \tag{5-20}$$

If the MSP biosensor captures the target species (Δm), its resonance frequency ($f_{\Delta m}$) is:

$$f_{\Delta m} = f_0\sqrt{\frac{M}{M+m_0+\Delta m}} = f_0\sqrt{\frac{M}{M+m_0}}\left(\frac{1}{\sqrt{1+\dfrac{\Delta m}{M+m_0}}}\right) \tag{5-21}$$

Therefore, the change in the resonance frequency due to the mass Δm can be written as:

$$-\Delta f_{\Delta m} = f_{m_0} - f_{\Delta m} = f_0\sqrt{\frac{M}{M+m_0}}\left(1-\frac{1}{\sqrt{1+\dfrac{\Delta m}{M+m_0}}}\right) \tag{5-22}$$

If the Δm is much smaller than the total mass of M and m_0, Equation (5-22) can be written as:

$$-\Delta f_{\Delta m} \cong f_0\sqrt{\frac{M}{M+m_0}}\left(1-\left(1-\frac{1}{2}\frac{\Delta m}{M+m_0}\right)\right) \quad (\Delta m << M+m_0) \tag{5-23}$$

134

Thus, the S_m of the MSP biosensor can be expressed as:

$$-\frac{\Delta f_{\Delta m}}{\Delta m} = \frac{f_0 \sqrt{\dfrac{M}{M+m_0}}}{\Delta m} \frac{1}{2}\frac{\Delta m}{M+m_0}$$

$$= \frac{f_0}{2(M+m_0)}\sqrt{\frac{M}{M+m_0}} \qquad\qquad (5\text{-}24)$$

$$= \frac{1}{2(M+m_0)}f_{m_0}$$

Based on Equation (5-24), the S_m of the MSP biosensor is determined by the status of the MSP biosensor with biological recognition elements.

5.2.4 Multiple-sensor Approach Based on MSPs

As discussed above, for AW devices, the smaller the size, the higher the sensitivity. However, according to the study in bio-reaction dynamics, very long response time is required for detection if the sensor size is very small. Additionally, when biosensors are utilized to detect target in the sample with very low concentration, the chance of the target species being captured by the sensor is very low. As a wireless free-standing sensor platform, MSP technology introduced here can provide a solution – multiple-sensor approach – for this challenge. As shown in Fig. 5-8, many MSP biosensors with the same dimensions can be employed simultaneously. Similar to magnetic beads, these MSPs can be stirred in solution/sample by a magnetic field. This is equivalent to bringing the MSP sensors to target species. Therefore, the multiple-sensor approach would significantly increase the possibility for the MSP sensor to react with target species. More importantly, each MSP itself is a sensor platform, and the response of one MSP sensor can be measured out of many other MSPs. That is, even if only one sensor bonds with the target

135

cells, it can be detected. There are 3 ways that can be employed to monitor the sensor response: (1) the sensors can be *in situ* monitored; (2) the sensors can be concentrated by a magnet close to the sensing system, and then analyzed, and (3) the sensors can be collected by a magnet and separated from the sample solution, and then analyzed by corresponding techniques.
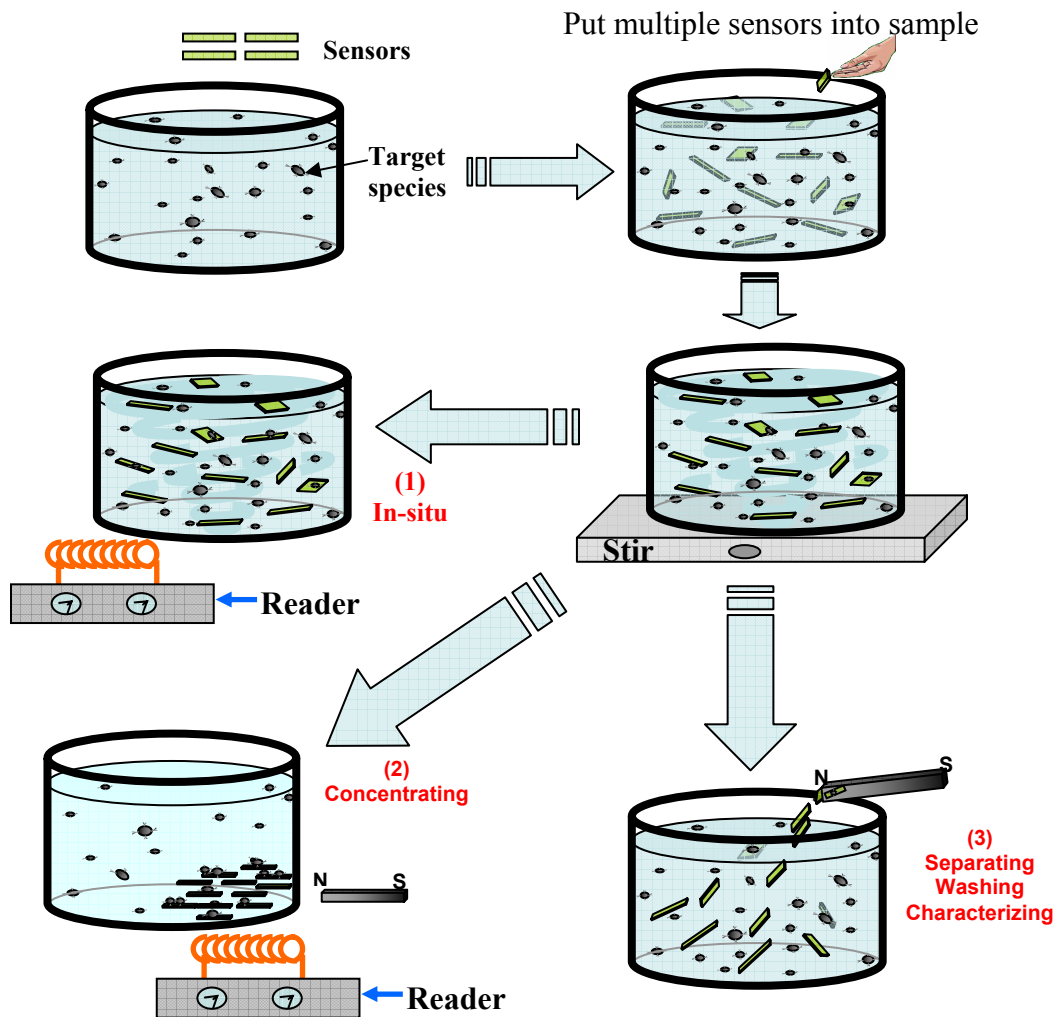
Fig. 5-8. Scheme of multiple-sensor approach based on MSPs.

Fig. 5-9 illustrates the response of the detection using multiple-sensor approach. The blue curve represents the resonance spectrum of MSP sensors before capturing the target species. If one/several MSP sensors capture the target species, its/their resonance frequency (wine peak) would shift away from the rest of the MSP sensor and can be identified out of other MSPs. Thus, multiple-sensor approach provides an easy way to detect interested species in very low concentration environment.
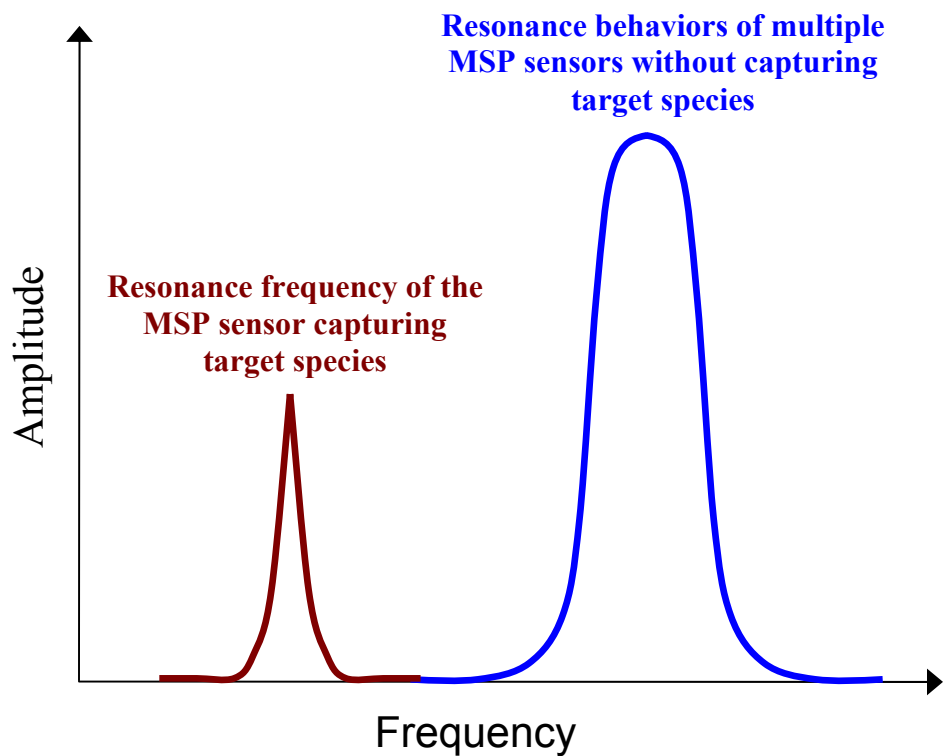
Fig. 5-9. Illustration of the response of the detection using multiple-sensor approach.

5.2.5 Multiple-target Approach Based on MSPs

Utilizing MSPs as sensor platforms also provides a simple approach – multiple-target approach – to simultaneously detect different targets. Several groups of multiple MSPs can be employed for the detection. MSPs in same group have the same dimensions

and immobilized with the same biological recognition element, which are operated using multiple-sensor approach discussed above. But for different groups, the dimensions of MSPs and the immobilized biological recognition elements are different. Therefore, MSPs in each group could capture the designed target species. Since the sizes of MSPs in different groups are different, the resonance frequencies of different groups can be easily determined by a single frequency scan. According to the discussed in previous section, for individual group, the shift in resonance frequency of one sensor can be identified out of other sensors. Fig. 5-10 illustrates the principle of this approach. With multiple-target approach, multiple interested targets can be easily detected simultaneously in the sample with very low concentration. Also, if it is needed, a group of reference MSPs, on which no bio-recognition elements is immobilized, can be employed to eliminate the effect of environmental change.
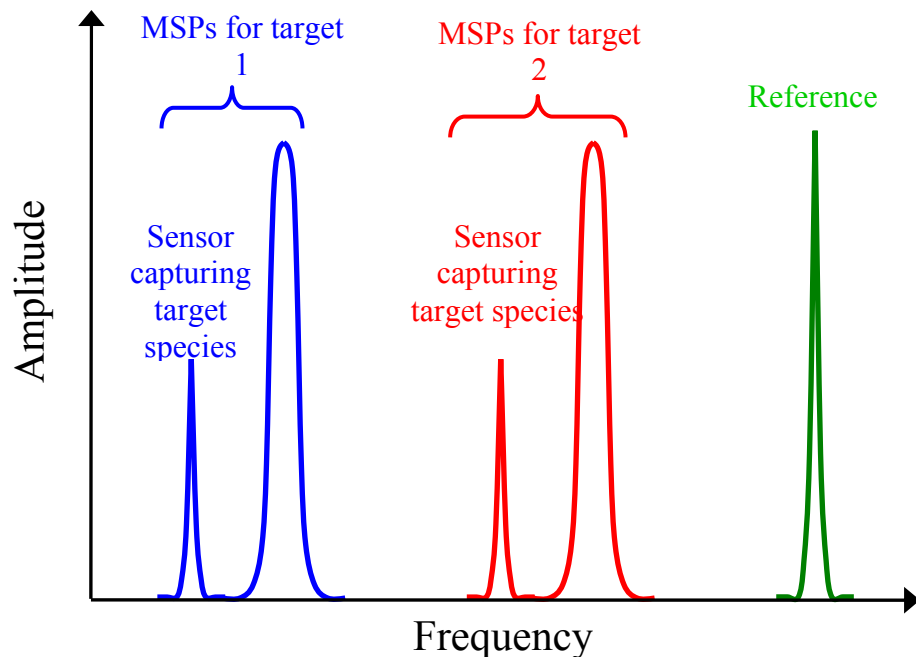
Fig. 5-10. Scheme of multiple-target approach based on MSP sensors to detect different targets simultaneously.

5.3 Experimental

5.3.1 MSP Sensor Platforms and the Material

In this study, a commercially available magnetostrictive material – 2826MB^{TM} ribbon from Honeywell (Morristown, NJ) – was used to make the MSPs. 2826MB^{TM} is a magnetic soft amorphous alloy with a composition about $Fe_{40}Ni_{38}Mo_4B_{18}$, which is widely used in developing magnetostrictive sensors. The thickness of the 2826MB^{TM} ribbon as received is $30\mu m \pm 1\mu m$. The physical and mechanical properties of 2826MB^{TM} ribbon are listed in Table 4-2.

The MSP sensor platforms were fabricated by dicing the 2826MB^{TM} ribbon into strips with designed dimensions using a micro dicing saw. The MSPs with the length of 25 mm ~ 1 mm, width of 5 mm ~ 200 μm, and thickness of 30 μm were fabricated. After dicing, the MSPs were ultrasonically cleaned with ethanol for 10 minutes, and then dried by N_2 gas.

5.3.2 Characterization of Resonance Behavior of MSPs

The resonance behavior of the MSPs was characterized using the interrogating systems discussed in Chapter 3. For the MSPs with bigger size (the length of the MSP bigger than 10 mm), their resonance behavior was characterized by setup A. The MSP was put into a sample chamber that is placed in the middle of the Helmholtz coil, where its oscillation was actuated by the driving magnetic field, which consists of a DC magnetic field less than 15 Oe and an AC field that has amplitude less than 0.1 Oe. The oscillation of the MSP results in the emission of a magnetic signal that is wirelessly sensed using a pair of pick-up coils. A lock-in amplifier (SRS830, Standford

139

research system, Sunnyvale, CA) was employed to measure the output of the pickup coil. Both the amplitude and phase output were recorded as function of frequency. The resonance spectra of the MSPs exhibit a sharp resonance peak in the amplitude signal. Therefore, as discussed in Chapter 3, the amplitude signal was used to characterize the resonance behavior of the MSP. The details of resonance frequency fitting and determination of the Q value were discussed in Chapter 3.

For the MSPs with smaller size (the length is smaller than 10 mm), setup B was used to characterize their resonance behavior. As described in Chapter 3, the MSP was placed in a test chamber with a homemade coil wound outside. The coil was connected to a network analyzer, which generates an AC signal to actuate the MSP and senses its response. For simplicity, the magnitude of S_{11} output from the analyzer is used to characterize the resonance behavior of the MSP. The determination of the resonance frequency and Q value of the MSP was discussed in Chapter 3.

In this study, the resonance frequencies of the MSPs with different sizes were studied. The effects of DC bias and AC driving field on the resonance behavior of MSPs were also investigated.

5.3.3 Mass Sensitivity of the MSPs

In order to characterize the mass sensitivity of MSPs, Gold (Au) was sputtered on the MSP surface as mass load using a sputter coater (PELCO SC-6, Ted Pella, Inc., Redding, CA). The resonance frequencies of the MSPs with different mass loads were measured. Based on the shift in the resonance frequency due to the mass loads, the mass sensitivity of the MSP can be obtained.

In this study, the mass sensitivities of MSPs with uniform mass load, as well as non-uniform mass load, were investigated.

5.4 Results and Discussion

5.4.1 Resonance Frequency and Q value of MSPs
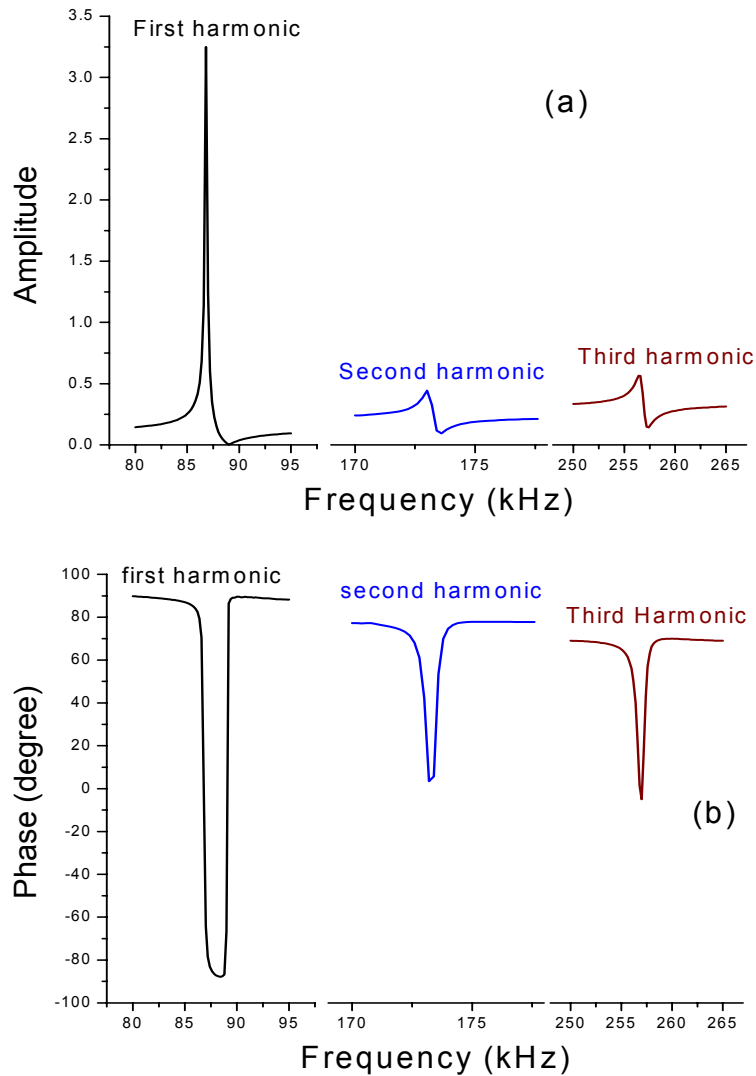
Fig. 5-11. The amplitude (a) and phase (b) signal measured by setup A from a MSP. The size of the MSP is 24.9 mm x 5.0 mm x 30 μm. For this MSP, first three harmonic vibration modes were presented.

Fig. 5-11 shows the resonance spectra of a MSP measured by setup A. The size of the MSP is 24.9 mm x 5.0 mm x 30 μm. In this experiment, the DC magnetic field of 12 Oe was employed, while the AC field has amplitude less than 0.1 Oe. For this MSP, the first three resonance modes were observed using a single scan. Based on the data shown in Fig. 5-11, the resonance frequencies are 86.81, 172.98, and 256.43 kHz, for first to third harmonic mode, respectively. They are consistent to the theoretical value calculated based on Equation (5-10), which are 86.52, 173.04, 259.56 kHz, respectively.
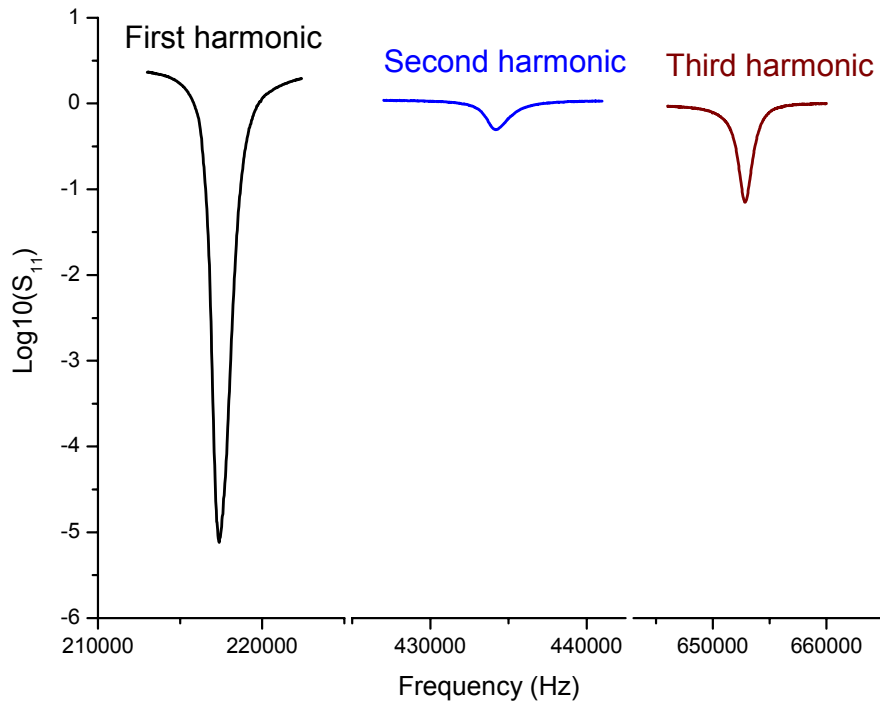
Fig. 5-12. The resonance spectra of a MSP measured using setup B. The size of the MSP is 10.0 mm x 2.0 mm x 30 μm. For this MSP, first three harmonic modes were presented.

Fig. 5-12 shows the resonance spectra of the first three resonance modes for a MSP measured by setup B. The size of the MSP is 10.0 mm x 2.0 mm x 30 μm. Based on data shown in Fig. 5-12, the resonance frequencies are 217.48, 434.33, and 652.93 kHz, for first to third harmonic mode, respectively. The results indicate that, for MSP, both odd and even harmonic mode resonance can be exited and sensed, and the resonance spectrum for multiple modes can be easily measured using a single scan.

During the measurement discussed above, the pickup coil was placed asymmetricly to the MSP, as shown in Fig. 5-13. Since, for even resonance mode, the length of the MSP keeps constant, the magnetic signal can be easily sensed for even mode if the MSP was placed as in Fig. 5-13.
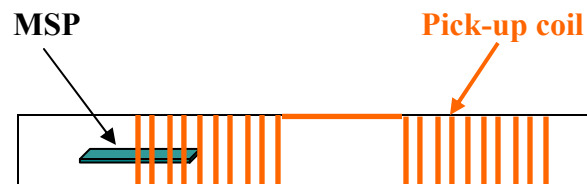
Fig. 5-13. Illustration of the position of MSP and pickup coil during multiple modes measurement.

The sharp resonance peak indicates that MSP sensors have high Q value. A variation was observed in Q value for different MSPs in the same size under same measurement conditions. The reason is that the variation in MSP's geometry due to the mechanical cutting strongly affects its Q value. The Q value higher than 1000 can be observed in air, which is much higher than that of MCs.

143

5.4.2 MSP Performance in Liquid

To study the performance of the MSP in liquid, the resonance behavior of an MSP, in the size of 10 mm x 1 mm x 30 μm, was characterized in air and distilled water using setup B. The resonance spectra of the first, second and third harmonic mode of this MSP in air and water are shown in Fig. 5-14 (a), (b) and (c), respectively. Based on the results shown in Fig. 5-14, the resonance frequencies and Q values of this MSP operating in different media were summarized in Table 5-1. Due to the damping effect of the liquid, the resonance frequency, signal amplitude and Q value of the MSP decreases when operating in liquid. However, the resonance frequency of the MSP in water is only slightly smaller than that in air. For all first, second and third harmonic modes, the Q values of the MSP in water are higher than 100, which are much higher than that of MCs operating in liquid. The damping effect caused by surrounding liquid on MSP is much smaller than that on MCs. The reason is that, for MCs operating in liquid, which are vibrating at flexural mode, the whole cantilever beam has to push the surrounding liquid; while for MSPs, whose vibration mode is longitudinal, only the cross section areas at two ends need to push the liquid. Therefore, the MSP exhibits a Q value about 10 times higher than MCs both in air and in liquid, which makes it a good candidate as a biosensor platform for real-time or in-vivo detection.

TABLE 5-1
MSP Performance in Air and Water

	First harmonic		Second harmonic		Third harmonic	
	air	water	air	water	air	water
Resonance frequency (kHz)	224.03	220.96	447.59	445.01	676.95	674.36
Q value	778	123	266	120	756	150
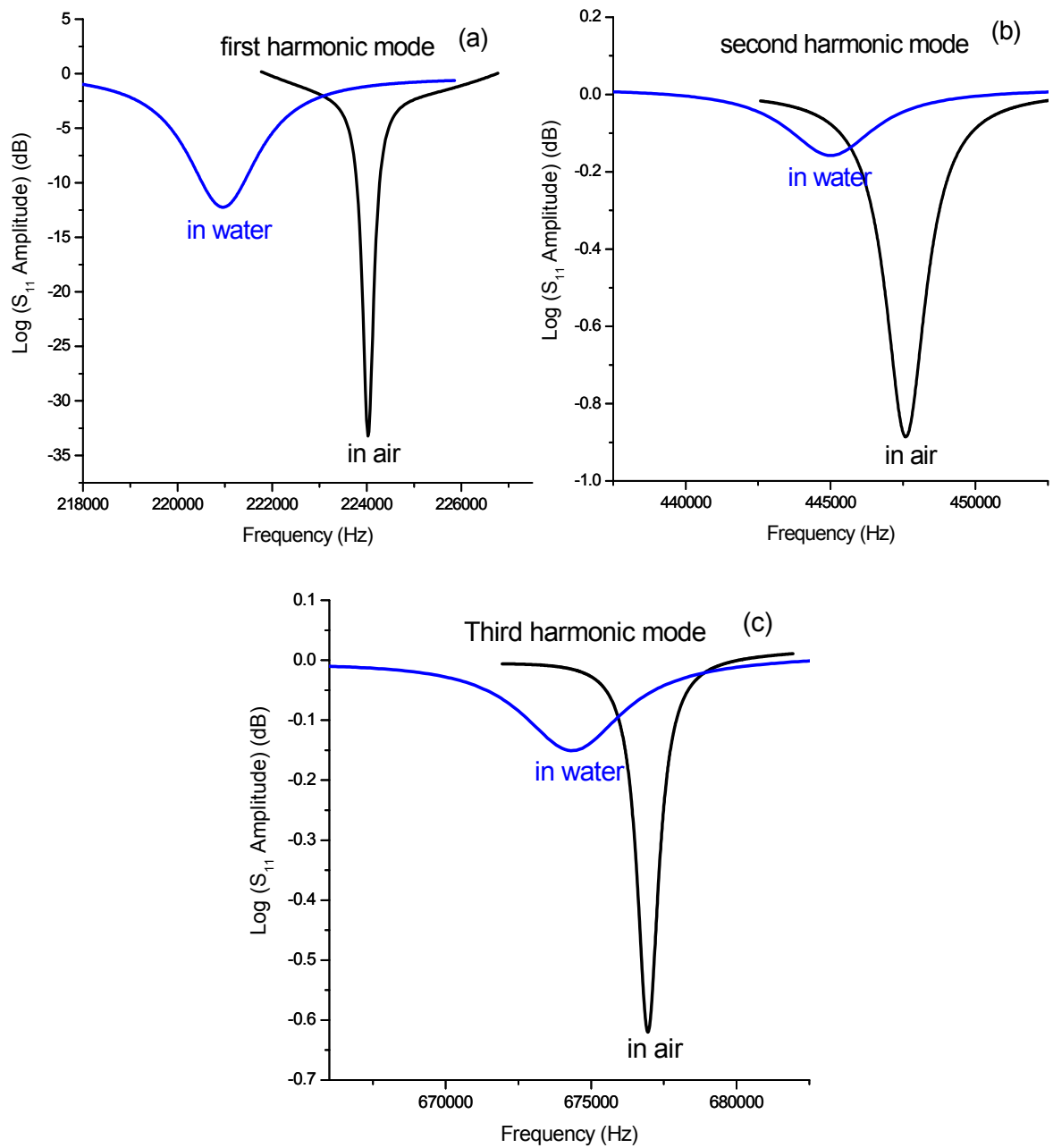
Fig. 5-14. MSP performance in air and water for (a) the first harmonic mode, (b) second harmonic mode, and (c) third harmonic mode.

5.4.3 Influence of DC Bias on Resonance Behavior of MSPs

The driving magnetic field for operating a MSP consists of two parts: a DC bias and an AC driving field. To study the influence of the DC bias on the response of the MSP, the resonance behavior of a MSP, in the size of 25 mm x 5 mm x 30 μm, was measured under same AC field (amplitude is 0.16 Oe MRS), but different DC biases. Fig. 5-15 shows the resultant resonance spectra of this MSP for the first harmonic mode.
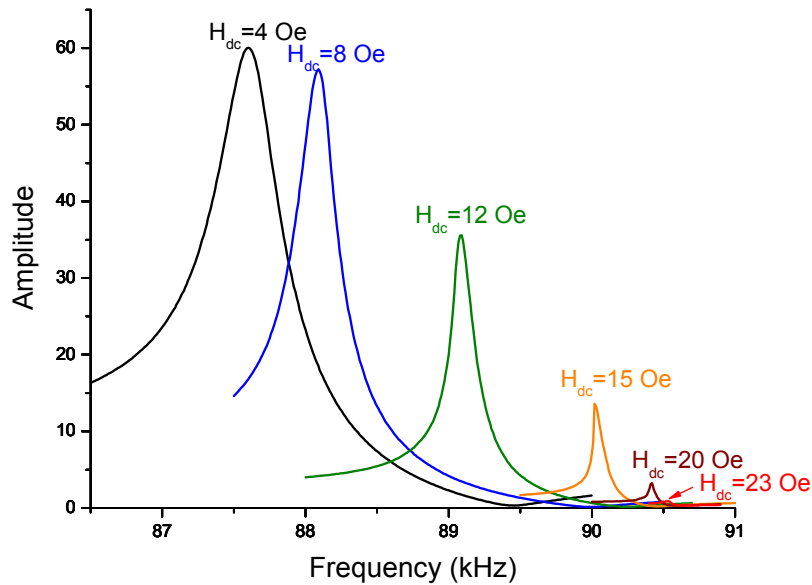
Fig. 5-15. The resonance spectra for the first harmonic mode of a MSP, which were measured under same AC field (amplitude is 0.16 Oe MRS), but different DC bias using setup A. The size of the MSP is 25 mm x 5 mm x 30 μm.

As shown in Fig. 5-15, with increasing DC bias, the amplitude of output resonance peak of the MSP decreases. According to the discussion in Chapter 1, the magnetostriction of a magnetostrictive material is an even function of the external magnetic field, as shown in Fig. 5-16. Under a certain DC bias, an enhanced linear response can be obtained. But the DC bias affects the piezomagnetic constant, thus the

amplitude of the output. If the DC bias is further increased to close to the saturation field, the output signal would become weaker with increasing DC bias, which is consistent with the experimental results shown in Fig. 5-15.
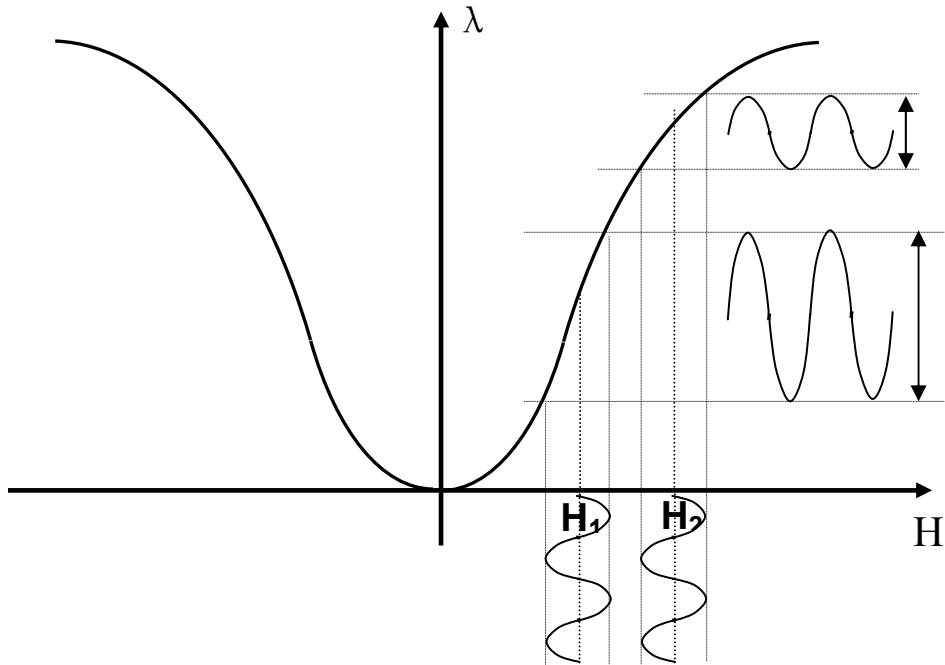
Fig. 5-16. Magnetostriction (λ) of a typical magnetostrictive material changing with external magnetic field (**H**).

Based on the results shown in Fig. 5-15, the resonance frequencies and Q value of this MSP measured under different DC biases were summarized in Table 5-2. The results show that, even though further increasing the DC bias will weaken the output signal, the resonance frequency and the Q value of the MSP increase. The reason is that the Young's modulus of the material increases with the increasing DC bias. Therefore, for MSP, we can choose an optimized DC bias to obtain a higher Q value, as well as reasonable high output.

147

TABLE 5-2

Resonance Behavior of a MSP (25 mm x 5 mm x 30 μm) Measured under Same AC field, but Different DC Biases

DC bias (Oe)	Resonance frequency (kHz)	Q value
4	87.6	169
8	88.1	304
12	89.1	446
15	90.02	1125
20	90.4	1292
23	90.5	1293

5.4.4 Influence of AC Driving Field on Resonance Behavior of MSPs

To drive the MSP sensor, a uniform AC magnetic field with a DC bias is applied on the sensor. From the technical point of view, it is difficult to obtain uniform AC magnetic field over a very large area. The magnetic field applied on the MSP might vary because of the non-uniformity of the magnetic field or variation in the distance between sensor and the driving field. Therefore, there is a great concern about the influence of AC field strength on the resonance behavior of the MSP. To study the influence of AC driving magnetic field, the spectrum for the first harmonic mode of a MSP in the size of 24.3 mm x 5 mm x 30 μm was measured under the different AC driving magnetic fields. By keeping the DC bias constant (12 Oe), AC magnetic fields with the amplitude of 0.04, 0.08, 0.16, 0.24, and 0.32 Oe (MRS) were applied as the driving field. The resultant resonance spectra of the MSP sensor under different AC driving fields were shown in Fig. 5-17 (a), while the normalized spectra were shown in Fig. 5-17 (b).
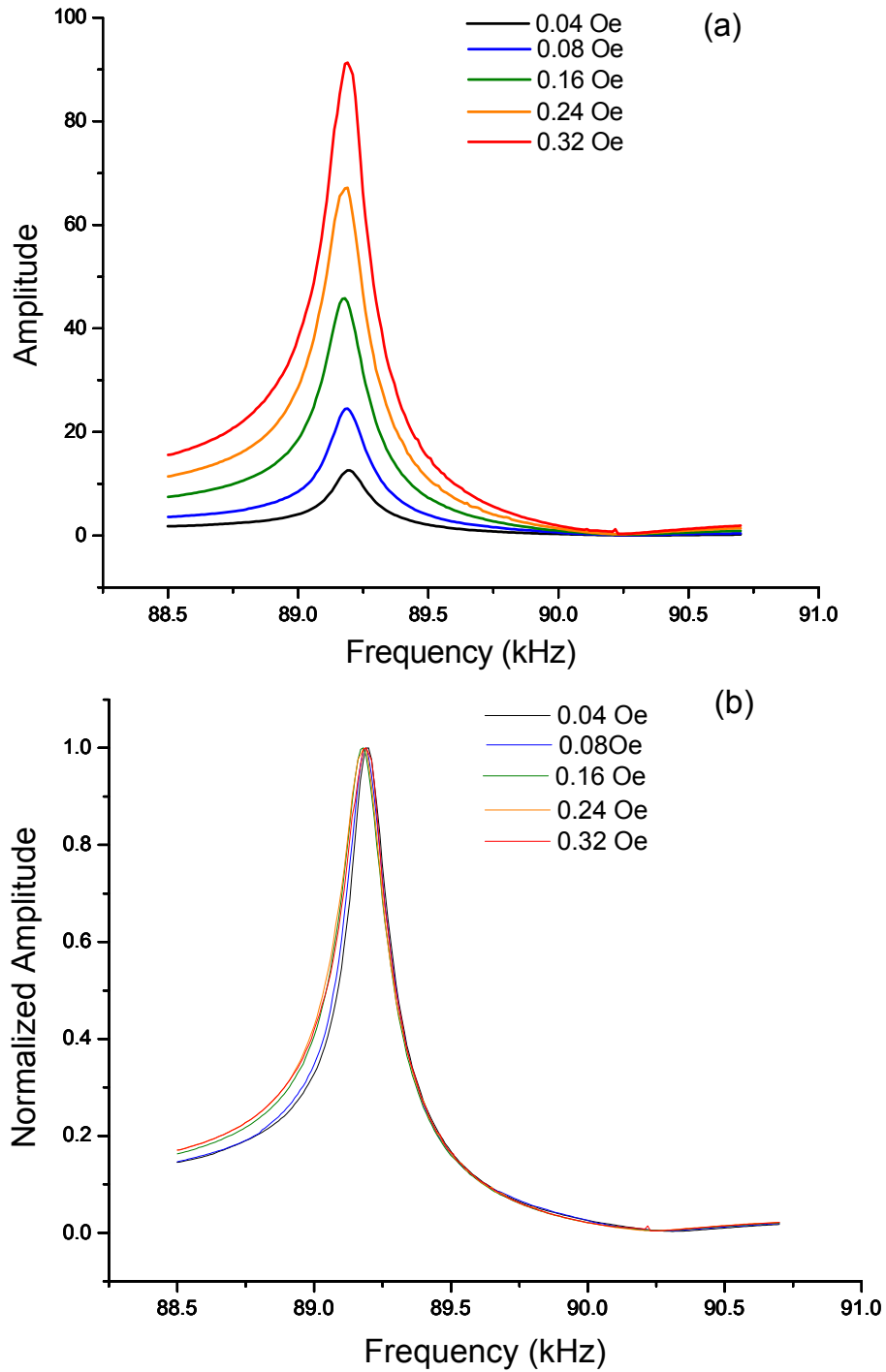
Fig. 5-17 (a) Spectra for the first resonance mode of a MSP, in the size of 24.3 mm x 5 mm x 30 μm, measured under the different AC driving magnetic fields. (b) Normalized spectra for the results shown in (a).

The resonance frequencies and Q values of the MSP under the AC field with different amplitudes were determined by fitting peaks shown in Fig. 5-17 used using Lorentz function. The results were summarized in Table 5-3. To estimate the fitting error, the resonance peak measured under AC field with amplitude of 0.32 Oe was fitted with different frequency ranges, and the results were listed in Table 5-4. The results indicate that the fitting will cause an error about ±0.004 kHz in the resonance frequency and ±39 in the Q value. Therefore, the variation in the resonance frequency and Q value shown in Table 5-3 can be considered as the fitting error. The normalized spectra shown in Fig. 5-17 (b) and the results shown in Table 5-3 revealed that, although the amplitude of the resonance frequency peak increases with increase of the amplitude of the AC driving field, the resonance frequency and Q value of the MSP is independent of the amplitude of the AC field. This makes it easy to build the operating system.

TABLE 5-3

Resonance Behavior of a MSP (24.3 mm x 5 mm x 30 μm) Measured under Same DC

Bias, but Different AC Fields

AC field (MRS)	Resonance frequency (kHz)	Q value
0.04 Oe	89.19	425
0.08 Oe	89.188	409
0.16 Oe	89.176	411
0.24 Oe	89.176	405
0.32 Oe	89.18	413

TABLE 5-4

Fitting Results Based on Lorentz Function with Different Fitting Ranges for the Resonance

Peak Shown in Fig. 5-15 Measured under AC Field with Amplitude of 0.32 Oe

Fitting range (kHz)	Resonance frequency (kHz)	Q value
88.75 – 89.5	89.187	446
88.75 - 90	89.183	413
88.5 – 89.5	89.18	388

5.4.5 Resonance Frequency Change with MSP's Lengths

For a MSP sensor, given the material, the resonance frequency of the MSP is only dependent on its length. The resonance frequencies for the first harmonic mode of the MSPs with different lengths were measured and were shown in the Fig. 5-18, where the solid squares represent the experimental data. Based on Equation (5-10), the theoretical resonance frequencies of MSPs with different lengths were calculated. The results were shown in Fig. 5-18 as the dotted line. The Young's modules, density, and Poisson ratio used in the calculation were 110 GPa, 7.9×10^3 kg/m^3, and 0.5, respectively. The results show that the measured resonance frequencies of the MSPs are consistent with the theoretical values, which indicates the validity of the design.
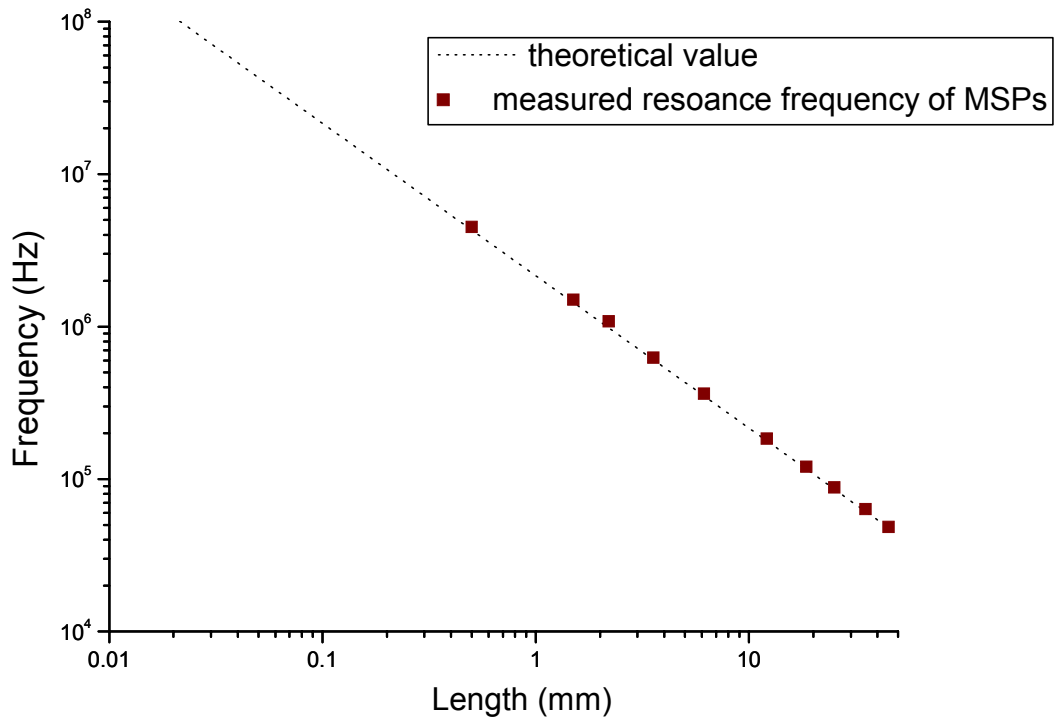
Fig. 5-18. Resonance frequencies for the first harmonic mode of MSPs with different lengths.

5.4.6 Sensitivity of MSPs with Uniform Mass Load

To characterize the S_m of MSP, Gold (Au) was uniformly sputtered on one side of the MSP surface as the mass loads. The mass loads were measured by a balance, and then the shifts in the resonance frequency due to different mass loads were measured. The shifts in the resonance frequency versus mass loads for MSPs with different dimensions were plotted in Fig. 5-19, where the first mode resonance frequency was used. Based on these data, the S_m of the MSPs with different sizes were obtained and listed in Table 5-5.
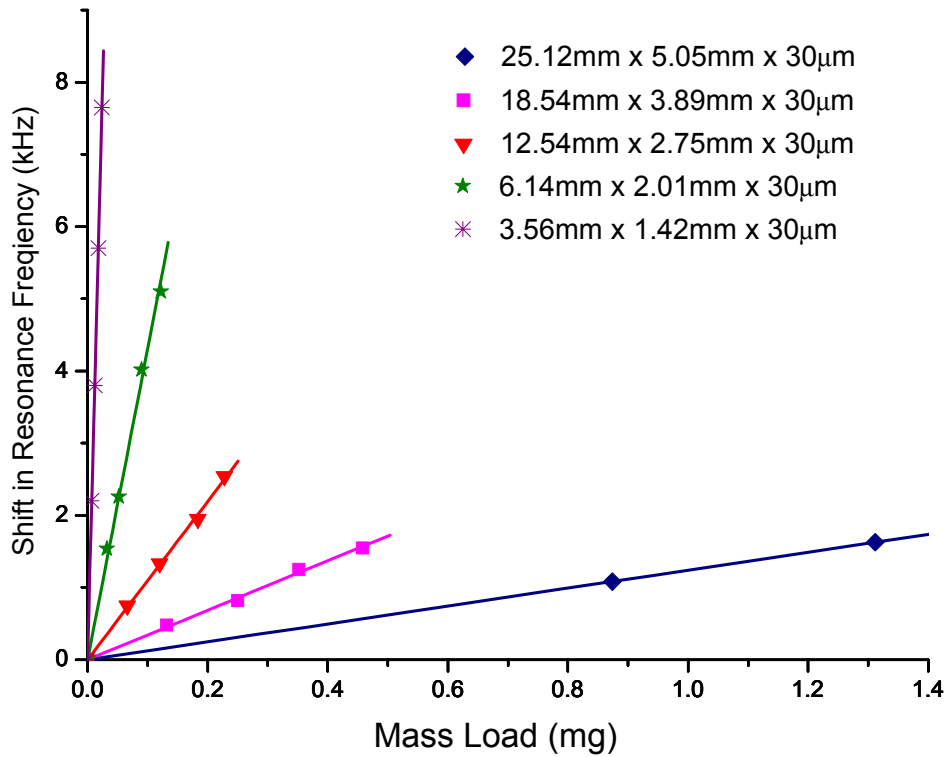
Fig. 5-19. Resonance frequency shift caused by uniform mass load for the MSPs with different dimensions. The first harmonic mode was used here.

TABLE 5-5

Mass Sensitivity of MSPs with Different Dimensions

MSP dimensions	Experimental mass sensitivity (kHz/mg) obtained from Figure 5-19	Corresponding mass sensitivity (kHz/mg) of the MSP with the same length and thickness, but $\alpha = 10$.
25.12mm x 5.05mm x 30μm	1.24	2.49
18.54mm x 3.89mm x 30μm	3.43	7.20
12.54mm x 2.74mm x 30μm	10.97	23.97
6.14mm x 2.01mm x 30μm	43.08	141.03
3.56mm x 1.42mm x 30μm	319.44	1274.17

153

According to Equation (5-18 a), if we keep the thickness and the ratio of the length to width constant, the S_m of the MSP would be only dependent on its length, as $S_m \propto 1/L^3$. Therefore, for convenience, the experimental mass sensitivities were converted to the corresponding mass sensitivities of the MSPs whose width is 1/10 of the length ($\alpha = 10$). The results were also listed in the Table 5-5 and plotted in Fig. 5-20 as green triangles. By keeping the ratio of MSPs length to width as 10 and the thickness as 30 μm, the theoretical S_m of MSPs with different lengths was calculated based on Equation (5-18 a) and also plotted in Fig. 5-20 as solid blue line. It is clearly shown that the experimental results agree very well with the theoretical values. As the size of the MSP decreases, its thickness would decrease too, which causes the further increase in the S_m. Therefore, the S_m of the MSPs in the thickness of 1 μm was calculated based on Equation (5-18 a) and plotted in Fig. 5-20 as solid wine line. The results shown in Fig. 5-20 indicate that, the MSP would be capable of detecting a mass of several picograms with length less than 100 μm. Considering the weight of a bacterium cell is about 1~2 pg, these MSPs are capable of detecting a single cell. Further decreasing the dimension, MSP would be able to detect viruses, even DNA. Therefore, for extremely sensitive detection, MSPs in size of micrometer to nanometer are desired.
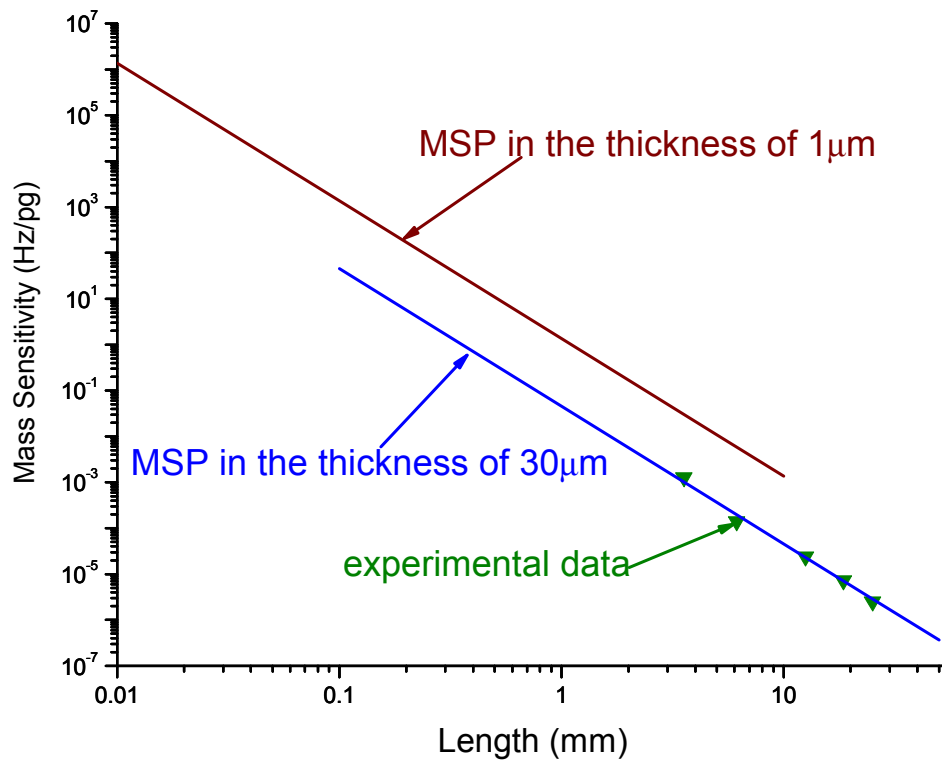
Fig. 5-20. Mass sensitivities versus lengths for MSPs with different dimensions. Solid triangles are experimental data; solid lines are the results obtained by the theoretical simulation. The ratio of the length to width of MSPs shown in this picture is 10.

5.4.7 Mass Sensitivity of MSPs with Non-uniformed Mass Load

As discussed previously, MSP can overcome the effect of non-uniform mass loads by operating the MSP under multiple resonance modes. Therefore, the effect of the mass load location on the MSP mass sensitivity was studied. In this study, the MSPs in the size of about 10 mm x 1 mm x 30μm were employed. Gold (Au) was sputtered at different areas on the MSP as mass loads. As shown in Fig. 5-21 (a), the mass loads were added on the MSP at the free ends, the middle (node   point for the odd resonance modes) and

the ¼ lengths from the end (node points for the second harmonic mode). The details of the MSP dimensions and the sized of mass loads in this experiment are shown in Fig. 5-21 (b).
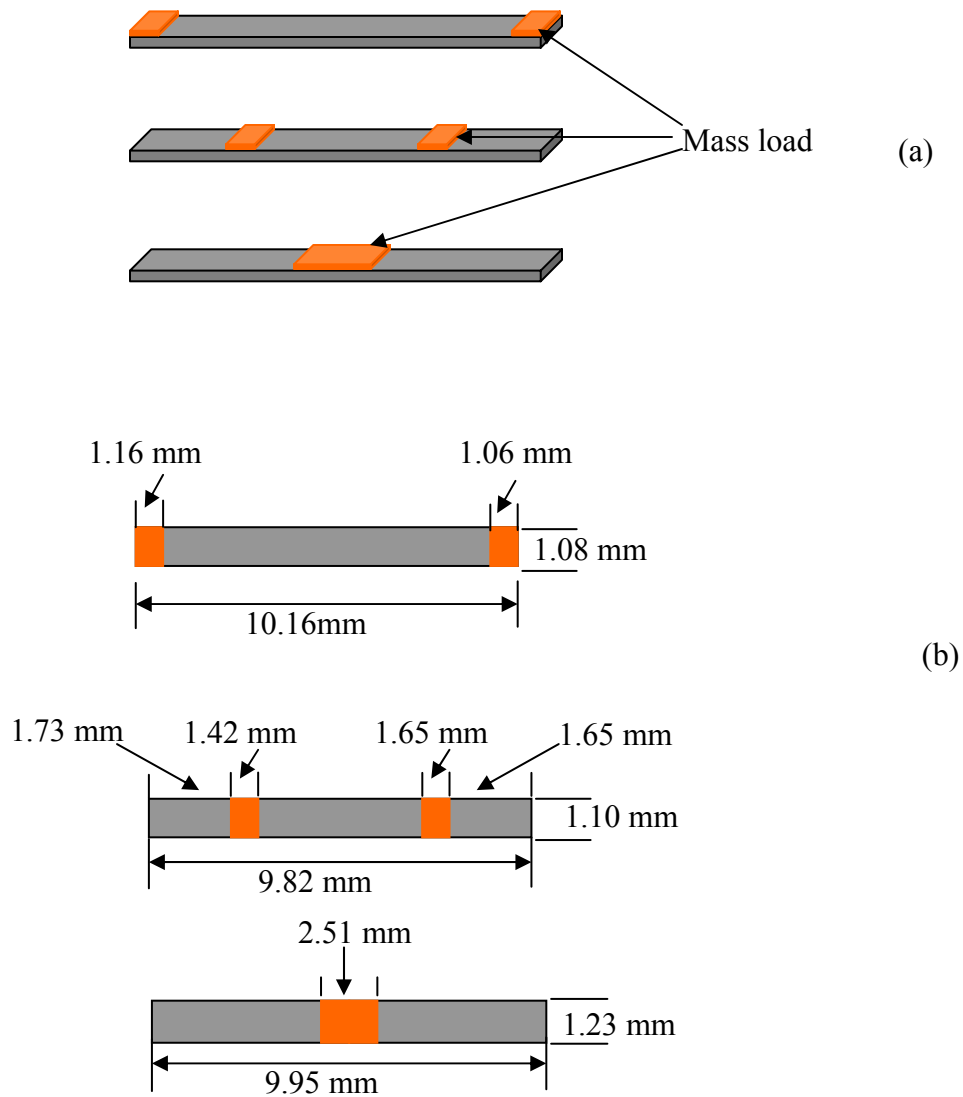
Fig. 5-21 (a). Non-uniform mass loads on the MSP surface; (b) The MSP dimensions and the mass load sizes for characterizing the mass sensitivity with non-uniform mass loads.

The mass loads on MSP surface can be calculated based on the volume and the density of Au. The mass volume is obtained from the deposition rate and time of Au (30 nm/min in this experiment) and the sizes shown in Fig 5-21 (b), while the density of Au used in the calculation is 19300 kg/cm^3 [12]. The MSPs with different mass loads were operated under first and second harmonic mode, and then the shifts in the resonance frequencies due to the mass loads at different locations were measured. The results were shown in Fig. 5-22 (a) for first harmonic mode, and Fig. 5-22 (b) for second harmonic mode. The red stars, blue triangles, and blue squares represent the resonance frequency shifts due to the mass loads at the free ends, the ¼ lengths from the end, the middle of the MSP, respectively. The results are consistent to theoretical analysis. Based on the results shown in Fig. 5-22, the mass sensitivities of the MSP for mass loads at different locations can be obtained and were summarized in Table 5-6. Based on Equation (5-18 a), the theoretical mass sensitivity due to uniform mass load for MSP in the size of 10 mm x 1 mm x 30μm was calculated and also shown in Table 5-6.
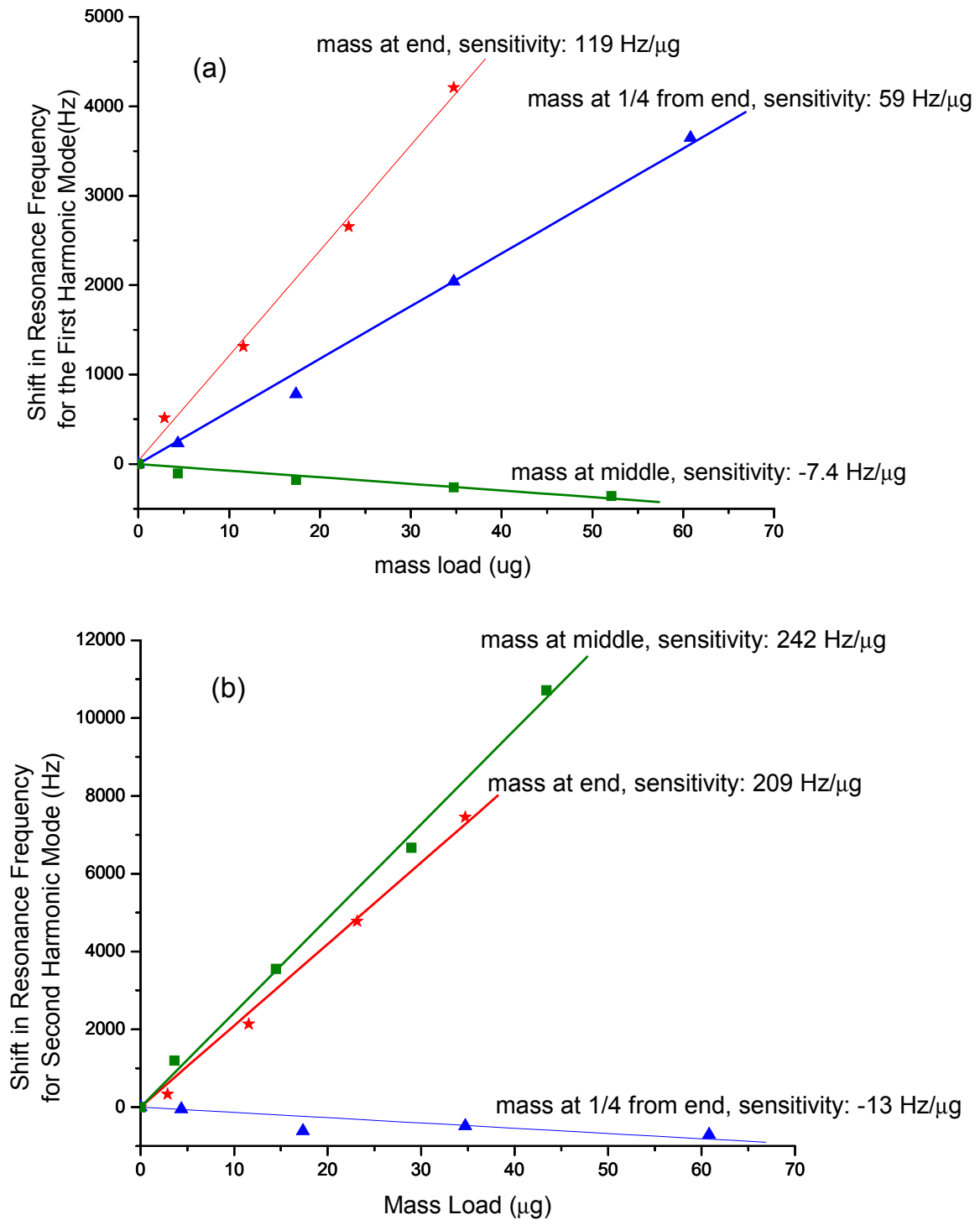
Fig. 5-22. Shifts in MSP resonance frequencies caused by the mass loads at different locations, where (a) is for first harmonic mode; (b) is for second harmonic mode.

158

TABLE 5-6

Mass Sensitivities of the MSP for Mass Loads at Different Locations

	S_m for first harmonic mode	S_m for second harmonic mode
Mass at free ends of MSP	119 Hz/µg	209 Hz/µg
Mass at the ¼ length from the end of MSP	59 Hz/µg	-13 Hz/µg
Mass at the middle of MSP	-7.4 Hz/µg	242 Hz/µg
Theoretical S_m due to uniform mass load for MSP with size of 10 mm x 1 mm x 30µm	45.5 Hz/µg	91 Hz/µg

The results indicate that, when MSPs are operated under first harmonic resonance, the MSP is most sensitive to the mass loaded at the free end, but can not detect the mass loaded at the middle, which is the node point for first harmonic mode. On the other hand, for second harmonic mode, MSP is very sensitive to mass loaded on the free ends as well as on the middle of the MSP, while the sensitivity is almost zero for the mass loaded at the ¼ length from the end. No matter where the mass is loaded, it can be detected by a corresponding harmonic mode.

5.4.8 Demonstration of Multiple-Sensor Approach

Multiple–sensor approach based on MSPs provides a simple method to bring the sensors to the target species, thus is able to detect target in very low concentration environment. For a very low concentration environment, only few sensors have the chance to capture the target cells even using the multiple–sensor approach. Here, we

demonstrate that individual MSPs respond to the mass load independently and can be detected out of bunch of MSP sensors.

To demonstrate multiple-sensor approach, 10 MSP sensors in the size of 12.5 mm x 2 mm x 30 μm were scanned together. As shown in Fig. 5-23 (a), a single big peak was observed in the spectra since the sensors have same resonance frequency. Then the mass load was added on one of the sensors. The 10 sensors were scanned together again, and the spectrum was shown in Fig. 5-23 (b). Comparing Fig. 5-23 (a) and (b), we can clearly see the shift in the resonance frequency of the sensor due the mass load: the resonance frequency peak of the sensor is separated from the peak of the rest sensors, and can be easily identified. This demonstrates that the multiple sensor approach works very well. Even if only one sensor captures the target cells, it can be identified out of other sensors. This approach provides a rapid and easy method to detect bacteria cells in extremely low concentration.
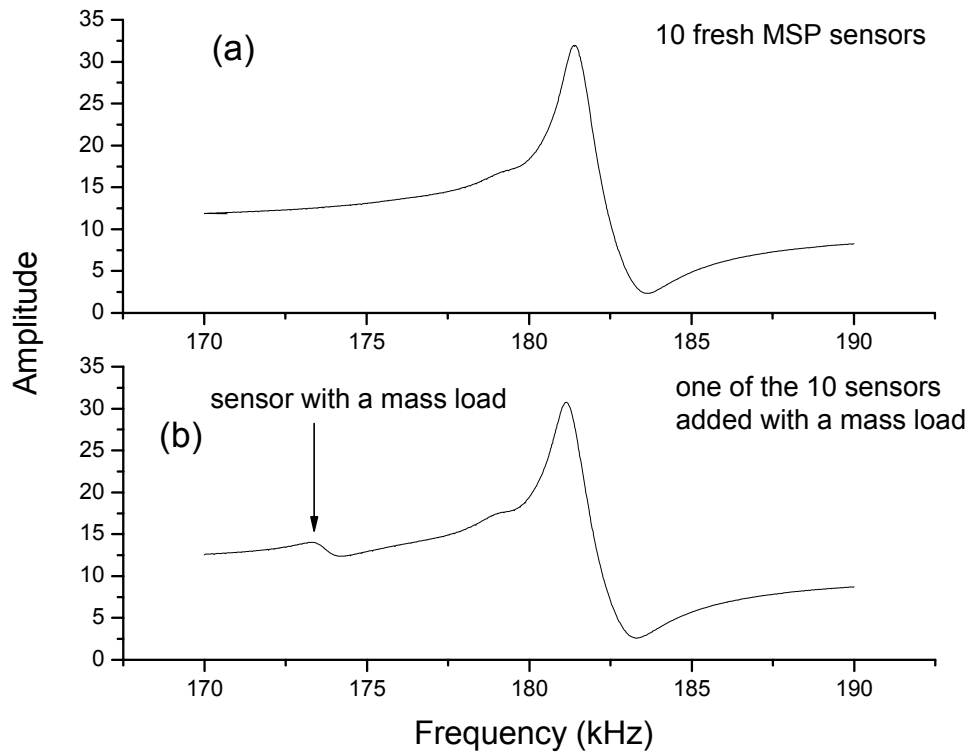
Fig. 5-23. Demonstration of multiple sensor approach.

5.4.9 Demonstration of Multi-target Detection

By employing several groups of MSPs, multiple target species can be detected simultaneously by the multi-target approach. To demonstrate the multiple-target approach, two groups of MSP sensors were employed and characterized together. Each group includes two MSP sensors with slight different length. One group of MSPs has longer lengths: MSP L1 is in the size of 25.05 mm x 5 mm x 30 μm, and MSP L2 is in the size of 25.23 mm x 5 mm x 30 μm; another group of MSPs has shorter lengths: MSP S1 is in the size of 23.05 mm x 5 mm x 30 μm; and MSP S2 is in the size of 23.34 mm x 5 mm x 30 μm. Two groups of MSPs were put in   the   test   chamber   and   their   resonance

161

frequencies were measured by a single scan. The results were shown in Fig 5-24 (a). It clearly showed that the resonance frequencies of all the MSPs can be identified and the resonance frequencies separated into two groups. Gold (Au) was sputtered on MSP L2 and MSP S1 surface as mass load, and then the resonance frequencies of the two groups were scanned again. The results were shown in Fig. 5-24 (b). For each group, the shift in the resonance frequency of the MSP with the mass load can be easily identified in Fig. 5-24 (b). This demonstrated that by employing MSP sensors, two or more interested species can be monitored simultaneously using multiple-target approach.
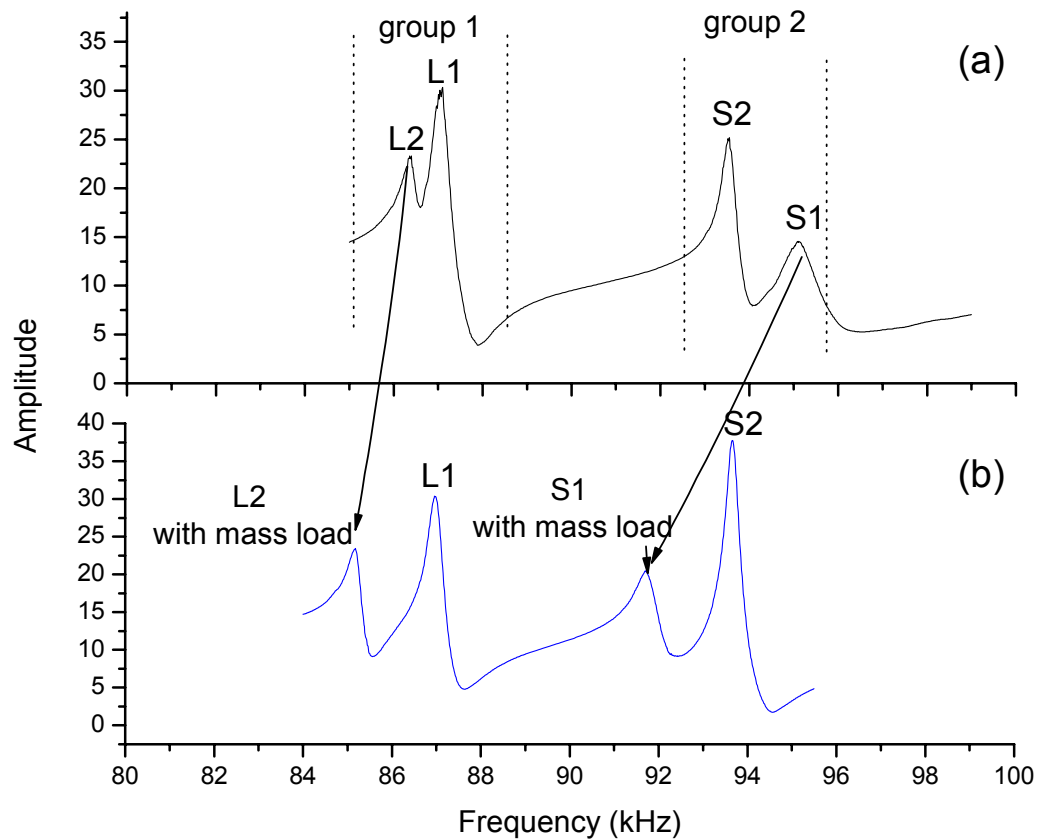
Fig. 5-24. Demonstration of the multiple-target approach.

5.5 Conclusion

The magnetostrictive particle (MSP) was introduced as a novel wireless AW sensor platform for developing high performance biosensor. Interrogated through magnetic field, MSPs don't need any physical connection for driving and sensing, which allows remote *in vivo* detection. This is the principle advantage of MSPs over other AW devices. The feasibility study of MSPs showed the experimental results agree with the theoretical values very well. Using as a single sensor platform, it was found that the MSP exhibit a mass sensitivity about 100 times higher and a Q value about 10 times higher than MCs. The mass sensitivity of the MSPs increases with the decrease of the MSP size. It was found that, theoretically, they have the capability to detect single bacteria cell when the length of the MSP sensor is less than 100 μm. By employing multiple MSPs, the performance of the MSP can be further improved using multiple-sensor approach and multiple target approach. The multiple sensor approach provides a rapid and easy method to detect target cells in extremely low concentration, while multiple-target approach allows two or more interested species are monitored simultaneously. Additionally, as a free-standing sensor, MSPs can detect a mass load attached at any location by operating it at both odd and even harmonic mode.

References

[1]   B. Ilic, D. Czaplewski, H. G. Craighead, P. Neuzil, C. Campagnolo, and C. Batt, "Mechanical resonant immunospecific biological detector," *Applied Physics Letters*, vol. 77, pp. 450-452, 2000.

[2]   C. Ziegler, "Cantilever-based biosensors," *Analytical and Bioanalytical Chemistry*, vol. 379, pp. 946-959, 2004.

[3]   Z. Y. Shen, W. Y. Shih, and W. H. Shih, "Mass detection sensitivity of piezoelectric cantilevers with a nonpiezoelectric extension," *Review of Scientific Instruments*, vol. 77, 2006.

[4]   P. Sheehan, "How diffusion causes problems for nanotechnology (and how to overcome them)," Naval Research Laboratory, 2007.

[5]   P. Gould, "Nanoparticles probe biosystems," *Materials Today*, vol. 7, pp. 36-43, 2004.

[6]   A. G. Gehring, C. G. Crawford, R. S. Mazenko, L. J. VanHouten, and J. D. Brewster, "Enzyme-linked immunomagnetic electrochemical detection of Salmonella typhimurium," *Journal of Immunological Methods*, vol. 195, pp. 15-25, 1996.

[7]   J. M. Nam, C. S. Thaxton, and C. A. Mirkin, "Nanoparticle-based bio-bar codes for the ultrasensitive detection of proteins," *Science*, vol. 301, pp. 1884-1886, 2003.

[8]   L. D. Landau and E. M. Lifshitz, *Theory of elasticity*: Pergamon Press, 1986.

[9]   J. Merhaut, *Theory of electroacoustics*: New York ; London : McGraw-Hill International Book Co., 1981.

[10]   D. S. Ballantine, White, R.M., Martin, S.J., Ricco, A.J., Frye, G.C., Zellers, E.T., Wohltjen, H., *Acoustic wave sensors: theory, design and physico-chemical applications*: Academic Press, 1997.

[11]   B. Ilic, Y. Yang, K. Aubin, R. Reichenbach, S. Krylov, and H. G. Craighead, "Enumeration of DNA molecules bound to a nanomechanical oscillator," *Nano Letters*, vol. 5, pp. 925-929, 2005.

[12]   R. A. Serway, *Physics for scientists and engineers*, second ed: CBS College Publishing, 1986.

CHAPTER 6

SYNTHESIS OF AMORPHOUS IRON-BORON ALLOY FOR

MAGNETOSTRICTIVE BIOSENSOR PLATFORM APPLICATION

6.1 Introduction

In the previous chapters, the theoretical simulations and the experimental results indicated that the sensitivity of the MSP and MSMC increases with decreasing sensor dimensions. Therefore, to obtain a highly sensitive sensor, the magnetostrictive alloy with feature sizes in microscale to nanoscale is required. At the same time, based on Equation (5-10), the resonance frequency of the sensor increases with the reducing length. That is, the smaller the sensor, the higher the S_m of the sensor, at the same time, the higher the resonance frequency f_0. For example, for MSPs made of commercial 2826MB^{TM} metglas in the length of 1 mm, 100 μm, 10 μm, and 1 μm, the resonance frequencies are 2.15 MHz, 21.5 MHz, 215 MHz, and 2.15 GHz, respectively.

Current research of magnetostrictive biosensor platforms are based on commercially available magnetostrictive materials, such as 2826MB^{TM} metglas [1-5]. These commercially available materials are amorphous Fe-based alloys, which exhibit a high Q value as discussed in Chapter 5. However, these magnetostrictive materials are cast by liquid-quenching technique: the molten alloy is projected onto a rotating cooling wheel, where it is cooled at the rate of 10^6 degree/s. The quick quenching freezes the microstructure of the alloy in its liquid state [6]. By employing this technique,

amorphous alloy ribbons, typically in width of 10 ~ 100 mm and thickness of 20 ~ 30 μm, are produced. It is not realistic to fabricate devices in the size of micrometer to nanometer using these ribbons. It is necessary to synthesize the magnetostrictive materials by the methodology that can be combined with micro/nano- structure fabrication process.

To obtain high performance biosensors with feature size in microscale to nanoscale, the magnetostrictive materials that have high Q value at high frequency are highly desired. However, at present, little research has been focused on developing magnetostrictive materials working at high frequency range. A great deal of attention has been spent on the development of magnetostrictive materials with giant magnetostriction. Giant magnetostrictive materials are excellent candidates for building actuators working at low frequency. However for sensor applications, Q value is more important than magnetostriction. As discussed in Chapter 1, magnetic soft materials exhibit a slim *M-H* loop, which is favorable for minimizing the energy loss and obtaining high Q value when vibrating under external magnetic field. Therefore, magnetically soft alloys are favorable for sensor applications. Even through there are soft magnetostrictive alloys, mostly amorphous alloys, commercially available and these materials have been extensively studied, little studies have been done on these materials at high frequencies.

In this research, the amorphous Fe-B alloy, with a composition about 80 atm% of Fe and 20 atm% B, was chosen as the magnetostrictive material for fabricating micro/nano magnetostrictive AW devices, since it exhibits favorable properties for AW sensor application. Table 6-1 shows the physical and mechanical properties of bulk $Fe_{80}B_{20}$ alloy prepared by liquid-quenching [7-9]. From the magnetic property point of view, the Fe-B alloy is magnetically soft [7]. Also, because of the amorphous structure, it exhibits

magnetic isotropy. Therefore, the magnetic domains can be easily switched by a small magnetic field. The Fe-B alloy is expected to exhibit high Q value when operated by AC magnetic field. The amorphous $Fe_{80}B_{20}$ alloy exhibits moderately high saturation magnetostriction, $\lambda_s \approx 31 \times 10^{-6}$ [7], which is larger than that of commercially available $2826MB^{TM}$ ($\lambda_s \approx 12 \times 10^{-6}$). From the mechanical property point of view, amorphous Fe-B binary alloy has a high Yong's modulus (~ 170 GPa) [9], which is favorable to obtain high Q value at oscillation. Besides, Fe-B alloy exhibits other favorable properties. For example, amorphous Fe-B alloy has high magneto-mechanical coupling efficiency (k_{33}^{max} = 0.64) [8, 10]; and the electric resistivity of $Fe_{80}B_{20}$ alloy is about 1.4 μΩ·m (which is about 20 times higher than that of Ni), which makes it possible to work at high frequency range with a good performance [7, 8]. Finally, from a process point of view, Fe-B alloy is a two-component system, which is relatively easier to synthesize and achieve desired composition than a multi-component system. Considering these facts, the Fe-B alloy with the composition about 80% Fe and 20% B is expected to be a good candidate for micro/nano MSPs fabrication.

The amorphous structure of the Fe-B alloy also makes it favorable for micro/nano fabrication process. Since the alloy is isotropic, there is no preferred growth direction during the synthesis of the material, which makes it easier to obtain a desired shape through micro/nano structure fabrication with designed performance.

TABLE 6-1

Properties of Bulk $Fe_{80}B_{20}$ Alloy Prepared by Liquid-quenching[7, 9, 11]

Density (kg/m^3)	7.39 x 10^3
Young's modulus (GPa)	166
Crystallization temperature (^{o}C)	448
H_c (Oe)	0.08
Squareness (Mr/Ms) (as cast)	0.51
Magnetostriction (λ_s) (10^{-6})	31
Electric resistivity ($\mu\Omega$m)	1.5
Poisson's ratio (σ)	0.3

Amorphous Fe-B alloy with the composition about 80% Fe and 20% B has been prepared by sputtering, and electrochemical deposition [12-14]. In this research, the Fe-B alloys were synthesized by electrochemical deposition. The electrochemical deposition process is compatible with Si-microfabrication process and template-based synthesis to fabricate micro and nano MSPs. In this chapter, Fe-B thin films were first synthesized and their properties are studied for AW sensor applications.

6.2 Experimental

6.2.1 Materials

The Fe-B thin films were electrochemically deposited from aqueous basic solution of iron sulfate heptahydrate ($FeSO_4 \cdot 7H_2O$), potassium tetrahydridoborate (KBH_4), sodium hydroxide (NaOH), and potassium sodium tartrate tetrahydrate ($KNaC_4H_4O_6 \cdot 4H_2O$), where $FeSO_4 \cdot 7H_2O$ provides the source for iron; KBH_4 works as the reductant as well as the resource of boron; NaOH is the pH control agent; and $KHaC_4H_4O_6 \cdot 4H_2O$ is the

complexing agent for preventing the formation of iron hydroxide precipitation.

$FeSO_4 \cdot 7H_2O$ (ACS, 99+% purity), KBH_4 (98% purity), and $KHaC_4H_4O_6 \cdot 4H_2O$ (ACS, 99.0 – 102.0%) were obtained from Alfa Aesar. NaOH (ACS, pellets, 97+% purity) was obtained from Aldrich Chemical Company. All the chemicals were used as received.

6.2.2 Preparation of Deposition Solution

The chemicals for preparing the deposition solution were weighted using a balance with a resolution of 0.0002 g. The preparation procedure is important for successfully making deposition solutions [12]. First, $KNaC_4H_4O_6 \cdot 4H_2O$ was dissolved in distilled water, whose amount was at least 80% of the amount of the final solution in order to prevent the precipitation. After $KNaC_4H_4O_6 \cdot 4H_2O$ was totally dissolved, $FeSO_4 \cdot 7H_2O$ was added into the solution and dissolved. At the same time, NaOH was dissolved in distilled water in another beaker. And then, it was added and mixed uniformly into the solution. Finally, KBH_4 was mixed into the solution until it completely dissolved. The solution was then ready for use.

6.2.3 Electrochemical Deposition of Amorphous Fe-B Thin Film

All the Fe-B films were deposited under galvanostatic deposition. The deposition process was controlled by Epsilon^{TM} electrochemistry analysis network from Bioanalytical System, Inc. For precise control, three electrodes configuration, including a reference electrode, a counter electrode, and a working electrode, was used. The scheme of deposition cell is shown in Fig. 6-1. This configuration can much better control the deposition process than two electrodes configuration. During the deposition, an external potential is applied to the cell, and the correspondent current goes through the electrodes.

There is a potential drop across the cell because of the solution resistance: potential drop (V) = current (I) x solution resistance (R) [15]. The I may change even if the V is constant, since R changes during deposition. Therefore, it is normally impossible to precisely control the applied potential and measure the current across the cell at the same time by the two electrodes system. In three electrodes system, the potential is controlled/measured between the working electrode and the reference electrode, where there is no current go through; while the current passes through between working electrode and counter electrode and is controlled. By this way, the deposition process can be precisely controlled.

In this research, a standard Ag/AgCl electrode, obtained from Bioanalytical System, Inc., was used as the reference electrode. A platinum mesh, in the size of 2 cm x 2 cm, was used as the counter electrode. The platinum mesh was obtained from Alfa Aesar. A glass slide covered with Cu(2.5 μm)/Cr(100 nm) bilayer is used as the working electrode. The Cr layer was first deposited by RF sputtering on the glass slide to form an adhesion layer, and then a Cu layer was deposited on the Cr layer by DC sputtering. The working electrode and the counter electrode were vertically placed in the plating bath and faced to each other. The Fe-B thin films were deposited on the surface of the working electrode under constant current density.
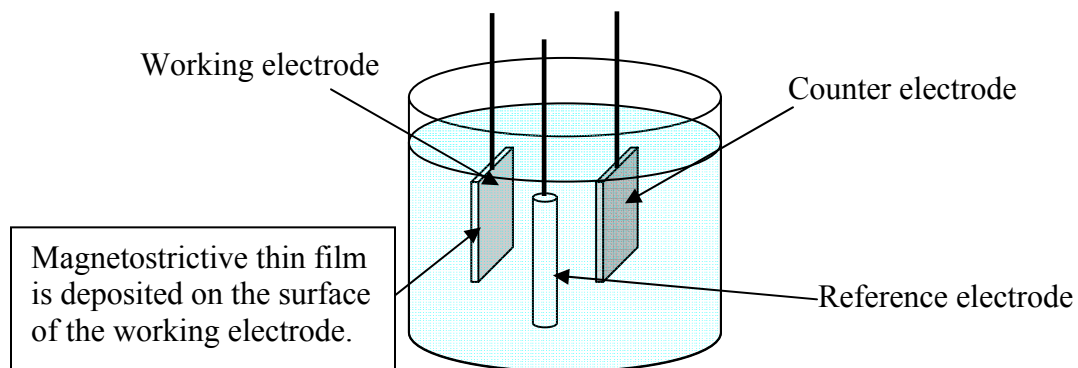
Fig. 6-1. Electrochemical cell for Fe-B thin film deposition.

In this research, the Fe-B films were deposited from plating baths with different concentration of potassium borohydrite (KBH_4). The compositions of plating bathes employed were listed in Table 6-2.

TABLE 6-2

Composition of Baths for Fe-B Thin Film Deposition

	Bath A	Bath B	Bath C	Bath D	Bath E	Bath F
$FeSO_4$	20 g/L	20 g/L	20 g/L	20 g/L	20 g/L	20 g/L
KBH_4	0 g/L	8 g/L	12 g/L	16 g/L	20 g/L	24 g/L
NaOH	16 g/L	16 g/L	16 g/L	16 g/L	16 g/L	16 g/L
$KNaC_4H_4O_6$	90 g/L	90 g/L	90 g/L	90 g/L	90 g/L	90 g/L

6.2.4 Characterization of the Fe-B Thin Film

6.2.4.1 The Microstructure Determination Using X-ray Diffraction

In this study, the microstructure of the deposited Fe-B thin films on the substrate was analyzed using Wide Angle XRD method.

Since the thickness of the Fe-B films were thin, when a symmetric θ - 2θ diffraction was performed, the X-ray beam would penetrate the Fe-B film and the diffraction pattern of the Cu substrate would superimpose on the diffraction pattern of the Fe-B films. There are two methods that can solve this problem. One method is to deposit the thick Fe-B film so that the X-ray beam can not penetrate the whole film and only the diffraction pattern of the Fe-B alloy can be obtained. But sometimes we also want the information of the thin films. Another method is to use Grazing-Incidence geometry diffraction. For grazing incidence X-ray diffraction, the incident X-ray beam is fixed at a small angle, and only the detector is scanning. When the incident angle is small enough, only an evanescent wave penetrates into the material and Bragg reflections are only coming from top structure of the materials, which avoids the scattering from the substrate.

In this research, two X-ray diffractometer systems were used to characterize the Fe-B thin films. One is a Rigaku system, and another one is a Philips X'Pert MRD PRO system. All the XRD scans were performed at room temperature.

For the Rigaku system, the XRD scans were performed using symmetric θ - 2θ diffraction. The X-ray source is Ni-filtered CuKα (wave length = 1.54 Å) radiation at 40 KV and 40 mA. Both thin Fe-B films and relative thick films (thickness > 10μm) deposited from different solutions were characterized by this system. For thin films, the diffraction peaks of Cu substrate can be observed.

172

The Grazing Incidence X-ray Diffractions were performed using the Philips X'Pert system. The X-ray source is a long-fine-focus, ceramic X-ray tube with Cu anode. The operating power is 45 KV and 40 mA. The incident angle was fixed at 5°.

The XRD pattern can be used to estimate the crystalline size of the materials. The diameter of the crystal size can be calculated using Sherrer's equation [16].

$$t = 0.9 \frac{\lambda}{B \cos \theta} \tag{6-1}$$

where t is the dimension of the crystal or the grain, λ is the wavelength of the X-ray, B is the width of the diffraction peak at its half maximum, and 2θ is the peak position.

6.2.4.2 Composition Determination using AES and XPS

The compositions of the surface of the deposited Fe-B films were analyzed using X-ray photoelectron spectroscopy (XPS), while the composition distribution along the Fe-B thickness was analyzed using Auger electron spectroscopy (AES).

Both AES and XPS are surface analysis techniques to determine the elemental composition and the chemical state of the atoms of the materials. XPS technique employs monoenergetic X-ray to irradiate the sample. The energy of X-ray photons is absorbed by atoms at the sample surface, causing the emission of electrons due to the photoelectric effect. The kinetic energy of emitted electrons represents the binding energy of the atoms of the materials. Since each element has a unique set of binding energies, by measuring the energies of photoelectrons emitted from the atoms, XPS can be used to identify the elements and determine the composition of the materials. The elemental binding energies vary with the chemical potential of the atom and polarization of compounds. Therefore, XPS can also used to identify the chemical state of the materials by analyzing the shifts in

the elemental binding energies [17].

In this research, the compositions of the surface of the Fe-B films were analyzed by XPS, which was performed using a Physical Electronics Quantum 2000 Scanning ESCA Microprobe. This system uses a focused monochromatic Al Kα x-ray source and a spherical section analyzer. The X-ray beam with 100 μm diameter was employed and incident normal to the sample, while the photoelectron detector was at 45° off-normal. The scan area was 1.4 mm x 0.2 mm rectangle on the sample. The compositions of the Fe-B film surface, and at depths of approximately 5 nm, 15 nm, 35 nm were analyzed by etching the film using 2 kV Ar^+ ion-beam. The sputter rate for these ion gun conditions was calibrated at a rate of 4.3 nm/min for a known SiO_2 reference material.

AES is widely used to determine elemental composition of materials by analyzing the Auger electrons emitted from the excited sample. The Auger electron emission is initiated by bombarding the sample surface with electrons. The incident electron can knock off the inner shell electrons of the sample atom and create an excited ion with inner shell vacancy. To relax to lower energy state, an electron from higher energy level drops to the inner shell vacancy, which results in the simultaneous emission of an Auger electron. The kinetic energy of the Auger electron equals to the energy difference of the ionized state and the relaxed final state, and is characteristic to the structure of the atom. By detecting the number of Auger electrons as a function of electron energy, AES can determine the elements and the concentration of the elements in the sample material. Except H and He, AES can detect all elements with high sensitivity [18].

To study the uniformity of the deposited Fe-B film along its growth direction, the composition profile along film thickness direction was analyzed by AES, which was

174

performed using a Physical Electronics Model 680 Nanoprobe. Fe-B films, 3 ~ 4 μm in thickness, deposited on Cu/Cr/glass substrate, were broken. The e-beam with a diameter of ~20 nm was focused on the cross-section surface of the films, and then the compositions of selected spots along the thickness were analyzed by the AES. Before the analysis, cross-section surface was sputtered off 50 nm to eliminate the contamination and the oxidation. The sputter rate for the ion gun was calibrated at a rate of 1.2 nm/min for a known SiO_2 reference material.

6.2.4.3 Magnetization Loop Measurement

The magnetization (M-H loop) of the Fe-B thin films were measured by a DSM model Vibrating Sample Magnetometer (VSM) with the H field applied parallel to the surface of the Fe-B thin films. The specimens used for the measure were the Fe-B thin films with the Cu/Cr (total 2.5 μm) substrate, as shown in Fig. 6-2.

Two groups of Fe-B thin films were studied. One group consisted of the films deposited from the solutions with different KBH_4 concentration (plating bath D, E and F). The thickness of the Fe-B films is 12 μm. Another group consisted of the films deposited form solution D, but with different thicknesses that are 50 nm, 3 μm, and 12 μm.
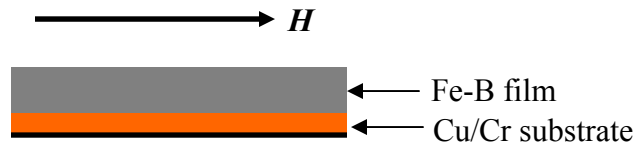
Fig. 6-2. Illustration of Fe-B film specimens used for magnetization loop measurement.

6.2.4.4 Resonance Behavior Characterization of Fe-B Alloy

The resonance behavior of Fe-B alloy was examined by measuring the resonance behavior of strip-like magnetostrictive resonators made from deposited Fe-B films. Three groups of resonators made of amorphous Fe-B films, deposited under current density of 5 mA/cm^2 from plating bath D, E and F, respectively, were studies in this research. The Fe-B films in the thickness of 12 μm was deposited on the Cu(2.5 μm)/Cr(100 nm) coated glass substrate, and then the film was peeled off from the glass slide with the Cu/Cr subsrate. The Fe-B/Cu/Cr film was cut to strips with different sizes by hand to form resonators. The resonance spectra of the resonators were measured using the set up B, which was descried in Chapter 3. The magnitude of S_{11} output from the analyzer is used to characterize the resonance behavior of the Fe-B resonators. The determination of the resonance frequency and Q value of the MSP was discussed in Chapter 3.

6.2.4.5 Thermal Stability of the Fe-B Thin Film

The thermal stability of the Fe-B thin films was studied by annealing the deposited films from bath D under N_2 atmosphere at 200, 300, and 400 ^{o}C for 1 hour. The heating rate is 10 ^{o}C /min, while the films were cooling to room temperature in the oven. The microstructures of the films before and after annealing were studied using The Grazing Incidence X-ray Diffractions, which were performed using the Philips X'Pert system. The X-ray source is a long-fine-focus, ceramic X-ray tube with Cu anode. All the XRD scans were performed at room temperature.

6.3 Results and Discussion

6.3.1 Electrochemical Deposition of Amorphous Fe-B Alloy

The Fe-B thin films were deposited from the aqueous solution containing of $FeSO_4 \cdot 7H_2O$, KBH_4, $NaOH$, and $KNaC_4H_4O_6 \cdot 4H_2O$. The reaction mechanisms for Fe-B alloy deposition have been discussed in several literatures [19-21]. The deposition process is the combination of the electrochemical process, which Fe is deposited on the working electrode surface under the external applied electric field, and the catalytic chemical process, which BH_4^- anions reduce Fe^{2+} to Fe with subsequent codeposition of Fe and B on the working electrode surface.

The process involves the dehydrogenation and oxidation of the BH_4^-.

$$BH_4^- + 4OH^- \rightarrow B(OH)_4^- + 2H_2 + 4e$$

$$BH_4^- + 8OH^- \rightarrow B(OH)_4^- + 4H_2O + 8e$$

The above reactions provide electrons for the reduction of iron and boron:

$$Fe_2^+ + 2e \rightarrow Fe$$

$$B(OH)_4^- + 3e \rightarrow B + 4OH^-$$
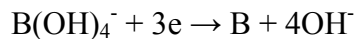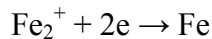
Fig. 6-3 shows the cyclic voltammogram (CV) of the deposition of Fe-B alloys on the working electrode at room temperature. The black line is the CV curve of the deposition from solution D, while the red line is the CV curve of the deposition from solution A. There is no KBH_4 in solution A. In this case, only Fe was deposited. The deposition conditions for these two solutions were same.

For plating bath D, at around -1200 mV, the deposition rate increased rapidly and a peak exhibits at about -1250 mV, indicating onset of a bulk deposition. For plating bath A, the deposition rate starts to increase   rapidly at about -1300mV and a peak

exhibits at about -1350 mV. The results indicate the chemical reduction of Fe^{2+} by KBH_4 on the working electrode surface increases the deposition rate and pushes the start of the bulk deposition to a lower voltage. KBH_4 is the source of the Boron, as well as the reduce agent for the deposition process.

The reaction mechanisms of Fe-B alloy deposition indicate H_2 evolution. H_2 bubbles can be seen forming and streaming off of the working electrode surface during depositions. For lower current densities, fewer bubbles evolve from the film surface; while for higher current densities, the rate of H_2 evolution is larger, thus more and larger bubbles will form. The strong H_2 evolution causes the film surface is rough and less compact. Therefore, to obtain Fe-B films with better quality, lower current densities (< 10 mA/cm^2) were be used in this research.
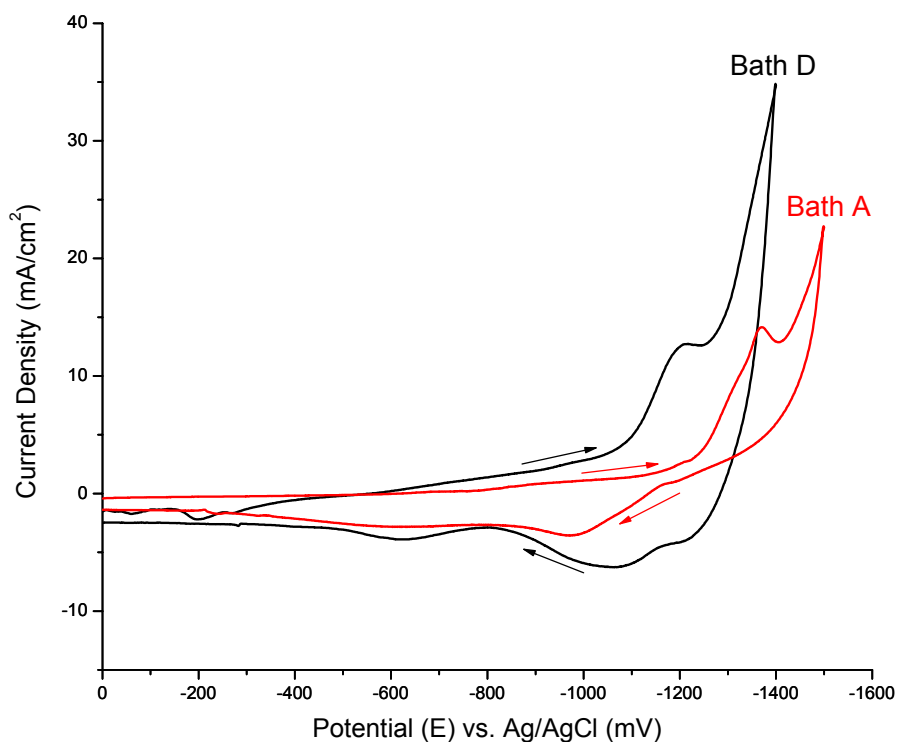
Fig. 6-3. Cyclic voltammogram of Fe-B deposition on Cu/Cr/glass working electrode.

178

6.3.2 Microstructure of the Fe-B Thin Films

The microstructure of the Fe-B film is critical for its properties. As discussed in the 'introduction' part, Fe-B alloy with amorphous structure is highly desired for fabrication of magnetostrictive AW devices. Based on literatures, the Fe-B alloys obtain amorphous microstructure when the B concentration is higher than 16 atm% [20, 21]. As the resource of Boron, the concentration KBH_4 in the deposition bath would affect the Boron composition in the Fe-B films, thus the microstructure of the films. The microstructures of the Fe-B films deposited from baths with different KBH_4 concentrations were studied by X-ray diffraction. Fig. 6-4 shows the XRD patterns of Fe-B films on Cu/Cr/glass substrate deposited from the solutions listed in Table 6-2. The films are in the thickness of $1 \sim 2$ μm, and their microstructures were studied by the Rigaku X-ray system. Since the thickness of the films is small, the diffraction peaks of Cu substrate can be observed in Fig. 6-4. The results in Fig. 6-4 show that, for the film deposited by the baths with lower concentration of KBH_4 (bath A, B), the diffraction peaks corresponding α-Fe reflections <110> and <211> can be clearly observed, which indicates the formation of crystallized Fe structure. For the films deposited by the baths with $KBH_4 \geq$ 16g/L (bath D, E and F), only the diffraction peaks from Cu substrate can be observed, which indicates the amorphous structure of the deposited Fe-B films. The result clearly shows that the microstructure of the films depends on the concentration of potassium borohydride in bath. This is consistent with other studies of electrochemically deposited Fe-B alloy [20, 21]. With increasing KBH_4 concentration in the plating bath, the concentration of Boron in the deposited Fe-B films increases, thus the microstructure of the film tends to become amorphous.
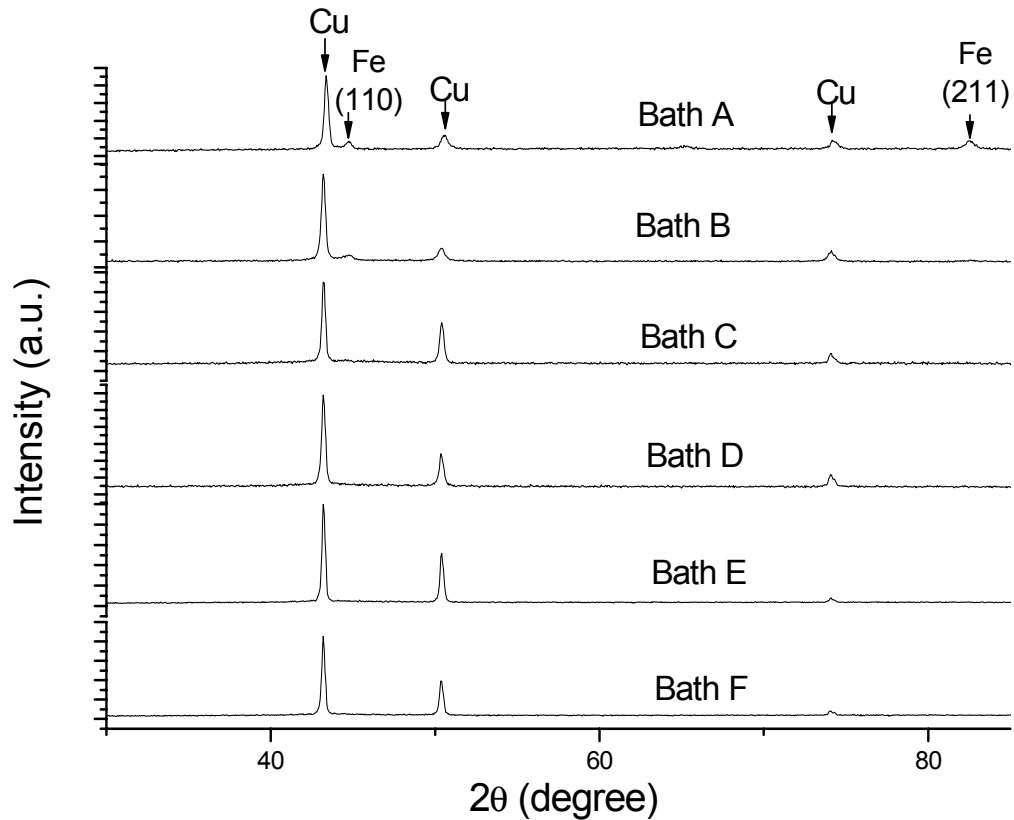
Fig. 6-4. XRD patterns of Fe-B thin films on Cu/Cr/glass substrate deposited by plating baths listed in Table 6-2.

To eliminate the effect of the Cu substrate on the X-ray diffraction patterns and confirm the amorphous microstructure, Fe-B films in the thickness of 12 μm were deposited on the Cu/Cr/glass substrate from plating baths C, D, E and F, and then the microstructures were studied by the Rigaku X-ray system. With this thickness, the X-ray beam can not penetrate the whole Fe-B film, and the diffraction patterns only come from the Fe-B film. The XRD patterns of these Fe-B films were shown in Fig. 6-5 as black curves. For the film deposited from bath D, E or F, there is only a broad halo exhibits on

the XRD pattern in the range of angle $2\theta = 40^o \sim 50^o$, which is the characteristic of amorphous Fe-B. Based on Equation (6-1), the sizes of the ordering range are 11.7, 10.5 and 11 Å for the films deposited from bath D, E and F, respectively. The wavelength of 1.54 Å for Cu Kα as X-ray source was used in the calculation. The results confirmed the amorphous microstructure in these films. However, for the film deposited from solution C, the diffraction peaks corresponding α-Fe reflections <110> and <211> appears in the XRD pattern, which indicates the formation of α-Fe crystallite because of the low B concentration.
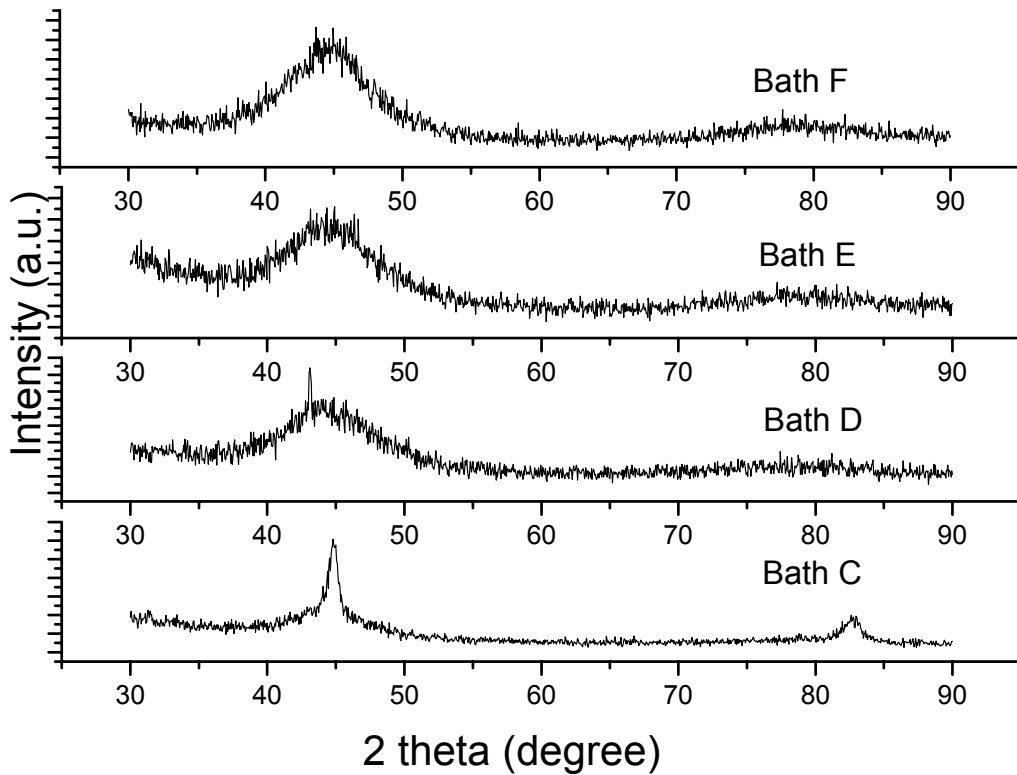
Fig. 6-5. XRD patterns of Fe-B films deposited on the Cu/Cr/glass substrate from plating baths C, D, E and F.
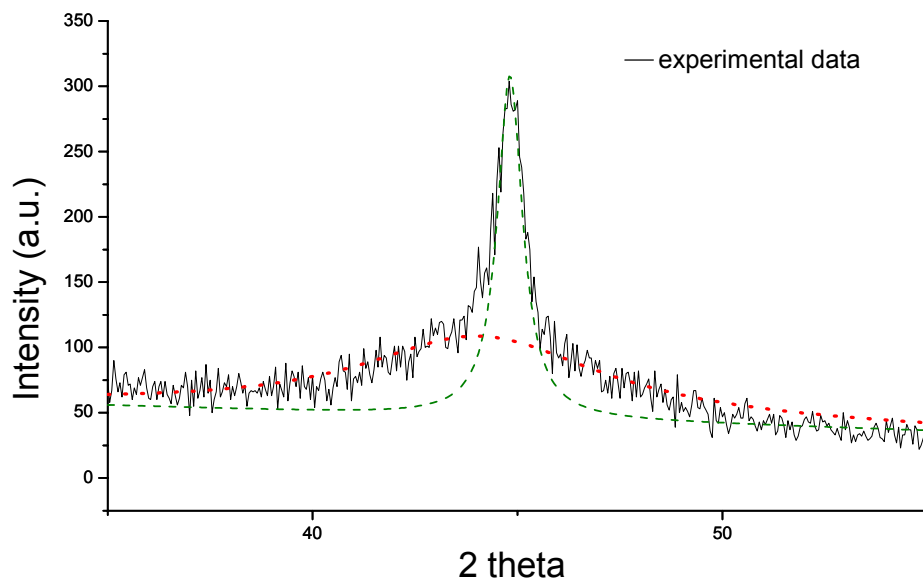
Fig. 6-6. XRD pattern ($40^{o} \sim 50^{o}$) of the film deposited from bath C and the fitting results based on Lorentz function. The black solid curve is the experimental data, while the red dotted curve and green dashed curve are the fitting results.

To further analyze the data, the XRD pattern ($40^{o} \sim 50^{o}$) of the film deposited from bath C was fitted using the Lorentz function. The fitted curves were shown in Fig. 6-6 as the red dotted curve and green dashed curve. The fitting results reveal a sharp diffraction peak superimposing on a broad halo, which indicates that both crystalline structure and amorphous microstructure forming in the film. The broad red dotted curve is correspondent to the amorphous structure, while the green dashed peak is the diffraction peak corresponding α-Fe reflection <110>. Based on Equation (6-1), the crystal size of α-Fe formed in the film is about 12 nm. Therefore, to obtain an amorphous microstructure, plating baths with KBH_4 concentration higher than 16 g/L are needed.

182

6.3.3 Composition of the Fe-B Film

The surface composition and the composition distribution along the depth of amorphous Fe-B films deposited from plating bath D were studied.

The compositions near the Fe-B film surface were analyzed by XPS in layers. Fig. 6-7 shows the XPS spectrum of the Fe-B film surface as deposited. The Fe-B film was deposited from plating bath D under a current density of 5 mA/cm^2, and in the thickness about 4 μm. From Fig. 6-7, besides Fe and B peaks, huge O peaks and small peaks of C, Ca and Na can be observed. The composition analysis based on data in Fig. 6-7 was summarized in Table 6-3. The results indicated that the surface of the "as formed" film is oxidized due to the contact with air. Also, absorbed carbon and contamination from the plating bath can be observed on the surface.
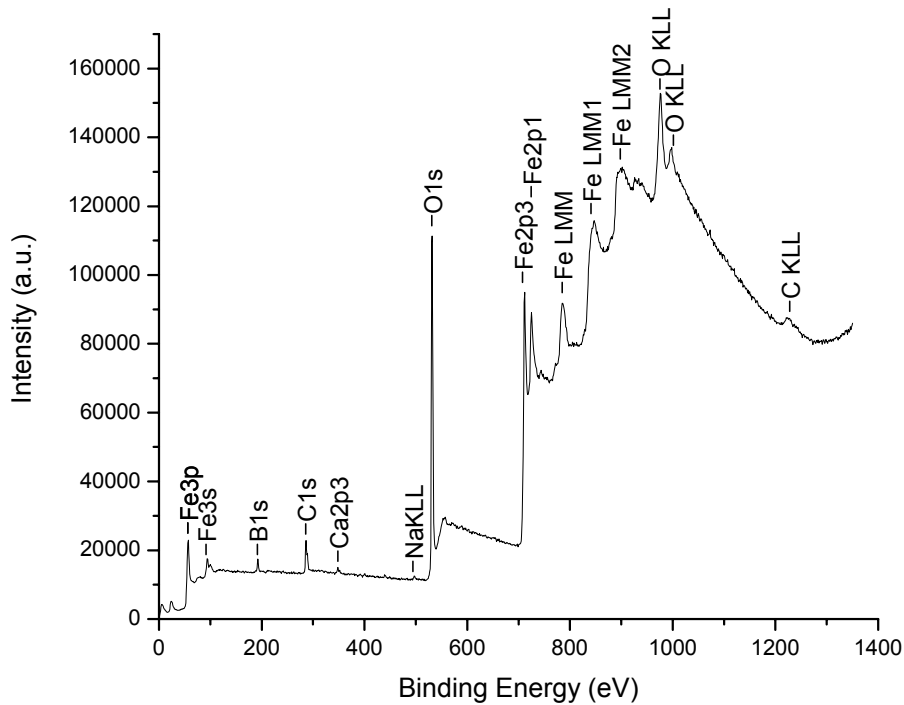
Fig. 6-7 The XPS spectrum of the Fe-B film surface as deposited. The Fe-B film was deposited from plating bath D under a current density of 5 mA/cm^2.

TABLE 6-3

Compositions of Fe-B Film Surface, and About 5 nm, 15 nm and 35 nm from the Surface.

The Film Was Deposited from Plating Bath D under a Current Density of 5 mA/cm^2

	B atm %	Fe atm %	O atm %	C atm %	Na atm %	Ca atm %	N atm %	Ar atm %
As formed	5.64	30.26	50.88	12.05	0.45	0.26	0.46	/
Etched off 5 nm	9.63	65.85	23.32	0.17	/	/	/	1.03
Etched off 15 nm	13.25	76.73	8.22	0.67	/	/	/	1.13
Etched off 35 nm	15.04	78.26	4.86	0.65	/	/	/	1.19

By etching the film using 2 kV Ar^+ ion-beam, the compositions of the Fe-B film at depths of approximately 5 nm, 15 nm, 35 nm were also analyzed using XPS, and the results were summarized in Table 6-3. The results show that the oxidation and contamination the surface can be removed by the Ar^+ ion-beam etching. The concentrations of O and C decrease dramatically along the depth, while the concentrations of B and Fe increase. After Ar ion-beam etching, some Ar atoms stick on the film and can be observed.

XPS is able to obtain information on chemical states from the variations in element binding energies due to differences in the chemical potential and polarizability of compounds. An obvious shift in B binding energy was observed on the XPS spectra of the film for different depths. Fig. 6-8 shows the B spectra for the film surface and about 5 nm, 15 nm, and 35 nm from the surface measured by XPS. On the film surface as deposited, the detected binding energy of B1s is 192.8 eV, which corresponds to the binding energy of B in the compound B_2O_3 [22]. After the surface was etched off 5 nm,

photoelectron peak for B1s split into two peaks: one corresponds to the binding energy of compound B_2O_3, while another one, with the binding energy of 188.1 eV, corresponds to the binding energy of pure Boron [22]. For the spectra at depths of 15 nm and 35 nm, the peak corresponding to compound B_2O_3 becomes very weak, while only a strong peak of B1s for pure Boron can be observed. The results clearly shows that the formation of oxidation on the film surface. After the oxidation is removed, the components exist in the chemical status as pure elements.
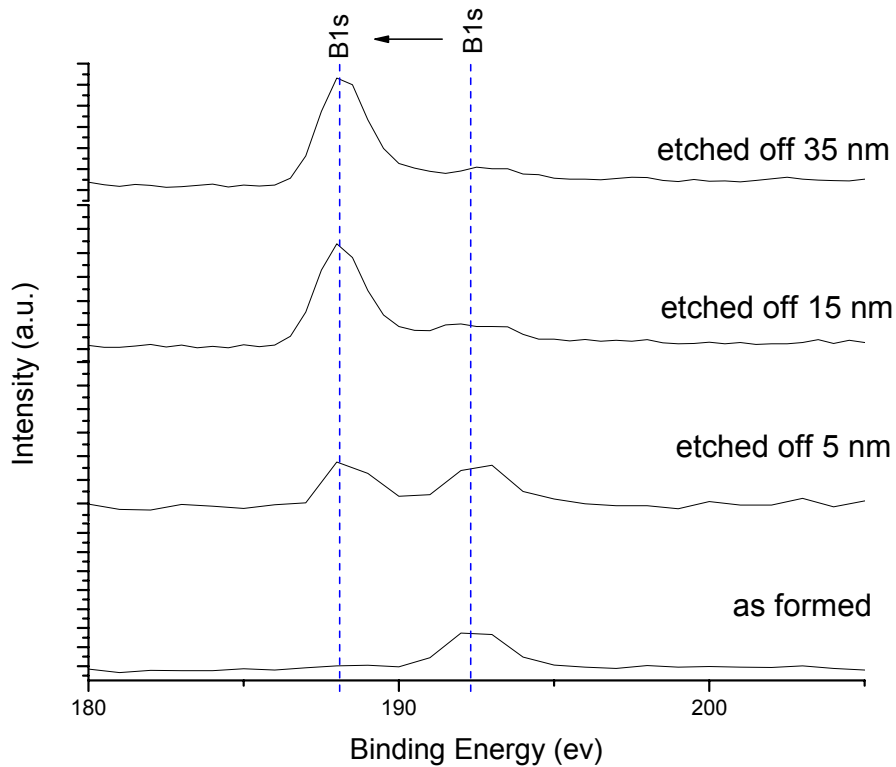
Fig. 6-8. XPS spectra of B1s for deposited Fe-B film surface and about 5 nm, 15 nm, and 35 nm from the surface. The Fe-B film was deposited from plating bath D under a current density of 5 mA/cm^2.

The composition of the deposited Fe-B film and the uniformity along its growth direction (thickness) was studied by AES. To perform the analysis, the Fe-B film deposited from plating bath D under current density of 5 mA/cm^2 was broken, and the cross section of the film was analyzed. Fig. 6-9 is the SEM image of the cross section of the Fe-B film. As shown on the image, 10 points were selected long the film thickness direction. The compositions of the 10 points were analyzed using AES, with the e-beam focused to a diameter of ~20 nm. Before the analysis, cross-section surface was sputtered off 50 nm by Ar ion beam to eliminate the contamination and the oxidation.

The compositions of the 10 points were listed in Table 6-4, while the contribution of the composition along the length direction was shown in Fig 6-10.
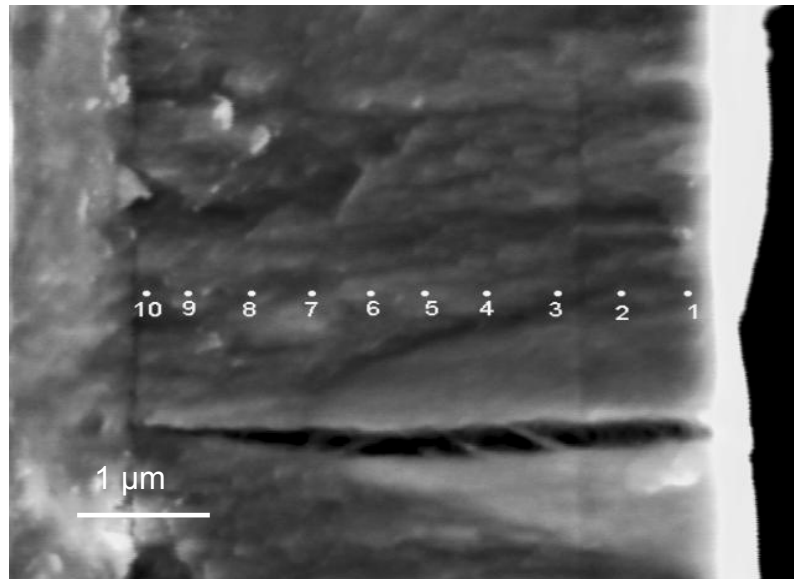
Fig. 6-9. SEM image of the cross-section of the Fe-B film deposited from bath D under current density of 5 mA/cm^2.

TABLE 6-4

Compositions of Fe-B film Deposited from Bath D under a Current Density of 5 mA/cm^2 along Its Thickness Direction

Atomic Concentration Table				Fe:B ratio	
Points	B (atm%)	O (atm%)	Fe (atm%)	**Fe (atm%)**	**B (atm %)**
1	13.74	42.94	43.32	**76**	**24**
2	20.84	13.9	65.26	**76**	**24**
3	18.75	12.1	69.14	**79**	**21**
4	18.51	12.94	68.56	**79**	**21**
5	19.55	11.75	68.69	**78**	**22**
6	20.75	12.74	66.51	**76**	**24**
7	19.93	13.12	66.95	**77**	**23**
8	20.64	13.96	65.4	**76**	**24**
9	20.17	15.96	63.87	**76**	**24**
10	6.48	40.07	53.45	**89**	**11**
average	17.936	18.948	63.115	**78**	**22**
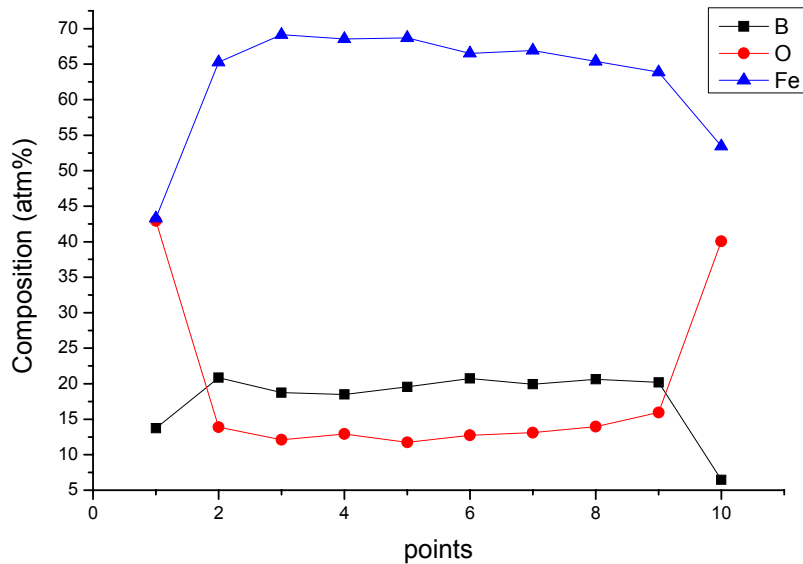
Fig. 6-10 Compositions of Fe-B film along its thickness direction. The film was deposited from bath D under a current density of 5 mA/cm^2.

The results show that Fe-B alloy, with designed composition (about 20 atm% B and 80 atm% Fe), was deposited from plating bath D. The composition distribution is uniform along the thickness direction except point 1 and point 10. From Fig. 6-9, point 1 is close to the film surface; the variation of the composition is due to the oxidization and contamination. Point 10 is very close to the Cu substrate. The oxygen should come from the oxidization of Cu electrode. Even though the composition is uniform, oxygen is present in the whole film. Since the plating solutions are alkalic and hydroxide ions participate in the electro-reduction process, the oxygen may be attributed to the hydroxide ions adhering to the film and the oxidation during the deposition. This behavior is also observed in the electrodeposition of Ni alloy [23]. Also, due to the internal stress, tiny cracks were observed in the deposited films, the oxygen might come from the oxidation occurring at the cracks' surface.

6.3.4 Magnetic Properties of the Fe-B films

The magnetization hysteresis loops of Fe-B films deposited from plating baths D, E and F are shown in Fig. 6-11. All the films were deposited under a current density of 5 mA/cm^2. The specimens used for the measurement were the Fe-B films, in the thickness of 12 μm, with the Cu/Cr (total 2.5 μm) substrate. Fig. 6-11 shows that all of these amorphous Fe-B alloys exhibit a soft magnetic property, as demonstrated by the slim loops. Based on the data in Fig. 6-11, the magnetic properties of these films were determined and summarized in Table 6-5. As shown in Table 6-5, the coercive field (H_c) of these films is about 10 Oe; while the squareness, which is defined as the ratio of the remanent (Mr) to saturation (Ms) magnetization, is around 0.1 ~ 0.2. The coercive field obtained here is much higher than that of   bulk Fe-B alloy. The reason is that the

measured sample is not pure Fe-B film, but the Fe-B film with Cu/Cr substrate. Due to the substrate, strong stress/strain exists in the Fe-B films as well as in the interface between the film and the substrate, which would affect the observed coercive field of the whole sample. Also, since the thickness of the films was thin and the magnetization was measured parallel to the film surface, the coercive field of the film would be higher than that of bulk Fe-B alloy due to geometry anisotropy. Still the deposited Fe-B films exhibit relative soft magnetic properties and slim hysteresis loops, which is favorable to obtain high magneto-mechanical coefficient and small heat loss. These properties make the amorphous Fe-B a good candidate as the active material for magnetostrictive acoustic devices.
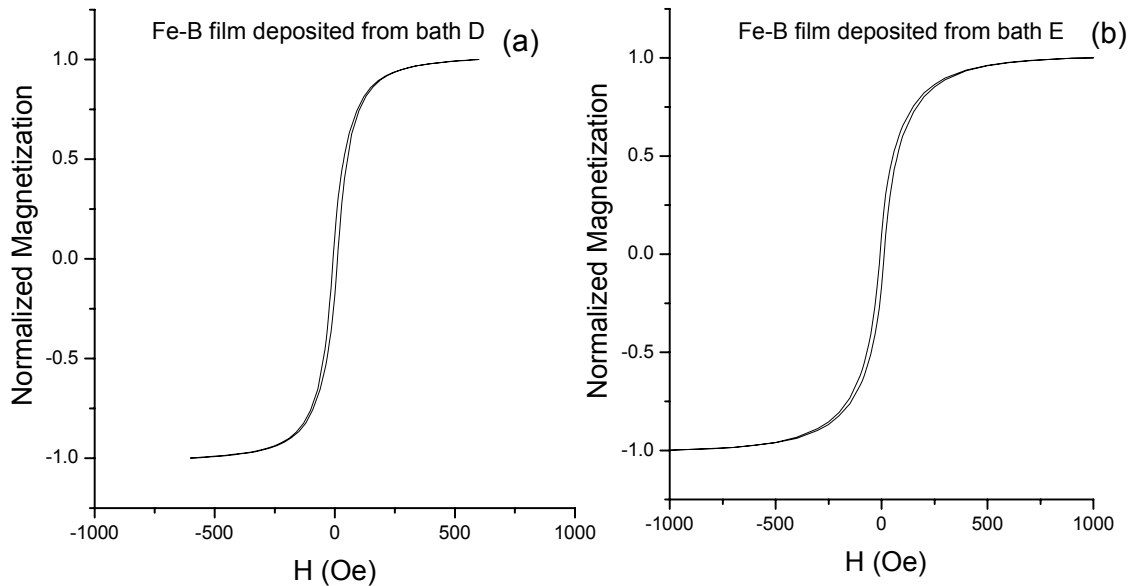
Fig. 6-11. Hystersis loops of Fe-B films deposited from bath (a) D and (b) E under a current density of 5 mA/cm^2.
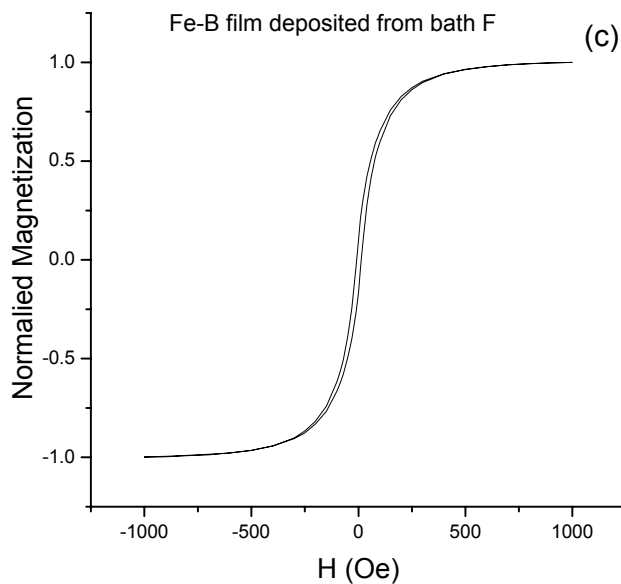
Fig. 6-11. Hystersis loops of Fe-B film deposited from (c) bath F under a current density of 5 mA/cm^2.

TABLE 6-5

Coercivity and Squareness of Amorphous Fe-B Films

	Film C	Film D	Film E	Average
H_c (Oe)	9.37	10.81	9.72	9.97 ± 0.75
Squareness (Mr/Ms)	0.15	0.13	0.21	0.16 ± 0.04

The magnetization hysteresis loops of Fe-B films deposited from solution D with different thicknesses were shown in Fig. 6-12, while their coercive fields (H_c) and squarenesses were listed in Table 6-6. The thickness of the Fe-B film is 100 nm, 3 μm and 12 μm, respectively, while the thickness of the Cu/Cr substrate is about 2.5 μm. The results show that the coercive field and the squareness of the Fe-B film increases with the decrease of the film thickness. The results indicate the strain/stress in the deposited film hardens the magnetic properties of the film. For electrochemical deposited film, due to

190

the mismatch between the film and the substrate lattice, strong strain/stress exists in the film, which would increase the coercive field and the squareness. The smaller the thickness of the film, the stronger the strain/stress. Therefore, the magnetic properties of the film become harder as the thickness decreases. The results shown in Table 6-6 also imply the effect of the surface of the Fe-B film and the interface between the Fe-B film and the Cu/Cr substrate on the magnetic properties. Since great amount oxygen exists in the surface, the surface and interface play an important role to block the movement of the domain wall and the switch of the magnetic domain. As the thickness of the film decreases, the volume percentage of the surface and interface in the film increases, thus the effect of them becomes more and more significant. This causes the film, in the thickness of 100 nm, to exhibit a much harder magnetic property than that of the film in the thickness of 12 μm.
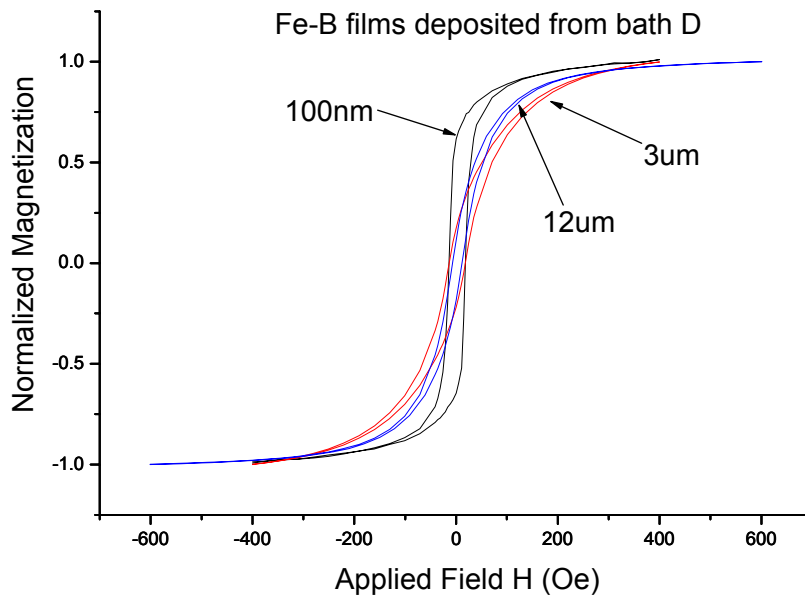
Fig. 6-12. Hystersis loops of Fe-B films deposited from bath D with different thicknesses.

TABLE 6-6

Coercivity and Squareness of Fe-B films Deposited from Bath D with Different

Thicknesses

Thickness	100 nm	3 μm	12 μm
H_c (Oe)	15.97	15.75	9.37
Squareness (Mr/Ms)	0.63	0.19	0.15

6.3.5 Resonance Behavior of deposited Fe-B Alloy

The resonance behaviors of plated Fe-B amorphous alloys were studied by analyzing the resonance spectra of strip-like magnetostrictive resonators, which consist of two layers: 12 μm Fe-B film and 2.5 μm Cu/Cr substrate.

The resonance frequencies and Q values of these resonators were determined setup B described in Chapter 3. The experimentally obtained first harmonic resonance frequencies versus reciprocal of the length for these resonators was plotted in Fig. 6-13, where the resonance frequencies of the resonators made from Fe-B film deposited from plating baths D, E and F were represented by black squares, green stars and red triangles, respectively. The results showed that, for all these three kinds of resonators, the resonance frequency linearly increases with the reciprocal of the strip length, which is as expected based on Equation (5-10). Based on material properties shown in Table 6-1 and Equation (5-10), the theoretical resonance frequencies of Fe-B resonators with different sizes were calculated, and shown in Fig. 6-13 as the blue line. The theoretical values exhibit higher resonance frequencies than experimental results. The reason is that, the resonance frequencies calculated from Equation (5-10) are for the naked strips made from

192

Fe-B alloy. However, the resonators used in the experiment consist of two layers: 12 μm Fe-B film and 2.5 μm Cu/Cr substrate. The Cu/Cr substrate is equivalent to the mass load for the Fe-B resonators, which will cause the resonance frequencies shift to lower values. Equation (5-17) indicates that the smaller the size of the resonator, the bigger the shift in the resonance frequency caused by the Cu/Cr substrate. Therefore, the difference between the theoretical value and the experiment results increases with the decreasing resonator size, which is consistent with the results show in Fig. 6-13.

The velocity of AW propagating in the material can be calculated based on Equation (6-2):

$$f_0 = \frac{v}{2L}$$
(6-2)

where f_0 is the fundamental resonance frequency of the free standing strip resonator; L is the length of the resonator; and v is the AW velocity in the material. Therefore, the slope of the resonance frequencies versus the reciprocal of lengths for the strip resonators represents the AW velocity in the material. Based on the results shown in Fig. 6-13, the experimental AW velocity in the films deposited from baths D, E and F are slightly different, which are 3736 ± 208 m/s, 3386 ± 139 m/s and 3124 ± 106 m/s, respectively. Considering the effect of Cu/Cr substrate as mass load, the AW velocities in these films would be higher than the experimental results. The films deposited from bath D exhibits higher AW velocity than the films deposited from baths E and F, thus is expected to have a higher Q value. Therefore, in this research, for fabricating micro/nano MSP, the Fe-B alloy was deposited from bath D.
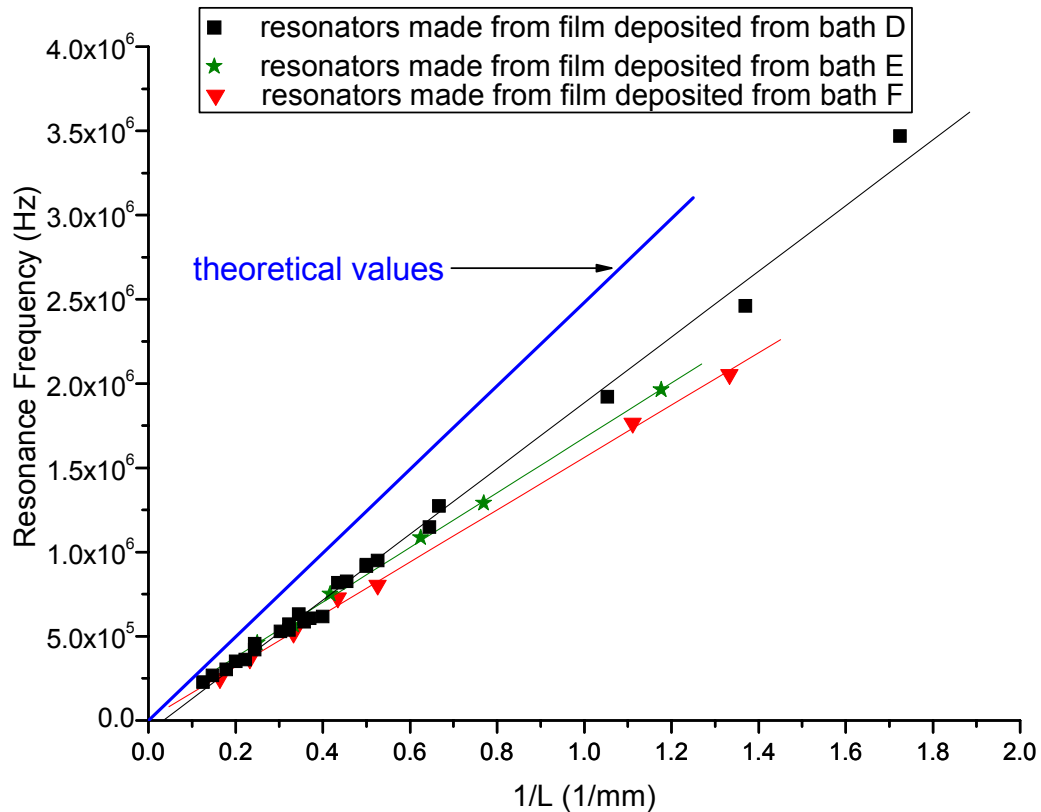
Fig. 6-13. Resonance frequency versus reciprocal of the length for the resonators made of Fe-B film on Cu/Cr substrate. The films were deposited from baths D, E, and F under a current density of 5 mA/cm^2.

The resonance behavior of the resonators was characterized from a kilohertz range up to a megahertz range. The Q values of the resonators were calculated based on the method discussed in Chapter 3. For all three kinds of resonators, a Q value over 200 can be observed even though the resonators were operated at the several megahertz range. The highest Q value was observed is 311. It should be noticed that, 1) the Q value of the resonators was affected by the shape of the resonator; 2) the resonators were made by Fe-

B alloy and Cu/Cr substrate. The resonators used in this study were cut by hand, by which the shapes were not accurately controlled. The imperfect shape will reduce the Q value. On the other hand, the Cu/Cr bilayer works as the mass load, which would greatly affect the Q value of the resonators. To simulate the effect of the substrate layer on the Q value of the resonators, commercial Metglas^{TM} 2826 MB ribbon (30 μm in thickness) was employed to make the magnetostrictive strip resonators with different sizes. The resonance behaviors of these strips were characterized using the setup B described in Chapter 3. Meanwhile, a Cu(5 μm)/Cr(100 nm) bilayer was deposited on Metglas^{TM} 2826 MB ribbon (30 μm in thickness) to form an equivalent mass load. The 2826 MB/Cu/Cr film was also cut into strips with different sizes to make the resonators, whose resonance behaviors were measured using same setup under same conditions as that for measuring resonators made of just Metglas^{TM} 2826 MB ribbon. The Q values of the resonators with and without Cu/Cr layer were compared, and the results were shown in Fig. 6-14. The solid squares are the Q values obtained for resonators made by Metglas^{TM} ribbon, where the average Q is almost 2000; while the solid triangles are the Q values obtained for resonators made by the 2826MB/Cu/Cr, where the average is about 600. It clearly indicates that the substrate layer greatly reduces the Q value of the resonators. Without the substrate, a Q value about 1000 would be expected for the amorphous Fe-B alloy itself. This indicates that the amorphous Fe-B alloy is a good candidate for fabricating high performance micro/nano magnetostrictive AW sensor platforms.
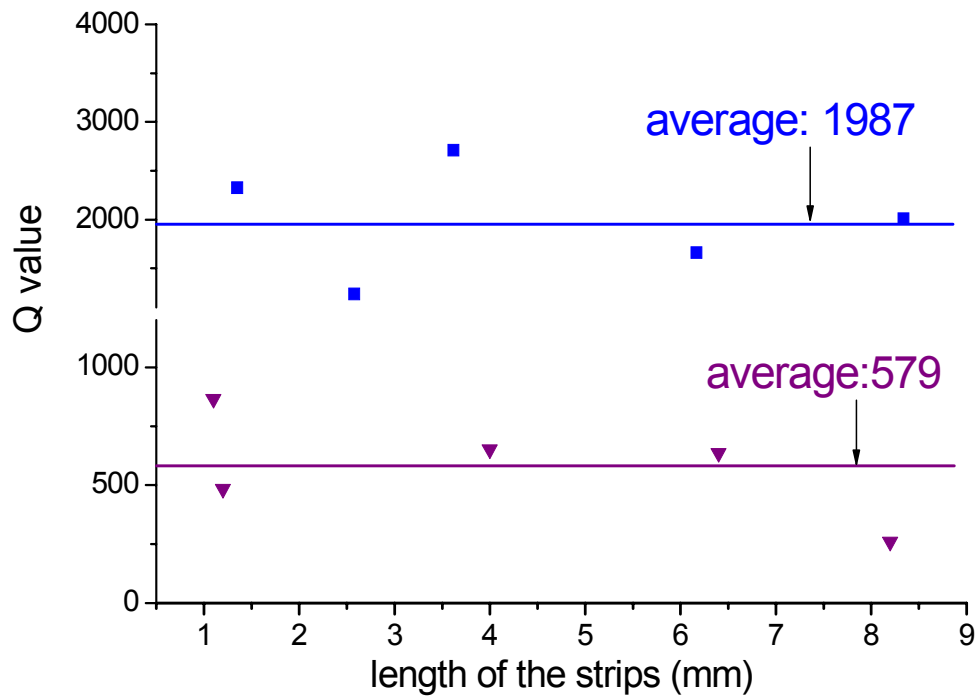
Fig. 6-14. Q values for the strips made of 2826 MB ribbon and 2826MB ribbon with Cu/Cr bilayer.

6.3.6 Thermal Stability of the Amorphous Fe-B Films

To study the thermal stability of the amorphous Fe-B films, Fe-B films deposited from bath D were annealed at 200, 300, 400, and 500 ^{o}C for 1 hour under N_2 atmosphere. The films were deposited under a current density of 5 mA/cm^2 and in a thickness of about 4 μm. The Grazing Incidence XRD patterns of the Fe-B films before/after annealing were shown in Fig. 6-15. Based on the XRD patterns and Equation (6-1), it is found that, after annealing at 200 and 300 ^{o}C, the sizes of the particles with ordering structure in the films are 12 and 11 Å, respectively, which reveals that the film remained an amorphous microstructure. But after annealing at 400 ^{o}C, the film shows diffraction peaks

196

corresponding α-Fe reflections <110> and <211>. But there is still a broad halo exhibited over the range of angle $2\theta = 40^{o} \sim 50^{o}$, which implies only part of the material is crystallized. Fitting the XRD pattern ($40^{o} \sim 50^{o}$) of the film annealed at 400 ^{o}C indicates that α-Fe crystal, in the size of 20 nm, formed in the amorphous film. After annealing at 500 ^{o}C, the XRD pattern exhibits strong diffraction peaks corresponding α-Fe reflections, which indicates the crystallization of the α-Fe. The Fe-B films exhibit good thermal stability up to 300 ^{o}C.
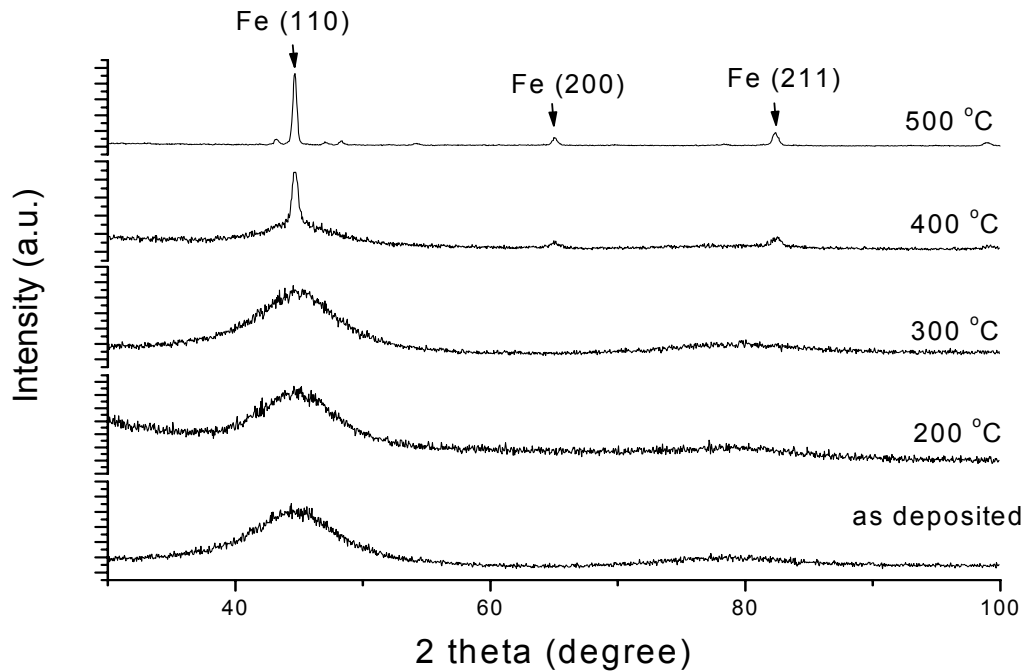
Fig. 6-15. XRD patterns of Fe-B films deposited from bath D after annealing at different temperatures.

The thermal stability of the amorphous Fe-B alloy also was studied by analyzing the resonance spectra of the resonators made from film deposited from bath D under a

current density of 5 mA/cm^2. The Fe-B film (12 μm in thickness) on Cu/Cr substrate (2.5 μm in thickness) was cut into strips with different sizes to form resonators. The resonance behaviors of the resonators were characterized using setup B. Then the resonators were heated to 250°C in N$_2$ atmosphere and cooled to room temperature. The heating rate is 10 ^{o}C/min, while the resonators were air-cooled in N$_2$ atmosphere. After the heat treatment, the resonance spectra of the resonators were measured again using the same setup with the same parameters as that were used before the heat treatment. The resonance frequencies and Q values for the resonators before/after heat treatment were determined. The results are shown in Table 6-7. After the treatment, the resonance frequency increased. Commercial 2826MB material was employed to evaluate the effect of the Cu/Cr substrate on the resonance behavior of the Fe-B film before/after the heat treatment. Two kinds of resonators were made: one is cut from commercial Metglas^{TM} 2826 MB ribbon (30 μm in thickness), another was cut from Metglas^{TM} 2826 MB ribbon with a Cu(5 μm)/Cr(100 nm) bilayer deposited on its surface. The same heat treatment and analysis as that done to the Fe-B/Cu/Cr resonators were performed to the resonators made of 2826 MB and 2826 MB/Cu/Cr. For both of the two kinds of resonators, the resonance frequencies increased about 1% after the heat treatment. It indicated that the increase of the resonance frequency of the resonators was not due to the heat treatment of the Cu/Cr substrate. It most likely was caused by the relaxation of internal stress of the deposited Fe-B alloy.

TABLE 6-7

Resonance Frequency and Q value for the Resonators Made from Fe-B Alloy Deposited

from Bath D before and after Heat Treatment

resonator	Length (mm)	Resonance frequency (Hz)		Q	
		Before annealing	After annealing	Before annealing	After annealing
1	2.1	915590	967740	110	187
2	3.1	570580	588520	34	86
3	2	924040	951910	67	44
4	5.6	304180	341810	180	87
5	4.1	419240	466180	81	89

6.3.7 Feasibility Study of Micro-Magnetostrictive Particle (MSP) Fabrication Based on Fe-B Alloy

In order to achieve extremely high sensitivity, miniaturize the size of the MSP sensor, and precisely control the desired dimensions, the feasibility of combining microelectronic fabrication methods and electrochemical deposition of Fe-B films to fabricate micro-MSP was explored. The purpose of the process design and preliminary work in this section is to provide a useful baseline for future work on micro-MSP fabrication.

Two fabrication processes were explored. One is a 'top down' process, which is to deposit the Fe-B film first, and then the MSPs are obtained by etching the film after covering the film with a patterned photoresist layer. Another process is a 'bottom up' process, which is to pattern a photoresist layer with the desired opening on a conductive substrate first, and then electrochemically deposit Fe-B alloy into the openings to obtain

micro-MSPs.

6.3.7.1 'Top Down' Fabrication Process

The current flow chart for this process was established, and shown as Fig. 6-16.

Fig. 6-16. Flow chart of 'top down' microelectronics fabrication of MSP.

The optimized process and parameters are described as follows. A thin Au layer (500 nm) was sputtered on the substrate (glass was used in this research) as the electrode for electrochemical deposition. Amorphous Fe-B film was then electrochemically deposited on the electrode/substrate from bath D. Next, a layer of AZ5214-E positive photoresist in a thickness of 1 μm was coated on the deposited film surface by spin coating the photoresist for 30 seconds at 3000 rpm. After spin coating, the sample was immediately placed on a hot plate for soft bake at 105 °C for 1 minute. Then the photoresist was exposed through the designed mask with ultraviolet light for 4 seconds. The photoresist was developed for 1 minute using the solution made of 1 part (volume) AZ400K™ and 2 part (volume) DI water, and then the sample was rinsed with DI water and dried with compressed sir. After the development, the pattern with MSP area coved with photoresist was formed on the Fe-B film surface, and the film was ready for etching. The etchant was made of distilled water and nitric acid (10 parts water (volume): 1 part acid (volume)). During the subtractive etching, the etchant was stirred by a magnetic stirrer. The patterned Fe-B film was immersed into the etchant for 2~3 seconds, and then immediately rinsed with DI water and dried with nitrogen gas. Finally, the film was rinsed with acetone to remove the remaining photoresist and then dried with nitrogen gas.

The fabricated MSPs were observed by an optical microscopy. Images for fabricated MSPs are shown in Fig. 6-17, where the designed size for MSPs shown in Fig. 6-17 (a) is 300 μm x 60 μm x 1 μm, while the designed size for MSPs shown in (b) is 110 μm x 20 μm x 1 μm. Due to the isotropic etching rate for amorphous materials, the size of fabricated MSP is slight smaller than the design size. Also, for thick films, slope can be observed on the MSP edge, as shown in Fig. 6-18.
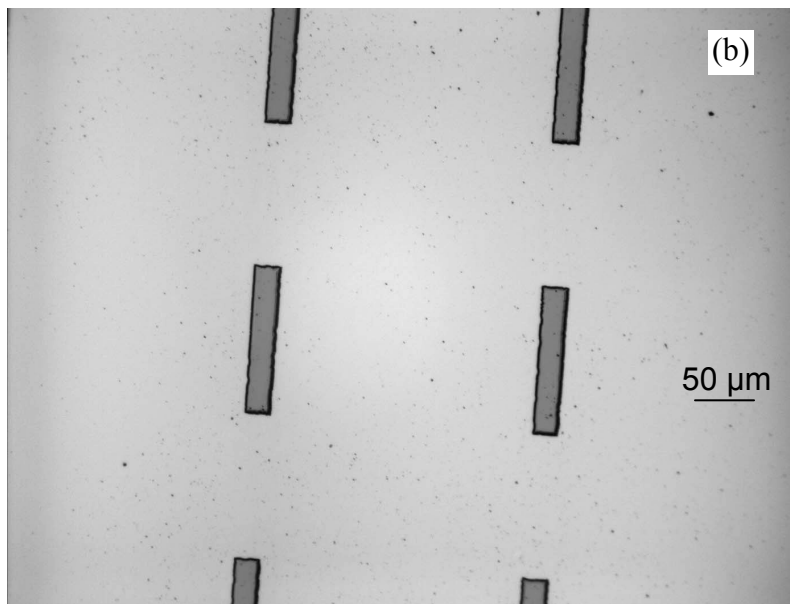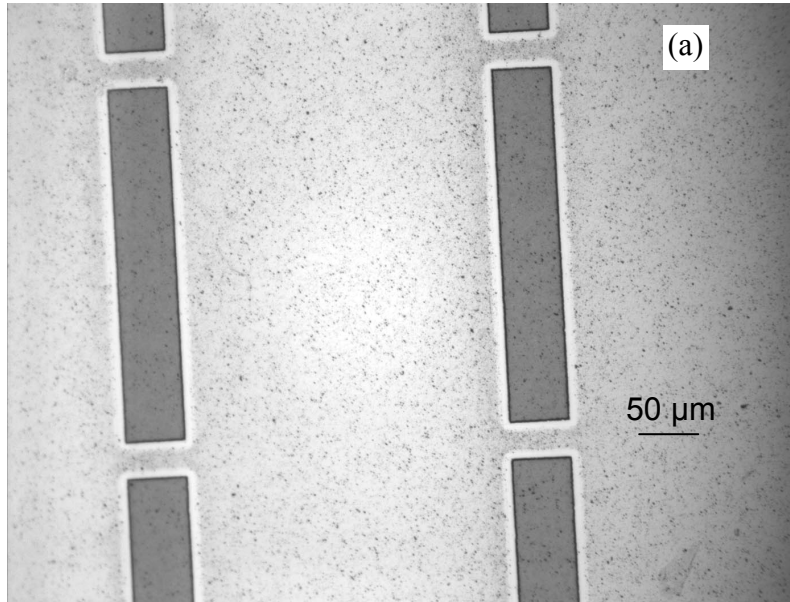
Fig. 6-17. Images for fabricated MSPs using 'top down' method. The designed size for MSPs shown in (a) is 300 μm x 60 μm x 1 μm, while the designed size for MSPs shown in (b) is 110 μm x 20 μm x 1 μm.
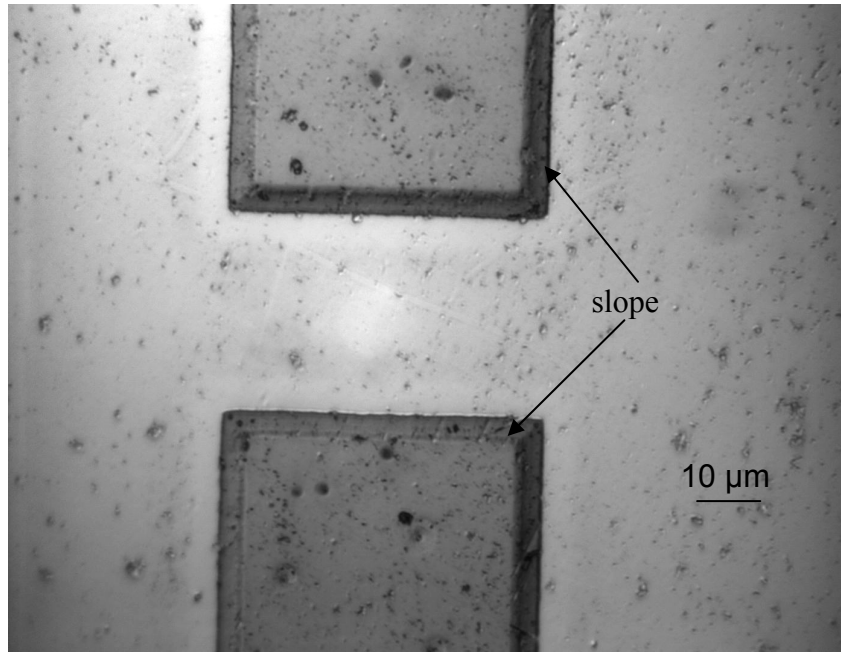
Fig. 6-18. Slope can be observed on the MSP edge for fabricated MSPs.

For the 'top down' process, besides microfabrication parameters, the quality of the plated Fe-B film greatly affects the quality of the fabricated MSPs. Small cracks caused by internal stress and big impurities due to a non-fresh plating bath will cause defects in fabricated MSPs. Fig. 6-19 (a) shows the defects in MSPs caused by the cracks in the original deposited Fe-B film; Fig. 6-19 (b) shows the defects on the edge of fabricated MSPS due to the impurities in the original film.
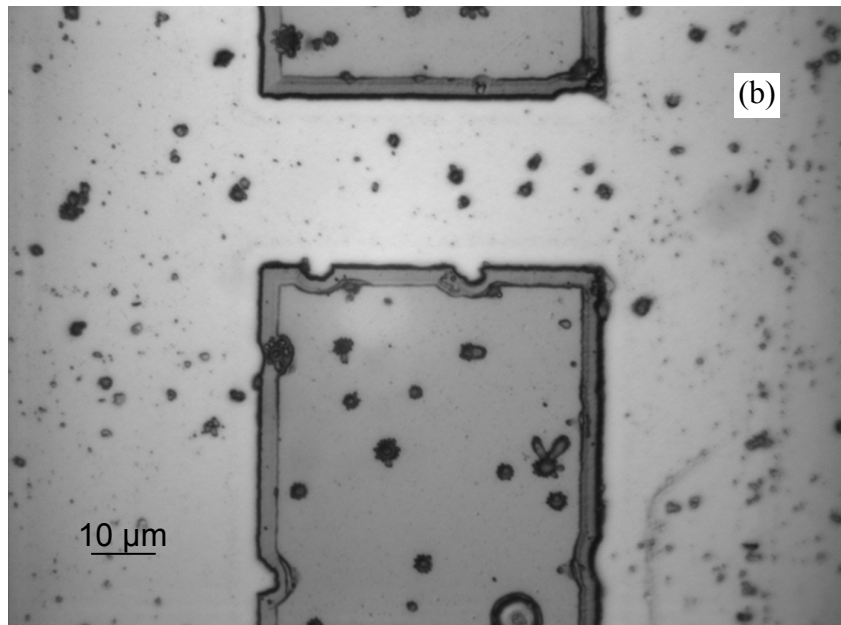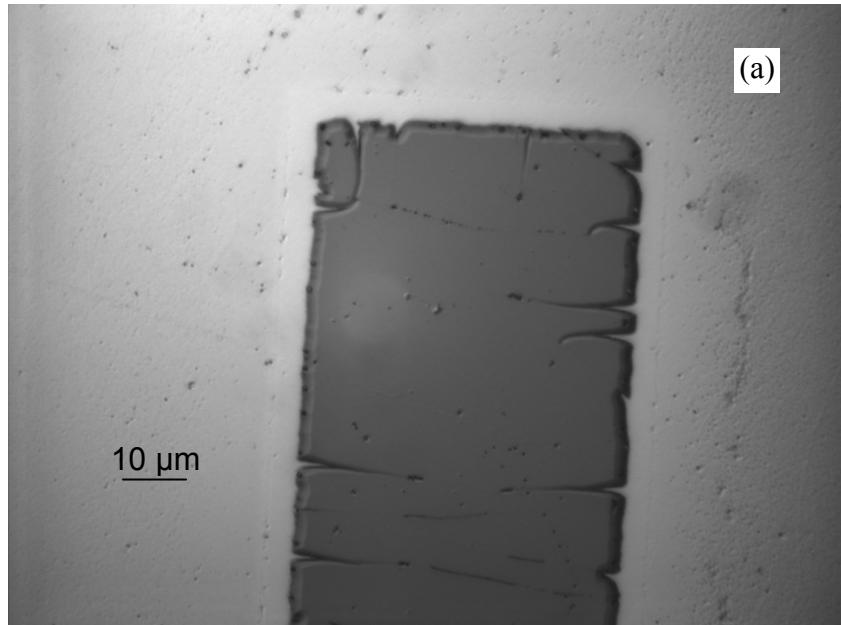
Fig. 6-19. (a) Defects in MSPs caused by the cracks in the original deposited Fe-B film;

(b) Defects on the edge of fabricated MSPs due to the impurities in the original film.

The MSPs were fabricated on the electrode/substrate. To obtain MSP sensors, a major issue that must be considered is how to release the fabricated MSPs from the substrate. It is not easy to release MSP from metal electrode. In later research, conductive polymers might be chosen to replace the metals to be the electrode. By this way, the MSPs can be released from the substrate by dissolving the conductive polymer after fabrication.

6.3.7.2 'Bottom Up' Fabrication Process

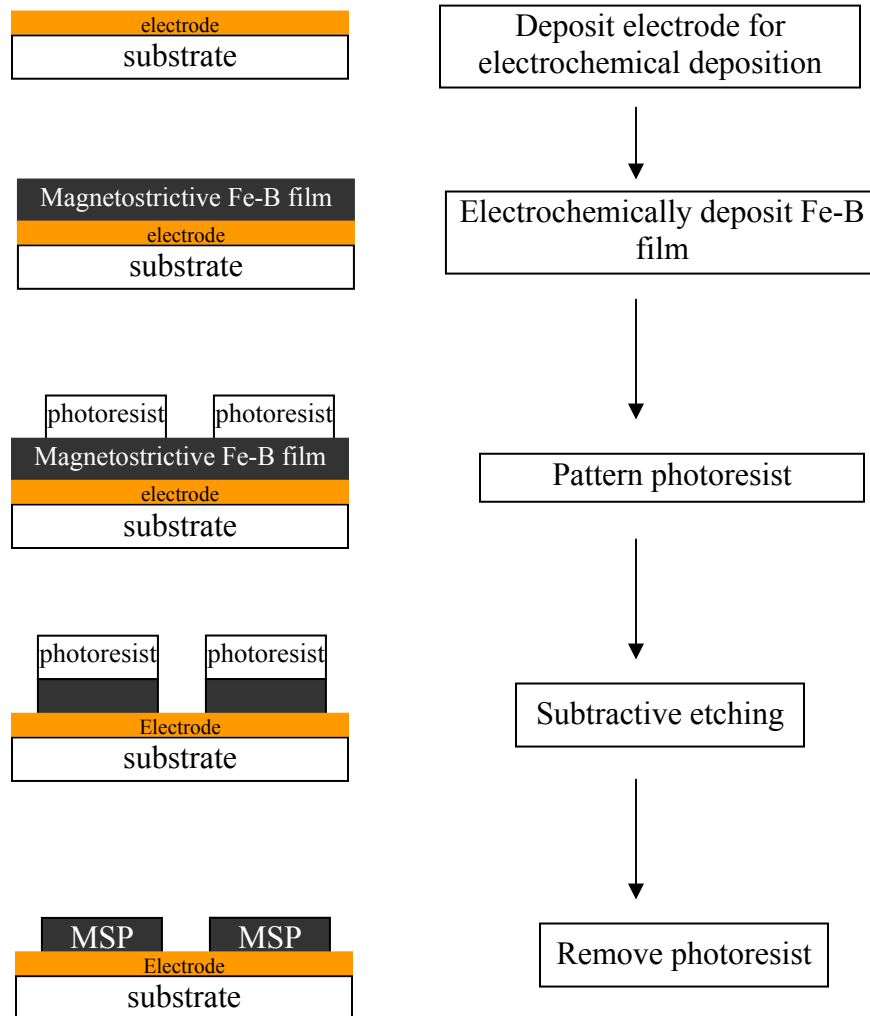The current flow chart for this process was shown as Fig. 6-20**.**
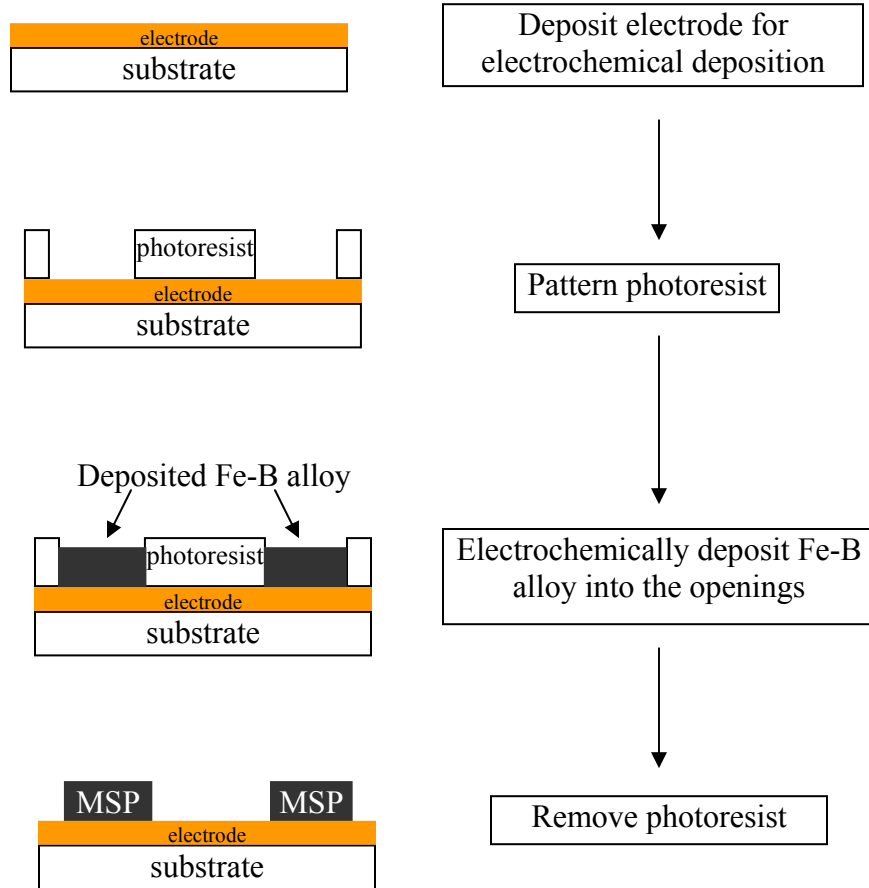
Fig. 6-20 Flow chart of 'bottom up' microelectronics fabrication of MSP.

The optimized process and parameters are described as follows. Since the plating baths for Fe-B alloy is alkalic, negative photoresist NANO^{TM} SU-8 2007 was used in this research. First, a thin Au layer (500 nm) was deposited on the glass substrate as the electrode for electrochemical deposition. And then the SU-8 photoresist was spin coated on the Au surface at 3000 rpm for 30 seconds. The sample was then immediately put on a hot plate for soft bake. The soft baking process is to bake the sample at 65 ^{o}C for 30 minutes and then 95 ^{o}C for one and half hour. After soft baking, the photoresist was exposed through the designed mask with ultraviolet light for 8 seconds. The sample was then put on the hot plate again for hard baking. The hard baking process is to bake the sample at 65 ^{o}C for 1 hour and then 95 ^{o}C for two hour. After hard baking, the photoresist was developed by putting into SU-8 developer for 4 minutes. The pattern was then ready for deposition. The Au electrode covered with the pattern was used as the working electrode, and the Fe-B alloy was deposited into the openings using the electrodeposition cell described as previous sections to form the MSPs with desired dimensions.

Fig. 6-21 (a) shows the SU-8 pattern on the Au electrode/substrate observed using optical microscopy, while Fig. 6-21 (b) shows the optical image of the MSP deposited in the opening. The MSPs were deposited from bath D under a current density of 5 mA/cm^2.

The main issue for this process also is how to release the MSPs from the substrate. Similar with the 'top down' process, a conductive polymer can be considered to be used as the electrode. Since SU-8 is very difficult to remove after the pattern is formed, a new type of photoresist might be needed to be explored.
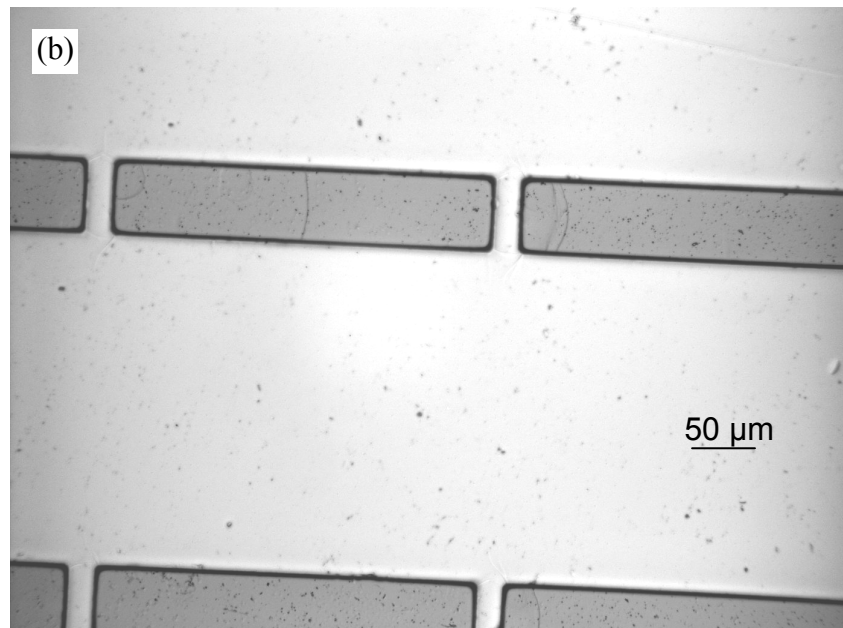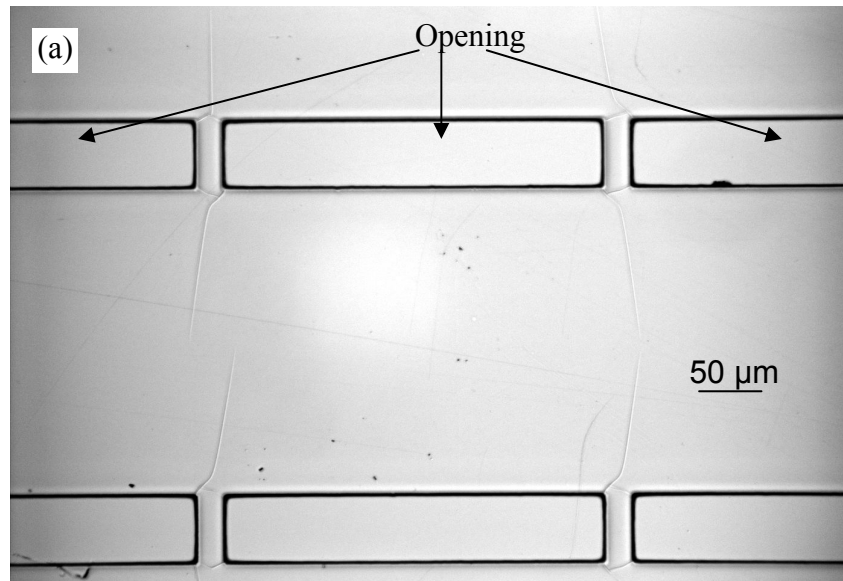
Fig. 6-21. (a) SU-8 pattern on the Au electrode/substrate; (b) the MSP deposited in the opening of patterned SU-8. The MSPs were deposited from bath D under a current density of 5 mA/cm^2.

6.5 Conclusion

The Fe-B thin films were synthesized using electrochemical deposition. The deposited films exhibit amorphous microstructure and uniform designed composition. The resonance behavior of amorphous Fe-B alloy as actuating materials for magnetostrictive sensor platforms were studied. The resonators made by plated amorphous Fe-B alloy exhibited high performance when the resonators were operated in a high frequency range. The plated amorphous Fe-B film also exhibited good thermal stability and soft magnetic properties. The plated amorphous Fe-B alloy is a good candidate for fabricating high performance AW sensor platforms in micro scale and might be suitable for fabricating magnetostrictive sensors in nanoscale.

References

[1]   L. G. Puckett, G. Barrett, D. Kouzoudis, C. Grimes, and L. G. Bachas, "Monitoring blood coagulation with magnetoelastic sensors," *Biosensors & Bioelectronics*, vol. 18, pp. 675-681, 2003.

[2]   C. A. Grimes, K. G. Ong, K. Loiselle, P. G. Stoyanov, D. Kouzoudis, Y. Liu, C. Tong, and F. Tefiku, "Magnetoelastic sensors for remote query environmental monitoring," *Smart Materials & Structures*, vol. 8, pp. 639-646, 1999.

[3]   K. G. Ong, K. F. Zeng, X. P. Yang, K. Shankar, C. M. Ruan, and C. A. Grimes, "Quantification of multiple bioagents with wireless, remote-query magnetoelastic microsensors," *Ieee Sensors Journal*, vol. 6, pp. 514-523, 2006.

[4]   J. Wan, H. Shu, S. Huang, B. Fiebor, I.-H. BChen, V. A. Petrenko, and B. A. Chin, "Phage-Based Magnetoelastic Wireless Biosensors for Detecting Bacillus Anthracis Spores," *IEEE Sensors Journal*, vol. 7, pp. 470 - 477, 2007.

[5]   R. Guntupalli, J. Hu, R. S. Lakshmanan, T. S. Huang, J. M. Barbaree, and B. A. Chin, "A magnetoelastic resonance biosensor immobilized with polyclonal antibody for the detection of Salmonella typhimurium," *Biosensors & Bioelectronics*, vol. 22, pp. 1474-1479, 2007.

[6]   E. T. Lacheisserie, D. Gignoux, and M. Schlenker, *Magnetism - Materials and Applications*: First Spring Science + Business Media, Inc, 2005.

[7]   E. P. Wohlfarth, *Ferromagnetic materials - A hand book on the properties of magnetically ordered substances*, vol. 1: North-Holland Publishing Company, 1980.

[8]   E. Lacheisserie, *Magnetostriction - Theory and Applications of Magnetoelasticity*: CRC Press, Inc., 1993.

[9]   R. Ray, R. Hasegawa, C. P. Chou, and L. A. Davis, "Iron-Boron Glasses - Density, Mechanical and Thermal-Behavior," *Scripta Metallurgica*, vol. 11, pp. 973-978, 1977.

[10]   M. A. Mitchell, A. E. Clark, H. T. Savage, and R. J. Abbundi, "Delta-E Effect and Magnetomechanical Coupling Factor in Fe80b20 and Fe78si10b12 Glassy Ribbons," *Ieee Transactions on Magnetics*, vol. 14, pp. 1169-1171, 1978.

[11]   C. P. Chou, L. A. Davis, and M. C. Narasimhan, "Elastic-Constants of Metallic Glasses," *Scripta Metallurgica*, vol. 11, pp. 417-423, 1977.

[12]   N. Fujita, M. Inoue, K. Arai, P. B. Lim, and T. Fujii, "Electrochemical deposition of amorphous FeB films with soft magnetic properties," *Journal of Applied Physics*, vol. 83, pp. 7294-7296, 1998.

[13]   N. Fujita, A. Tanaka, E. Makino, P. T. Squire, P. B. Lim, M. Inoue, and T. Fujii, "Fabrication of amorphous iron-boron films by electroless plating," *Applied Surface Science*, vol. 114, pp. 61-65, 1997.

[14]   I. Carabias, A. Martinez, M. A. Garcia, E. Pina, J. M. Gonzalez, A. Hernando, and P. Crespo, "Magnetostrictive thin films prepared by RF sputtering," *Journal of Magnetism and Magnetic Materials*, vol. 290, pp. 823-825, 2005.

[15]   *Instruction Manual for BAS Epsilon for Electrochemistry*: Version 1.50.69, 2004.

[16]   B. D. Cullity, *Elements of X-ray Diffraction*, second ed: Addison-Wesley Publishing Company, Inc., 1978.

[17]   D. Briggs, *Handbook of X-ray and Ultraviolet Photoelectron Spectroscopy* Heyden, 1978.

[18]   C. L. Briant and R. P. Messmer, *Auger Electron spectroscopy* Academic Press, 1998.

[19]   J. Vandenmeerakker, "On the Mechanism of Electroless Plating .2. One Mechanism for Different Reductants," *Journal of Applied Electrochemistry*, vol. 11, pp. 395-400, 1981.

[20]   W. Y. Hu and B. W. Zhang, "Electroless Deposition of Iron-Boron Alloys," *Transactions of the Institute of Metal Finishing*, vol. 71, pp. 30-33, 1993.

[21]   E. V. Rakovich, T. V. Gaevskaya, and V. V. Sviridov, "Composition and properties of electrodeposited iron-boron films," *Russian Journal of Applied Chemistry*, vol. 73, pp. 1167-1172, 2000.

[22]   "Handbook of X-ray Photoelectron Spectroscopy," *Physical Electronics Company*.

[23]   S. Gadad and T. M. Harris, "Oxygen incorporation during the electrodeposition of Ni, Fe, and Ni-Fe alloys," *Journal of the Electrochemical Society*, vol. 145, pp. 3699-3703, 1998.

CHAPTER 7

SYNTHESIS OF AMORPHOUS FE-B NANOWIRES AS MAGNETOSTRICTIVE

BIOSENSOR PLATFORM

7.1 Introduction

As discussed in chapter 4 & 5, the sensitivities of the MSPs and MCs increase with the decrease in their dimensions. To achieve a extremely high sensitivity, these sensors in micro/nano-scale are required.

One-dimensional nanostructures, such as nanowires and nanobelts, exhibit unique properties and provide new opportunities to develop revolutionary sensors. In recent years, chemical or biological sensors based on nanowires/nanobars have attracted lots of attention due to their great potentials as high performance sensors [1-4]. For example, the use of metal-oxide nanowires as gas sensors has been widely investigated. The principle of conventional metal-oxide gas sensors is that, the adsorption of gas molecules on the sensor surface causes a significant change in its electrical conductance. Since the nanowires possess very large surface-to-volume ratios which can overcome the absorption limitation of conventional solid-state sensors, gas sensors based on nanowires can obtain extremely high sensitivity [1]. Different types of metal-oxide nanowires as chemical sensor platforms have been studied. Gas sensors based on single-crystal/polycrystalline SnO_2 nanowires have been fabricated and well characterized. These sensors exhibit excellent sensitivity toward CO, ethanol, and NO_2 [5-7]. It has

211

been demonstrated that a detection limit of ~3 ppm and response/recovery times of several seconds were achieved using SnO_2 nanowire based sensors for detecting NO_2 [5]. Recently, gas sensors based on CdO, ZnO, and In_2O_3 nanowires have been fabricated, and exhibited high sensitivity and fast response time toward NO_2, ethanol, and NH_3, respectively [8-10]. Gas sensor fabricated based on carbon nanotubes also exhibit excellent performance. They can fingerprint a range of gases by monitoring the electrical breakdown of distinct gases at carbon nanotube tips. Also, they are not affect by the changes in the environment, such as temperature, humidity, and gas flow [11]. Based on the MEMS fabrication and nanowires technology, nanowire field-effect transistors (FETs) have been successfully developed and used as chemical sensors as well as biological sensors [3]. In a bulk FET, a semiconductor is used to connect the metal source and drain electrodes, in which the current between the source and drain is controlled by the voltage applied to the gate electrode on the semiconductor. A nanowire FET has similar configuration as that of bulk FET, but uses a single nanowire as the conducting channel between the source and drain electrode. The binding of molecules on the nanowire surface greatly affect its conductance. This feature makes nanowire FETs ultra-sensitive sensor platforms. The fabrication of Si-nanowire FET sensors, which were used to detect pH value and a variety of biomolecules, have been reported. The detections of single viruses and single-stranded DNA have been demonstrated using the sensors based on Si-nanowire FET [3]. Very recently, a novel biosensing platform using nanowires that consist of submicrometer layers of different metals was built [12]. By laying the different metals in specific orders, the nanowires with different characteristic patterns can be formed. These nanowire patterns can be rapidly identified by the optical reflectance

212

images, while fluorescence images are used to obtain the information of the target biological species binding on the antibodies that are immobilized on the nanowire surfaces. These nanowires form a new barcode system, which have been used to detect a variety of pathogens ranging from anthrax, smallpox to botulinum [12].

Since nanomaterials exhibit unique properties and great potential applications, the fabrication of high quality one-dimensional nanostructures has been intensively studied [13-17]. Many methods for synthesizing nanostructures have been developed, such as chemical vapor deposition [18, 19], wet chemistry [13], E-beam lithographic fabrication [20, 21], laser ablation [22], and template synthesis [17, 23, 24]. Template synthesis is the most widely used approach to grow nanomaterials with desired morphology, which was first used by C.R. Martin and his group [17, 25]. This method uses a template as a model to control the shape and the size of the nanostructures. A variety of templates have been employed, such as organic gelators [26], Proteins [27, 28], DNA [29], or carbon nanotubes [30-32]. Most of the template syntheses use two kinds of porous membranes, track-etching polycarbonate membranes and anodic aluminum oxide membranes [16, 17, 23, 25]. These membranes contain a large number of cylindrical pores with uniform diameters in the nanoscale. They are inexpensive, with high pore densities, while membranes with different pore size can be obtained based on the requirement. The desired materials are grown inside the pores of the templates, and after growth, the template can be removed to obtain individual nanomaterials or a nanomaterial array. Large area ordered one-dimensional nanostructures with high density and high aspect ratio can be fabricated using these porous membranes.

Porous track-etching polycarbonate membranes are made by bombarding the

polycarbonate film with charged particles in a nuclear reactor. When the particles pass through film, they break the chain of the polymer and leave the damaged tracks in the film. And then the film is put into a strong etchant, by which the damaged tracks are etched away to form the pores. The pore density of the membranes is controlled by the time that the polycarbonate films are exposed to the nuclear particles, while the pore size is precisely controlled by the etching time, etchant concentration and etching temperature [25].

Porous alumina membranes are obtained by electro-oxidation of high purity Al foil in an acidic solution. During the oxidation, a porous oxide layer is grown on the Al foil. Under constant potential, pores with uniform diameter can be formed and self-arrange into a hexagonal pattern. The pores propagate through the oxide layer and are perpendicular to the surface of the Al foil. The pore size and pore density are controlled by the anodizing potential [23, 25].

The synthetic approaches of growing materials into porous membranes include electrochemical deposition [23], chemical deposition [33], chemical polymerization [34], and sol-gel deposition [16, 25]. Electrochemical deposition is the most popular method. Fabrications of different kinds of nanomaterials using template-based electrochemical deposition have been reported. Most of metal nanowires with crystalline structures, such as Au [35], Ag [36, 37], Pt [38], Cu [39, 40], Pb [41], Zn [42] etc., have been fabricated using this method, since they can be easily electrochemically deposited. Many metal oxides, such as Cu_2O [43, 44], SnO_2 [45], In_2O_3 [46], and TiO_2 [47], as well as semiconductors, such as Bi_2Te_3 [48, 49], CdTe [23, 50], CdSe [23, 51], etc., have been successfully deposited by this method.

A big part of template based electrochemical synthesis is to fabricate magnetic nanostructures. Nanostructures of many ferromagnetic materials including Fe [52-54], Ni [17, 55], Co [56], and their alloys, such as Co-Fe [56], Fe-Ni [57, 58], Ni-Cu [59], et al., have been synthesized using template-based electrochemical deposition. The characterization of these nanostructures demonstrated that they have unique properties, such as highly anisotropic magnetization, enhanced coercivity, and abnormal temperature dependence of the coercivity, which indicate promising potential applications in high density information storage and high performance sensors [17, 60]. Up to date, most of these studies are devoted to the materials with crystalline structure and relative harder magnetic properties. Just a few investigations in nanostructures of amorphous materials, such as CoFeB and $Fe_{0.88-x}Co_xP_{0.12}$ alloy, have been reported [61, 62]. Also, even through magnetostrictive materials have wide applications in industry, there are few studies in one-dimensional nanostructures of magnetostrictive materials. Only recently, McGary et al. reported the fabrication of giant magnetostrictive Galfenol (GaFe) nanowires [63].

The purpose of this study is to fabricate magnetostrictive nanowires using template-based electrochemical deposition for the development of highly sensitive sensor platforms. In this study, Fe-B nanowires were fabricated by electrochemically depositing amorphous Fe-B alloy into ion track-etched polymer membranes. Amorphous Fe-B nanowires and nanowire arrays, in diameter ranging from 50 to 200 nm, have been fabricated. The nanowire arrays and individual nanowires were characterized using scanning electron microscopy (SEM), transmission electron microscopy (TEM), as well as Auger electron spectroscopy (AES).

215

7.2 Experimental

7.2.1 Fabrication of Amorphous Fe-B Nanowires and Nanowire Arrays

The magnetostrictive Fe-B nanowires and nanowire arrays were fabricated using template-based electrochemically deposition method. The amorphous Fe-B alloy was deposited from aqueous basic solution of $FeSO_4 \cdot 7H_2O$, KBH_4, $NaOH$, and $KNaC_4H_4O_6 \cdot 4H_2O$. Based on previous optimization, the deposition solution with the composition list in Table 7-1 was used for the fabrication. The solutions were prepared using the same procedure described in chapter 6 for Fe-B thin film deposition.

Commercially available polycarbonate membranes were used as the templates. The SPI-Pore™ polycarbonate membranes, circular in shape (thickness 6~10 μm, diameter 2.5 cm), were purchased from Structure Probe, Inc [64]. Templates with pore diameters of 200 nm, 100 nm, 50 nm, and 10 nm were employed for the fabrication. To form the electrical contact for the nanobar deposition, the membrane was first sputter coated with a very thin layer Au (~50 nm) on one side. This thin layer Au can not cover the pores. The membrane was then electroplated with Au using the sputtered Au layer as seed. A three-electrode electrochemical cell was employed for the deposition. That is, the standard Ag/AgCl electrode is used as the reference electrode; the platinum mesh is used as the counter electrode; and the polycarbonate with the Au side facing the counter electrode as the working electrode. The deposition was controlled using an Epsilon™ electrochemistry analysis network from Bioanalytical System, Inc., while commercially available Orotemp 24 solution was used as the deposition solution. The Au was deposited under a current density of 0.2 mA/cm^2 for 20 minutes. After the deposition, the Au layer (~ 500 nm) completely covered the pores   to serve as the electrical contact. Epoxy

was then applied to the Au side for electrical insulation.

To precisely control the deposition process, the three-electrode configuration, again, was employed for Fe-B nanowire fabrication. The polycarbonate membrane prepared as above was used as the working electrode, with the bare side facing the counter electrode during the deposition. The deposition was under constant current density: 5 mA/cm^2 and 10 mA/cm^2. The current density was evaluated based on the template size, pore size and pore density. The temperature was kept at 22±2 ^{o}C during the deposition. After the synthesis of the Fe-B nanobars, the membrane template was dissolved by Cl$_2$CH$_2$.

TABLE 7-1

Composition of Amorphous Fe-B Alloy Deposition Solution

	KNaC$_4$H$_4$O$_6$	NaOH	FeSO$_4$	KBH$_4$
Composition	90 g/L	16 g/L	20 g/L	16 g/L

The procedure of the Fe-B nanowire fabrication is shown in Fig. 7-1.

I   Porous membrane

I   Top view

II   Deposit bottom Au-electrode

Bottom Au electrode

III   Electrical insulate the Au electric contact by Epoxy

Bottom Au electrode

IV   E-C deposit Fe-B alloy

Bottom Au electrode

nanowires

V   Dissolve membrane

Bottom Au electrode

Side view

V

3-D view
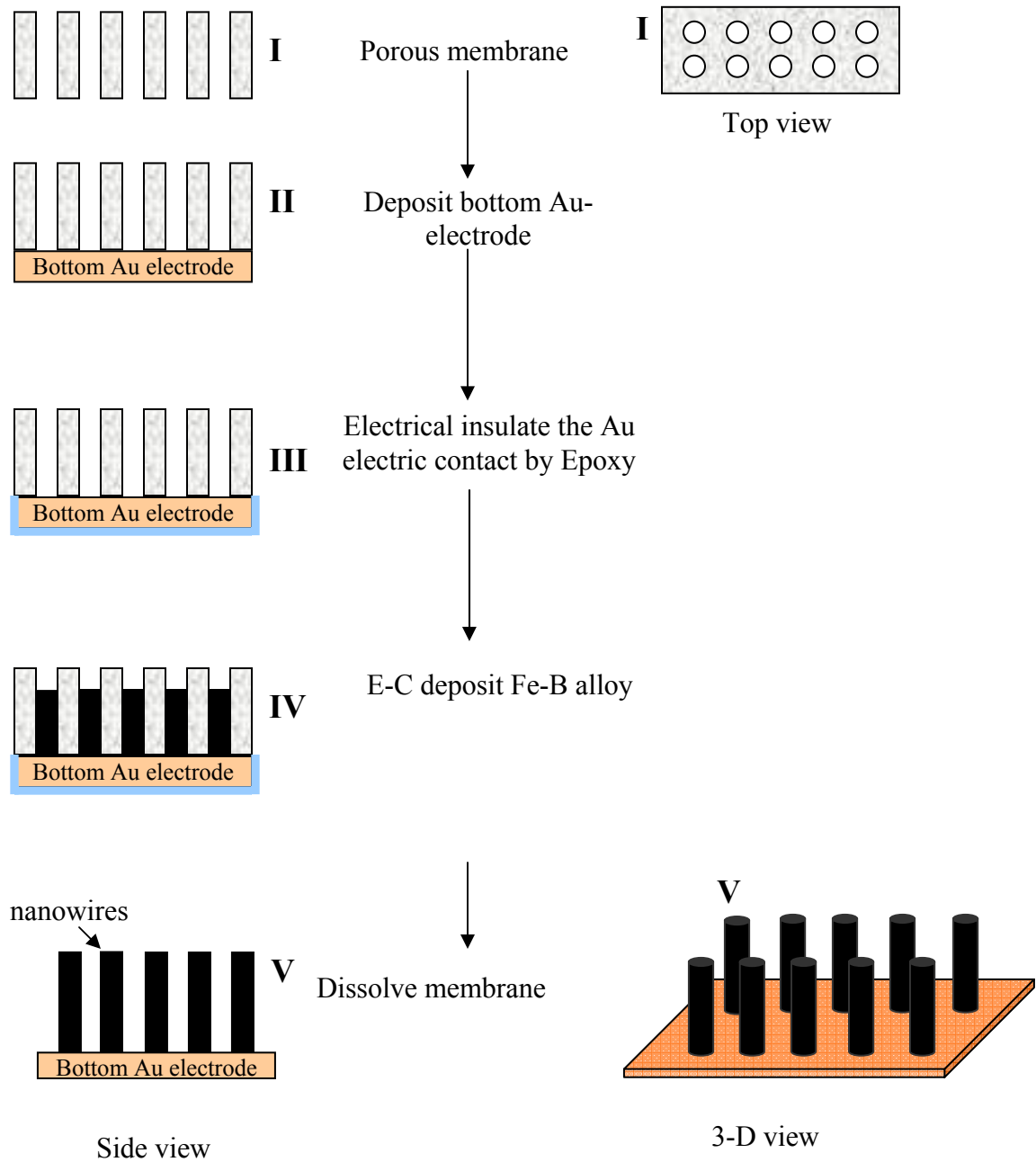
Fig. 7-1. Template synthesis of Fe-B nanowires.

218

7.2.2 Characterization of Fe-B Nanowires and Nanowire Arrays

7.2.2.1 Morphology of Fe-B Nanowires and Nanowire Arrays

The morphology of the individual nanowires and nanowire arrays were observed using scanning electron microscopy (LEO 982 SEM). Before the observation, the polycarbonate template was dissolved by Cl_2CH_2. To observe the individual nanowires, the Au electrode was first polished off by #2000 polish paper after the fabrication. The template was then dissolved, while the individual nanowires were collected by a magnet.

7.2.2.2 Microstructure of Fe-B Nanowires

High-resolution transmission electron microscopy (JEOL 2010 HRTEM) was used to characterize the morphology and microstructure of the Fe-B nanowires. The Fe-B nanowires were placed on the Cu TEM grid coated with lacy carbon for the observation.

7.2.2.3 Composition of Fe-B Nanowires

The composition of individual Fe-B nanowires was studied by Auger electron spectroscopy (Physical Electronics Model 680 Nanoprobe). Individual nanowires were released from the substrate. The e-beam with a diameter of ~20 nm was focused on individual nanowires. The compositions of selected spots along the length were analyzed by the AES. The outer surface of the nanowire was removed by Ar ion-beam sputtering and its composition was determined as a function of depth (relative to SiO_2). By this way, the compositions of the individual nanowire along the length direction as well as along the diameter direction were studied.

7.2.2.4 Thermal Stability of Fe-B Nanowairs

Similar as the Fe-B thin film, the thermal stability of the Fe-B nanowires was studied by annealing the nanobars at 200, 300, and 400 ^{o}C for 1 hour in a N_2 flow. The morphology and microstructure of the nanowires annealed at different temperatures were characterized by HRTEM and electron diffraction.

7.2.2.5 Magnetic Properties of Fe-B Nanowire Arrays

The magnetization (M-H loop) of the Fe-B nanowire arrays were measured by a DSM model Vibrating Sample Magnetometer (VSM). The samples were the nanowire arrays on the Au substrate with the template. The measurement was made with the H field applied parallel to nanowire axis (out of substrate plane) and perpendicular to the nanowire axis (in the substrate plan). The nanowire arrays with different diameters and lengths were measured.

To analyze the dipolar reaction between nanobars, two samples with multi-layer nanowires were prepared. Sample A was made of layers of Fe-B nanowires, 200 nm in diameter and of 4.5 μm in the length, inside the membrane. 5 layers of the membranes with nanowires were put together layer by layer using tape. And then it was cut to a 3 mm x 0.5 mm rectangular shape. The scheme is shown in Fig. 7-2. Sample B was prepared from nanowires in 50 nm diameter with the length of 3 μm. The membrane was dissolved by Cl_2CH_2, and then the nanowires were collected and aligned by a magnet on a small piece of wafer. A piece of tape was cover on the nanowires to fix them on the wafer. The SEM image of this sample is shown in Fig. 7-3. For both sample A and B, the M-H loop was measured along the direction 1, 2 and 3 marked on the Fig. 7-2 and 7-3.

Top View

Membrane

3mm

0.5mm [nanowires sample] ← Nanowires

⊗ Direction 3

Direction 1

Direction 2

Side view

|||||| ← nanowires

Nanowires in template (5 layers)

tape → [multilayer sample]

Direction 3
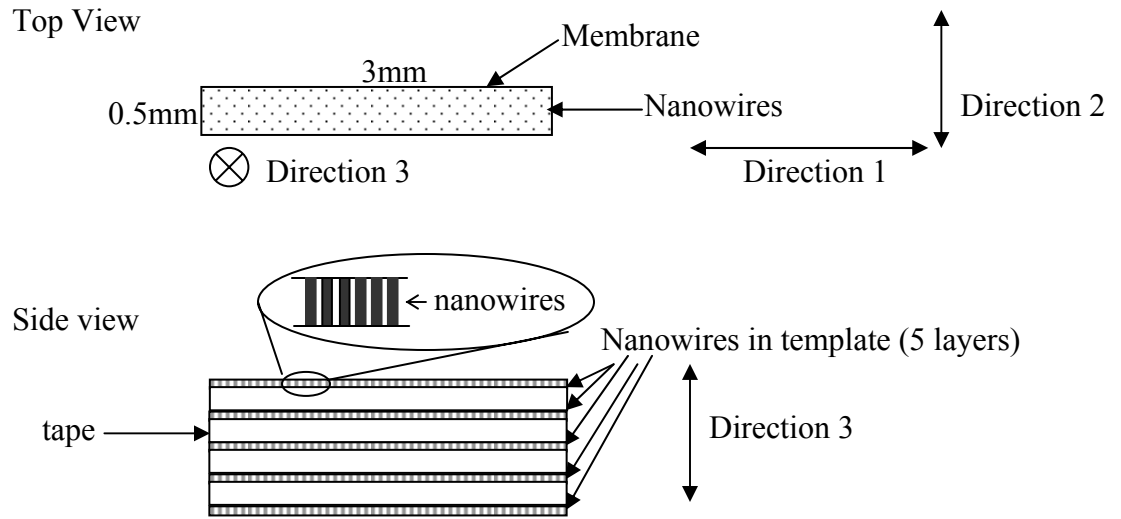
Fig. 7-2. Scheme of rectangular sample with several layers of nanowires in the diameter of 200 nm and the length of 4.5 µm.

nanowires

wafer

Direction 3

Direction 1

Direction 2: normal to the surface

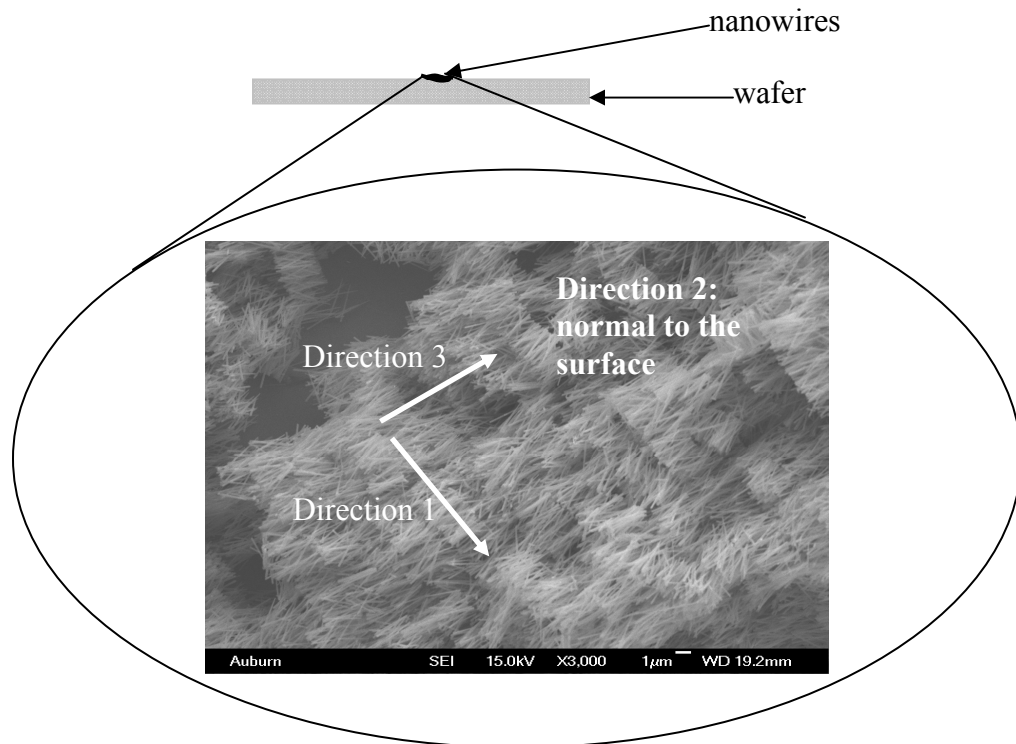Auburn   SEI   15.0kV   X3,000   1µm   WD 19.2mm

Fig. 7-3. SEM image for multilayer sample B.

221

7.3 Results and Discussions

7.3.1 Morphology of Fe-B Nanowires

SEM images of Fe-B nanowires fabricated in templates with pore sizes of 10 nm-200 nm are shown in Fig. 7-4. The images show Fe-B nanowires (2-5 μm in length) with different diameters fabricated in high density. Nanowires with uniform length can be fabricated on a substrate (as shown in Fig. 7-4 (a) and (b)) so that a sensor array can be fabricated, or can be released from the substrate to get individual nanowires (as shown in Fig. 7-4 (c) and (d)). Fig. 7-4 (e) and (f) are SEM images of individual nanowires fabricated using templates with pore size of 200 nm and 50 nm, respectively. The images revealed that the nanowires have very flat end. This morphology is expected for amorphous materials due to the isotropic growth in all direction. The flat end is very favorable for obtaining high Q value when the nanowire is operated as a resonator, since uneven ends of the nanowire gives a variation in the wire length direction and causes lower Q value. The SEM images indicated that there was no morphologic difference between the nanowires with different diameter/length and formed under different current densities. Since the polymer template is relatively soft, the pore morphology is not strictly defined. Therefore, it is observed that the diameter of nanowires increases slightly along the pore axis. Thus the final diameters of the nanowires are bigger than the pore sizes of the template. The SEM images of the nanowire arrays show that the overlap between the nanowires can be observed. This is because the nanowires were synthesized in commercial ion track membranes, in which the angle between the pore axis and the surface normal can be as high as 30°. The condition is worse for membranes with bigger

pores, and becomes better for membranes with smaller pore size (bigger pore distance).
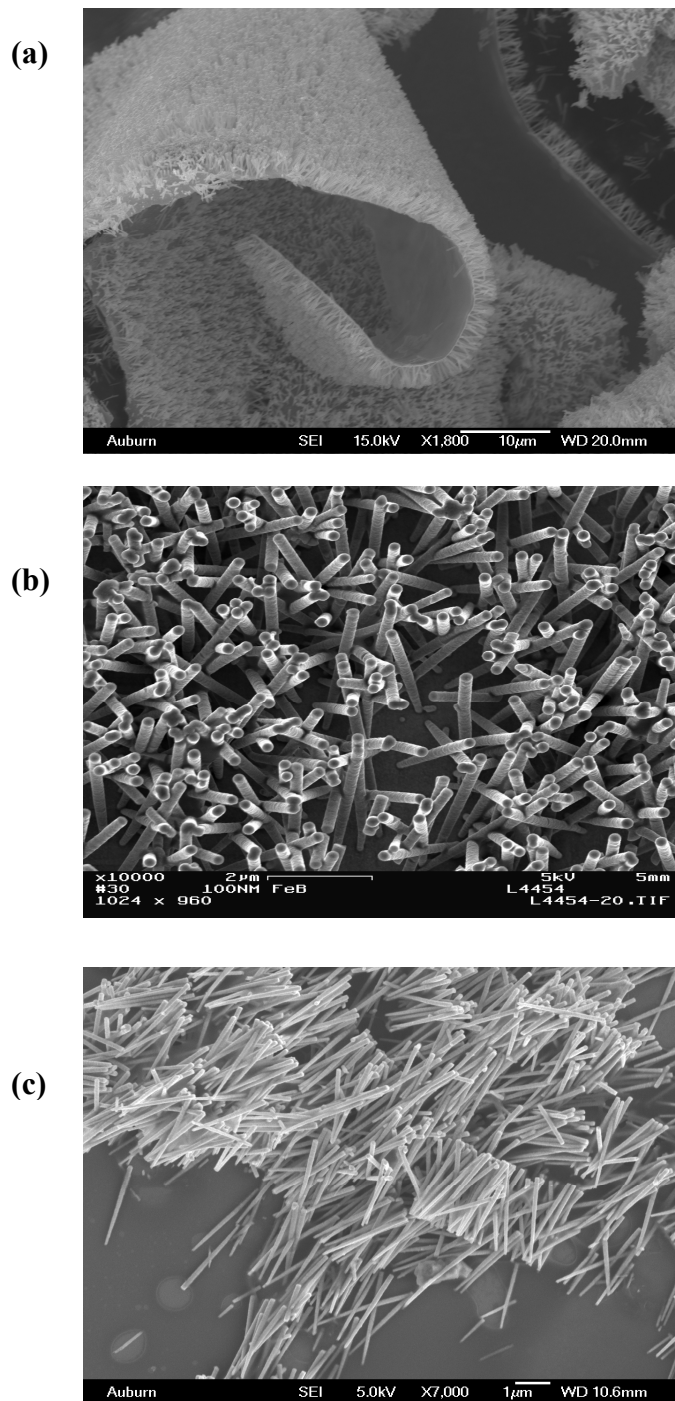
Fig. 7-4. SEM images for Fe-B nanowires and nanowire arrays fabricated in the template with the pore size of (a) 200 nm, (b) 100 nm, and (c) 50 nm.

(d)
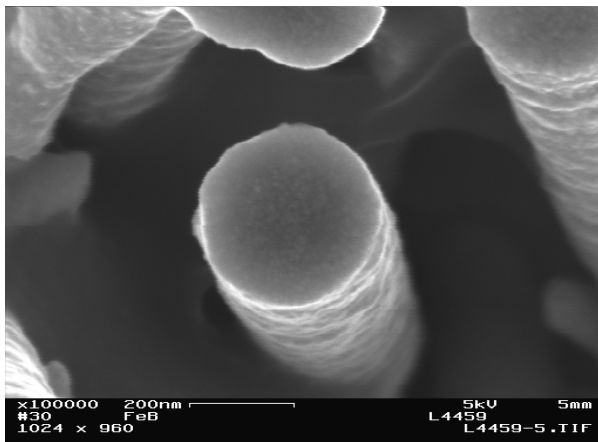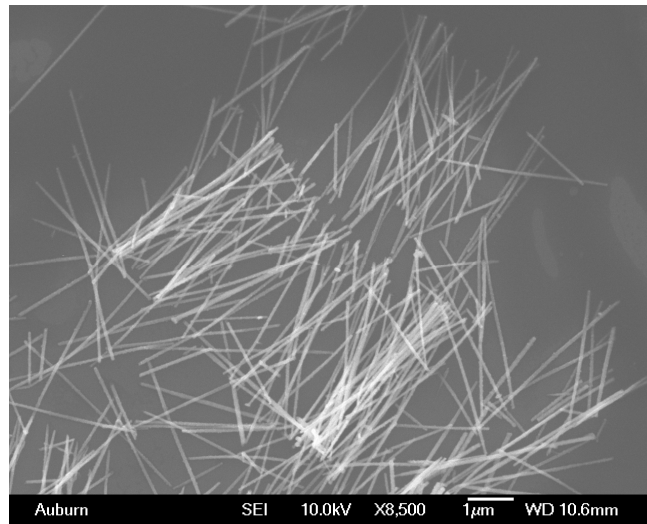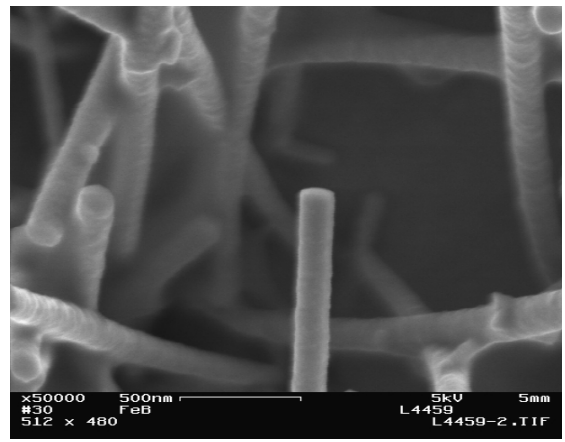
(e) **(f)**

Fig. 7-4 SEM images for Fe-B nanowires and nanowire arrays fabricated in the template with the pore size of (a) 200 nm, (b) 100 nm, (c) 50 nm, and (d) 10 nm; and focused SEM images of individual nanowire fabricated in the template with the pore size of (e) 200 nm, and (f) 50 nm.

7.3.2 Microstructure of Fe-B Nanowires

Fig. 7-5 shows the TEM image and the electron diffraction patterns of a Fe-B nanowire fabricated in the template with pore size of 50 nm. To study the details of the microstructure of the nanowire, the individual nanowire was characterized with the electron diffraction focused on the selected areas (SAED) along the nanowire. The electron diffraction patterns revealed that the microstructure of the nanowires is amorphous, and the results confirmed that the Fe-B nanowire has a uniform amorphous microstructure along the length. Fig. 7-6 is the TEM image and electron diffraction pattern of a Fe-B nanowire fabricated in the template with pore size of 10 nm. The diffraction pattern also reveals that the microstructure of the nanowire is amorphous. Nanowires with different lengths and diameters were characterized, and all exhibited a uniform amorphous microstructure. The Fe-B nanowires fabricated by template-based electrochemical synthesis exhibit same amorphous microstructure as that of Fe-B films.

Fig. 7-5. (a)TEM image of the Fe-B nanowires fabricated in template with pore diameter of 50 nm; (b) Electron diffraction patterns of this nanowire; (c) Focused TEM image of the Fe-B nanobars fabricated in template with pore diameter of 50 nm.
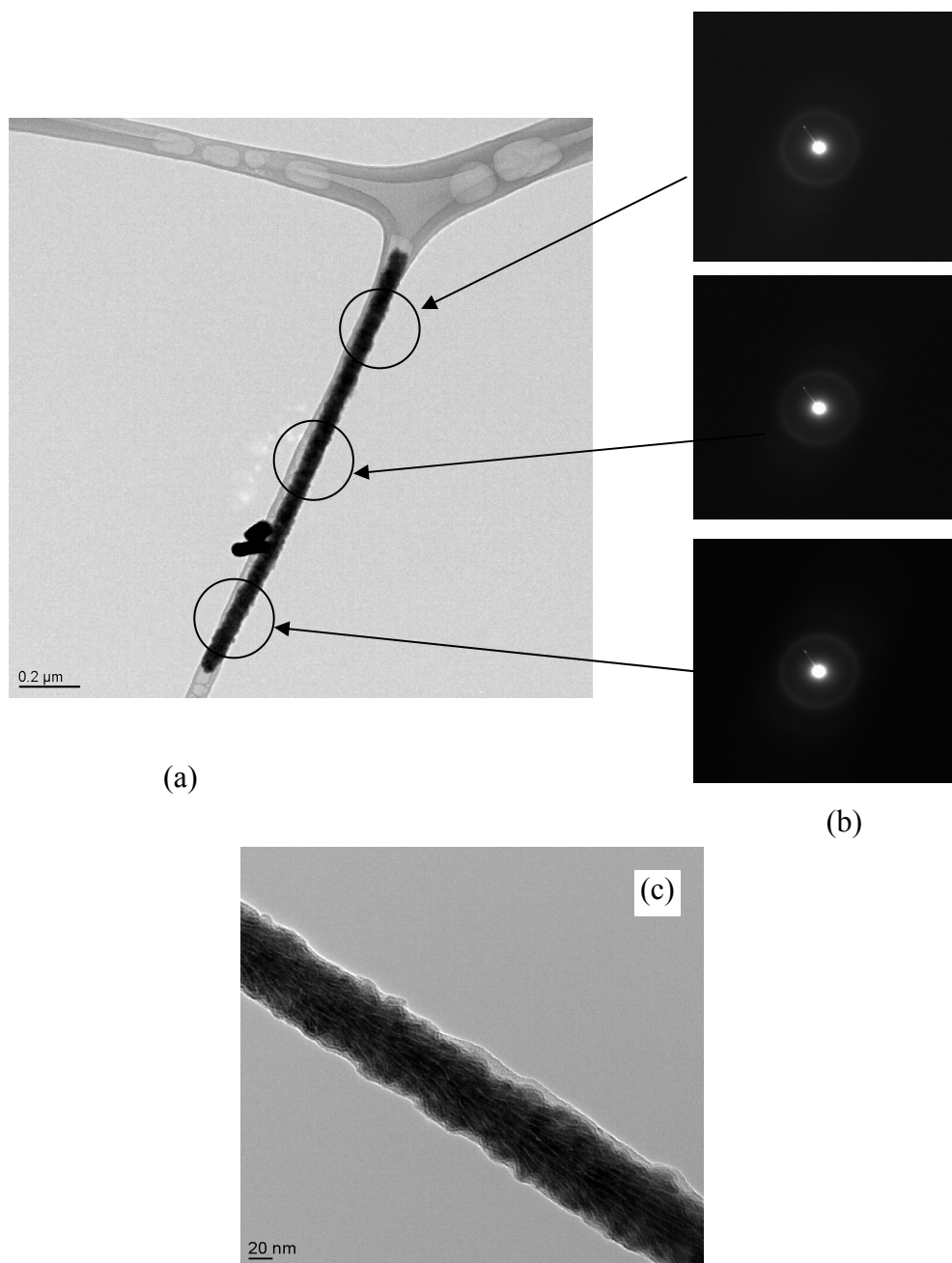
Fig. 7-6. (a)TEM image of a Fe-B nanowire fabricated in template with pore diameter of 10 nm; (b) Selected area electron diffraction patterns of this nanowire; (c) Focused TEM image of Fe-B nanowire fabricated in template with pore diameter of 10 nm.

7.3.3 Composition of Fe-B Nanowires

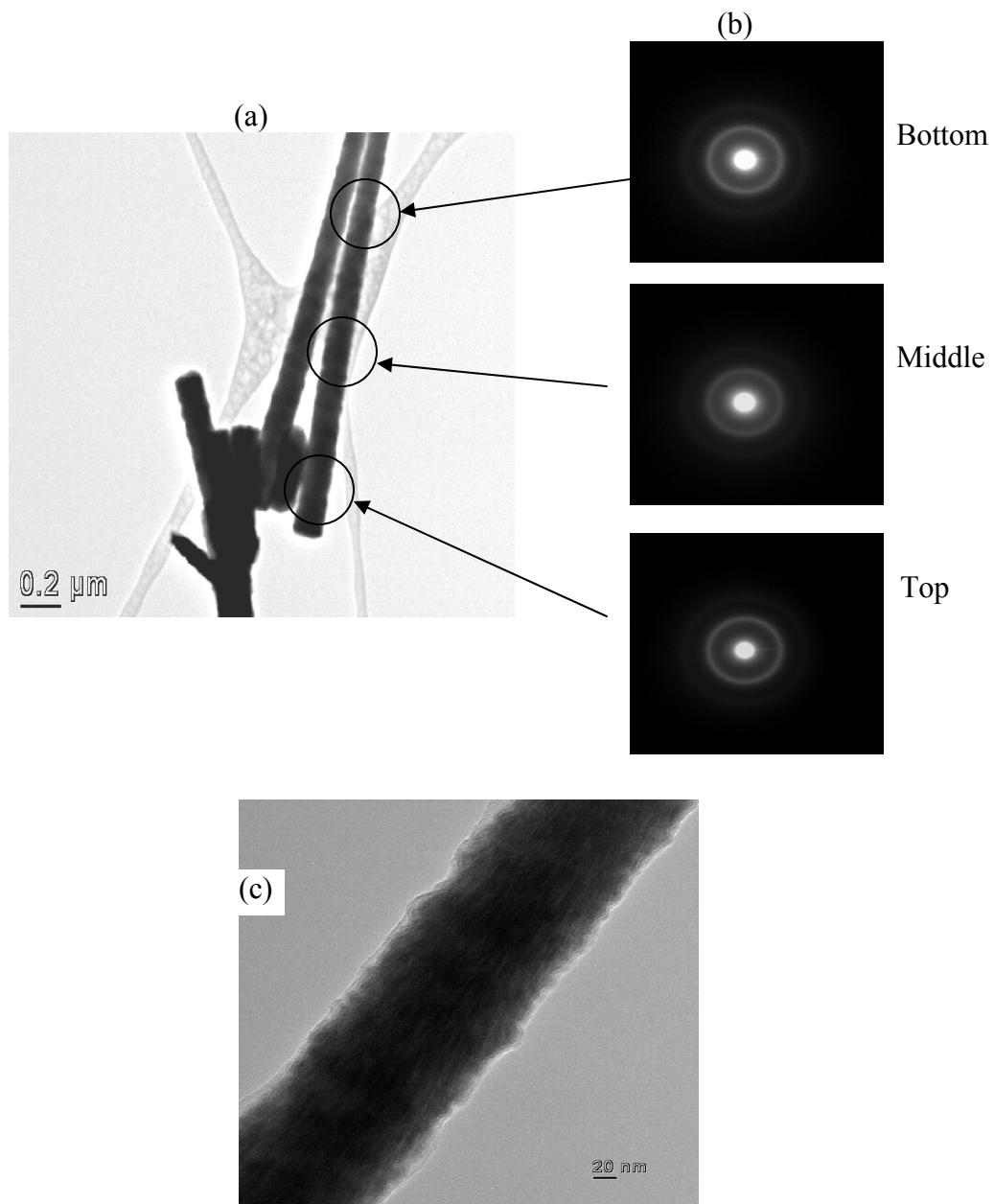The composition of individual Fe-B nanowires was determined by Auger electron spectroscopy. An individual nanowire, as shown in Fig. 7-7 (a), was placed on the Cu TEM grid coated with lacy carbon. This nanowire is deposited using the template with the pore diameter of 50 nm under a current density of 5 mA/cm^2. The electron beam was focused on selected points along the nanowire, and then combined with the Ar ion-beam sputtering etching, the compositions of nanowire surface, and at depths of approximately 5 nm, 10 nm, 18 nm, 30 nm and 42 nm from the surface, were measured. The composition distribution of this nanowire is shown in Fig. 7-7 (b) and (c). Fig. 7-7 (b) shows the composition contribution of the middle of the nanowire (point 6) along its diameter direction (at depths from the surface). A large concentration of oxygen was observed at the surface of the nanowire, which indicates the existence of an oxide layer on the outermost surface. It is believed that this oxidation layer is related to the passivation of nanowires in air. After removal of ~10 nm of the outermost surface, the concentration of the oxygen dramatically drops and remains constant (as does Fe and B) through the interior of the nanowire. To analyze the composition of the nanowire along its length direction, the compositions of 10 points along its length were characterized, after the nanowire was sputtering etched off 30 nm to eliminate the effect of the oxidation layer. The results were shown in the Fig. 7-7 (c). The analysis results revealed a fairly uniform composition distribution along the nanobar length direction. Except for points 1 and 10, which were located at the end of the nanowire, the variation in the ratio of Fe to B composition along the nanowire length direction was less than 3%. The analysis demonstrated that the whole nanowire exhibits uniform composition distribution except a

very thin oxidation layer (less than 10 nm) covering the surface.

The composition contribution along the length direction of a nanowire deposited under a current density of 10 mA/cm^2 is shown in Fig. 7-8. This nanowire was also fabricated in the template with pore diameter of 50 nm. The nanowire was placed on a Si wafer. After sputtering off 30 nm, the compositions of the 10 points along the length were analyzed. The results shown in Fig. 7-8 revealed a similar uniform composition: the composition shows very small variation, expect point 1 and 10.

These results demonstrate that the Fe-B nanowires fabricated by template-based electrochemical deposition exhibit uniform composition. A small amount of O can be observed through the nanobars. Same as the deposition of Fe-B films, the existence of oxygen may be attributed the hydroxide ions in the alkalic plating solutions.

In this study, the atomic concentration was determined using the Auger peak signal of each element. It should be aware that the results may be affected by many factors, such as the primary electron beam energy, the efficiency of the detector, sample surface roughness, and the tilt angle of the sample [67]. Therefore, errors may arise from the system and the measurements. Additionally, in the case of analyzing the sample in nano scale, the signal may not completely come from the sample itself. Even though the electron-beam with 20 nm diameter was focused on the nanowire, about 10 % of the signal can be attributed to the material outside of the selected area, even the substrate. This may further increase the error in the resultant composition.
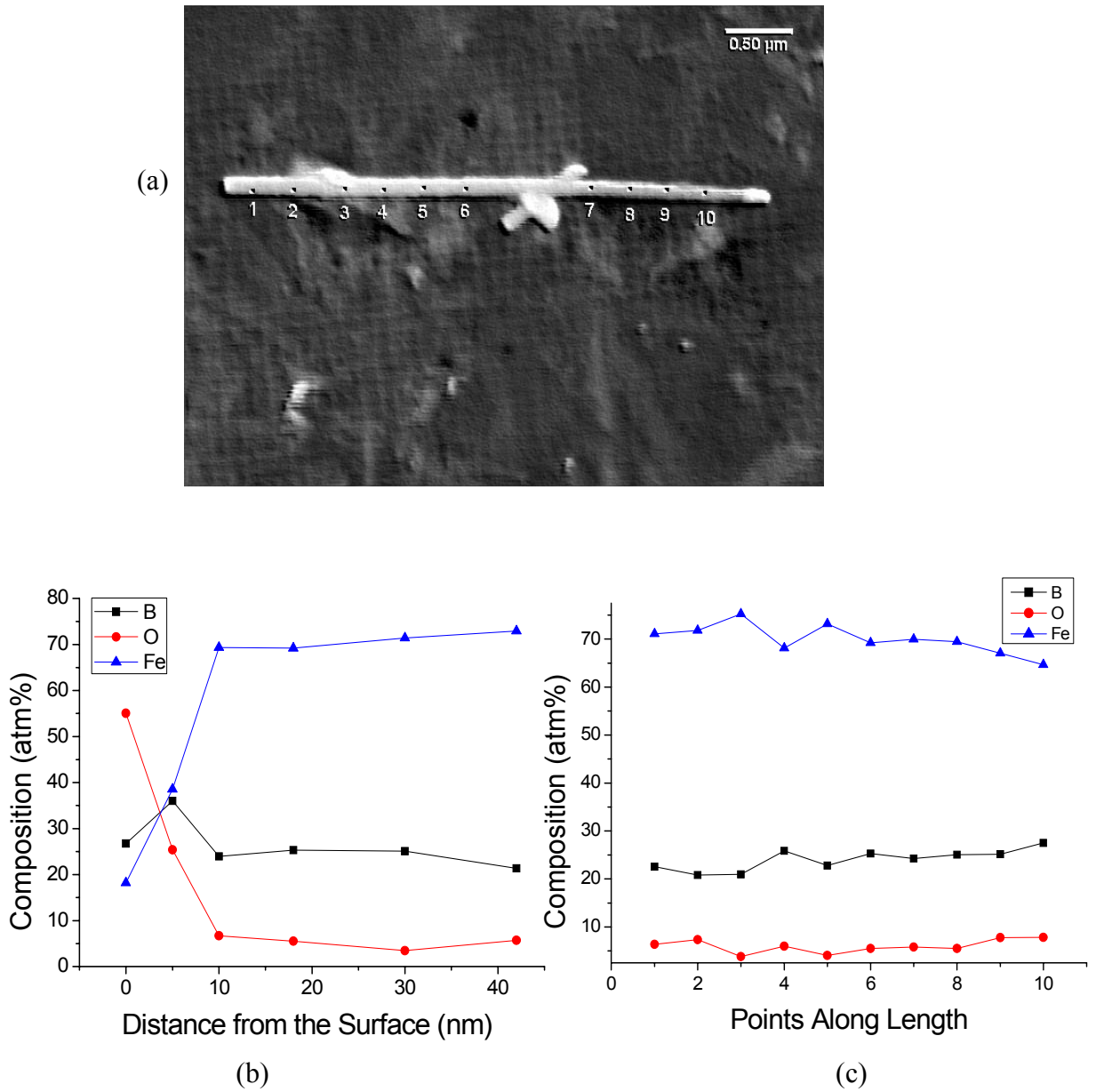
Fig. 7-7. (a) Individual nanowire deposited in the template with pore diameter of 50 nm under a current density of 5 mA/cm^2; (b) Composition distribution of point 6 on this nanowire along its diameter direction; (c) Composition distribution of this nanowire along its length direction.
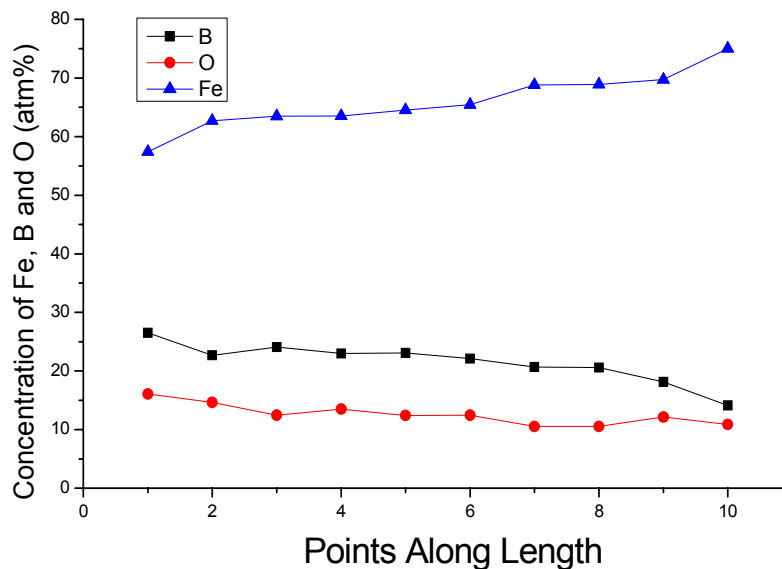
Fig. 7-8. Composition distribution along the length direction of a nanowire deposited in the template with pore diameter of 50 nm under a current density of 10 mA/cm^2.

7.3.4 Thermal Stability of Fe-B Nanowire

The thermal stability of the Fe-B nanowires was studied by annealing the nanowires in the N$_2$ environment. The TEM images and electron diffraction patterns of the nanowires annealed at 200, 300, and 400 ^{o}C for 1 hour are shown in Fig. 7-9, 7-10, and 7-11, respectively. The results showed that the nanowires maintained an amorphous microstructure after annealing at 200 ^{o}C and 300 ^{o}C. After annealing at 400 ^{o}C, the crystalline structures appear in the nanowires. Comparing the electron diffraction pattern with the standard electron diffraction patterns, it was found that BCC iron and FeO crystal formed after annealing at 400 ^{o}C. The Fe-B nanowires exhibit a good thermal stability.

231
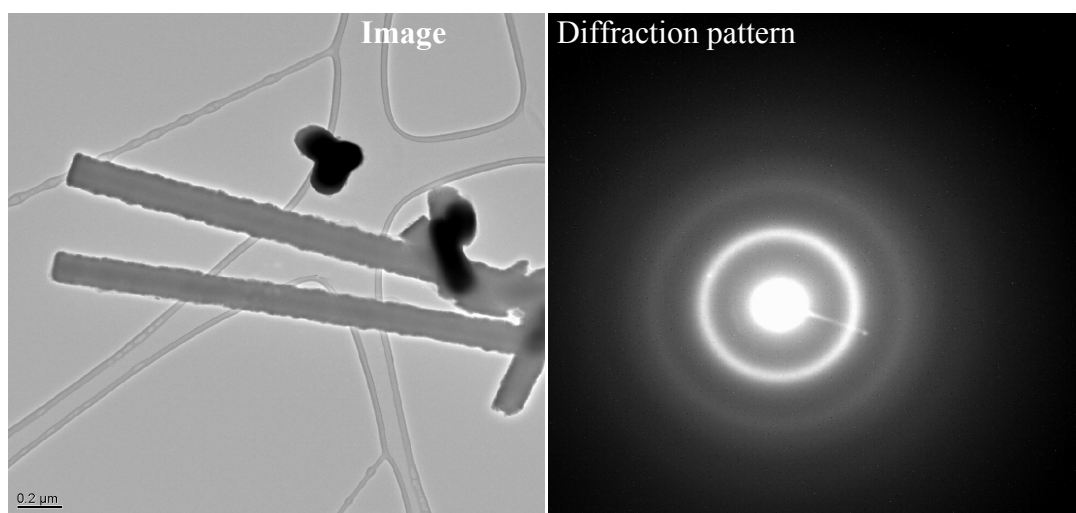
Fig. 7-9. The TEM image and diffraction pattern of Fe-B nanowires fabricated in template with pore diameter of 50 nm and annealed at 200 ^{o}C for 1 hour.
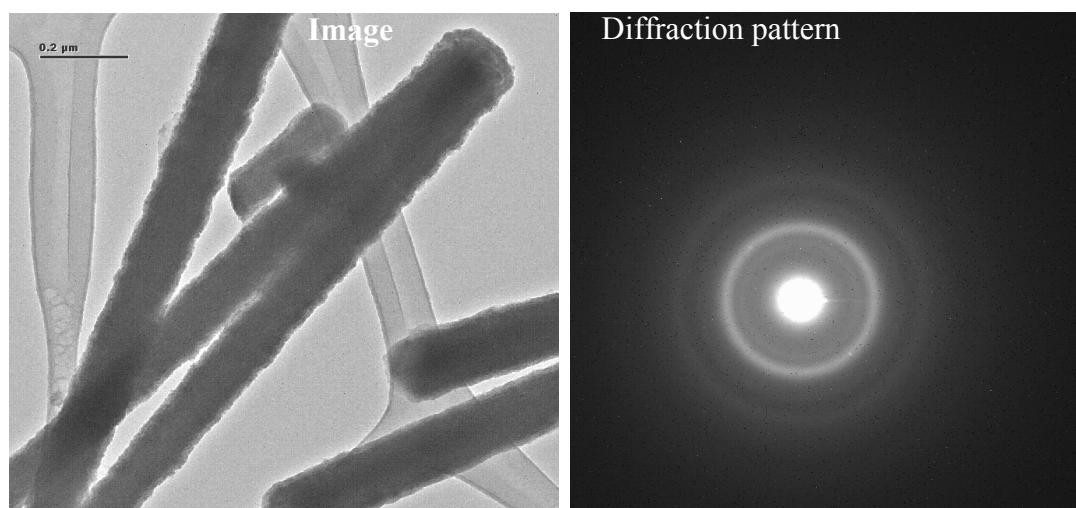
Fig. 7-10. The TEM image and diffraction pattern of Fe-B nanowires fabricated in template with pore diameter of 50 nm and annealed at 300 ^{o}C for 1 hour.

Image

Diffraction pattern

50 nm

Pattern of BCC Fe

(022)
(112)
(002)
(011)

Pattern of FeO

(004)
(113)
(222)
(022)
(002)
(111)
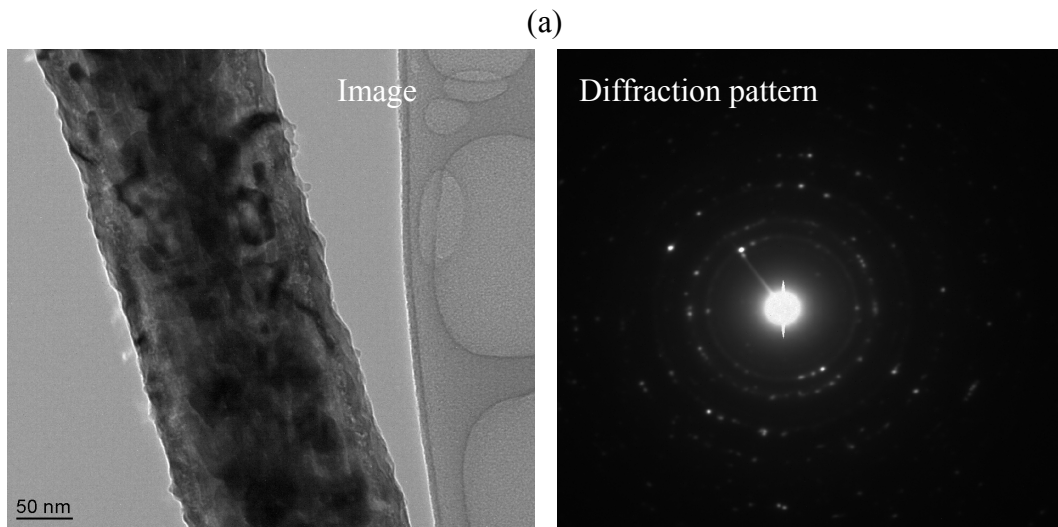
(b)

Fig. 7-11. (a) The TEM image and diffraction pattern of the Fe-B nanowire fabricated in template with pore diameter of 50 nm and annealed at 400 ^{o}C for 1 hour. (b) The comparison of standard electron diffraction patterns of BCC Fe and FeO with the electron diffraction pattern from (a).

7.3.5 Magnetic Properties of Fe-B Nanowires

The magnetization hysteresis loops for nanowire arrays fabricated in the membranes with pore diameter of 200, 100 and 50 nm are shown in Fig. 7-12. The magnetic field was applied perpendicular to the membrane (out-of-plane), thus parallel to the long axis of nanowires, as well as parallel to the membrane (in-plane), thus perpendicular to the long axis of nan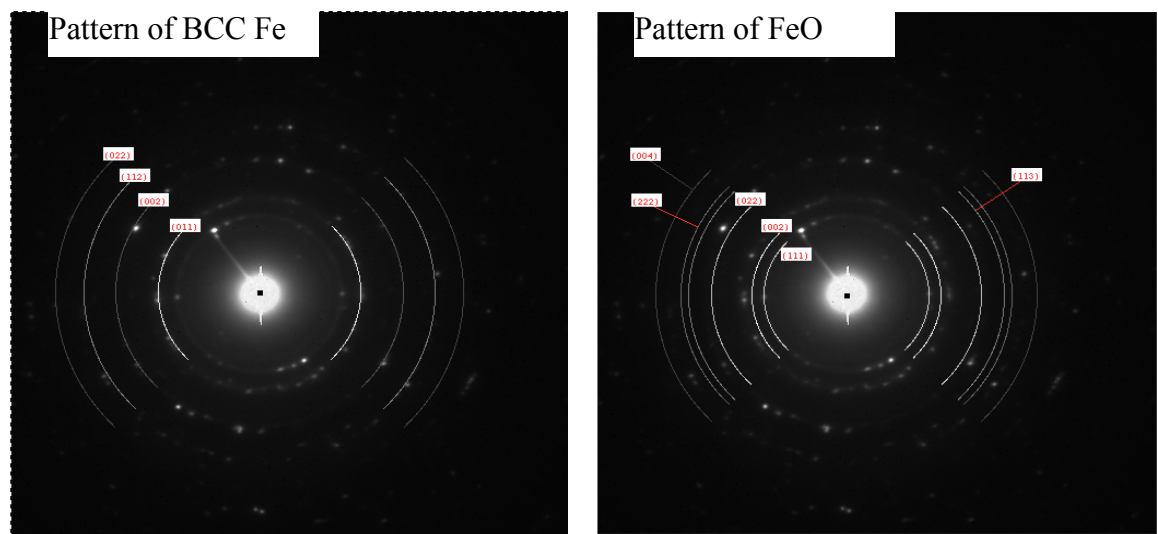owires. The conditions of the nanowires and their magnetic properties were listed in Table 7-2. With the diameter reduced from 200 nm to 50 nm, the coercivitive field along out-plane increased from 12 Oe to 164 Oe, while the coercivity of in-plane increased from 19 Oe to 335 Oe. For the nanowires in the diameter of 200 nm and the length of 1.8 μm, the easy axis of magnetization is along the in-plane direction; while for other nanowires, the out-of-plane is the easy axis of magnetization. All the nanowires exhibit very small squareness both in-plane and out-of-plane.

Since the nanowires have an amorphous microstructure, the magnetocrystalline anisotropy can be neglected. The coercivity of the nanowire arrays increases with the decrease of the nanobar diameter. The enhancement of the coercivity is due to the tendency of single-domain formation in the nanobars with very small diameter [17, 65]. The overall magnetic behavior of the nanowires is determined by the competition of the shape anisotropy and magnetostatic interaction between the nanowires.

It is observed that, for nanowires in the diameter of 200 nm and the length of 1.8 μm, the easy axis of magnetization is along the in-plane direction. A micromagnetic simulation performed by Ciureanu et al. demonstrated that the saturation field (M_S) of a ferromagnetic array is affected by the interaction field between nanowires along the in-plane direction and out-of-plane direction [61]. When the in-plane interaction field is

larger than $(2\pi/3)M_S$, the interaction field will cause the easy axis of magnetization along the in-plane direction [61]. For the nanowires in diameter of 200 nm, considering the small distance between the nanowires due to the high pore density (3 x 10^8 pores/cm^2 according to the manufacturer) and the overlap between the nanowires, the interaction field in the array is very large. This will cause the in-plane axis to be the easy axis of magnetization. However, for the nanowires in diameter of 200 nm and length of 4.5 μm, the length/diameter ratio is bigger. This indicates shape anisotropy has more effect, and the easy axis of magnetization is observed along the out-of-plane direction.

For the nanowire arrays with smaller diameter, the interaction field is smaller, where the shape anisotropic will dominate the magnetic behavior. The nanowires fabricated in this study exhibited large length/diameter ratio, which is more than 20 for nanowires in diameter of 100 nm and more than 60 for nanowires in diameter of 50 nm. The shape anisotropy tends to align magnetic moments along the wire direction because of the large aspect ratio. As shown in the hysteresis loop, the "easy axis of magnetization" is along the out-of-plane direction for the nanowires in diameter of 100 nm and 50 nm.

However, it should be note that, for all nanowire arrays, the coercivity along the wire direction is smaller than the coercivity perpendicular to the wire direction. This phenomenon was observed in the Co nanowires also deposited in the polycarbonate membranes [17]. The pore density in commercial ion track etched membranes is about 4 ~ 6 x 10^8 pores per centimeter according to the manufacturer, but the pores are not well-parallel. There are strong dipolar interactions between the dense but not well-paralleled nanobars formed in the commercial membranes. Research showed that the interaction between the nanowires would decrease the coercivity [66]. This effect is much stronger in

out-plane axis than in in-plane axis. This might strongly decrease the out-plane coercivity to a value that is smaller than in-plane coercivity.

The magnetic properties of multi-layer Fe-B nanowires (sample A and sample B) were summarized in Table 7-3. The hysteresis loops of these two samples exhibit similar magnetic behavior as the single layer nanowires. The easy axis of magnetization is still along the wire direction with smaller coercivity. It indicated that dipolar interactions between nanowires have much stronger effect along wire direction than that perpendicular to wire direction.
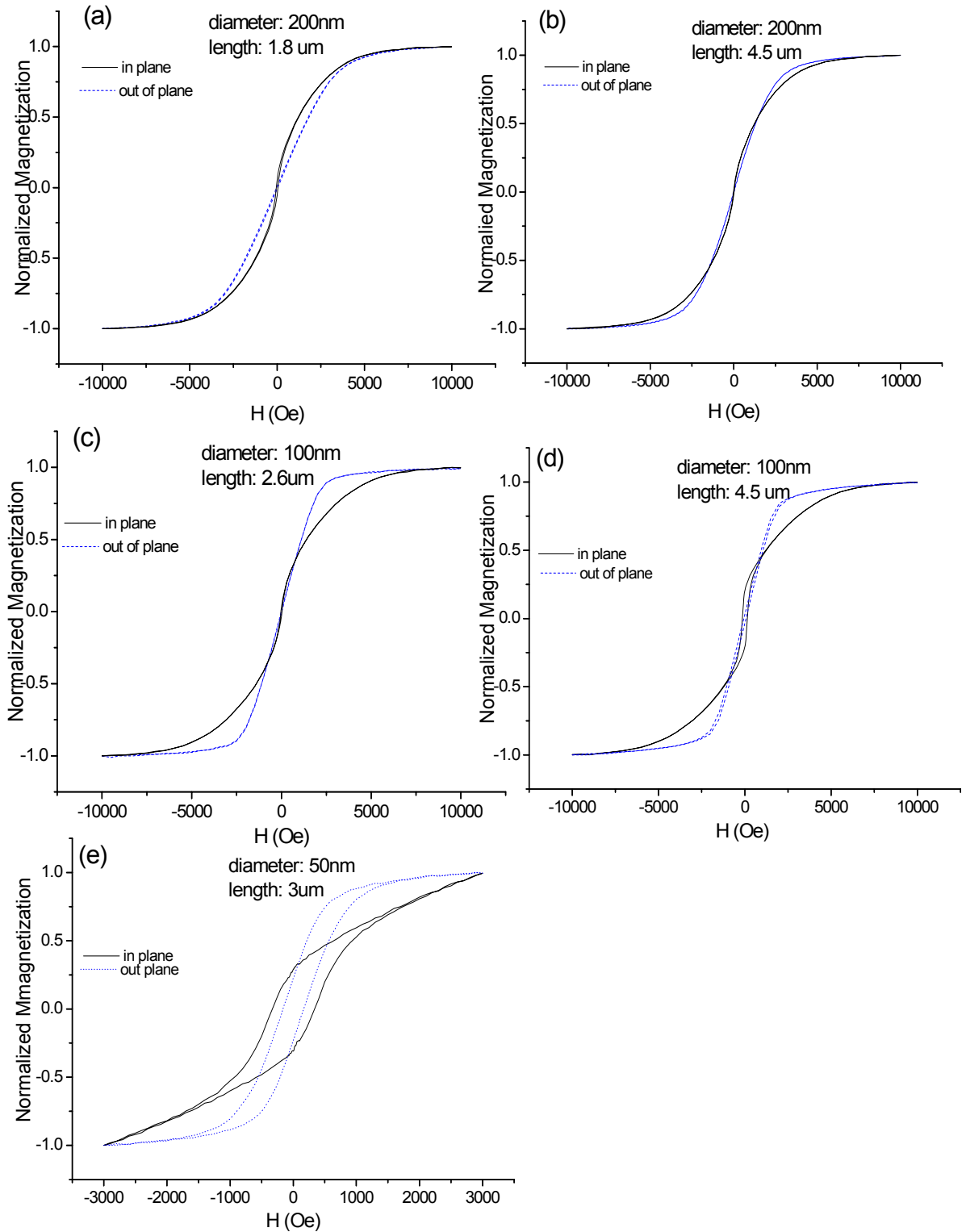
Fig. 7-12. Magnetization hystersis loops of nanowires with diameter of 200 nm (a, b), 100 nm (c, d) and 50 nm (e).

TABLE 7-2

Coercivity for Amorphous Fe-B Nanowires

		200 nm		100 nm		50 nm
	Length (μm)	1.8	4.5	2.6	4.5	3
Hc (Oe)	In plane	45	19	28	142	335
	Out of plane	32	12	17	62	164
Squareness	In plane	0.06	0.02	0.03	0.2	0.3
(Mr/Ms)	Out of plane	0.01	0.005	0.01	0.03	0.2

TABLE 7-3

Coercivity of Multi-layer Fe-B Nanowires along Different Directions

		Direction 1	Direction 2	Direction 3
Sample A	Hc (Oe)	24	19	13
Sample B	Hc (Oe)	299	321	214

7.4 Conclusion

To fabricate an extremely sensitive magnetostrictive sensor platform, Fe-B nanowires were synthesized using a template-based electrochemical deposition method. The composition and microstructure of the Fe-B nanowires are directly related to their performance as a biosensor platform. The Fe-B nanowire arrays and individual nanowires were characterized using scanning electron microscopy (SEM), transmission electron microscopy (TEM), as well as Auger electron spectroscopy (AES). Morphologically, nanowires have a very flat top and a smooth cylindrical surface, which are critical factors

for obtaining high performance as sensor platforms. Structurally, electron diffraction reveals that the Fe-B nanowires are amorphous. AES analysis indicates that Fe-B nanowirers show no significant compositional variation along the length direction. It is found that the nanowires were covered by an oxidation layer of a typical thickness of ~ 10 nm. It is believed that this oxidation layer is related to the passivation of nanobars in air. High temperature annealing and subsequent structural analysis indicate that the Fe-B nanowires possess a good thermal stability. The magnetization loop of the Fe-B nanowire arrays revealed the nanowires exhibit soft magnetic properties. The study demonstrated the fabrication of Fe-B nanowires as ultra-sensitive magnetostrictive sensor platforms.

References

[1]   A. Kolmakov and M. Moskovits, "Chemical sensing and catalysis by one-dimensional metal-oxide nanostructures," *Annual Review of Materials Research*, vol. 34, pp. 151-180, 2004.

[2]   D. H. Reich, M. Tanase, A. Hultgren, L. A. Bauer, C. S. Chen, and G. J. Meyer, "Biological applications of multifunctional magnetic nanowires (invited)," *Journal of Applied Physics*, vol. 93, pp. 7275-7280, 2003.

[3]   F. Patolsky, G. F. Zheng, and C. M. Lieber, "Nanowire-based biosensors," *Analytical Chemistry*, vol. 78, pp. 4260-4269, 2006.

[4]   Z. W. Pan, Z. R. Dai, and Z. L. Wang, "Nanobelts of semiconducting oxides," *Science*, vol. 291, pp. 1947-1949, 2001.

[5]   M. Law, H. Kind, B. Messer, F. Kim, and P. D. Yang, "Photochemical sensing of NO2 with SnO2 nanoribbon nanosensors at room temperature," *Angewandte Chemie-International Edition*, vol. 41, pp. 2405-2408, 2002.

[6]   E. Comini, G. Faglia, G. Sberveglieri, Z. W. Pan, and Z. L. Wang, "Stable and highly sensitive gas sensors based on semiconducting oxide nanobelts," *Applied Physics Letters*, vol. 81, pp. 1869-1871, 2002.

[7]   A. Kolmakov, Y. X. Zhang, G. S. Cheng, and M. Moskovits, "Detection of CO and O-2 using tin oxide nanowire sensors," *Advanced Materials*, vol. 15, pp. 997-+, 2003.

[8]   X. Liu, C. Li, S. Han, J. Han, and C. W. Zhou, "Synthesis and electronic transport studies of CdO nanoneedles," *Applied Physics Letters*, vol. 82, pp. 1950-1952, 2003.

[9]   Q. Wan, Q. H. Li, Y. J. Chen, T. H. Wang, X. L. He, J. P. Li, and C. L. Lin, "Fabrication and ethanol sensing characteristics of ZnO nanowire gas sensors," *Applied Physics Letters*, vol. 84, pp. 3654-3656, 2004.

[10]   D. J. Zhang, C. Li, X. L. Liu, S. Han, T. Tang, and C. W. Zhou, "Doping dependent NH3 sensing of indium oxide nanowires," *Applied Physics Letters*, vol. 83, pp. 1845-1847, 2003.

[11]   A. Modi, N. Koratkar, E. Lass, B. Q. Wei, and P. M. Ajayan, "Miniaturized gas ionization sensors using carbon nanotubes," *Nature*, vol. 424, pp. 171-174, 2003.

[12]   J. B. H. Tok, F. Y. S. Chuang, M. C. Kao, K. A. Rose, S. S. Pannu, M. Y. Sha, G. Chakarova, S. G. Penn, and G. M. Dougherty, "Metallic striped nanowires as multiplexed immunoassay platforms for pathogen detection," *Angewandte Chemie-International Edition*, vol.   45, pp. 6900-6904, 2006.

[13]   X. Wang and Y. D. Li, "Solution-based synthetic strategies for 1-D nanostructures," *Inorganic Chemistry*, vol. 45, pp. 7522-7534, 2006.

[14]   A. K. Wanekaya, W. Chen, N. V. Myung, and A. Mulchandani, "Nanowire-based electrochemical biosensors," *Electroanalysis*, vol. 18, pp. 533-550, 2006.

[15]   Q. Gu, C. D. Cheng, R. Gonela, S. Suryanarayanan, S. Anabathula, K. Dai, and D. T. Haynie, "DNA nanowire fabrication," *Nanotechnology*, vol. 17, pp. R14-R25, 2006.

[16]   P. Aranda and J. M. Garcia, "Porous membranes for the preparation of magnetic nanostructures," *Journal of Magnetism and Magnetic Materials*, vol. 249, pp. 214-219, 2002.

[17]   J. S. J. T. M. Whitney, P. C. Searson, C. L. Chien, "Fabrication and Magnetic Properties of Array of Metallic Nanowires," *Science*, vol. 261, pp. 1316-1319, 1993.

[18]   L. Zhang, R. Tu, and H. J. Dai, "Parallel core-shell metal-dielectric-semiconductor germanium nanowires for high-current surround-gate field-effect transistors," *Nano Letters*, vol. 6, pp. 2785-2789, 2006.

[19]   X. M. Cai, A. B. Djurisic, and M. H. Me, "GaN nanowires: CVD synthesis and properties," *Thin Solid Films*, vol. 515, pp. 984-989, 2006.

[20]   W. Fritzsche, K. J. Bohm, E. Unger, and J. M. Kohler, "Metallic nanowires created by biopolymer masking," *Applied Physics Letters*, vol. 75, pp. 2854-2856, 1999.

[21]   P. D. Miller, C. P. Liu, W. L. Henstrom, J. M. Gibson, Y. Huang, P. Zhang, T. I. Kamins, D. P. Basile, and R. S. Williams, "Direct measurement of strain in a Ge island on Si(001)," *Applied Physics Letters*, vol. 75, pp. 46-48, 1999.

[22]   A. M. Morales and C. M. Lieber, "A laser ablation method for the synthesis of crystalline semiconductor nanowires," *Science*, vol. 279, pp. 208-211, 1998.

[23]   Y. Chen, "Template-directed electrosynthesis of nanostructures ", vol. Ph. D.: Auburn University, 2004.

[24]   K. Jain and S. T. Lakshmikumar, "Porous alumina template based nanodevices," *Iete Technical Review*, vol. 19, pp. 293-306, 2002.

[25]   A. Huczko, "Template-based synthesis of nanomaterials," *Applied Physics a-Materials Science & Processing*, vol. 70, pp. 365-376, 2000.

[26]   Y. Ono, K. Nakashima, M. Sano, Y. Kanekiyo, K. Inoue, J. Hojo, and S. Shinkai, "Organic gels are useful as a template for the preparation of hollow fiber silica," *Chemical Communications*, pp. 1477-1478, 1998.

[27] R. Bhattacharya, C. R. Patra, S. F. Wang, L. C. Lu, M. J. Yaszemski, D. Mukhopadhyay, and P. Mukherjee, "Assembly of gold nanoparticles in a rod-like fashion using proteins as templates," *Advanced Functional Materials*, vol. 16, pp. 395-400, 2006.

[28] Y. Ono, Y. Kanekiyo, K. Inoue, J. Hojo, M. Nango, and S. Shinkai, "Preparation of novel hollow fiber silica using collagen fibers as a template," *Chemistry Letters*, pp. 475-476, 1999.

[29] W. Shenton, T. Douglas, M. Young, G. Stubbs, and S. Mann, "Inorganic-organic nanotube composites from template mineralization of tobacco mosaic virus," *Advanced Materials*, vol. 11, pp. 253-+, 1999.

[30] Y. G. Wang, Q. H. Li, T. H. Wang, X. W. Lin, V. P. Dravid, and S. X. Zhou, "In situ growth of nanowire on the tip of a carbon nanotube under strong electric field," *Applied Physics Letters*, vol. 86, 2005.

[31] T. Sainsbury and D. Fitzmaurice, "Carbon-nanotube-templated and pseudorotaxane-formation-driven gold nanowire self-assembly," *Chemistry of Materials*, vol. 16, pp. 2174-2179, 2004.

[32] M. Gao, L. Dai, and G. G. Wallace, "Glucose sensors based on glucose-oxidase-containing polypyrrole/aligned carbon nanotube coaxial nanowire electrodes," *Synthetic Metals*, vol. 137, pp. 1393-1394, 2003.

[33] C. A. Huber, T. E. Huber, M. Sadoqi, J. A. Lubin, S. Manalis, and C. B. Prater, "Nanowire Array Composites," *Science*, vol. 263, pp. 800-802, 1994.

[34] H. Masuda and K. Fukuda, "Ordered Metal Nanohole Arrays Made by a 2-Step Replication of Honeycomb Structures of Anodic Alumina," *Science*, vol. 268, pp. 1466-1468, 1995.

[35] W. B. Zhao, J. J. Zhu, and H. Y. Chen, "Photochemical synthesis of Au and Ag nanowires on a porous aluminum oxide template," *Journal of Crystal Growth*, vol. 258, pp. 176-180, 2003.

[36] G. Riveros, S. Green, A. Cortes, H. Gomez, R. E. Marotti, and E. A. Dalchiele, "Silver nanowire arrays electrochemically grown into nanoporous anodic alumina templates," *Nanotechnology*, vol. 17, pp. 561-570, 2006.

[37] X. Y. Sun, F. Q. Xu, Z. M. Li, and W. H. Zhang, "Cyclic voltammetry for the fabrication of high dense silver nanowire arrays with the assistance of AAO template," *Materials Chemistry and Physics*, vol. 90, pp. 69-72, 2005.

[38] C. D. Merritt and B. L. Justus, "Fabrication of microelectrode arrays having high-aspect-ratio microwires," *Chemistry of Materials*, vol. 15, pp. 2520-2526, 2003.

[39]   Y. Fukunaka, M. Motoyama, Y. Konishi, and R. Ishii, "Producing shape-controlled metal nanowires and nanotubes by an electrochemical method," *Electrochemical and Solid State Letters*, vol. 9, pp. C62-C64, 2006.

[40]   Y. Konishi, M. Motoyama, H. Matsushima, Y. Fukunaka, R. Ishii, and Y. Ito, "Electrodeposition of Cu nanowire arrays with a template," *Journal of Electroanalytical Chemistry*, vol. 559, pp. 149-153, 2003.

[41]   Y. T. Pang, G. W. Meng, L. D. Zhang, W. J. Shan, X. Y. Gao, A. W. Zhao, and Y. Q. Mao, "Arrays of ordered Pb nanowires with different diameters in different areas embedded in one piece of anodic alumina membrane," *Journal of Physics-Condensed Matter*, vol. 14, pp. 11729-11736, 2002.

[42]   J. G. Wang, M. L. Tian, N. Kumar, and T. E. Mallouk, "Controllable template synthesis of superconducting Zn nanowires with different microstructures by electrochemical deposition," *Nano Letters*, vol. 5, pp. 1247-1253, 2005.

[43]   J. Oh, Y. Tak, and Y. Lee, "Electrodeposition of Cu2O nanowires using nanoporous alumina template," *Electrochemical and Solid State Letters*, vol. 7, pp. C27-C30, 2004.

[44]   X. M. Liu and Y. C. Zhou, "Electrochemical synthesis and room temperature oxidation behavior of Cu nanowires," *Journal of Materials Research*, vol. 20, pp. 2371-2378, 2005.

[45]   M. J. Zheng, G. H. Li, X. Y. Zhang, S. Y. Huang, Y. Lei, and L. D. Zhang, "Fabrication and structural characterization of large-scale uniform SnO2 nanowire array embedded in anodic alumina membrane," *Chemistry of Materials*, vol. 13, pp. 3859-3861, 2001.

[46]   M. J. Zheng, L. D. Zhang, G. H. Li, X. Y. Zhang, and X. F. Wang, "Ordered indium-oxide nanowire arrays and their photoluminescence properties," *Applied Physics Letters*, vol. 79, pp. 839-841, 2001.

[47]   X. Y. Zhang, L. D. Zhang, W. Chen, G. W. Meng, M. J. Zheng, and L. X. Zhao, "Electrochemical fabrication of highly ordered semiconductor and metallic nanowire arrays," *Chemistry of Materials*, vol. 13, pp. 2511-2515, 2001.

[48]   L. Li, Y. W. Yang, X. H. Huang, G. H. Li, and L. D. Zhang, "Pulsed electrodeposition of single-crystalline Bi2Te3 nanowire arrays," *Nanotechnology*, vol. 17, pp. 1706-1712, 2006.

[49]   C. G. Jin, X. Q. Xiang, C. Jia, W. F. Liu, W. L. Cai, L. Z. Yao, and X. G. Li, "Electrochemical fabrication of large-area, ordered Bi2Te3 nanowire arrays," *Journal of Physical Chemistry B*, vol. 108, pp. 1844-1847, 2004.

[50]   A. W. Zhao, G. W. Meng, L. D. Zhang, T. Gao, S. H. Sun, and Y. T. Pang, "Electrochemical synthesis of ordered CdTe nanowire arrays," *Applied Physics a-Materials Science & Processing*, vol. 76, pp. 537-539, 2003.

[51]   D. S. Xu, X. S. Shi, G. L. Guo, L. L. Gui, and Y. Q. Tang, "Electrochemical preparation of CdSe nanowire arrays," *Journal of Physical Chemistry B*, vol. 104, pp. 5061-5063, 2000.

[52]   J. B. Wang, X. Z. Zhou, Q. F. Liu, D. S. Xue, F. S. Li, B. Li, H. P. Kunkel, and G. Williams, "Magnetic texture in iron nanowire arrays," *Nanotechnology*, vol. 15, pp. 485-489, 2004.

[53]   M. Kroll, W. J. Blau, D. Grandjean, R. E. Benfield, F. Luis, P. M. Paulus, and L. J. de Jongh, "Magnetic properties of ferromagnetic nanowires embedded in nanoporous alumina membranes," *Journal of Magnetism and Magnetic Materials*, vol. 249, pp. 241-245, 2002.

[54]   Y. Peng, H. L. Zhang, S. L. Pan, and H. L. Li, "Magnetic properties and magnetization reversal of alpha-Fe nanowires deposited in alumina film," *Journal of Applied Physics*, vol. 87, pp. 7405-7408, 2000.

[55]   C. L. Xu, H. Li, G. Y. Zhao, and H. L. Li, "Electrodeposition and magnetic properties of Ni nanowire arrays on anodic aluminum oxide/Ti/Si substrate," *Applied Surface Science*, vol. 253, pp. 1399-1403, 2006.

[56]   H. R. Khan and K. Petrikowski, "Synthesis and properties of the arrays of magnetic nanowires of Co and CoFe," *Materials Science & Engineering C-Biomimetic and Supramolecular Systems*, vol. 19, pp. 345-348, 2002.

[57]   H. Chiriac, A. E. Moga, M. Urse, and T. A. Ovari, "Preparation and magnetic properties of electrodeposited magnetic nanowires," *Sensors and Actuators a-Physical*, vol. 106, pp. 348-351, 2003.

[58]   T. Ohgai, L. Gravier, X. Hoffer, and J. P. Ansermet, "CdTe semiconductor nanowires and NiFe ferro-magnetic metal nanowires electrodeposited into cylindrical nano-pores on the surface of anodized aluminum," *Journal of Applied Electrochemistry*, vol. 35, pp. 479-485, 2005.

[59]   A. Encinas, M. Demand, L. Vila, L. Piraux, and I. Huynen, "Tunable remanent state resonance frequency in arrays of magnetic nanowires," *Applied Physics Letters*, vol. 81, pp. 2032-2034, 2002.

[60]   P. D. McGary, L. W. Tan, J. Zou, B. J. H. Stadler, P. R. Downey, and A. B. Flatau, "Magnetic nanowires for acoustic sensors (invited)," *Journal of Applied Physics*, vol. 99, 2006.

[61]   M. Ciureanu, F. Beron, L. Clime, P. Ciureanu, A. Yelon, T. A. Ovari, R. W. Cochrane, F. Normandin, and T. Veres, "Magnetic properties of electrodeposited CoFeB thin films and nanowire arrays," *Electrochimica Acta*, vol. 50, pp. 4487-4497, 2005.

[62]   D. S. Xue, J. L. Fu, and H. G. Shi, "Preparation and magnetic properties of Fe-0.88_xCoxP0.12 amorphous nanowire arrays," *Journal of Magnetism and Magnetic Materials*, vol. 308, pp. 1-4, 2007.

[63]   P. D. McGary and B. J. H. Stadler, "Electrochemical deposition of Fe1-xGax nanowire arrays," *Journal of Applied Physics*, vol. 97, 2005.

[64]   SPI Supplys, "Standard White Polycarbonate "Track Etch" Membrane Filters."

[65]   A. H. Morrish, *The physical principles of magnetism*: New York, Wiley 1965.

[66]   Q. F. Liu, C. X. Gao, J. J. Xiao, and D. S. Xue, "Size effects on magnetic properties in Fe0.68Ni0.32 alloy nanowire arrays," *Journal of Magnetism and Magnetic Materials*, vol. 260, pp. 151-155, 2003.

[67]   "Handbook of Auger Electron Spectroscopy", Physical Electronic Company.

CHAPTER 8

PERSPECTIVES

(1) As discussed previously, to obtain an extremely high sensitivity, MSMCs in a very small size are required. At current stage, the MSMCs are hand-made, which makes the fabrication of micro/nano-MSMC and the control of the MSMC's quality difficult. At next stage, the micro-fabrication of MSMC should be explored using the established microfabrication process based on amorphous Fe-B alloy. The objectives should be: 1) to fabricate the MSMCs with precisely controlled dimension, morphology, and quality; 2) to develop MSMC arrays; 3) to fabricate and characterize MSMC in micro/nano scale; 4) to perform the practical biological detection using MSMC biosensors.

(2) Fe-B nanowires were fabricated as nano-scale magnetostrictive biosensor platforms in this research. Since the nanowires should have very high resonance frequencies, the resonance behavior of the nanowires has not been characterized and the performance of the Fe-B alloy at giga-hertz range remains unknown. The current system has to be extended to characterize sensors with very high resonance frequency. Both frequency-domain and time-domain technology should be explored.

(3) To fabricate micro/nano MSP/MSMC with high performance, the immobilization of self-assembled monolayer (SAMs) of   some chemicals on the sensor surface has

to be studied in order to replace the gold layer used currently, since the gold layer (~40 nm thick) would be a extremely high mass load for micro/nano MSP/MSMCs. The SAM should be dense in order to protect the sensor from corrosion. The free end of the SAM has to be active to react with antibody/phage.